Turbine Design Combining Shaping and Flow Injection by Using Multiscale Methodology



Penghao Duan

Lady Margaret Hall

University of Oxford

Supervisor: **Prof. Li He**

A thesis submitted in partial fulfilment of

the degree of Doctor of Philosophy

Jan 2021

Acknowledgements

When I start writing up this part of the thesis, it has been the midnight. The dark views outside of the window absorb my memory of the four years that I have spent on my DPhil program. I feel so lucky that it has been a journey full of joy and excitement. I know, it is because of the help from people around me.

Let me begin by thanking my research adviser, Prof. Li He. He kept me on courses and served as my go-to source whenever I encountered difficulty. His insightful view of the problem always levels up the quality of my research. He gave me the freedom to organize my research time. He has set an extraordinary example for me not only as a scholar but also as a family man.

I am also grateful to my friends in Oxford over the past four years. Thank Harry Hien Phan for always discussing the academic problems with me. Thank Feng Wang, Min Yao and Haiteng Ma for giving their pieces of advice. Thank Hassan Saad Ifti for the kindness and smiles. Thanks to all my friends, Xiaodong Shi, Chen Chen, Zhoudan Pan, etc., for those days of laughing together and sharing thoughts. A special thanks go out to Mr Craig Parson for the patient IT support and for saving my disk.

Much gratitude goes to the China Scholarship Council and Lady Margaret Hall for the generous financial support.

Lastly, and most importantly, I thank my family - my dad, who supported every decision I made; my mom, who devoted her heart into the family; and the one, who completed me and brought harmony to my days.

Time is like a river. It may splash but never stop. I know we have to move on, but I'm so grateful that we had met and shared such a wonderful journey.

Abstract

Recent research suggests that the over tip leakage (OTL) flow at the transonic turbine tip exhibits several unique flow features such as the interaction with the cooling flow, the acceleration at divergent duct, the shock-boundary layer interaction and the choking at the rear portion of the tip. These flow features require the tip geometry optimization (shaping) to be considered together with tip cooling design (flow control). The blade designs that are generally used in the open literature suggest the shaping and the cooling flow control to be conducted sequentially: first, the shape of the blade is optimized, then the cooling holes are added to the uncooled blade for further optimization. However, because of the interactions between the cooling flow and the main flow, the non-linear nature of the flow in the turbine tip suggests that a potential gain may be obtained by combining blade shaping and cooling flow control.

Due to the significant disparity of the length scales between the cooling holes and the turbine blade, the combination of the cooling design and the tip geometry shaping tends to be too computationally expensive to be employed. The multi-scale method is adopted in a commercial solver to provide a fast and accurate solution for the turbine tip cooling optimization. The method uses source terms added to the coarse mesh to generate the solution close to the one obtained with a well-resolved mesh. The source terms are found to present not only the influence of mesh resolution but also the flow injection. The multi-scale results have been validated against the experimental data and the fine mesh results. The agreement shows the potential for this method to be used in cases with large length scale disparity. It is also the first-of-its-kind work to implement the multi-scale methodology in a commercial solver.

Following up the multi-scale method, a parameterization system and an optimization system are built to optimize the turbine cascades and the turbine stages using the multi-objective genetic algorithm (MOGA). Two

optimization approaches are compared: a) a sequential method that optimizes an uncooled shape first and then the cooling configuration, and b) a method that optimizes shaping and cooling concurrently. The concurrent method is found to obtain the aerothermal performance that cannot be achieved by sequential optimization. Moreover, by adding the cooling, the performance ranking of the uncooled blades in terms of the aerodynamic efficiency is changed. These observations are due to the interaction between the coolant and the tip leakage flow. They indicate that the coolant injected at the tip is not passive. By altering the tip leakage flow structure, the coolant can reduce the tip leakage loss. More detailed observations of the flow field indicate that the influence of the squealer height towards the aerodynamic efficiency is caused by two competing effects: the blockage effect to reduce the tip leakage mass flow rate and the sudden expansion loss effect to generate additional losses.

By identifying the vortices in the uncooled turbine stage and the 'equivalent cascade case', a unique vortex structure is found in the squealer cavity due to the relative movement of the casing. The moving casing forms a Casing-driven Cavity Vortex (CCD) along the cavity suction side and induces a counter-rotating Pressure-side Separation Vortex (PSV). The vortex pair changes the flow path of the OTL flow and thus influences the leakage mass flow rate. Furthermore, between the two counter-rotating vortices, the vortex pair entrains the base flow, which induces a high heat flux strip.

In the cooled turbine stage, the vortex pair blocks the leakage flow and makes the blockage effect brought by the cooling flow less effective. Thus in the optimization of the turbine stage, only in the flat tip, the cooling injection is found to improve the efficiency. As the squealer height increases, the vortices divert the original path of the cooling flow and entrain the hot leakage flow to attach to the tip surface. Thus, unlike the cases in the turbine cascade where the cooling effectiveness increases with the squealer height, in the turbine stage, as the squealer height increases, the cooling performance may reduce.

Contents

1 Introduction **1**

1.1 Research Background 2
1.2 Research Questions 6
1.3 Research Objectives 6
1.4 Organization of Report 7

2 Literature Review **8**

2.1 Optimization Used in Turbomachinery Design 8
2.1.1 Blade Design 8
2.1.2 Cooling and Flow Control 9
2.1.3 Shaping and Flow Control Combination 10
2.1.4 Multi-scale Method 11
2.2 Turbine Tip Design 12
2.2.1 Research Gaps in Turbine Design 12
2.2.2 Tip Designs to Improve Aerothermal Performance 14
2.3 Flow Features of the Transonic Turbine Tip 17

3 Methodology **20**

3.1 Two Levels of Modelling 20
3.1.1 Two Methods of Optimization Procedures 20
3.1.2 Two Types of Operating Conditions 21
3.1.3 Two Levels of Turbine Models 21
3.2 Baseline Solver Specifications and Guidelines 23
3.3 Multi-scale Methodology 24
3.3.1 Implementation of Multi-scale Method 27
3.4 Optimization System 28
3.4.1 Parameterization System of 3D HP Turbine Stage 29
3.4.2 Optimizer 31

3.4.3 Multidisciplinary Objective Functions 34
3.5 Summary 40

4 Methodology Validation **41**
4.1 Simple Concept Illustration Case for Multi-scale Method 41
4.2 Validation with Experimental Data 45
4.3 Multi-scale Method for Turbine Tip Cooling Simulation 51
4.4 Applicability of Multi-scale Method in Commercial Solver 55
4.5 Summary 56

5 Turbine Stage Design **58**
5.1 Blade Parameterization System 58
5.1.1 2D Blade Profile Parameterization 58
5.1.2 Explanation on Keeping Third-order Continuity 61
5.1.3 3D Blade Parameterization 64
5.1.3.1 Radial Equilibrium Condition 64
5.1.3.2 3D Stacking Line 66
5.2 Domain Blocking System 67
5.3 Parameterization of Other Design Features 69
5.3.1 Squealer Parameterization 70
5.3.2 Tip Cooling Parameterization 70
5.4 Other Blade Parameterization Systems 71
5.4.1 Blade Cooling Parameterization 71
5.4.2 Purge Flow Parameterization 73
5.5 Stage Design 74
5.5.1 Midspan Blade Profile Design 75
5.5.2 Baseline Blade Stacking 81
5.6 CFD Simulation of Subsonic Turbine Stage 82
5.6.1 Numerical Attributes for Flow Solver 82
5.7 Summary 88

6 Uncooled Turbine Blade Analysis **89**
6.1 Cascade with Varying Squealer Height 89
6.2 Turbine Stage with Varying Squealer Height 91
6.2.1 Optimization of Turbine Squealer Height 91
6.2.2 Over Tip Leakage Mass Flow Rate Variation 96
6.2.3 Vorical Structure in Turbine Stage 98

6.2.3.1 Vortex Identification and Quantification Method . . 98
6.2.3.2 Vortical structure 101
6.2.3.3 Explanation of Casing-Driven Cavity Vortices (CCV) 103
6.2.3.4 Explanation of Pressure-Side Separation Vortices (PSV) 105
6.2.3.5 Impact of Vorical Flow Structure 106
6.2.4 Tip Loss Generation Analysis 110
6.2.4.1 Total Loss in the Turbine Stage 110
6.2.4.2 Loss Sources in the Turbine Stage 113
6.2.4.3 Out-tip Mixing Loss Model 116
6.2.4.4 Choking in the Transonic Stage 122
6.2.4.5 Influence of Squealer Height on Heat Transfer Performance 123
6.3 Summary 128

7 Cooled Turbine Blade Analysis 129
7.1 Aerothermal Optimization (cascade) 130
7.1.1 Cascade Optimization Conducted Sequentially 130
7.1.2 Cascade Optimization Conducted Concurrently 132
7.1.3 Impact of Flow Injection on Efficiency 133
7.1.4 Impact of Squealer Height on Heat Transfer 135
7.2 Aerothermal Optimization (Turbine Stage) 136
7.2.1 Stage Optimization Conducted Sequentially 138
7.2.2 Stage Optimization Conducted Concurrently 139
7.2.3 Impact of the Cooling Configuration 141
7.2.4 Impact of the Squealer Height 144
7.3 Summary 146

8 Conclusions and Suggested Future Work 149
8.1 Sequential and Concurrent Optimizations 149
8.2 Transonic and Subsonic Stages 150
8.3 Turbine Cascades and Turbine Stages 151
8.4 Suggested Future Work 151

Bibliography 152

List of Figures

1.1 Purge flow path llustrated as the blue arrows. 2
1.2 Diagram of blade cooling flow. 3
1.3 Comparison of working flow between sequential and concurrent design method. 4

2.1 Separation bubble on the pressure side of the tip. 15

3.1 Flow chart for the implementation of the multi-scale method in CFX. 29
3.2 Flow chart of optimization system. 30
3.3 Parameterization system for a cooled 3D turbine blade with 32 cooling slots. 32
3.4 Mesh for a cooled 3D turbine blade with 32 cooling slots. 33
3.5 Overview of the Optimization flow chart. 34
3.6 The technical "juggling" problem of the turbine designer 35
3.7 Conceptual expansion process of cooled turbine. 37

4.1 Computational domain of the simple concept illustration case. 42
4.2 Process to collect the source terms from block 2 and block 5. 43
4.3 Normalized heat flux at the bottom wall. 44
4.4 Normalized temperature along AB-AB line 45
4.5 Propagation of the source terms from block 2 and block 5 to block 3 and block 4. BCs stands for the boundary conditions. 46
4.6 Normalized heat flux at the bottom wall. The heat flux is normalized by Equation 4.1. In plot *c*), the source terms are propagated to block 3 and block 4 to reproduce the fine mesh solution. 47
4.7 Normalized temperature along AB-AB line. The temperature is normalized by the stagnation temperature at the mainstream inlet. The line AB-AB is obtained by the intersection of the cross-section plane A-A in Figure 4.1 and the cross-section plane B-B in Figure 4.3. . . 48

4.8 HTC contours on the uncooled tip. 48
4.9 Circumferential averaged HTC value at the tip along axial chord for uncooled blade. 49
4.10 HTC contours on the squealer with nine cooling holes near the pressure side. 50
4.11 Circumferential averaged HTC values at the tip along axial chord for the blade with nine cooling holes near the pressure side. 51
4.12 Mesh of the computational domain in the transonic tip cooling case. . 52
4.13 Cooling configurations of 12 cooling holes for Case 1 and Case 2. . . 53
4.14 Normalized heat flux contours on the tip for Case 1. Multi-scale method with and without injection both can reproduce the fine mesh solution. 54
4.15 Circumferential averaged normalized heat flux at tip in Case 1. . . . 55
4.16 Normalized heat flux contours on the tip for Case 2. 55
4.17 The circumferential averaged normalized heat flux at the tip in Case 2. 56

5.1 11 parameters to parameterize airfoil 60
5.2 $Curv1$, $curv2$ and $curv4$ are generated by ninth order Bezier curves which are formed by 10 control points 62
5.3 Surface-curvature Distribution - Four blades have the same pressure side curve but different curvature distribution in suction side curve . 63
5.4 Different Performance of Four Blades with Different Curvature Distribution 64
5.5 Local cylindrical coordinate system for 3D stacking NURBS 67
5.6 Twist and tapper of the blade in the parameterization system 68
5.7 Optimized 2D block using shifted periodic topology. 69
5.8 3D stator and rotor blocks 70
5.9 The parameterization of squealer 71
5.10 2D block when the squealer is added at the blade 72
5.11 The block at the tip is split to accommodate the cooling slot 73
5.12 The blocks with or without injection holes are inserted into the cooling slots 74
5.13 $m \times n$ matrix used to represent blade cooling system. 75
5.14 Turbine stage design procedure 76
5.15 The velocity triangle of the baseline model. 77
5.16 Correlation of stagger angle for typical turbine blade sections. 78

5.17 Equivalent radius of curvature r_{ss} and triangle $\triangle O_r - pt3_{up} - pt3$ used to compute the throat width, t, and the unguided turning, $\delta_{unguided}$. . 79
5.18 Blade 2D profiles at different radial sections in the stator and the rotor of the subsonic stage 81
5.19 Blade 2D profiles at different radial sections in the stator and the rotor of the transonic stage 82
5.20 Comparison of the blade midspan profiles in the subsonic and transonic turbine stage 83
5.21 Radial variation of the flow coefficient, the loading coefficient and the reaction for rotor. 84
5.22 Computational domain of the subsonic turbine. 84
5.23 Computational domain of the transonic turbine. 85
5.24 Baseline model efficiency in the subsonic and the transonic stages shown in Turbine Smith's Chart. 86
5.25 Loading plots of the rotor blade at the midspan and the 95% span in the subsonic and transonic stages. 87

6.1 Variation of the aerodynamic efficiency, the OTL mass flow rate and sudden expansion loss with increasing squealer height at two different tip clearances 90
6.2 Flow chart of optimization system. 93
6.3 Sampling and iterations of optimization. 94
6.4 Optimization of the squealer height in the subsonic and the transonic stage. 95
6.5 Comparison of the efficiency and normalized heat load in the subsonic and the transonic stage. 95
6.6 The tip periphery surface and the squealer periphery surface used to investigate the OTL flow. 96
6.7 The OTL mass flow rate at various squealer height for the subsonic and the transonic turbine stage. 97
6.8 The mass flux vectors along the tip periphery surface are plotted for the squealer height of 0%, 0.5% and 3%. 99
6.9 Identification and quantification of the vortex in the tip region. 101
6.10 Vortical structures in the squealer tip region. 102
6.11 The vortical structures in the baseline case and two test cases. 104
6.12 Schematic for the generation of the CCV. 104

6.13 The velocity field generated by an inviscid wall is kinematically equivalent to an image vortex. 105
6.14 Schematic for the generation of the PSV. 106
6.15 The 2D streamlines combined with the velocity vectors at axial cut plane with 15% of the axial chord. 107
6.16 The vortex structure at the tip. This example is taken at the squealer height of 3% in the transonic stage. 107
6.17 The mass flow rate deficit can be explained by the vortex structure at the tip. This example is taken at the squealer height of 3% in the transonic stage. 108
6.18 The vortical structures of the OTL flow at the tip region for the subsonic and the transonic rotors with and without squealer tip. 109
6.19 The velocity vector plot at the axial cut plane for the subsonic and the transonic rotors with and without squealer tip. 110
6.20 Computation of the equivalent efficiency. 111
6.21 The variations of the efficiency and the equivalent efficiency with increasing squealer height for both the subsonic and the transonic stages. 113
6.22 Three sources of total loss generated in the turbine stage: the baseline loss, the in-tip loss and the out-tip loss. 115
6.23 Variation of the in-tip loss with increasing squealer height in the subsonic and transonic stage. 116
6.24 Mixing loss model used to compute the out-tip loss. 117
6.25 Three terms in Equation 6.25 used to compute the out-tip loss. 119
6.26 Two terms in Equation 6.26 are used to compute the velocity difference between the main flow and the OTL flow in the main flow direction. . 121
6.27 Comparison of the out-tip loss computed by the CFD results shown in section 6.2.4.2 and by the loss model. 122
6.28 Mach number contour at the tip region in the subsonic and the transonic stages with flat tip. 123
6.29 Variation of the normalized heat load with squealer height in the subsonic and transonic stages. 124
6.30 Variation of the heat load ratio on the tip rim, cavity floor and cavity wall with squealer height in the subsonic and transonic stages. 124
6.31 Heat flux contours on the cavity wall with various squealer height in the subsonic and the transonic stages. 126

6.32 Heat flux contours on the tip with various squealer height in the subsonic and the transonic stages. 127
6.33 Turbulent viscosity ratio plot on the pressure side edge of the flat tip in the subsonic and transonic stages. 128

7.1 Tip optimization (cascade) conducted in a sequential manner. h_{sq} is the squealer height. 131
7.2 Tip optimization (cascade) combining squealer height and flow injection 133
7.3 134
7.4 Comparison of cases with the highest and lowest efficiency when the squealer height is 1% of the span. 136
7.5 Example to illustrate the heat transfer performance varying with the squealer height 137
7.6 Aerothermal optimization (turbine stage) obtained by the sequential optimization and the concurrent optimization. 140
7.7 Concurrent aerothermal optimization (turbine stage). 141
7.8 The performance of the cooled turbine stage with flat tip. 143
7.9 The performance of the cooled turbine stage with squealer height of 0.5%. 145
7.10 The cooling effectiveness at various squealer height but the same cooling configuration. 146
7.11 The interaction between the vortex and the cooling flow. 147

List of Tables

4.1 Comparison of three simulations in the validation case. 50

5.1 11 parameters to generate blade profile. 59
5.2 11 parameters and flow angles at the midspan of the stator and the rotor in the subsonic and the transonic stages. 80
5.3 Additional key parameters in the stages. 80
5.4 Boundary conditions of the subsonic and the transonic turbine stages. 85

6.1 Boundary conditions for the test cases. 102

7.1 Boundary conditions of the cooling flow in the transonic turbine stages. 138

Nomenclature

Abbreviations

1	Station at the stator inlet
2	Station at the interface between the stator and the rotor
3	Station at the rotor exit
abs	Absolute frame of reference
c	Coolant inlet
C^1	First order continuity
C^3	Third order continuity
Coarse	Blocks all using coarse mesh
DOE	Design of experiments
exit	Exit
EXP	Experimental Data
Fine	Blocks using all fine mesh
HP	High pressure
HTC	Heat transfer coefficient
in	Inlet
is	Isentropic process
m	Parameters at the midspan
main	Mainstream
norm	Non-demensional normalized term

$NURBS$ Non-uniform rational basis spline

OTL Over tip leakage

PS Pressure side

rel Relative frame of reference

RMS Root mean square

$RMSE$ Root mean square error

$sqPS$ Squealer rim at the pressure side

$sqSS$ Squealer rim at the suction side

SA Spalart-Allmaras turbulence model

$SRST'$ Spatial resolution related source terms

SS Suction side

SST $k-\omega$ SST model turbulence model

$uncool$ Results obtained from the uncooled cases

Letters

A Area

C Chord length

C_{ax} Axial chord length

C_D Discharge coefficient

C_L Normalized tangential loading acting on the blade surface

C_p Heat capacity at constant pressure

C_x Length of the computational domain in x direction

D Corrected mass flow rate per unit area

e Internal energy

eff Film cooling effectiveness

f Body force

$f_{centrifugal}$ Centrifugal force

f_m Purge flow mass fraction

f_u Swirl fraction of the rim speed

h Heat transfer coefficient

h_{sq} Squealer height

h_t Stagnation enthalpy

I Cost function

k_{air} Air thermal conductivity

$\dot{m}$ Mass flow rate

M Mach number

Nu Nusselt number

p Pitch

P Pressure

$P_{0,cool}$ Coolant inlet stagnation pressure

$P_{0,in}$ Mainstream inlet stagnation pressure

P_{ex} Exit static pressure

P_t Stagnation pressure

q Heat flux

r Curve radius

r_{LE} Leading edge radius

r_{TE} Trailing edge radius

R Specific gas constant

R_c Advection and diffusion terms discretized in the coarse mesh

R_f Advection and diffusion terms discretized in the fine mesh

s Specific entropy

Δs Spefic entropy generation rate

$\Delta \dot{S}_{baseline}$ Baseline loss assuming the rotors have no tip clearance

$\Delta\dot{S}_{in-tip}$ Loss generated by the OTL flow inside of the tip gap region

$\Delta\dot{S}_{out-tip}$ Loss generated by the OTL flow outside of the tip gap

$\Delta\dot{S}_{total}$ Total loss accounted by the entropy flux difference

$\dot{S}'''_{gen}$ Volumetric entropy generation

t Throat width

T Static temperature

$\overline{T_w}$ Average wall temperature

T_{ad} Adiabatic temperature

T_{norm} Normalized wall temperature

T_t Stagnation temperature

T_{var} Normalized temperature variance

T_w Wall temperature

u Velocity

u_θ Tangential velocity

u_{ax} Axial velocity

u_{diff} Normalized velocity difference between the tip leakage flow and main flow in the main flow direction

u_{rel} Relative axial velocity

U Rotating Velocity

v Specific volume

v_{rel} Relative circumferential velocity

V Volume

ΔV_c Volume of the element in the coarse mesh

ΔV_f Volume of the element in the fine mesh

W Conservative flow variables

W_c Conservative flow variables solved in coarse mesh

$W_{f\to c}$ Conservative flow variables projected from the fine mesh to the coarse mesh

W_f Conservative flow variables solved in fine mesh

x Axial direction

x^+ Non-dimensional parameters to measure the mesh spacings in x direction

y Tangential direction in 2D blade profiles

$\dot{y}$ First order derivative of y coordinates

$\ddot{y}$ Second order derivative of y coordinates

y^+ Non-dimensional first cell distance when the wall normal direction is along y axis

Y Total pressure loss

z^+ Non-dimensional parameters to measure the mesh spacings in z direction

Symbols

α Angle between the over tip leakage flow and the main flow

$\alpha_{stagger}$ Stagger angle

α_x Sweep angle

β_{LE} Leading edge metal angle

β_{TE} Trailing edge metal angle

$\delta_{unguided}$ Unguided turning

$\epsilon_{wedge,LE}$ Leading edge wedge angle

$\epsilon_{wedge,TE}$ Trailing edge wedge angle

η Aerodynamic efficiency

γ Ratio of specific heats

κ Curvature

ρ Density

σ Standard variance

σ_{ij} Stress term

Vectors

$\vec{F_i}$	Mass flux vector at ith piece in the tip periphery surface
$\vec{A}$	Area vector normal to the surface
$\vec{u}$	Velocity vector

Chapter 1

Introduction

The gas turbine has been widely used in power generation and aviation due to their compactness, flexibility and reliability. Gas-fired turbine engines are also components in a portfolio of renewable energy sources such as wind and solar energy. The wide usage of gas turbine has encouraged generations of engineers to develop various techniques to improve gas turbine efficiency. Increasing Turbine Entry Temperature (TET) is among the most efficient methods. However, since TET has been raised well above the alloy's melting point, the turbine structure has to be protected by thermal barrier coating and cooling flow, known as coolant, taken from the final stages of the compressor.

The cooling system for the first stage turbine includes blade film cooling flow and purge flow. The blade cooling flow, pumped from the blade root and passing through the internal channel of the blade, is ejected from the cooling holes to form a thin, cool, insulating blanket along the external surface of the turbine blade to reduce the surface temperature. It mainly consists of three zones: the leading edge zone (Zone 1), the pressure and suction surfaces zone (Zone 2) and the blade tip region (Zone 3) as shown in Figure 1.2. Zone 1 is cooled by both jet impingement and film cooling. Zone 2 is cooled by coolant passing through a serpentine rib-roughened internal channel shown on the right. The purge flow is used to purge the gaps between stator and rotor to prevent the hot gas from being ingested into the unprotected cavity zone, as shown in Figure 1.1.

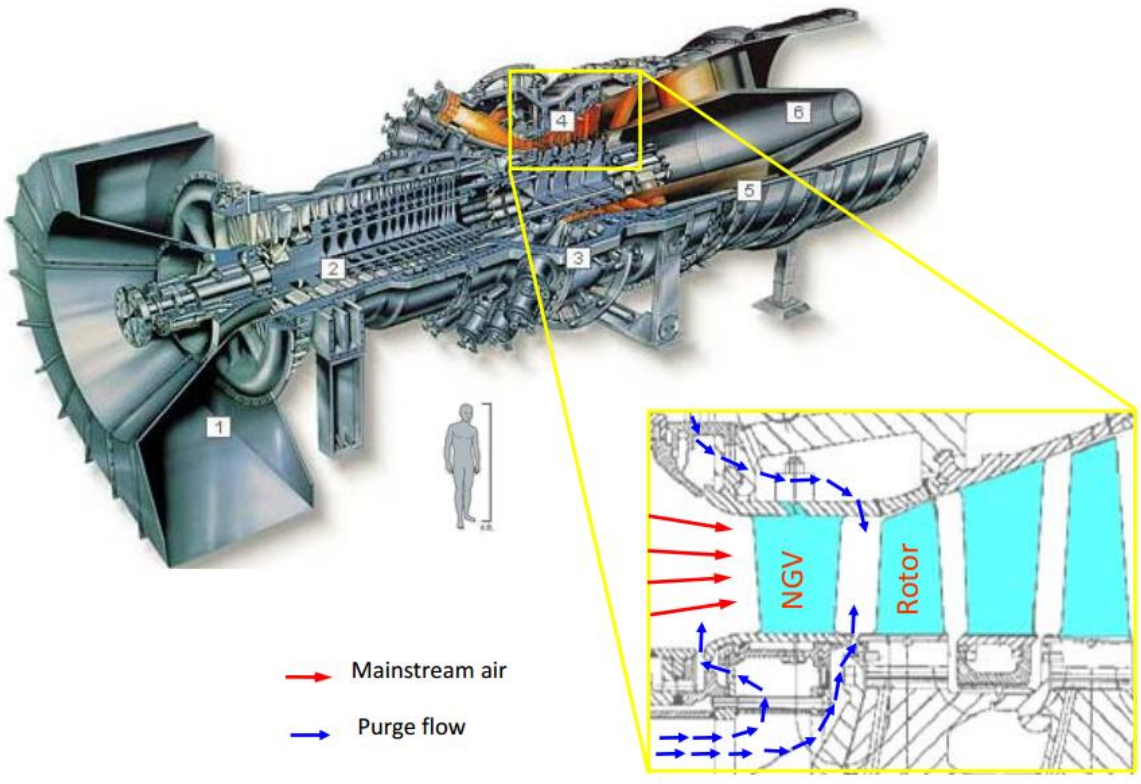


Figure 1.1: Purge flow path illustrated as the blue arrows. This diagram is taken from Zlatinov [63].

1.1 Research Background

Assuming the design problem as a cost function $I(\vec{X})$ for a design vector $\vec{X}$ in a defined design space, the optimization is posed as the search for the optimal value of $I(\vec{X})$ satisfying a set of constraints of $\vec{X}$. The cost function represents the relationship between the design vector and the design objectives. When the relationships are mathematically well-defined, analytical methods can be used to derive an optimum value of a given cost function. When the relationships are too difficult for analytical models, the complete search over the whole design space offers the hope to find the optimum. Contrary to search methods that uses 'brute force' to explore the whole design space, optimizers use algorithms such as the gradient descent method or genetic algorithms to find the optimum more efficiently. The optimizers generally start with a few samples to represent the design space using Design of Experiments (DOE). Then a metamodel (such as polynomial model, Kriging mode, Artificial Neural Network (ANN), etc.) is built to predict the optimum. Iterations are used to gradually improve the metamodel. Once the accuracy of the metamodel's prediction passes a chosen

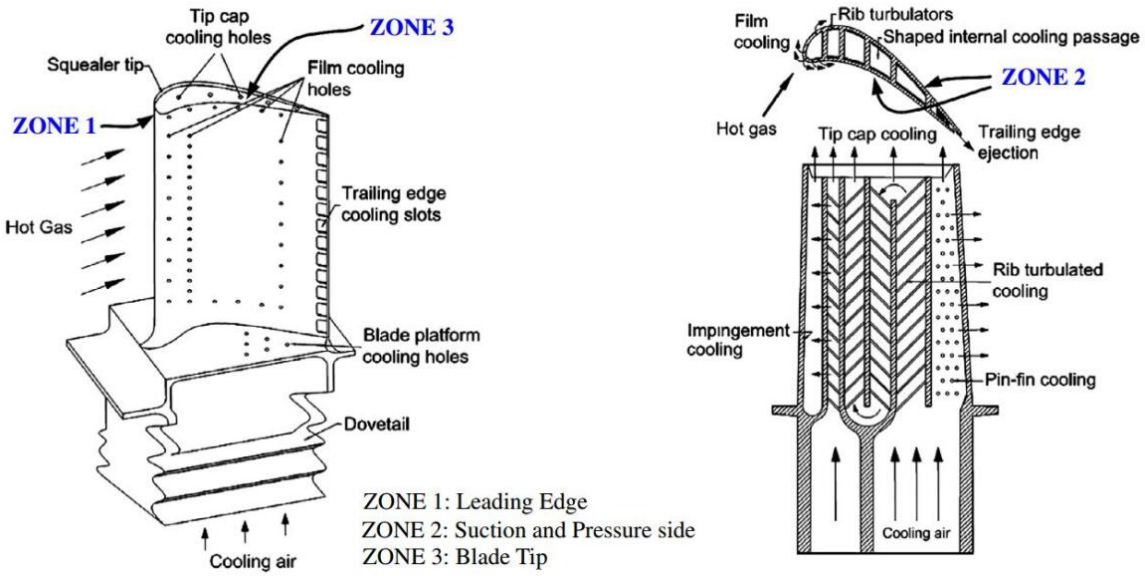


Figure 1.2: Diagram of blade cooling flow taken from Han [40].

threshold, the optimum is deemed to be found.

Optimization of turbine blades is an essential topic in turbine design. Because of the cooling holes on the turbine blade surface, both the blade shape and the cooling need to be taken into account in the optimization. From open literature, the majority of the articles document optimization of the blade shape and cooling independently/sequentially. Although it does not necessarily represent current practice across industry, most of the published research to date document the sequential optimization. Sequential optimization involves several rounds of iterations among different departments. First, the aerodynamic department generates the blade profiles using a parameterization method. The CFD simulations will evaluate the blade performance without considering the heat transfer. Then the preliminary geometry is passed to the heat transfer department, known as cooler, to conduct heat transfer studies. When the cooler introduces the cooling flow (purge flow and blade cooling flow) into the passage, the turbine loss is expected to increased due to the interaction between the coolant and the main flow and the deteriorated blade profile changed by the cooling flow. If the efficiency decreases too much or the mechanical stress is too high, at least one round of iteration is necessary.

Sequential optimization is time-consuming and requires great human efforts. Moreover the efficiency obtained is easy to be trapped in the local optimization. This project aims to construct a concurrent design, combining the aerodynamicists' task

and the coolers' task together to design the turbine blade concurrently, as shown in Figure 1.3. It is expected that the concurrent design is capable of finding the global optimum and reducing iterations.

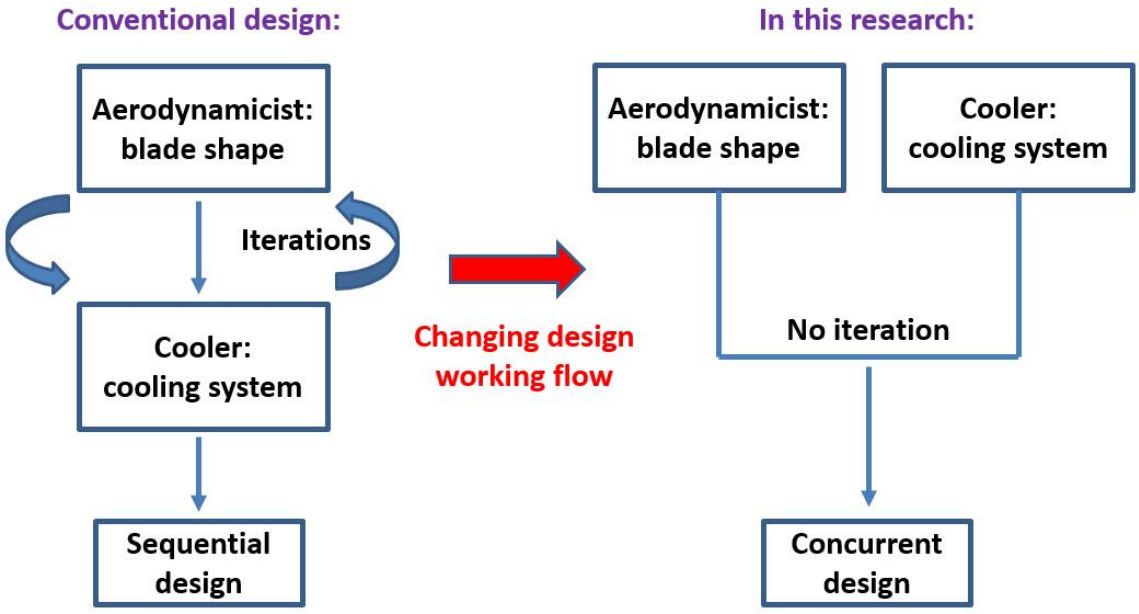


Figure 1.3: Comparison of working flow between sequential and concurrent design method.

The concurrent design is rather difficult not only because it is against the design conventions inherited from old fashion blades which have no cooling system, but also due to the lack of design guidelines. At the stage of preliminary aerodynamic design, several design guidelines, such as Simple Radial Equilibrium (SRE) equation, can still be derived from the simplified version of the momentum equation, as shown in Equation 1.1. However, when the cooling is taken into account, the energy equation, Equation 1.2, is introduced into the system. The complexity of the multiphysics (aerodynamics and thermodynamics) involved in the flow field makes it almost impossible to form effective design guidelines without using experimental correlations for both the uncooled and the cooled blade.

$$\frac{\partial \rho u_i}{\partial t} + \frac{\partial \rho u_i u_j}{\partial x_j} = \rho f_i + \frac{\partial \sigma_{ij}}{\partial x_j} \tag{1.1}$$

$$\rho \frac{D(e + \frac{u_2}{2})}{Dt} = -\frac{\partial q_i''}{\partial x_i} + q_i''' + \frac{\partial \sigma_{ij} u_j}{\partial x_i} + \rho f_i u_i \tag{1.2}$$

Additionally, the concurrent design faces other difficulties: the lack of design guidelines and the larger number of design variables involved in the preliminary design stage. These problems require more CFD simulations to estimate the performance compared to the sequential design. Instead of sweeping all the possible combinations of the design variables, the optimization system takes only a few numbers of representative tests to build a metamodel and uses the metamodel to predict the optimum design.

An advantage of using an optimization method is that the designer can treat the optimization system as a black box. The system is fed with the input information and can determine the optimized results without further design guidelines. Using the optimization system, the sufficient amount of trial-and-error-based CFD simulations will automatically sort out the answers. Thus by combining blade shape optimization (shaping) and cooling optimization (flow control), both the aerodynamicists' and the coolers' work can be done at the same time and therefore the traditional sequential turbine design can be ultimately replaced by concurrent design which certainly offers numerous benefits: an improved performance, a shortening of the design cycle and a reduction of the human effort.

Despite the difficulties, concurrent optimization for turbine design offers numerous merits: an improved performance, a shortening of the design cycle, and reduced human effort. With the advance of high-performance computing technology, the optimization techniques have been increasingly applied to turbine design. Previous work has indicated that optimization techniques can bring favourable results in the design of the blade profile and the cooling system. Although aerodynamicists and coolers have extensively used shaping and flow control, respectively, these two techniques are rarely implemented concurrently. This research aims to develop an optimization system that can design the turbine blade and cooling system concurrently.

In recent research, the transonic turbine tip with the cooling flow has exhibited several flow features such as the interaction between the coolant and the main flow, choking at the rear portion of the blade, shock wave, etc. These features impact the aerothermal performance of the tip and make the transonic turbine design different to the subsonic turbine design. Therefore, the difference between the subsonic turbine and the transonic turbine is investigated.

Moreover, the turbine cascade and the turbine stage are also compared in this research. Since the experiments are mainly conducted in the turbine cascade, the

design and optimization systems are first validated in the turbine cascade. However, because the turbine cascade omits the relative movement of the casing, the turbine stage is simulated to represent the case that is more representative of the real engine condition. The contrast between the turbine cascade and the turbine stage illustrates the influence of the rotating casing.

1.2 Research Questions

This work aims to develop an optimization system that can design the turbine blade and cooling system concurrently by combining shaping and flow control. Upon the way to obtain that goal, several research questions should be answered:

1. **What is the advantage of the concurrent optimization over the sequential one?** The sequential optimization mainly has two limitations: 1) numerous iterations involved between shaping and flow control; 2) tendency to be stuck at a local optimum. In order to verify that concurrent optimization is free of such limitations, these two optimization systems have to be compared.

2. **What are the required attributes of a technical approach to building the comparison?** The concurrent method may induce higher computational cost. It is one of the reasons why rare research work has been done on this topic. The challenge of this research questions is to sort out a proper method that can be computationally affordable without losing too much accuracy.

3. **Once the concurrent optimization is completed, what kind of flow features can we learn from it?** The turbine working in the transonic region has shown several unique flow features comparing to the subsonic one. These features induce different design guidelines in the transonic turbine design.

1.3 Research Objectives

To answer the research questions proposed in Section 1.2, the following research objectives are pursued:

1. To generate turbine blades of high performance for both subsonic and transonic stages using the developed blade design system;

2. To implement a novel algorithm to obtain a fast and accurate simulation of the turbine in the presence of cooling holes;

3. To explore and analyze the gain of optimization by combining shaping and flow control;

4. To investigate the unique features observed from the results of the optimization.

1.4 Organization of Report

The organization of the thesis is as follows:

In chapter 2, the research questions proposed in chapter 1 are reviewed correspondingly from the previous research.

In chapter 3, the methods implemented in this thesis are discussed. The multiple levels of the modelling, the multi-scale method and the optimization system used in this research are introduced.

In chapter 4, the CFD set-up and the multi-scale method are validated against the experimental data. The agreement between the CFD results and the experimental data is documented for the numerical method employed in this thesis.

In chapter 5, a parameterization system is developed to generate the turbine geometry using 11 parameters. The system is used to design a subsonic stage and a transonic stage working at the same Reynolds number.

In chapter 6, the turbine cascades and the turbine stages with various squealer height are simulated. The results of the subsonic and the transonic turbine stages are compared. The loss analysis is implemented to explain the different performance of the two stages.

In chapter 7, the cooling holes are added into the transonic turbine cascades and the transonic turbine stages. The optimization conducted sequentially is compared with the one conducted concurrently. The influences of the shaping and the cooling injection are also investigated.

In chapter 8, the results and the findings of this thesis are concluded. Some general suggestions for possible future work are also introduced.

Chapter 2

Literature Review

In this chapter, the present state of research in the transonic turbine design is reviewed. First, the optimization of the turbine blade using blade shape optimization (shaping) and cooling optimization (flow control) are taken in to account respectively. Then, the previous researches on the turbine tip designs are reviewed.

2.1 Optimization Used in Turbomachinery Design

This section will first discuss the turbine blade design method used in the open-literature. Then the flow control techniques applied in the open literature domain are reviewed. After that, the previous work on the optimization of the cooling system is presented. Moreover, the preliminary attempts to combine shaping and flow control are reviewed to pinpoint the future research direction. Finally, the multi-scale method used in the optimization to reduce the computational cost is reviewed.

2.1.1 Blade Design

In most of the turbomachinery preliminary design, the throughflow calculation based on Wu's S1/S2 theory [14] is implemented. In Wu's theory, two sets of surface, the blade to blade surface, S1, and the hub-to-tip surface, S2, are employed to calculate the 3D flow field iteratively. The throughflow calculation can be conducted in different methods: the streamline curvature method and the matrix throughflow method. The streamline curvature method provides a computationally more stable calculation for solving the flow fields and thus has been used in the code of Denton [42], Smith [57], and Navak [86]. However, the throughflow calculation also has its limitations: 1) the axial symmetry assumption in the passage implies an infinite number of blades.

The blade forces acting between the blades and the fluid are taken into account by the body force terms in the equation of motion. 2) the streamlines are not straight as could be supposed. They usually have specific curvatures that are maintained if the forces exerted on the fluid particle are in an equilibrium state described by the equilibrium equation. Therefore the preliminary design has to be evaluated by the 3D Navier-Stokes solver to verify its feasibility.

Shaping, i.e. blade shape optimization, in turbomachinery has been extensively implemented to improve blade performance. It has been used for turbine by Arnone et al. [1] and Oyama et al. [4], for radial compressor by Casey et al. [67], Braembussche et al. [19], Lotz et al. [87], Hehn et al. [2] and Buyukli et al. [96], for steam turbine by Yin et al. [68] and also for components such as nacelle by Zhong et al. [105] and endwall by Liu et al. [30] and Li et al. [15]. According to different requirements of accuracy and computational efficiency, different optimization algorithms have been applied: gradient-based optimization e.g., Alonso et al. [45], surrogate model (such as response surface method, e.g. Buyukli et al. [96], Kriging model, e.g. Liu et al. [30] and Artificial Neural Networks (ANN), e.g. Braembussche et al. [19]) and evolutionary algorithms (such as Genetic Algorithm (GA), e.g. Arnone et al. [1]). Some algorithms also combine the advantages of two algorithms by utilizing two-level optimizations, such as genetic and gradient (simplex method) combined algorithms, e.g. Lotz et al. [87] and genetic and Kringing surrogate combined model, e.g. Zhong et al. [105]. The objective of the optimizations is to increase the isentropic efficiency, to expand the operating range, to reduce structural stress e.g. Lotz [87] and to reduce the acoustic signature e.g. Hehn et al. [2].

2.1.2 Cooling and Flow Control

Flow control had been used since 1904 when Prandtl [55] controlled separation based on the boundary layer theory. After a century of development, it has been broadly used in turbomachinery to manipulate a flow field to effect the desired change. There are two types of flow control techniques: passive flow control which implements geometry modification to control the local flow field and active flow control which requires extra energy to apply blowing or suction. Hergt et al. [3] in DLR performed an extensive experimental study of passive flow control in a highly loaded compressor cascade to decrease the separation and reduce the losses by means of vortex generators at cascade sidewalls. The vortices generated enhanced the mixing between the main stream and the decelerated boundary layer at the sidewall to reduce the corner

separation. Culley et al. [18] used impulsive injection from a stator vane suction surface in a low-speed axial compressor to reduce separation. Staats et al. [61] applied active flow control to mitigate the periodic flow separation phenomena caused by the periodic non-steady outflow condition. Zander et al. [102] employed synthetic jet actuators to reduce the secondary losses in a two-dimensional stator cascade.

Optimization techniques also have been broadly utilized in the turbine cooling system design. Yang et al. [56] implemented analytic functions generated from response surface methodology to optimize the aerothermal performance of jet impingement cooling channels. The topology structures of the cooling channels are delicately parameterized by a binary topology number that represents the serial or parallel status of each cooling channel. Verstraete et al. [99] optimized an HP turbine blade with internal cooling channels by the method of conjugate heat transfer (CHT). Two-level optimization has been implemented: the first GA generated geometries are evaluated by a rapid but less accurate metamodel analysis (ANN or Radial Basis Function (RBF) network). Then the metamodel predicted optimum geometry is compared with a more accurate but computationally much more expensive CHT analysis to train the metamodel. The self-learning system can decrease the number of evaluations from 1000 to less than 100. Song et al. [104] instead of using two-level optimization, implemented a data mining technique to reduce the number of design variables. Works also have been done for film cooling systems. Johnson et al. [46] optimized an HPT vane pressure side film cooling array by adopting a GA technique. The cooling flow is simulated as a transpiration boundary condition, which adds a source term to the governing equation on cells close to the injection hole. Tang et al. [34] built an optimization system investigating the turbine profiled endwall design in the presence of internal cooling tubes and purge slot. In her work, only the varied endwall profile is optimized. The cooling and purge flow parameters are fixed in the optimization system.

2.1.3 Shaping and Flow Control Combination

Although shaping and flow control has been independently studied for years, there have been relatively few published works to combine them together. Lu et al. [95] built a 3D optimization platform that is capable of optimizing turbine blades with film cooling, although the mesh of the film cooling tube is too coarse to catch the real flow feature. Several preliminary results have indicated that the shaping of the blade can influence the cooling effectiveness. However, since their work mainly

focuses on building the platform, the difference between the sequential design and the concurrent design is untouched. Thus no implication on the design sequence can be derived from this work. Zhang and He's work [62], which is one of few if not only optimizations work to use shaping and flow control concurrently. Their work implementing the Kriging surrogate model investigates the optimization method combining shaping and flow control for two 2D cases: compressor blade and circulation controlled airfoil representing internal and external aerodynamics, respectively. It shows that the concurrent optimization system can find out the global optimum while the sequential optimization tends to be stuck at less optimal solutions unless iterations are implemented. It is in line with the turbine designers' experience that the sequential design always requires iterations. Zhang's work validates the advantage of concurrent optimization in 2D cases. Based on his conclusion, the research in this thesis is to develop an optimization system that can design the turbine blade and cooling system concurrently by combining squealer height variation and tip cooling hole position.

2.1.4 Multi-scale Method

A more advanced design that combines shaping and cooling design without relying on the previous experience of low-speed turbine design requires an efficient numerical tool to resolve both the 3D turbine main flow and the cooling flow. In a typical transonic turbine blade tip, the difference of the length scale between the turbine blade and the cooling holes is around 100 times. Due to such a large disparity of the length scales, the computational cost is rather expensive compared to the case without cooling holes. This is one of the main reasons that few works have been done to the aerothermal design of the cooled transonic turbine blade tip. Andreoli et al. [101] recently performed a multi-objective optimization of the tip geometry to reduce both the aerodynamic loss and the heat load at the turbine blade tip. A novel parameterization strategy is implemented to generate arbitrary rim shapes around the cooling holes. However, since the locations and geometries of the cooling holes are fixed, the optimization focuses solely on shaping without changing the cooling design.

To deal with the problems characterized by two distinctive and disparate length scales, Papadakis and Bergeles [28] presented a local grid refinement method and applied it to a three-dimensional turbulent recirculating flow. It improves the accuracy compared with a coarse mesh and saves the computational time. He [51] [52] [53] [54]

proposed the block spectral method to efficiently obtain high-resolution results with relatively low-resolution mesh. In the case where a large number of repeated small-scale elements (such as cooling holes) are presented in the large-scale global domain, the multi-scale method should be preferred. Duan and He [76] showed the first-of-its-kind work to implement the multi-scale methodology in a commercial solver. The application of the method to turbine blade tip cooling brings a useful tool to handle the computational duty in the transonic tip aerothermal design.

2.2 Turbine Tip Design

In this section, the previous research on turbine tip design is reviewed. The research gaps existed in the turbine design are identified which lead to a direct comparisons between a transonic stage and a high subsonic stage as presented in this thesis. Then the tip design configurations in the previous studies are documented.

2.2.1 Research Gaps in Turbine Design

In previous turbine tip experiments a linear cascade setup has been widely used [50] [97] [31] [31] as a convenient tool to validate the CFD solver and to explore the flow physics at the tip. However, because of the upstream non-uniformity and the relative movement between the blade tip and the casing in the engine representative condition, the results obtained from the cascade are likely be different from those in the real engine. Rahim et al [5], Rahim and He [6] show that the upstream influences, in either NGV geometry changes (radial blade lean), or distorted inlet conditioning (hot streak and swirl), may have a considerable impact on the rotor tip heat transfer characteristics. Atkins et al. [84] find that the interaction between NGV and the rotor produces a time-varying flow field that induces varying flow conditions within the tip gap. A more widely recognized factor certainly missing in a linear cascade is the rotation of the blades, which further increases the complexity and the flow, and thus the validity of the cascade results for predicting the performance of an engine. Yang and Feng [17] reported the major effect of the rotation coming from the relative motion of the casing. In the rotating blades, the relative movement of the casing, the centrifugal force and the Coriolis force make the flow field different from the one in the cascade. As such, in addition to the cascade simulation, the stage configuration needs to be considered for tip aerothermal research.

In terms of relevant flow regimes, note firstly that most of the understanding of the OTL flow stems from low speed cascade tests (Bindon[72]; Palafox et al. [74]; Krishnababu et al. [50]; etc.) where "the pressure driven" mechanism is dominant. These low-cost data simplify the problem and provide insight into the flow physics at the turbine tip. However, as the Mach number increases, the compressibility effect becomes important. The design wisdom developed in the low speed cascade can hardly be extrapolated to the transonic case. Therefore, the performance of the transonic turbine has been investigated in the recent researches. Because in a typical turbine blade the peak pressure along the blade suction side is at the mid portion of the blade, the maximum pressure difference across the tip is greater than the one through the blade passage. Moreover, the high flow curvature as the OTL enters the tip gap induces lower local pressure. Thus, comparing to the passage flow, the over tip leakage (OTL) flow becomes supersonic. It is shown that as the exit Mach number becomes greater than 0.8, the majority of the tip leakage flow is supersonic [7]. Several flow features have been found in the transonic turbine tip [39] [64] [94]. Choking and shock wave are found in the transonic turbine tip. At the tip, the separation bubble generated along the blade pressures side forms a convergent-divergent duct for the OTL flow. Due to the supersonic nature of the flow at the transonic turbine tip, the OTL flow can be choked through the duct. Because choking acts as a limiter to the OTL mass flow rate, Zhang and He [79] explored the potential to increase the blade loading without proportionally paying the tip leakage loss penalty. Moreover, shocks also play important roles towards the aerothermal performance of the transonic turbine tip. At the tip, oblique shock waves are generated within tip gap and result in shock-boundary layer interactions. Zhang et al. [83] presented the first-of-its-kind experimental work to demonstrate the heat transfer stripes caused by the shock boundary interaction. Similar observations are also reported by O'Dowd et al. [22] and Zhang et al. [78]. In some situations, the oblique shock can also becomes normal shock. In more recent research Ma et al. [33] illustrates the first transonic flat tip cooling experimental results. They find a low Nusselt number stripe caused by a normal shock train downstream of cooling injection.

Among the existing work on the tip in both the low speed cascades and the transonic cascades, there is a gap for the high subsonic cases which has not been widely studied. The high subsonic turbine is used in the two-stage high pressure turbine. Nonetheless, there is very limited work in the public domain to investigate the OTL flow in the high subsonic turbine except for some work on the $GE - E^3$ (Kwak [38] Liu et al. [106] Jiang et al.[89]). In this thesis, the turbine stages are designed specifically

for the research purpose. In these cases, unlike $GE - E^3$, the blade configuration is deliberately simplified: 1) the blade counts between the stator and the rotor is 1:2 so that there is no need to run the whole annular case or rescale the blade; 2) the meridional duct is constant so that the stator-rotor gapping as well as the axial location of the purge slot can be easily adjusted. Therefore, the blade row interaction effect and the stator-rotor gapping effect can be conveniently studied in future research. It is however worth noting that a change of blade count from the original design leads to further complications and uncertainties, while it is possible to rescale reasonably to maintain the main parameters, e.g., the chord/pitch ratio, a meaningful rescaling of the blading would be much more difficult. Wheeler et al [9] investigated the tip-leakage losses in subsonic and transonic blade rows and found the two blades have several qualitative differences. However, the work is conducted in the cascade.

Given the state of the art as reviewed above, there is a clear need for research on the blade tip aerothermal behavior in a turbine stage configuration, particularly with systematic contrast and comparisons between a transonic and a high subsonic stage. This leads to the primary motivation of the present work to design and optimize two stages predominantly for turbine blade tip research. Both stages should have the same Reynolds number to help isolate Mach number effects. In the light of previous research on stator-rotor interactions with various steady and unsteady flow modelling fidelities, extra considerations are also given with some further constraints:
a) The NGV-rotor blade count ratio should be chosen to keep a small computational domain, to facilitate high fidelity. A such, a NGV-rotor blade count ratio of 1:2 is taken for both stages.
b) A constant area duct is chosen for both stages. This will enable to vary NGV-rotor intra row gap distance, conveniently and constantly, to facilitate to examine the aerothermal performance and sensitivity of the rotor under influence of different NGV-rotor interactions.

2.2.2 Tip Designs to Improve Aerothermal Performance

As the OTL flow entering the tip region along the tip edge, a separation bubble is formed as shown in Figure 2.1. Since a vena-contracta is generated by the separation bubbles, the OTL flow shows different features in the subsonic and the transonic stages. In the subsonic stage, the OTL flow is mainly subsonic, as the flow passes the convergent-divergent nozzle, the flow is decelerated downstream of the vena-contracta.

The deceleration induces the adverse pressure gradient and increases the turbulent mixing. In the transonic stage, because the OTL flow is mainly supersonic, downstream of the vena-contracta the flow is accelerated. Thus an accelerating pressure gradient is formed and the separation bubble is shortened.

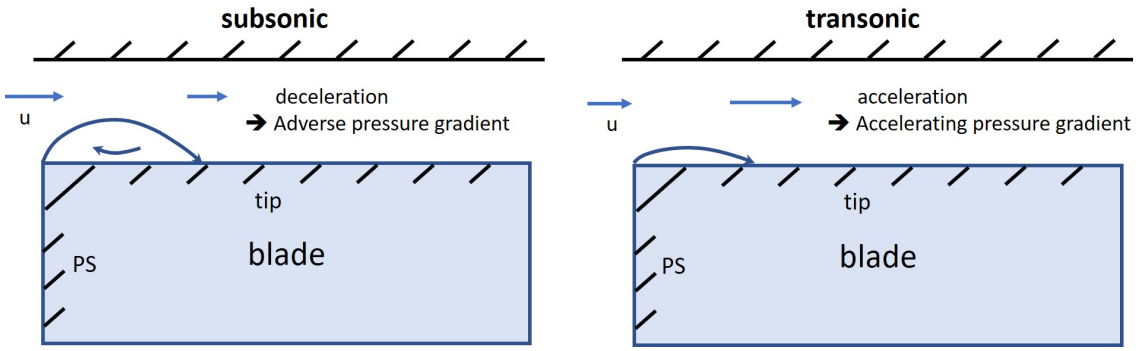


Figure 2.1: Separation bubble on the pressure side of the tip in the subsonic and the transonic rotors.

In order to improve the performance of the tip, several tip designs have been proposed. Among the various types of tips investigated in the previous research, two common designs are the winglet and the squealer. In the winglet, an overhang is introduced into the passage to reduce the pressure gradient between the pressure side and the suction side and hence the over tip leakage (OTL) mass flow rate. Coull et al. [41] used a winglet to improve the efficiency and the thermal performance in the unshrouded turbine. The overhang on the early suction side is found to mitigate the OTL mass flow rate and turn the leakage flow in a more streamwise direction. It was found that this was because it displaces the tip leakage vortex away from the tip, the impingement caused by the interaction between the OTL flow and the base flow is reduced. Thus, the heat load is also reduced.

In the squealer, a recessed cavity at the tip is implemented to causes an additional separation so that the sealing effect is improved and the discharge coefficient is reduced. Key and Arts [71] compared the aerodynamic losses for the flat tip and the squealer tip using experimental data. They found that the squealer tip provided a decrease in velocity through the tip gap reducing loss generation.. Hofer and Arts [97] investigated the aerodynamic performance of the flat tip and the squealer tip in the presence of the cooling flow. Wheeler et al. [9] gave a detailed study on the loss mechanism of the transonic turbine tip with and without squealer. The convergent-divergent duct caused by the separation bubble at the blade pressure side was found to have a influence on the aerodynamic performance. The tip leakage loss in the

transonic blade is less sensitive to the increasing blade loading than for a subsonic blade. Mischo et al. [10] found that the recessed blade tip can reduce the Nusselt number and increase efficiency. Kwak and Han [37] [38] measured the heat transfer coefficient(HTC) and film-cooling effectiveness on the flat tip and the squealer tip in a linear cascade. They found that compared to the flat tip, the squealer tip can reduce both the OTL flow and the heat transfer coefficient. Andreoli et al. [101] implemented a novel parameterization system to arbitrarily generate the tip rim shape to improve both the aerodynamic loss and the heat load. Duan and He [76][77] optimized the squealer tip by combing shaping and flow injection using the multi-scale method and found the cooling flow may have influence to the aerothermal performance of the transonic turbine tip.

A combination between the winglet and the squealer is also studied by Schabowski and Hodson [107] [108]. Their optimum winglet-cavity tip generates lower loss at all of the tested tip gaps ranging from 0.4% to 2.5% of span. Aerodynamic and thermal performance can also be considered simultaneously. However, the recent research indicates that the aerothermal performance of the turbine is dependent not just on the rotor blade tip geometry. In the present work, attention is drawn to the flow conditioning of tip aerothermal research in two closely relevant aspects: a) turbine configuration setup (e.g. cascade or stage) to be adopted; b) flow regimes (e.g. Reynolds number and Mach number) to be considered.

The other aspect of the OTL flow is interaction between the main flow and the cooling flow. The Turbine Entry Temperature (TET) has been pushed well above the melting point of the alloy because in the modern engine. As one of the most vulnerable parts in the turbine blade as indicated by Bunker [88], cooling flow is injected at the tip to prevent the overheat. Various geometry has been implemented to improve the aerothermal performance. Mhetras et al. [90] used a cutback squealer design to drain out the accumulated coolant in the cavity. It results in higher effectiveness at the trailing edge. O'Dowd et al. [22] found the cooled winglet can generate less loss than an uncooled winglet. Some other researchers also investigated the possibility of cooling the blade with better cooling configurations. Park et al. [47] compared the heat transfer performance of three cooling designs with a single row of cooling holes located along the camber line, near the pressure side rim and the suction side rim. They suggested that some of the holes should be placed near the pressure side. Yang et al. [17] found the cooling holes located near the pressure side or the combination of camber line and near pressure side injection had a better cooling performance than

the camber line arrangement, especially at high blowing ratios. More works were also reviewed by Xue and Ng [92].

2.3 Flow Features of the Transonic Turbine Tip

Over the decades, several unique features have been found in the transonic turbine blade tip region.

First, in the conventional design philosophy, the cooling flow is deemed to be passively transported with the main flow. However, recent research has found that the cooling flow at the transonic tip may have interactions with the OTL flow. Wang et al. [109] found that the coolant blockage effect in a flat tip is much more significant than the one in a squealer tip. Thus by partially replacing the squealer cavity with a flat shape, the cooling performance can be improved without bringing more aerodynamic loss. He also showed that the transonic tip cooling flow could move the tip choking location downstream and generate additional vortical flow structures. Ma et al. [31] [32] demonstrated both experimentally and computationally that distinctive high HTC stripes are observed at transonic turbine blade tip especially when the cooling holes are distributed along the blade pressure side. The high HTC stripes are attributed to the impingement heat transfer augmentation caused by the counter-rotating vortex pair generated by the neighbouring cooling flow. The high HTC region is also found at the frontal portion of the transonic tip where the OTL flow is subsonic. Therefore the interaction between the coolant and the base flow is not confined in transonic flow. All these works suggest that the coolant can change the flow structure at the tip. Therefore by adequately designing the cooling configurations, the coolant may reduce the tip leakage loss. Another challenge brought by the interactions between the coolant and the OTL flow is that the cooling design is not superposable. Previously the film cooling flow is deemed to form a thin, low-temperature, insulating blanket along the external surface of the blade. The cooling holes can be added to the uncooled blade without generating disturbance to the mainstream. It leads to the sequential optimization workflow. Firstly the uncooled blade is optimized based on the aerodynamic performance. Then the cooling design is worked out completely relied on the optimized uncooled blade hoping that the cooled blade still has the best aerodynamic efficiency.

Secondly, the OTL flow at the transonic blade tip exhibits the transonic natures, such as the acceleration at the divergent duct, the shock-boundary layer interaction,

etc. It, in turn, induce different aerothermal performance comparing to the subsonic blade. The transonic features of the OTL flow in transonic turbine blade have been reported by several previous research, such as Moore and Elward [39], Dunn and Haldeman [64], Thorpe et al. [94] and Zhang and He [80]. He attributed it to the convergent-divergent duct caused by the separation bubble at the blade pressure side. Both Zhang et al. [78], and O'Dowd [22] have demonstrated the evidence of the heat transfer stripes caused by the shock boundary layer interactions.

Moreover, the aerodynamic performance and the heat transfer performance seem to be less correlated at the transonic tip. Teng et al. [91] found that in the subsonic tip, the loss generation and the heat transfer are closely correlated: the larger OTL loss corresponds to the higher heat transfer. However, in O'Dowd's experiments [21], an HP turbine blade tip under subsonic and transonic conditions showed the completely opposite trends of heat load along the axial direction. At the rear portion of the blade where both the OTL flow velocity and the wall shear stress are high, the heat transfer level represented by the circumferential averaged Nusselt number is found to be low. The similar observation is also found in Zhang and He's experimental and CFD results [82]. Virdi et al. [8] investigated the heat transfer performance of a transonic turbine blade tip at varying tip gap size. At the frontal portion of the blade where OTL flow is subsonic, as tip gap increases, both the aerodynamic loss and the heat load increase. However, at the rear portion when the OTL flow becomes transonic, the increasing tip gap brings higher loss but lower heat load. These findings have shown that the aerodynamic loss and the heat transfer are no longer closely correlated in the transonic tip.

These unique flow features exhibited in the transonic turbine blade tip bring new challenges to the designers. The conventional design wisdom in low-speed turbine blade tip design can no longer be inherited at least in the following aspects:

1) The conventional sequential design procedure, which first optimizes the blade shape and then adds cooling holes onto the already optimized blade, is questionable to be implemented in the transonic turbine blade tip design. Because of the interaction between the tip cooling flow and the baseflow, the well-organized flow in the uncooled tip will be heavily deteriorated by the coolant. Therefore the influence of the coolant should be considered at the stage of the shape design.

2) Due to the transonic nature shown at the tip, the transonic turbine blade tip scaled from the subsonic blade cannot have a similar aerothermal performance. Wheeler

et al. [7] scaled a transonic turbine blade from a subsonic one by matching the Reynolds number and the blade loading. The comparison between these two blades demonstrates that the blade tip heat transfer performance in both the heat transfer coefficient and the recovery temperature is influenced by the Mach number. The high flow Mach number leads to the pressure side corner separation bubble to reattach and the shock-boundary layer interaction to be intensified. Therefore the heat transfer coefficient in transonic tip is different from the one in the subsonic tip. Moreover, the high speed flow also results in large local variation in recovery temperature. Thus the previous well designed low-speed blade tips can no longer be used for scaling.

3) Since the aerodynamic loss and the heat transfer are no longer closely correlated at the transonic tip, the design with the lowest loss does not automatically apply to the lowest heat transfer. It challenges the aerodynamics dominant design consideration and indicates that an aerodynamically optimized blade may have poor performance in heat transfer. Therefore the "decoupled" aerodynamic loss and heat transfer need to be considered separately as two design objectives. More specifically, it is necessary to implement the multi-objective optimization.

Due to these unique flow features exhibited in the transonic turbine tip, the design of the turbine tip have multi-disciplinary effects. The tip shaping can influence both the aerodynamics loss and the heat transfer of the turbine. The cooling flow not only changes the heat load but also alter the flow structure at the tip. Zhang and He [81] proposed the possibility to improve the tip design by combining shaping and flow control. It leads to the new thoughts for the transonic turbine blade tip cooling design. One of the few work is from Zhang and He [62] where the optimization was implemented to combine the compressor blade shaping and circulation flow control. Recently De Maesschalck et al. [13] implemented a novel parameterization method to optimize the turbine squealer tip geometries with varying cooling injection. In their work, sequential and concurrent optimization are not compared. The major discussions focus on how to add cooling to three already optimized tips. In this paper, the problem is discussed from a different angle. The difference brought in by the concurrent optimization is illustrated by comparing the sequential and the concurrent design methods. The results show that the potential performance improvements may be lost by using the pre-optimized tip shape in the cooling design.

Chapter 3

Methodology

In this chapter, the methods implemented for turbine cooling optimization are introduced. First, the multiple levels of the modeling are applied to investigate the flow mechanisms of the cooled turbine blade. Then the multi-scale method is used in the simulations of the cooling flow. It is shown to improve the computational efficiency while maintaining the accuracy of the cooling flow computation where large length scale discrepancy exists. Finally, optimization techniques employed to optimize the turbine squealer and the cooling configuration are presented. The genetic algorithm is selected to obtain the Pareto Front of the multi-objective optimization.

3.1 Two Levels of Modelling

To systematically investigate the mechanisms associated with turbine optimization, two levels of modeling are implemented. In this work multiple models of turbine operating in two working conditions with or without tip cooling are studied.

3.1.1 Two Methods of Optimization Procedures

In this work, two methods of optimization procedure are examined to investigate the influence of the optimization sequence on the performance of the optimized transonic turbine. These two optimization procedures are the "shaping-flow control" sequential optimization and the "shaping-flow control" concurrent optimization.

The "shaping-flow control" sequentially optimized model, being self-explanatory, is utilized to optimize the baseline model in a sequential manner. First, the baseline model without a cooling system is optimized by the shaping technique. Then by adding a cooling system into the shaping optimized blade, flow control is implemented

to optimize the cooling system. The work flow adopted in the "shaping-flow control" sequentially optimized model represents the one generally used in the open literature. In the following, the "shaping-flow control" sequentially optimized model will be named in short as Sequential Model.

The "shaping-flow control" concurrently optimized model is implemented to compare with the sequential model. To build this model, first, the cooling system is added into the baseline model, then both the blade shape geometry and the cooling system are optimized concurrently by using shaping and flow control simultaneously. In the following, the "shaping-flow control" concurrently optimized model will be named in short as Concurrent Model.

The comparison of the two models aims to answer the research questions proposed in Chapter 1. The optimized design obtained from the Concurrent Model is expected to be different from the one generated by Sequential Model. Their differences indicate the potential of improving the turbine design by re-organizing the optimization sequence.

3.1.2 Two Types of Operating Conditions

In this research, turbines working at the subsonic regime and transonic regime are simulated to represent the different operating conditions. As introduced in Chapter 2, the transonic turbine has shown several unique flow features comparing to the subsonic one. Therefore both of two operating conditions are evaluated. From Wheeler's work [7], the transonic turbine cannot be simply scaled from the subsonic blade. Therefore the blade operating at different working conditions need to be designed separately. A parameterization system is used to generate these two sets of blades. More details on the design of the two turbine stages will be introduced in Chapter 5.

3.1.3 Two Levels of Turbine Models

Two types of turbine models: turbine cascade and turbine stage, are implemented in this study to illustrate the difference of the aerothermal performance brought by the relative casing movement. When the aerodynamic performance is discussed, the adiabatic boundary conditions is employed on the blade wall to analyze the loss. There are also several papers on the thermodynamic correction of loss for heat transfer such as [60] so that the loss analysis can be conducted in the non adiabatic cases. When the heat transfer performance is taken into account, in the uncooled cases the constant

wall temperature boundary conditions are implemented to evaluate the heat flux on the wall and in the cooled cases the adiabatic wall boundary conditions are used to evaluate the cooling effectiveness.

In the turbine cascade, a 3D straight turbine blade without casing rotation is examined. It is a simple and representative model that illustrates the flow pattern of the blade passage. Since there is no relative rotation of the casing, the cascade experiments are much more convenient and affordable. In the cascade the flow loss and the efficiency can be computed by two methods:

1) the total pressure difference between the inlet and the exit:

$$Y = \frac{P_{t2} - P_{t3}}{P_{t3} - P_3} \tag{3.1}$$

where P_{t2} is the total pressure at inlet, P_{t3} and P_3 are the mass flow averaged total pressure and static pressure at the exit.

2) the entropy flux rate difference 3.2 between the inlet and the exit:

$$\Delta s = \frac{1}{\dot{m}}(\int_V \dot{S}'''_{gen} dV) = \frac{1}{\dot{m}}(\int_{A_3} s\rho\vec{u} \cdot d\vec{A} - \int_{A_2} s\rho\vec{u} \cdot d\vec{A}) \tag{3.2}$$

where $\dot{S}'''_{gen}$ is the volumetric entropy generation rate, V is the control volume, A_2 and A_3 are the control surfaces at the inlet and the exit, s is the specific entropy, $\vec{u}$ and $\vec{A}$ are the flow velocity and surface area vectors at the control volume boundary surface.

The relationship between the entropy generation and the variation of the stagnation temperature and the stagnation pressure can be derived by combining the first and the second law of thermodynamics as shown in Equation 3.3:

$$\frac{\Delta s}{R} = \frac{\gamma}{\gamma - 1} \ln T_{t3}/T_{t2} - \ln P_{t3}/P_{t2} \tag{3.3}$$

where P_t and T_t are the stagnation temperature and the stagnation pressure; 2 and 3 indicate the inlet and exit of the computational domain.

For adiabatic flow in a stationary passage (i.e. steady flow), the total temperature is constant. The first term in Equation 3.3 is zero. Therefore the two methods shown in Equation 3.1 and Equation 3.2 are equivalent through

$$\Delta s = -R \ln P_{t3}/P_{t2} \tag{3.4}$$

The turbine cascade omits several important features of the real engine such as casing relative movement. In the turbine, the relative rotation of the casing generate a shear layer to drag the over tip leakage flow from the suction side to the pressure side. This will influence the over tip leakage mass flow rate, which is one of the most critical parameters for turbine tip performance. Therefore, the turbine stages model is also examined in this research.

In the turbine stage, because extra work is done by the relative movement of the casing, the total temperature is not constant. Thus Equation 3.4 is no longer valid. The total-total efficiency of the uncooled stage are defined by the ratio between the actual work and the ideal work

$$\eta = \frac{h_{t,1} - h_{t,3}}{h_{t,1} - h_{t,3,is}} \tag{3.5}$$

where station 1 and station 3 represent the stator inlet and the rotor outlet; h_t is the stagnation enthalpy; $h_{t,is}$ is the ideal stagnation enthalpy assuming the process from station 1 to station 3 is isentropic.

If the specific heat at constant pressure, c_p, is constant through the passage, Equation 3.5 can be further written as

$$\eta = \frac{1 - \frac{T_{t,3}}{T_{t,1}}}{1 - (\frac{P_{t,3}}{P_{t,1}})^{\frac{\gamma-1}{\gamma}}} \tag{3.6}$$

From this definition, the aerodynamic efficiency of the uncooled stage can be conveniently compared with the experimental data such as "Smith chart". The evaluation of the aerodynamic performance in the cooled blade will be discussed in Section 3.4.3.

3.2 Baseline Solver Specifications and Guidelines

The baseline case is computed using ANSYS CFX steady solver. The advection discretization scheme is set to be second order throughout the computational domain. The turbulence numerics are high resolution where the second order is used in areas with low variable gradients and the first order is used in areas with high variable gradients. $k - \omega$ SST model is implemented to close the turbulence term. Since the flow working condition ranges from subsonic to transonic region, the total energy model including viscous work term is used in the heat transfer model. The time step is set to be 0.0002 s (about 20% of through-flow time) . Convergence is defined by a combination of low residual and constant value from the monitor points.

The hypothetical turbine stage modeled in this work has 32 stators and 64 rotors. Due to the periodicity of the flow field in the steady simulation, to minimize computing resource requirements only one stator and one rotor are simulated per row. The stator domain is stationary. The rotor domain has a rotating velocity along the axial axis. The mixing plane interface is employed between the stator exit and the rotor inlet. It delivers a circumferential uniform flow to the rotor domain. For the rotor in the turbine stage, the casing wall has a counter-rotating velocity to keep the wall stationary in the absolute frame of reference. In most cases, except for those used for computing the heat transfer coefficient (HTC), the adiabatic wall boundary conditions are used for the wall.

3.3 Multi-scale Methodology

In this research the multi-scale method is used to run the simulations of the turbine blade with cooling holes. In previous researches [51] the multi-scale method is used to obtain an accurate fine mesh solution using a coarse mesh. The work shown here is the first-of-its kind work to implement this method in the commercial solver. Moreover by properly collecting the source terms, the coarse and uncooled mesh is able to generate the fine mesh solution with coolant injection.

Consider a problem like turbine tip cooling, in the global domain there are many similar small-scale elements such as cooling holes. To resolve the flow around these small elements, the local mesh has to be fine enough compared to the length scale of these small elements. However due to the large disparity (> 100 times at turbine tip) in length scales between the small elements and the global domain, the locally refined mesh greatly increases the cell number of the whole mesh when the structured mesh is used. Simply put, for the conventional aerodynamic efficiency/loss prediction of a typical mesh, the main mesh resolution requirement tends to be marked in the wall normal direction, i.e. y^+. As for a mesh suitable for cooling prediction, on the other hand, one will have to consider x^+ and z^+ as well. In a wall oriented coordinate system y^+ is taken to be the wall normal (thus y^+). x^+ typically (though not always) is the main streamwise direction, and z^+ the lateral (typically looking into the paper), x^+ and z^+ are defined accordingly as non-dimensional parameters to measure the mesh spacings in these two directions

The block spectral method proposed by He [54] can be adopted to solve this problem with far less amount of the locally refined mesh. In this method, the whole compu-

tational domain is decomposed into two parts: a coarse base mesh domain which is the main body of the flow field and a large number of small-scale blocks which are embedded in the base mesh domain. The communication and interaction between the base mesh and the small-scale blocks are partially through the interface planes: the base mesh captures the large-scale disturbance of the main flow and as such provides a right environment/boundary condition for the small-scale blocks. The small number of fine mesh blocks resolve the high gradient flow. They are used to generate and propagate the impact of the local refinement to the coarse blocks thus collectively. Once the interactions between the fine and coarse mesh blocks are fully captured (i.e. the multiscale solution converges), the solution with only a small number of fine mesh blocks should be equivalent to a solution where the whole domain is fully covered by fine mesh blocks.

Considering a flow field governed by the 3D Navier-Stokes equation in a simple form:

$$\frac{\partial W}{\partial t} + R(W) = 0 \tag{3.7}$$

where W is the vector consists of five elements representing the five conservative variables; R is the residual representing the advection and diffusion terms as a function of W.

Therefore the steady state equation at the local fine mesh block is written as:

$$R_f(W_f) = 0 \tag{3.8}$$

where W_f is the fine mesh solution and R_f is the residual representing the spatial discretization of the advection fluxes and diffusion terms in the fine mesh.

Now supposing a coarse mesh is used in the local block, the poorly resolved but converged solution satisfies:

$$R_c(W_c) = 0 \tag{3.9}$$

where W_c is the coarse mesh solution and R_c represents the coarse mesh discretised residual. Clearly there is discrepancy between the fine mesh solution, W_f, and the coarse mesh solution, W_c. Their difference represents the influence of the mesh resolution. To compare these two solutions on the same coarse mesh, the fine mesh solution can be transferred to the coarse mesh through the volume-weighted average:

$$W_{f\to c} = \frac{1}{\Delta V_c} \sum W_f \delta V_f \tag{3.10}$$

where $W_{f\to c}$ is the fine mesh solution projected on the coarse mesh; δV_f is the volume of the element in the fine mesh; ΔV_c is the corresponding volume of the element in the coarse mesh. Due to the difference between $W_{f\to c}$ and W_c, the fine-to-coarse mesh solution will not satisfy the flow equation discretized on the coarse mesh:

$$R_c(W_{f\to c}) \neq 0 \tag{3.11}$$

To balance the equation, we are reminded of a general situation of Reynolds-averaging for the turbulent flow. Due to the nonlinearity of the advective fluxes, the residual calculated by the time-averaged flux would not balance unless we introduce Reynolds stress terms. Similarly, for periodic unsteady flows, the time-averaged equations can only be balanced if we introduce 'unsteady stress' terms (Ning and He [103]).

Here, we introduce equivalently lumped source terms to represent all the extra terms due to the spatial averaging. This leads to a balanced equation shown as:

$$R_c(W_{f\to c}) + SRST' = 0 \tag{3.12}$$

where $SRST'$ is short for the spatial resolution related source terms. In general, $SRST'$ represents the unbalanced term in the governing equation when certain initial condition is put into the equation. The imbalance can be attributed to the mesh resolution or the unsteadiness depending on the type of the initial conditions. For instance, if the governing equation is discretized on the coarse mesh while the initial condition is the fine mesh results, $SRST'$ represents the unbalanced term caused by the spatial resolution. A more general and detailed discussion on $SRST'$ is also shown in He's paper [54].

Once the source terms are obtained, they can be added to the equations discretized on the coarse mesh. Then the solution of the augmented equation on the coarse mesh will be the equivalent fine mesh solution as transferred to the coarse mesh, which is the target solution. Thus we now have two tasks:

a) To establish a small number of fine mesh blocks as long as they are sufficient to be used to generate the source terms;

b) To propagate the source terms to the coarse mesh blocks of the whole domain.

Note that these two tasks are linked together to reflect the interactions between the local fine mesh blocks and the global coarse mesh domain. a) without b) would lead to a highly resolved local region subject to an incorrect environment. b) without

a) will lead to an unresolved (thus incorrect) global flow field. A meaningful multi-scale solution is reached only when the interactions between the two parts are fully captured as the interactive solution is converged.

For the present case, to resolve a large amount of the cooling holes, only a small set of blocks need to be refined to compute the source terms that can balance $SRST'$. Equation 3.12 itself provides a convenient way to compute $SRST'$ because the flux residual using the fine-to-coarse mesh solution can be easily calculated. Therefore by compensating $SRST'$ in the Equation 3.12, a fine-to-coarse mesh solution is obtained on the coarse mesh. The mesh-pointwise block spectra is used to establish the block-to-block variation for the source terms at the rest of the blocks.

Given the aforementioned interactive nature between the local fine mesh blocks and the global course mesh domain, iterations are needed to make the source terms produced in the fine mesh blocks finally converge with the right environment/boundary condition provided by the coarse blocks.

3.3.1 Implementation of Multi-scale Method

The flow chart in Figure 3.1 shows the process to implement the Multi-scale Method in the commercial solver, ANSYS CFX. The commercial solver is employed mainly because the solver has been ubiquitously used and validated in the previous studies. It guarantees the reliability of the baseline solution and provides a common platform that enables other researchers to implement the multi-scale method. In this method the small-scale blocks that are embedded in the base mesh are divided into two groups: the fine blocks and the coarse blocks. The fine blocks are fine enough to resolve the local high gradient flow. The coarse blocks have the same mesh density with the base mesh which are far less than enough to obtain the right solution due to the high disparity of the length scales between the base mesh block and the small-scale blocks. The fine blocks are used to collect the source terms that can represent the influence of the mesh resolution. In CFX, the source terms can be obtained from the residuals of the coarse mesh solution that uses the fine mesh results as the initial guess. During this process, the fine mesh results are projected into the coarse mesh. It then generates the residual on the coarse mesh.

These residuals are collected and used as the source terms to balance the equation discretized on the coarse mesh. However, experience has shown that one single iteration in CFX is not enough to collect the correct source terms. Therefore, several

iterations are needed to collect the source terms interactively. When the variation of the RMS of the collected source terms between two sequential iterations is smaller than a specific value (e.g. $< 1\%$), it is deemed that the right source terms have been collected.

Once the source terms at the fine blocks are collected, they can be propagated into the neighbouring coarse blocks. In the distribution of the small-scale blocks, the fine blocks are loosely distributed at the exterior boundary so that the source terms can be interpolated rather than extrapolated. In this work the Kriging interpolation is used.

In the first iteration by adding the source terms to the coarse blocks, the influence of the mesh resolution can be partially manifested. However, because in the first iteration the source terms are computed in the scenario that the coarse blocks have no source terms, they are not obtained in the right boundary condition that all embedded blocks are the fine blocks. Therefore iterations are needed so that the source terms computed in the fine blocks can gradually "feel" the refinement of the coarse blocks. Here the coarse blocks are not refined by increasing the mesh density but by adding the source terms. In such case by the time that the source terms get converged, the source terms computed are under the right boundary condition that all blocks are refined (either by mesh refinement or by source terms). Thus an equivalent fine mesh solution can be obtained from the coarse mesh. Here the convergence of the outer loop is reached when the variation of the RMS of the propagated source term between two sequential iterations is lower than a certain value. Therefore there is a two-level iteration loop in the whole process: the inner one is to collect the source terms in the locally embedded fine blocks; the outer one is to build the communications between the local fine blocks and the coarse blocks so that the source terms are obtained at the right environment/boundary conditions. The iterations to collect the source terms are needed only in the commercial solver. In an open sourced code, the collection of the source terms can be obtained instantaneously by simply reading the right hand side value of the discretized differential equations. The need for iterations in the outer loop is likely to be related to the flow field.

3.4 Optimization System

This part presents the optimization system for both shaping and flow control, which generally consists of three parts: the parameterization system, the flow solver and

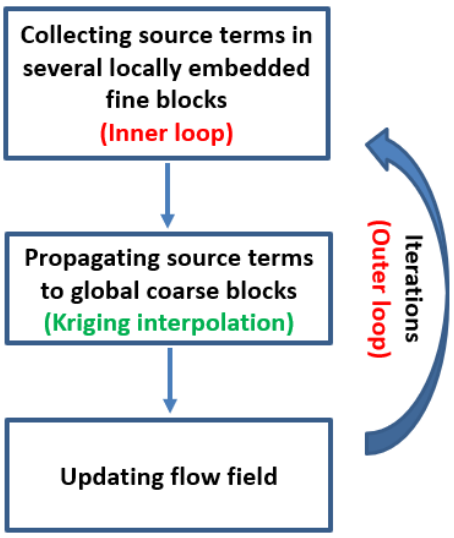


Figure 3.1: Flow chart for the implementation of the multi-scale method in CFX.

the optimizer, as shown in Figure 3.2.

3.4.1 Parameterization System of 3D HP Turbine Stage

The parameterization system is conducted in a 2D-3D manner: first a 2D blade profile is generated at each layer along the radial direction, then the 2D profiles are transferred to 3D and stacked along the stacking line to generate the 3D blade. A similar 2D-3D parameterization strategy is also implemented in Denton's Multall code [44].

In this study, both the tip squealer height and the cooling configurations are optimized. A parameterization system written in Matlab is built to accommodate the variation of these design parameters. First, the 2D blade profiles are generated by an 11-parameter method modified from Pritchard's work [58]. Then a 3D stacking line is drawn to guide the 2D blade profiles from hub to tip so that the 3D turbine blade geometry can be stacked. The 3D stacking line is specified by the value of the lean angle, the sweep angle, the twist angle and the tapered angle. Within the blade profile, one additional section is added to form the cavity for the squealer. The squealer height is controlled by the distance between the tip section and the cavity floor section.

In addition to the parameterization of the blade geometry, a blocking system is developed to form the 3D turbine blade block so that the structured mesh of the computational domain can be automatically generated in ICEM CFD. The blocking system

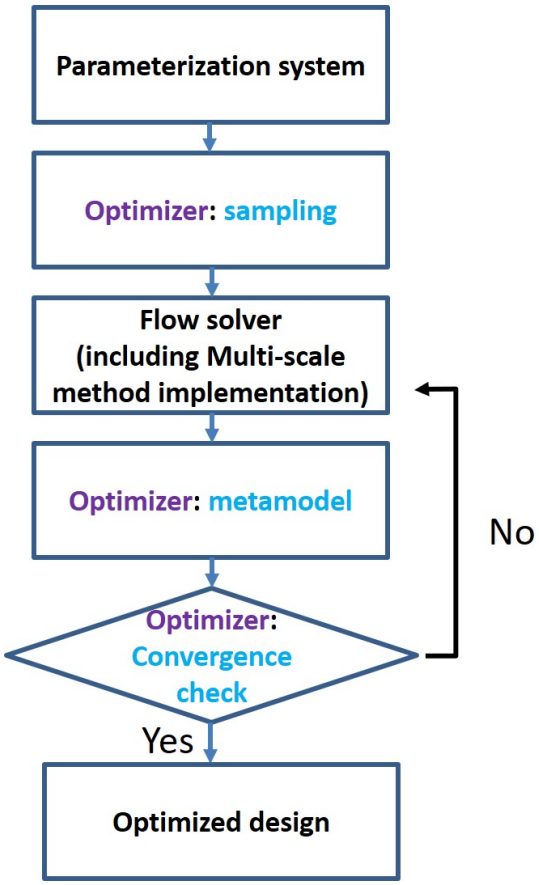


Figure 3.2: Flow chart of optimization system.

is also built in the 2D to 3D form. For high turning blade due to the restriction of the periodicity, the typical O-block strategy tends to bring high skewness. Therefore in the blocking system, the shifted periodic topology by Li [29] is implemented to decrease the skewness. The blocking system also adjusts the angles of the blocking lines to improve mesh quality. In this research, the block at the tip is split to accommodate as many cooling slots as possible, so that the potential positions for injection can cover the whole squealer. These cooling slots are distributed along the pressure side, the camber line and the suction side. Therefore the parameterization of the cooling configuration can be represented by a binary string where '0' represents no injection, and '1' represents coolant injection. For the slots without injection, the base mesh block is inserted. For the slots with coolant injection, the injecting effect can be obtained by either inserting cooling hole blocks or adding source terms on the base mesh block. The whole process of block generation is illustrated in Figure 3.3.

From Figure 3.3, the block line of the cooling slot is extended to the freestream. The extension is mainly constrained by the need to include the hole topology during

the mesh generation using ICEM CFX. The cooling block and the freestream block with different mesh densities are connected by the interface in CFX. Except for this method, other mesh generation techniques such as overset meshes, mesh adaption and the use of unstructured meshing can also be employed for the cooling hole mesh. However given the time limitations of this project, the thesis only considers the multi-scale method approach applied to structured grids.

Once the blocking is completed, the 3D turbine blade can be meshed accordingly using ICEM CFD script. The structured mesh for the cooled turbine is illustrated in Figure 3.4. The details will be delineated in Chapter 5.

3.4.2 Optimizer

From Figure 3.2, the optimizer mainly consists of three parts: sampling, metamodel and convergence check. The sampling generates a series of representative geometries of the turbine by alternating the design variables in the parameterization system. In this thesis, only the hole position and squealer height are varied in the parameterization system. The representative geometries are generated by the Design of Experiment(DOE) method. Then these representative geometries are imported into the flow solver to evaluate their performances. The metamodel builds a relationship between the geometries and the performances and uses this relationship to predict the optimum. The convergence check will put the predicted optimum into the flow solver to examine whether the predicted optimum is consistent with the CFD computed results. If so, the relationship built by a metamodel is deemed to be valid, and the optimization system is converged. Otherwise, when the criteria of the convergence check fail, the CFD computed results will use a new sample in the flow solver for the further refinement of the metamodel.

In the turbine cooling design, both aerodynamic efficiency and heat transfer performance are evaluated. The multi-dimension of the objective function in this problem requires a multi-objective optimizer. Considering the simplicity of the implementation of the method in the specific case where the cooling configuration is optimized in multi-objective optimization, the genetic algorithm is chosen in this study. The cooling configuration can be easily parameterized by a binary string with '1' and '0' to represent if the location has a cooling hole or not. The binary string has the same format as the chromosome used in the genetic algorithm. In the genetic algorithm, the multi-objective genetic algorithm (MOGA) can be used. Among the MOGAs, the Non-dominated Sorting Genetic Algorithm (NSGA-II) is chosen because, in widely

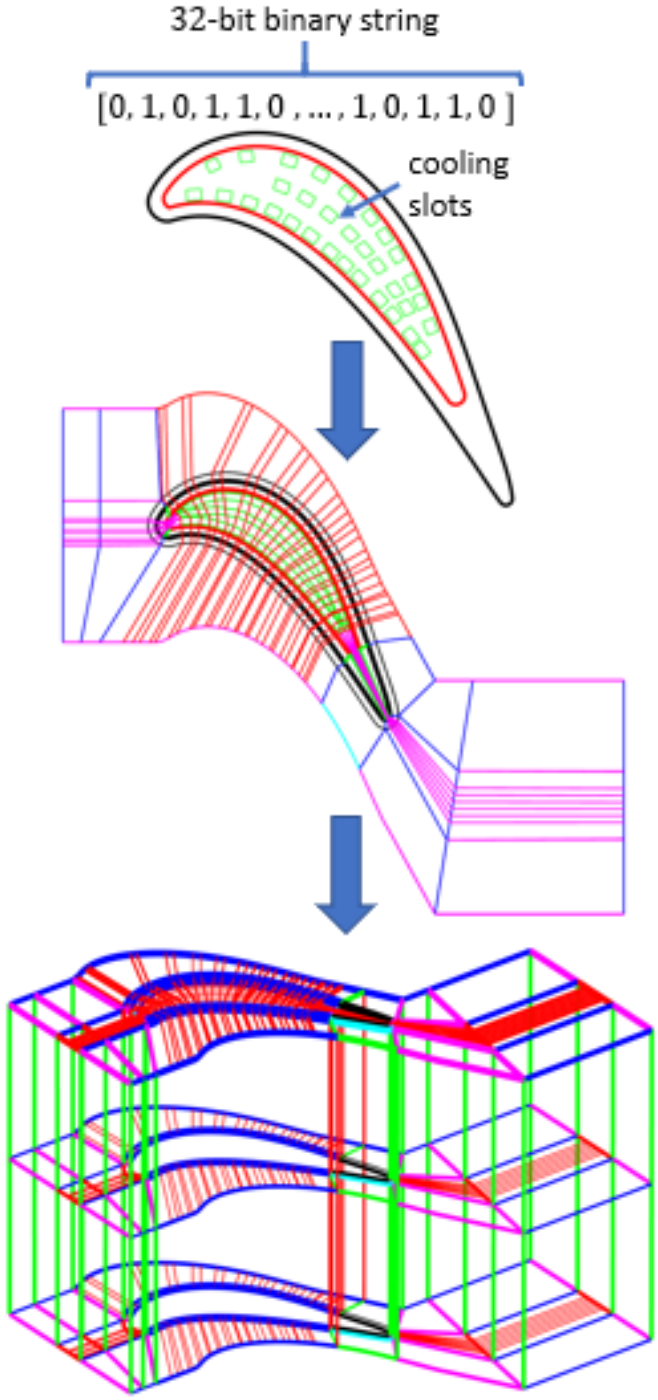


Figure 3.3: Parameterization system for a cooled 3D turbine blade with 32 cooling slots.

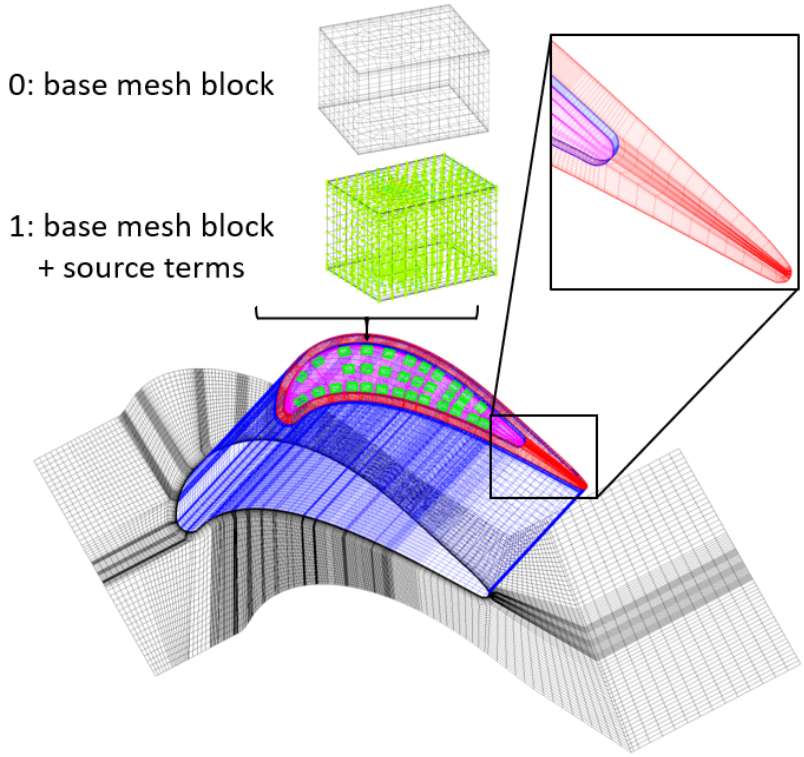


Figure 3.4: Mesh for a cooled 3D turbine blade with 32 cooling slots.

tested cases, it has shown better performance over other MOGAs (VEGA, HLGA, NPGA) [23].

There are several other optimization algorithms, such as the gradient descent method and the hybrid method that combines the genetic algorithm with the gradient-based optimizer. In this work, the gradient descent method is less suitable for optimizing the discrete distribution of cooling holes compared to the genetic algorithm. Moreover, the multi-objective optimization in the gradient-based optimizer requires multiple metamodels and a multi-objective ranking system which is more difficult to implement than the NSGA-II in the genetic algorithm. Thus, the gradient descent method is not used in this thesis.

The flow chart of the optimization is illustrated in Figure 3.5. The NSGA-II algorithm is based on Deb et al.'s work [49] with slight modifications to control the number of cooling holes. The first iteration implements the DoE to generate 30 individuals with varying squealer heights or cooling configurations. By applying the parameterization system stated previously, the geometry and the mesh of the 30 individuals are obtained. CFX is used to run the simulation and to output three objectives of each design.

Within the NSGA II optimizer, the multi-objective non-dominated sorting algorithm can rank the individuals based on the value of the objectives and the spread of the solutions (crowding distance). According to the ranking, the superior individuals are chosen to be the parents so that by crossovering and mutating the parents' chromosomes the new individuals (offsprings) can be generated. As the number of the cooling holes is controlled in this research, the newly created individuals out of the NSGA II optimizer can be passed on to the next generation only if the number of the cooling holes is equal to the assigned value. In this study, each generation has 10 new offsprings. By running the loop iteratively, the Pareto front is formed to obtain the optimal design which combines both the aerodynamic loss and the heat transfer performance. The optimization is deemed to be converged when the maximum value of the efficiency and the cooling effectiveness, and the minimum value of the temperature variance does not change in two consecutive iterations.

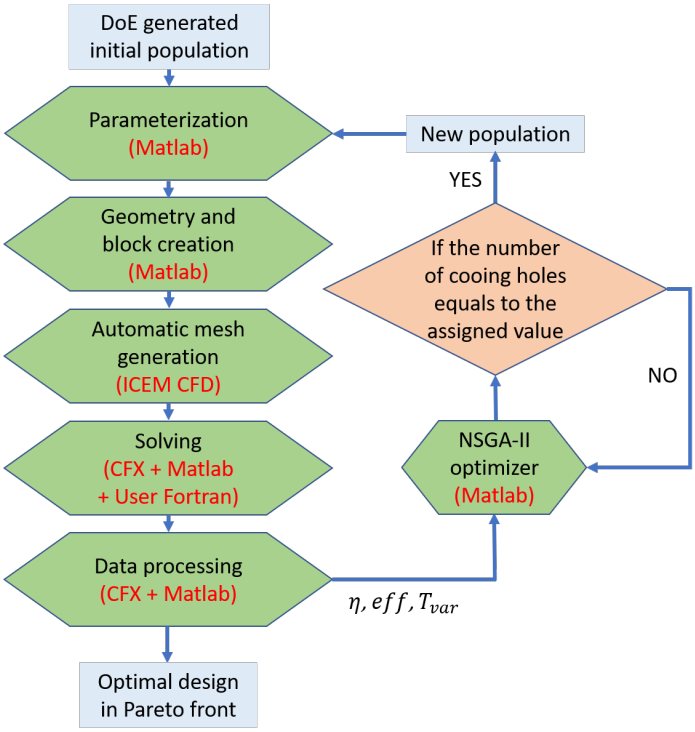


Figure 3.5: Overview of the Optimization flow chart.

3.4.3 Multidisciplinary Objective Functions

The objective function evaluates the turbine performance and provides an optimizing target for the optimization system. However, the evaluation of the turbine performance is never simple. As shown in Figure 3.6 multidisciplinary issues have to be

considered by turbine designers. The appropriate objective functions should sufficiently integrate these issues to reflect realistic engine performance. Therefore, the aerothermal performance of the turbine tip cooling design is measured by three objectives: the aerodynamic efficiency η, the film cooling effectiveness eff and the normalized temperature variance T_{var}.

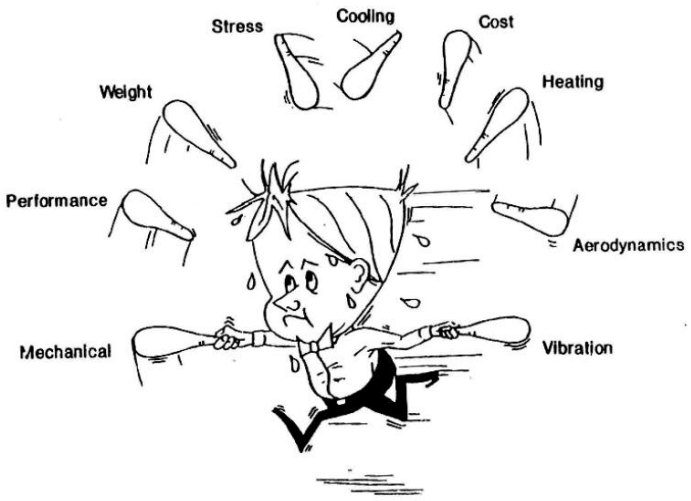


Figure 3.6: The technical "juggling" problem of the turbine designer [73].

In the cascade with adiabatic wall boundary conditions, the aerodynamic efficiency η represents the ratio of the kinetic energy at the exit to the one obtained isentropically from the inlet condition and the exit condition for both the mainstream and the cooling flow as computed here:

$$\eta = \frac{\frac{1}{2}\dot{m}_{exit}U_{exit}^2}{\dot{m}_{in}C_pT_{t,in}[1-(\frac{P_{exit}}{P_{t,in}})^{\frac{\gamma-1}{\gamma}}]+\sum\dot{m}_cC_pT_{t,c}[1-(\frac{P_{exit}}{P_{t,c}})^{\frac{\gamma-1}{\gamma}}]} \tag{3.13}$$

where $\dot{m}$ is the mass flow rate, U is the mass averaged velocity, T_t is the mass averaged total temperature, P and P_t is the mass averaged static and total pressure, C_p is the specific heat at constant pressure. The $exit$, in and c represent the locations at the exit, the inlet and the coolant inlet.

Because the evaluation of efficiency in the cooled turbine stage is difficult to define, this work adopts the most widely used method of Hartsel [35]. Based on this, the various streams of turbine flow is assumed to expand independently to the exit condition, as in Figure 3.7. The overall efficiency $\eta_{overall}$ represents the aerodynamic performance of the turbine. Generally $\eta_{overall}$ is defined as the ratio of the real work

w_{real} to the ideal work w_{ideal} as in Equation 3.14. Figure 3.7 illustrates the conceptual expansion process of the cooled turbine. Two flow streams, the main flow indicated as 1 and the blade cooling flow indicated as c, enter the turbine where work w_{real} is exerted and leaves the turbine as the mixed flow indicated as 3.

$$\eta_{overall} = \frac{w_{real}}{w_{ideal}} \tag{3.14}$$

The ideal work $w_{ideal,con}$ is calculated by Equation 3.15 where $T_{t,i-3,is}$ is the isentropic stagnation temperature assuming flow i expands isentropically to the status of mixed flow 3 as illustrated in $s - T_t$ diagram in Figure 3.7. Adiabatic wall boundary conditions are implemented. $T_{t,i-3,is}$ can be computed by equation 3.16 where P_{ti}^{wa} and P_{t3}^{wa} are the work averaged stagnation pressure; γ is the heat capacity ratio. According to Cumpsty and Horlock [70] the work averaged stagnation pressure instead of mass averaged one is used to give the correct work output when the flow leaves an ideal turbine. The work averaged stagnation pressure for flow 3 and i can be computed by the same Equation 3.17 where (T_t and $(T_t/P_t^{\frac{\gamma-1}{\gamma}})^{ma}$ are the mass averaged value of corresponding flow.

$$w_{ideal,con} = c_p \sum(\dot{m}_i T_{t,i}^{ma}) - c_p \sum(\dot{m}_i T_{t,i-3,is}) \tag{3.15}$$

$$T_{t,i-3,is} = T_{t,i}^{ma} (\frac{P_{t,3}^{wa}}{P_{t,i}^{wa}})^{\frac{\gamma-1}{\gamma}} \tag{3.16}$$

$$P_t^{wa} = (\frac{T_t^{ma}}{(T_t/P_t^{\frac{\gamma-1}{\gamma}})^{ma}})^{\frac{\gamma-1}{\gamma}} \tag{3.17}$$

By implementing the first law of thermodynamics, the real work can be computed in Equation 3.18 where i represents flow 1 or c; c_p is the specific heat in constant pressure; T_t^{ma} and $\dot{m}_i$ are the mass averaged stagnation temperature and the mass flow rate of corresponding flow.

$$w_{real} = c_p \sum(\dot{m}_i T_{t,i}^{ma}) - c_p T_{t,3}^{ma} \sum(\dot{m}_i) \tag{3.18}$$

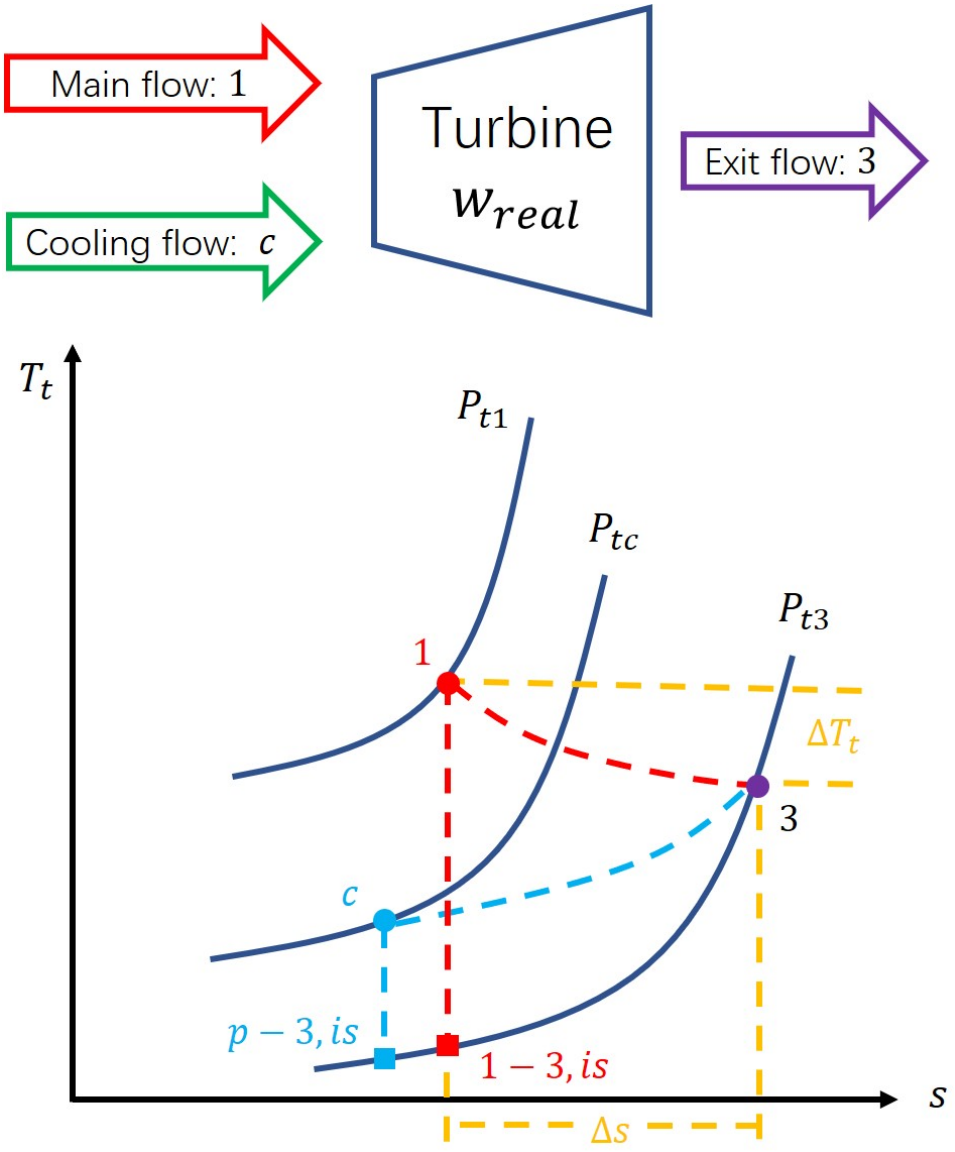


Figure 3.7: Conceptual expansion process of the cooled turbine.

Therefore the efficiency of the turbine is evaluated by the variation of the Equation 3.6:

$$\eta = \frac{\dot{m}_m(T_{t,1} - T_{t,3}) + \sum \dot{m}_m(T_{t,c} - T_{t,3})}{\dot{m}_m T_{t,1}(1 - (\frac{P_{t,3}}{P_{t,1}})^{\frac{\gamma-1}{\gamma}}) + \sum \dot{m}_c T_{t,c}(1 - (\frac{P_{t,3}}{P_{t,c}})^{\frac{\gamma-1}{\gamma}})} \tag{3.19}$$

The adiabatic film cooling effectiveness of the cooled blade represents the temperature reduction caused by the coolant ejected from the film cooling holes as calculated in Equation 3.20:

$$eff = \frac{T_{aw,uc} - T_{aw,c}}{T_{aw,uc} - T_{t,c}} \tag{3.20}$$

where $T_{aw,uc}$ is the adiabatic wall temperature in the uncooled case, $T_{aw,c}$ is the adiabatic wall temperature obtained in the cooled case, and $T_{t,c}$ is the total temperature at the coolant inlet. If not specified, the wall in this work represents the cavity floor, the cavity wall and the squealer rim. The value of the film cooling effectiveness is between 0 and 1. When eff equals to 0, the wall temperature is equal to the one in the uncooled case. This means the film cooling does not reduce the wall temperature. When eff equals to 1, the coolant completely cooled the wall to the coolant total temperature which represents the perfect cooling outcome.

It is noted that the cooling effectiveness is simply one factor to account for the heat transfer performance of the tip. In the previous research [31] the coolant injection has been shown to increase the heat transfer coefficient downstream of the cooling flow where the cooling effectiveness is low. Thus, the overall performance of the film cooling needs to be evaluated in terms of the net heat flux reduction which takes into account both the adiabatic wall temperature and the heat transfer coefficient.

The driving temperature on the wall is the recovery temperature. The recovery temperature represents the aerodynamic heating of the surface immersed in the flow. It can be computed by Equation

$$T_r = T_\infty(1 + r\frac{\gamma - 1}{2}M_\infty^2) \tag{3.21}$$

where T_∞ and $M_\infty$is the freestream temperature and Mach number; r is the recovery coefficient which is not a constant. For the front stagnation point, r is 1; in a laminar boundary layer on a flat plate, $r = \sqrt{Pr}$ for Prandtl number $0.5 < Pr < 10$; in a turbulent boundary layer on a flat plate, $r = \sqrt[3]{Pr}$ for Prandtl number close to 1. The difference between the freestream flow temperature and the recovery temperature increases with the freestream flow Mach number. Thus, in the high speed flow, the freestream flow temperature can not be used as the driving temperature. In this

study, the recovery temperature is represented by the adiabatic wall temperature in the case without cooling.

Considering the heat flux without film cooling, we have:

$$q_{uc} = h_{uc}(T_{r,uc} - T_{w,uc}) \tag{3.22}$$

where h_{uc} is the heat transfer coefficient in the uncooled case; $T_{r,uc}$ is the recovery temperature in the uncooled case which equals to the adiabatic wall temperature in the uncooled case, $T_{aw,uc}$; $T_{w,uc}$ is the metal temperature in the uncooled case. Equation 3.22 can also be understood by the linear variation of the heat flux with the wall temperature in two cases: one is the adiabatic case where the heat flux is 0 and wall temperature is $T_{aw,uc}$; the other one is the case with the isothermal wall where the heat flux is q_{uc} and the temperature is $T_{w,uc}$. Assuming the constant value of the heat transfer coefficient in this range of variation, we can obtain Equation 3.22.

If we use the same definition for the case with film cooling, we have:

$$q_c = h_c(T_{r,c} - T_{w,c}) \tag{3.23}$$

where h_c is the heat transfer coefficient in the cooled case; $T_{r,c}$ is the recovery temperature in the cooled case which equals to the adiabatic wall temperature in the cooled case, $T_{aw,uc}$; $T_{w,c}$ is the metal temperature in the cooled case, we can suppose it is equal to the uncooled wall temperature.

Thus, by combining Equation 3.22 and Equation 3.23, the net heat flux reduction is defined by

$$NHFR = \frac{q_{uc} - q_c}{q_{uc}} = 1 - \frac{h_c}{h_{uc}} \frac{T_{aw,c} - T_w}{T_{aw,uc} - T_w} \tag{3.24}$$

To reduce the computational cost, in this work only the cooling effectiveness is taken into account. NHFR should be considered in future work.

In addition to the film cooling effectiveness, the thermal fatigue caused by the non-uniformity of the temperature distribution is another concern to break down the turbine tip. The non-uniformity of the temperature field brings high thermal fatigue which is a different dimension to measure the heat transfer performance of the tip. Therefore another objective, the normalized temperature variance, T_{var}, is used to indicate the non-uniformity of the wall temperature distribution. It is calculated by the Equation 3.25.

$$T_{var} = \frac{\sigma(T_w)}{\overline{T_w}} \tag{3.25}$$

where $\sigma(T_w)$ is the standard variance of the wall temperature, $\overline{T_w}$ is the average wall temperature. For the tip study, the computation is calculated over the squealer floor and the tip rims.

Other variables, such as the heat transfer coefficient, although is not used in this study as design objective, is widely implemented to evaluate the heat transfer performance. The heat transfer coefficient (HTC, h) is computed by the Newton's law of cooling:

$$q = h(T_{ad} - T_w) \tag{3.26}$$

where q is the wall heat flux, T_w is the wall temperature, and T_{ad} is the adiabatic wall temperature. In the experiments, the impulse method as shown by Oldfield [65] can be used to process the data. In the CFD simulations, h and T_{ad} are obtained from the linear regression between q and T_w. HTC is computed using two-point method as shown in Equation 3.27:

$$h = \frac{q_1 - q_2}{T_{w1} - T_{w2}} \tag{3.27}$$

where 1 and 2 denote the two cases with different isothermal wall temperature; q is the heat flux on the wall and T_w is the wall temperature.

3.5 Summary

In this Chapter the methodology implemented in this thesis is introduced. Three two-level models are introduced to compare the sequential optimization with the current optimization, to have turbine working in both high subsonic and transonic regions and to contrast cascade with stage. These models investigate the important factors that affect the performance of the tip: the optimization sequence, the operating condition and the relative movement of the casing wall. The details of their influence on the flow behaviour will be discussed in Chapter 6. Then the multi-scale method is briefed to show the potential of reducing the number of mesh nodes of the structured mesh in presence of large length scale disparity. Finally the optimization system is used to search for the design of cooling position and squealer height with the optimal aerothermal performance.

Chapter 4

Methodology Validation

In this chapter, the multi-scale method introduced in Chapter 3 is validated against both the experimental data and the fine mesh simulations. From the validation, the multi-scale method is shown to be consistent with the experiments. Comparing to the fine mesh solution with coolant injection, the multi-scale method generates the results with similar accuracy but using the coarse mesh without cooling hole which reduces the number of nodes required by the cooling simulation.

4.1 Simple Concept Illustration Case for Multi-scale Method

Before applying the multi-scale method to the transonic turbine blade tip, a simple concept illustration case is used to verify the multi-scale method and to demonstrate the implementation in ANSYS CFX. The computational domain is shown in Figure 4.1 where five cuboidal cooling holes in green are embedded in the coarse main flow channel. The base mesh shown in red has 40,800 elements. Each embedded fine block has 18,576 elements. Each embedded coarse block has 2,064 elements. The embedded coarse blocks have the same mesh density as the base mesh. Compared to the embedded coarse blocks, the embedded fine blocks are refined three-times denser in both x and z directions. The mesh density in y direction is as same as the base mesh to keep the same level of wall resolution. The directions of x and y axes are shown in Figure 4.1.

The boundary conditions are shown in Figure 4.1 where $P_{0,in}$ and $T_{0,in}$ are the stagnation pressure and stagnation temperature at the mainstream inlet; P_{ex} is the static pressure at the exit plane. The five cooling holes have the same inlet condition where

the stagnation pressure, $P_{0,cool}$, and the stagnation temperature, $T_{0,cool}$, are assigned. The walls have no-slip and isothermal boundary conditions.

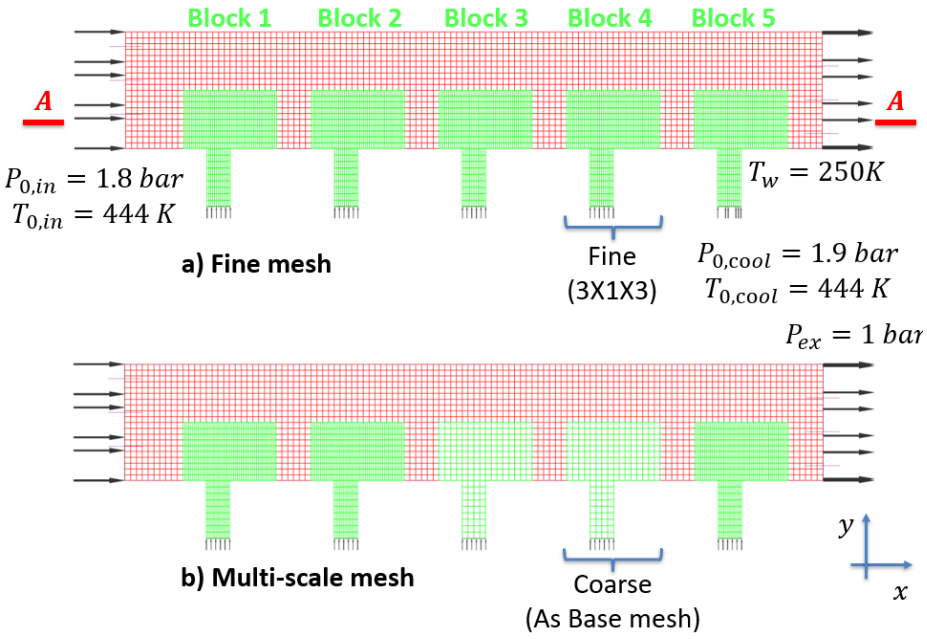


Figure 4.1: Computational domain of the simple concept illustration case.

There are two steps to implement the multi-scale method. In the first step, the source terms are collected from block 2 and block 5 as shown in Figure 4.2. It is obtained by projecting the fine-coarse mixed solution to the coarse mesh as the initial guess. In the fine-coarse mixed solution, block 2 and block 5 are refined while block 3 and block 4 are coarse. In coarse mesh, block 2 to 5 are all coarse. From this process, the residuals are obtained and used as the source terms.

The converged source terms added on the coarse mesh can reproduce the fine-coarse mixed solutions as show in Figure 4.3. In the figure the heat flux is normalized by Equation 4.1:

$$q_{normalized} = \frac{qC_x}{k_{air}(T_{01} - T_w)} \tag{4.1}$$

where q is the wall heat flux, C_x is length of the computational domain in x direction; k_{air} is the air conductivity at 250 K (equals to the wall temperature); T_{01} is the stagnation temperature at inlet and T_w is the wall temperature.

Figure 4.4 presents more quantitative results where where the normalized temperature along the intersection line AB-AB in the three cases is illustrated. While the fine-coarse mixed solution is shown in red, the coarse solution shown in blue can be improved by adding source terms as shown in the green line.

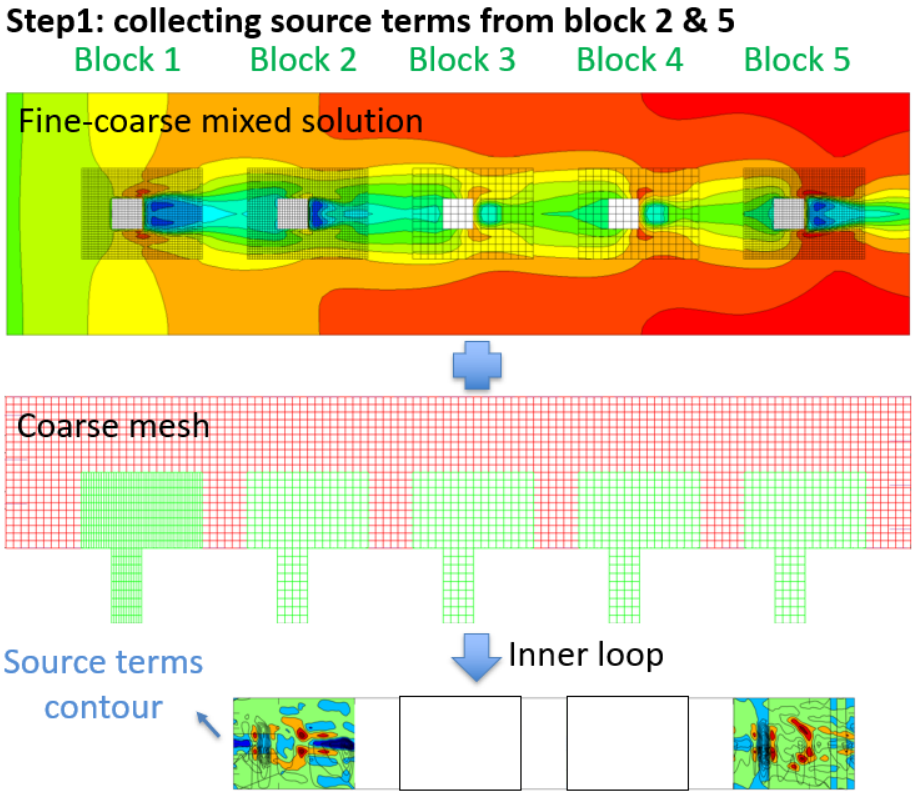


Figure 4.2: Process to collect the source terms from block 2 and block 5.

In the second step, the source terms in block 2 and block 5 are propagated to block 3 and block 4 by the Kriging interpolation, as shown in Figure 4.5. The Kriging method builds a surrogate model between the physical positions of the cells in the block and the source terms in the seven flow equations including the continuity equation, the three momentum equations, the energy equation and two equations for the turbulence kinetic energy and the turbulence eddy frequency because the $k-\omega$ SST turbulence model is used in this study. Since iterations are involved in the propagation of the source terms, in this case the final converged source terms are found to be insensitive to the interpolation method. Both the linear interpolation and the Kriging interpolation are able to get the converged source terms and reproduce the fine mesh results.

From the propagation, the effect of mesh refinement is added in these two coarse blocks. Since the source terms in the first iteration are obtained from the scenario that block 3 and block 4 are coarse without any source terms, they do not provide the right boundary condition. Therefore in the next iteration, the propagated source terms obtained from the previous iteration are added into the block 3 and block 4

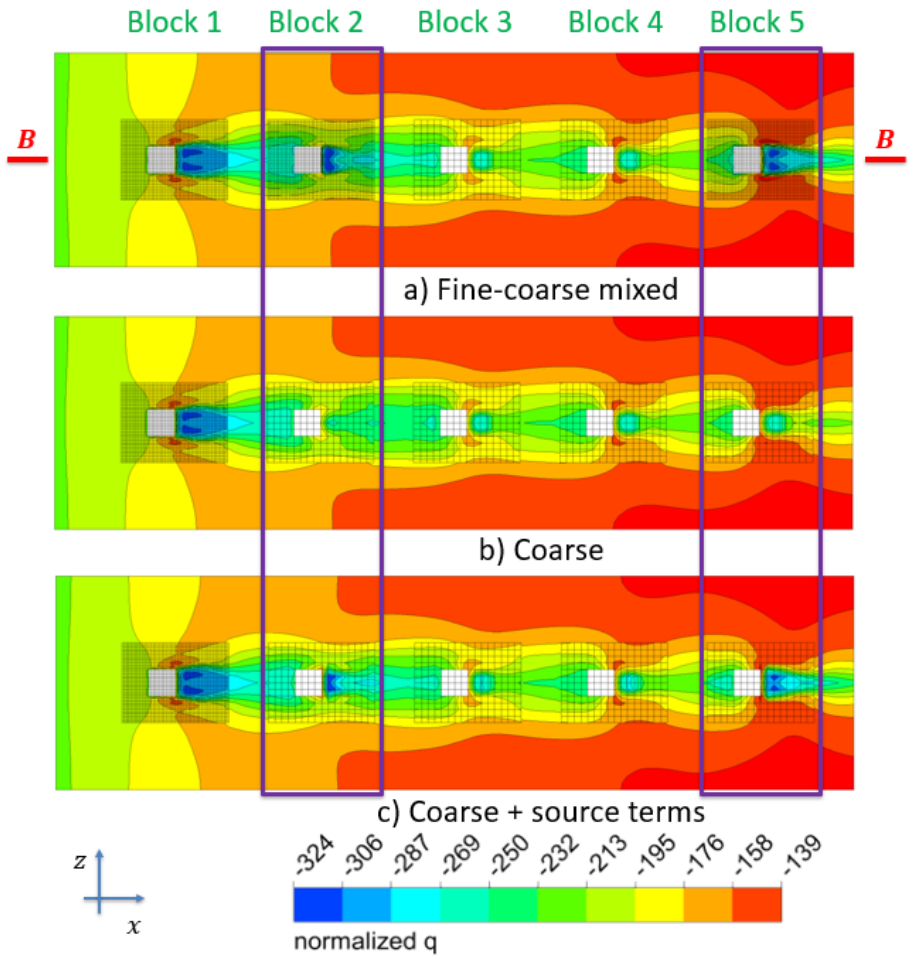


Figure 4.3: Normalized heat flux at the bottom wall. In plot *c*), the source terms are collected and added on block 2 and block 5 to reproduce the find-coarse mixed solution. The source terms are only added to Block 2 and Block 5 to verify if the local coarse mesh is able to reproduce an equivalent fine-mesh solution when the source terms are added.

to 'partially' represent the refinement of these two blocks. This improves the source terms collected from block 2 and block 5 in the next iteration, because these two blocks are under an improved boundary condition. Thus after several iterations, the finally converged source terms are under the right boundary condition that all the blocks are refined.

The influence of the converged source terms can be shown in Figure 4.6. In the figure, plot *a*) shows the fine solution where all the five holes are refined; plot *b*) is the coarse results where block 3 and block 4 are coarse; plot *c*) is the multi-scale solution where the source terms are propagated to the coarse blocks. By comparing plot *b*) and plot *c*) with plot *a*), the propagated source terms are shown to improve the solution in

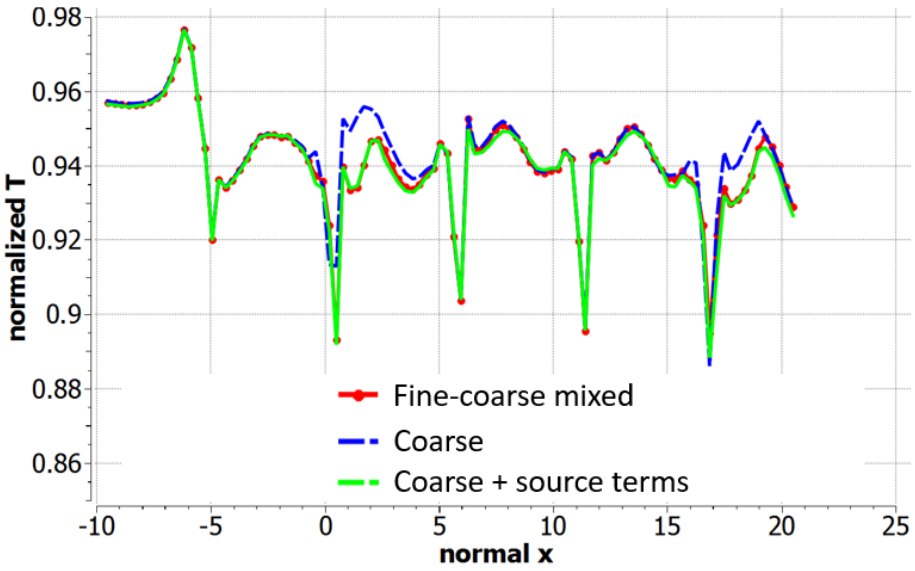


Figure 4.4: Normalized temperature along AB-AB line. The temperature is normalized by the stagnation temperature at the mainstream inlet. The line AB-AB is obtained by the intersection of the cross-section plane A-A in Figure 4.1 and the cross-section plane B-B in Figure 4.3.

block 3 and block 4. More quantitative results are shown in Figure 4.7. Relative to the fine mesh solution shown in red, the coarse solution shown in blue can be improved by the propagated source terms as shown in the green line.

Comparing to the fine mesh, the multi-scale method reduces the number of mesh nodes. However, the two-level iteration loop mentioned earlier consumes additional time to collect the source terms in the multi-scale method. Therefore the computational time in the multi-scale method is comparable to the fine mesh solution. Noted in this simple concept illustration case, only two coarse blocks use source terms to reduce the mesh resolution. In a more general case, where a large number of the coarse blocks are implemented, the time spent on collecting the source terms can be compensated by the time saved from reducing the number of mesh nodes.

4.2 Validation with Experimental Data

In this section the multi-scale method is validated against Ma's [31] [32] experimental data. In Ma's papers, a transonic blow-down wind tunnel is employed to conduct the transient heat transfer experiments on a cascade. The test section is located inside a testing plenum. The tip surface temperature history is recorded by an infrared (IR) camera through a zinc-selenide (ZnSe) IR window. To stabilize the flow field the

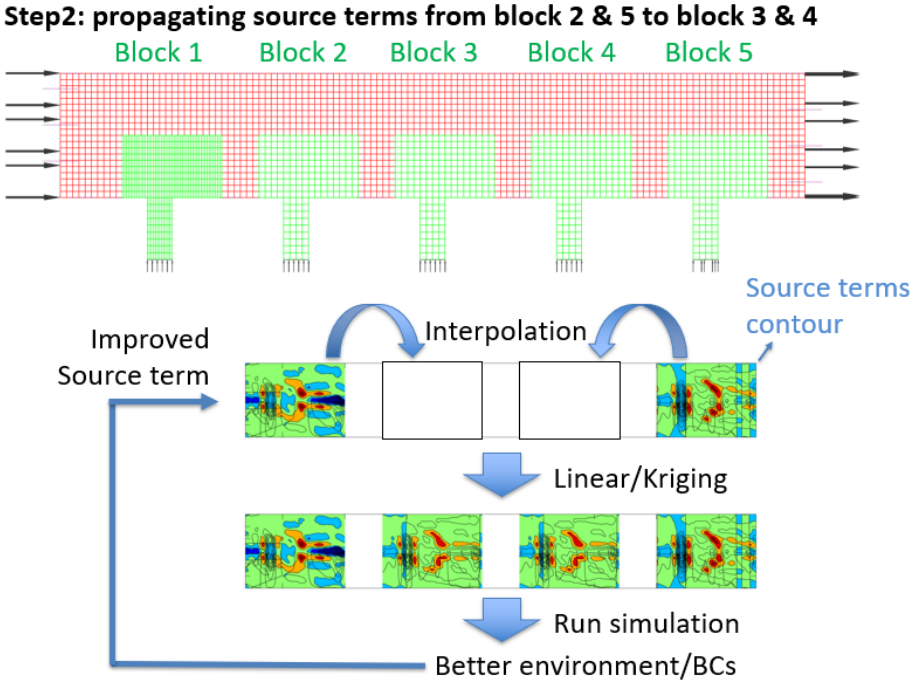


Figure 4.5: Propagation of the source terms from block 2 and block 5 to block 3 and block 4. BCs stands for the boundary conditions.

coolant supply system was precooled for 30 minutes before the blow-down experiment. A heater mesh installed to heat up the mainstream flow is turned on for five seconds after the opening of the control valve.

Two squealer tip configurations used in Ma's experiments [31] are validated here: the uncooled blade and the blade with nine cooling holes on the tip cavity floor near the pressure side. In both the simulations, the $k-\omega$ SST model is employed in ANSYS CFX. The grid size is 5 million. y^+ value on the tip is about 1 to resolve the near-wall boundary layer. The boundary conditions for the experiments and the CFD set-up are the same with those in Ma's paper: $P_{0,in} = 1.8\ bar$, $T_{0,in} = 300\ K$, $P_{0,cool} = 1.98\ bar$, $T_{0,cool} = 270\ K$ and $P_{ex} = 1.01\ bar$. The inlet turbulent intensity is approximated to 1%. The HTC used here is computed by Equation 3.27 where the two different isothermal wall temperatures are 250 K and 260 K.

To validate the results, a parameterization system is built by the author to reproduce the geometry of the turbine blade shown in Ma's paper. The details of the parameterization system is elaborated in Chapter 5. For the cooled turbine, the embedded mesh has two types: the fine block with 0.1 million cells and the coarse block with 2k cells. The fine and coarse blocks have the same spanwise nodes distribution. In

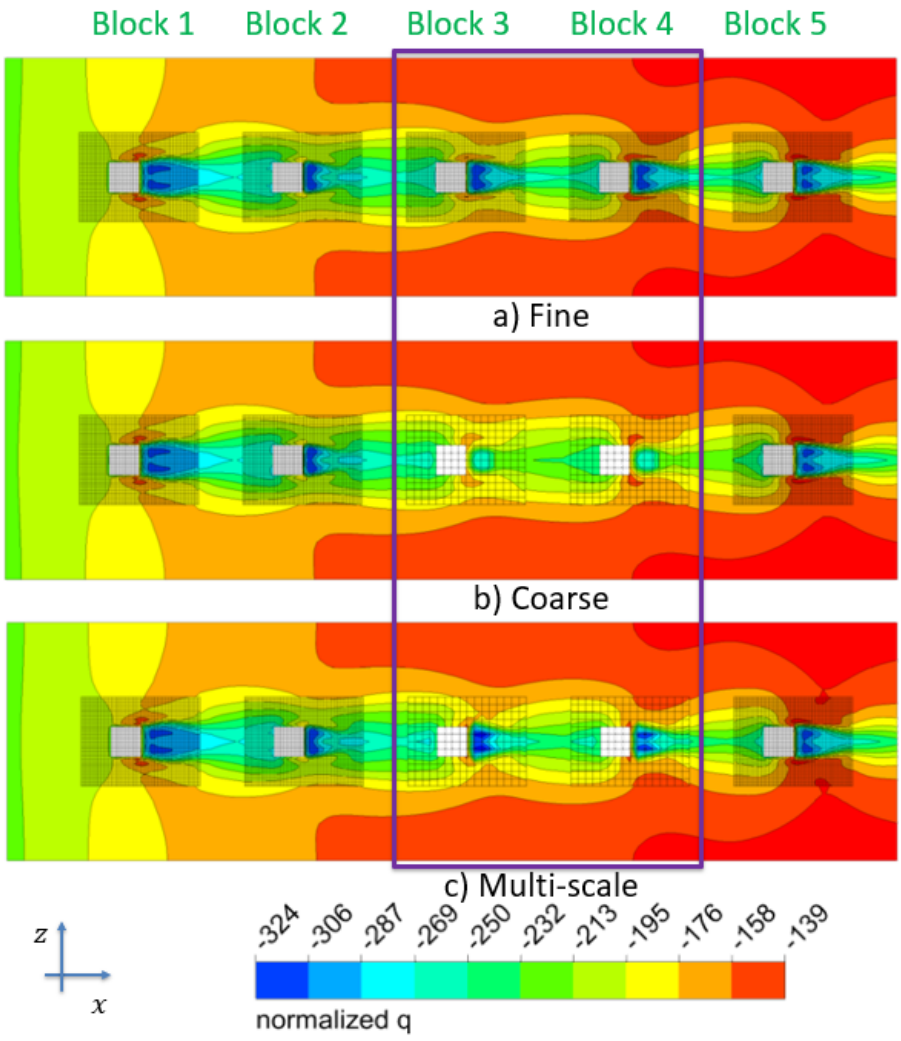


Figure 4.6: Normalized heat flux at the bottom wall. The heat flux is normalized by Equation 4.1. In plot *c*), the source terms are propagated to block 3 and block 4 to reproduce the fine mesh solution.

axial and circumferential directions, the ratio of nodes number between the fine and coarse blocks are 5.

First, the CFD set-up without using the multi-scale method are validated. In Figure 4.8 the HTC contours on the uncooled tip is demonstrated. Here 'EXP' stands for the experimental data. 'Ma's SST' represents the CFD results computed and shown in Ma's paper. 'SST' is the author's CFD results using $k-\omega$ SST as the turbulence model. Because the boundary conditions implemented in this study is the same with those in Ma's paper, the differences between Ma's SST results and the author's SST results in Figure 4.8 are deemed to be caused by the influence of the solver and the mesh. In Ma's work the solver is Fluent while in this study CFX is implemented as the

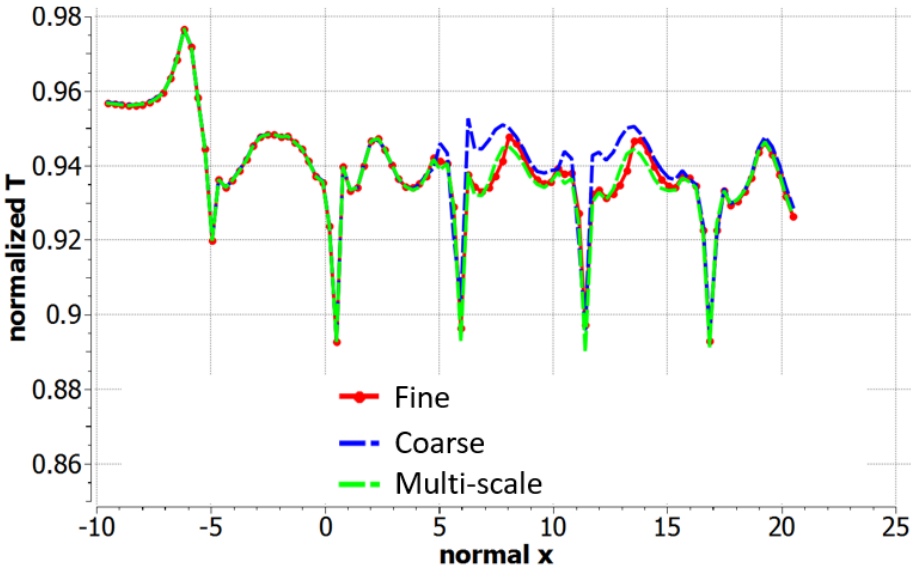


Figure 4.7: Normalized temperature along AB-AB line. The temperature is normalized by the stagnation temperature at the mainstream inlet. The line AB-AB is obtained by the intersection of the cross-section plane A-A in Figure 4.1 and the cross-section plane B-B in Figure 4.3.

solver. Moreover, since the meshes in these two studies are generated independently, it is inevitable to induce the local differences of the mesh density or quality. However, it is noted that both of the results capture the distinctive high HTC strip at the frontal portion of the tip.

The same notification will be used in Figure 4.9 where the quantitative study is illustrated. In Figure 4.9 the circumferential averaged HTC values at the tip along axial direction are plotted. Comparing to the experimental data, the relative Root Mean Square Error (RMSE) of the circumferential averaged HTC in Ma's results is 16%; in the author's results is 22%.

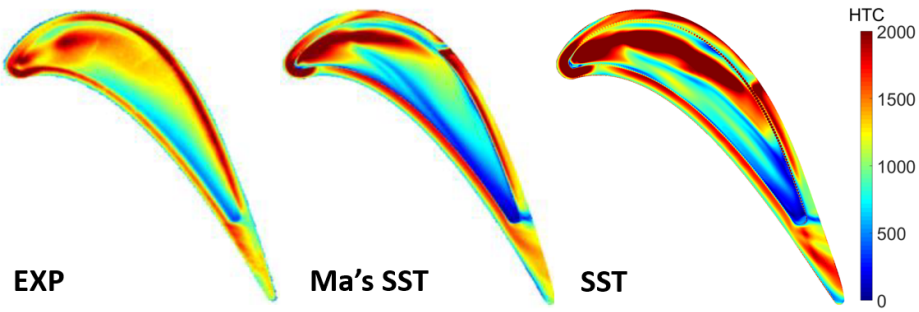


Figure 4.8: HTC contours on the uncooled tip.

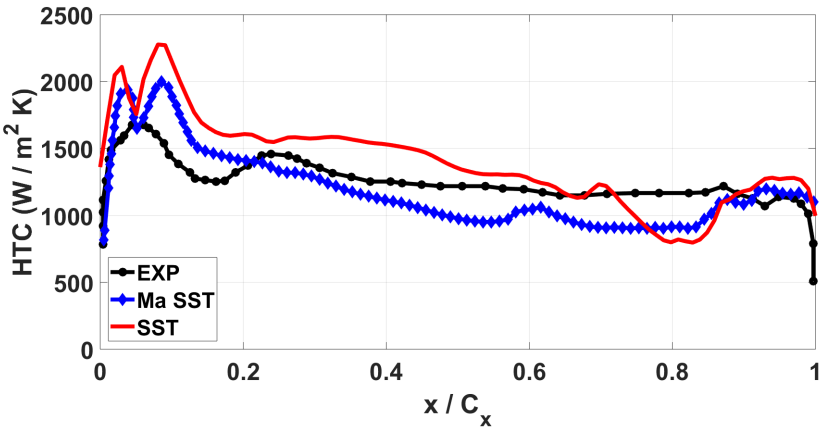


Figure 4.9: Circumferential averaged HTC value at the tip along axial chord for uncooled blade.

After CFD set-up being validated in the uncooled blade, the multi-scale method is implemented in the case with nine cooling holes near the pressure side. Among the nine cooling holes, the first, the fifth and the ninth holes are fine blocks. The rest are coarse blocks.

In Figure 4.10, Ma's experimental data are shown in plot *a*). The results with all nine resolved holes are shown in plot *b*). From the comparison between the experimental data and the CFD results, there is general qualitative agreement on some of the flow structures. However, several details are different and the levels of heat transfer coefficient in CFD results are much higher than the one in the experiments. The detailed reasons for these discrepancies need to be discussed in the future work.

Downstream of the cooling holes the distinctly high HTC strips are observed. In plot *c*), all the blocks use coarse mesh. A rather different HTC contour is found. The HTC strips computed from the coarse block are shorter and weaker due to the poorly resolved cooling holes. In plot *d*) and plot *e*), the multi-scale method is shown to improve the results in the coarse block. Plot *d*) shows the results using the source terms from the first outer loop iteration. Plot *e*) shows the results using the converged source terms. Ten iterations are found to be sufficient for the source terms to converge. The comparison between plot *d*) and *e*) illustrates the necessity to iterate the source terms. By adding the converged source terms into the coarse blocks, the improved results agree well with the resolved results shown in plot *b*).

The more quantitative results are shown in Figure 4.11. It exhibits the circumferential averaged HTC value at the tip along the axial chord for the blade with nine cooling

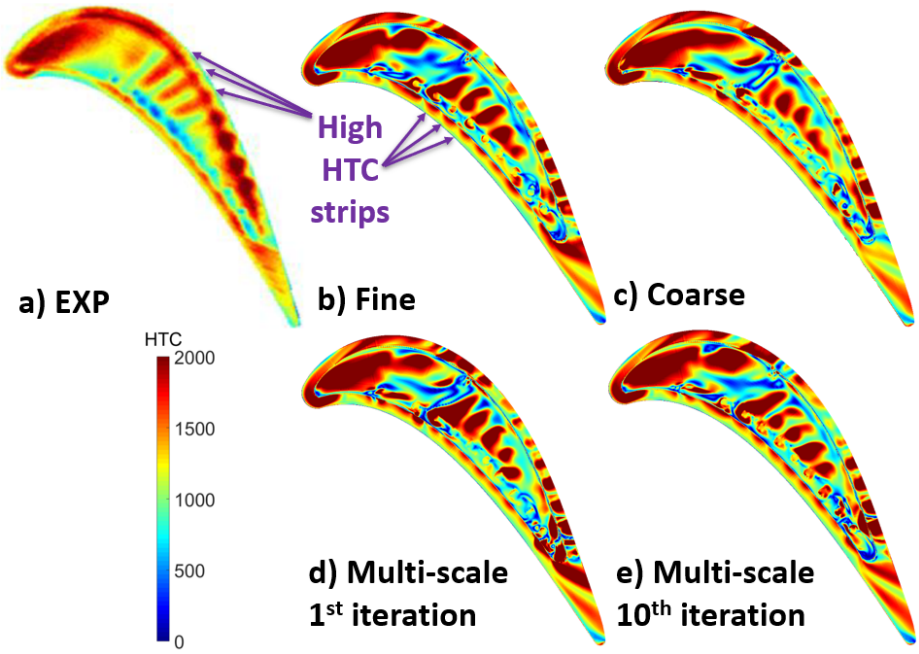


Figure 4.10: HTC contours on the squealer with nine cooling holes near the pressure side.

holes near the pressure side. The fine mesh results in red are consistent with Ma's experimental data in black. The coarse results shown in blue have discrepancies comparing to the resolved solution in red. However, by adding the converged source terms, the improved results shown in green is rather close to the resolved solution. Comparing to the experimental data, all the three simulations have a similar RMSE of 15%.

The comparison of the relative RMSE, the total number of mesh nodes and the computational time are shown in Table 4.1. Here the RMSE is the error of the circumferential averaged HTC values at the tip relative to the fine mesh results. The computational time is normalized by the fine mesh computational time.

Table 4.1: Comparison of three simulations in the validation case.

Case	RMSE	No. of mesh nodes	computational time
Fine	0%	$6.36M$	1
Coarse	10%	$5.03M$	0.7
Multi-scale	7%	$5.35M$	0.9

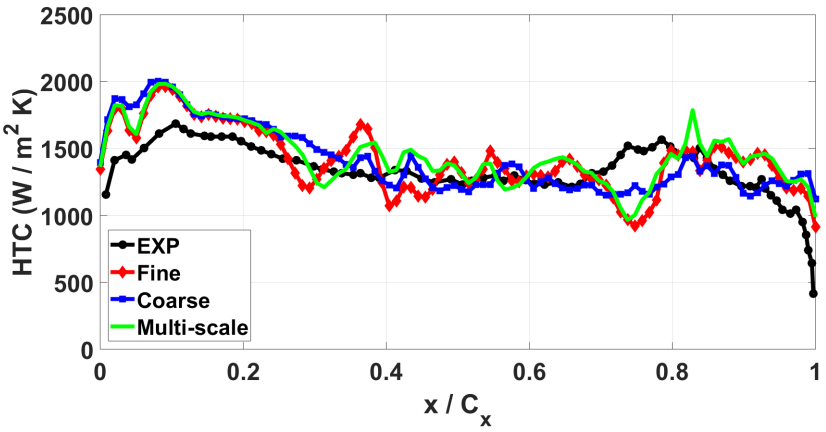


Figure 4.11: Circumferential averaged HTC values at the tip along axial chord for the blade with nine cooling holes near the pressure side.

4.3 Multi-scale Method for Turbine Tip Cooling Simulation

After the multi-scale method is verified by the simple case and validated against the experimental data, it now can be implemented in the transonic turbine blade tip cooling design. Two cases with different configurations of 12 cooling holes are used to illustrate the implementation of the multi-scale method.

The mesh is automatically generated by the parameterization system introduced in the previous section. The mesh of the computational domain is shown in Figure 4.12. The two cooling configurations are illustrated in Figure 4.13. In the figure, the red and the pink lines are the base mesh. The green lines are the mesh of the embedded blocks. Two types of mesh density can be chosen for the 12 cooling holes: the fine block of 100k cells with the internal hole geometry and the coarse block of 7k or 3k cells with or without the internal hole geometry. In Case 1, eight cooling holes are refined, and four cooling holes are coarse. In Case 2, six cooling holes are refined, and the other six cooling holes are coarse. The cooling configuration in Case 2 is different from the one in Case 1 to show that the multi-scale method can be used in various cooling configurations. The fine blocks are used to collect the source terms and to propagate the source terms to the coarse blocks. Both Case 1 and Case 2 use the same blade geometry and the same boundary condition as those in the experiment validation case. The isothermal wall temperature is 250 K.

Figure 4.14 shows the normalized heat flux contours on the tip from the fine results,

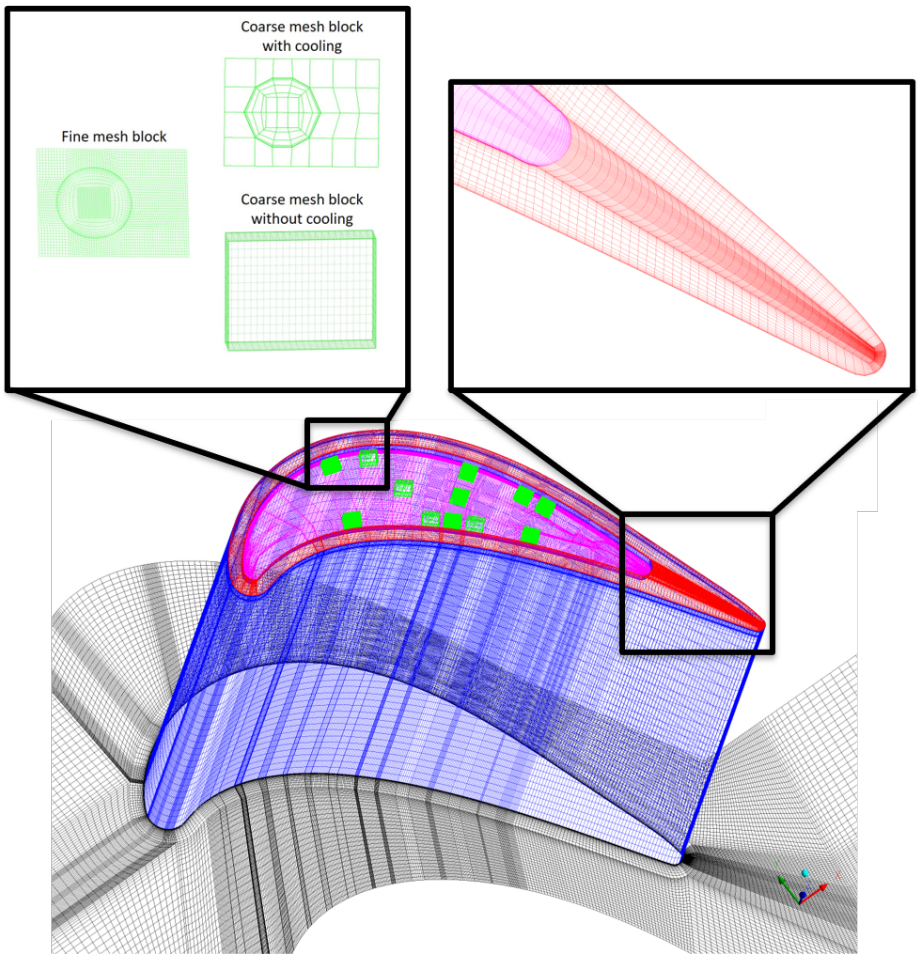


Figure 4.12: Mesh of the computational domain in the transonic tip cooling case. For the embedded cooling blocks, two types of blocks are used: the fine blocks with the internal hole geometry and the coarse block with or without the internal hole geometry.

the coarse results and the multi-scale method computed results. The heat flux is normalized by Equation 4.1. Their differences are highlighted by the red dashed circles. It is noted that with the multi-scale method, the high heat transfer region (blue) missed in the coarse mesh solution can be re-generated by the propagated source terms. Also, in the fine results there is only one low heat transfer strip (red) while in the coarse results there are three. The multi-scale results can successfully reproduce the single strip. At the rear portion of the squealer, the coarse results wrongly predict a high heat transfer strip (blue) which are eliminated in the multi-scale results.

The more quantitative results are shown in Figure 4.15. Relative to the fine solution in red, the multi-scale solution in green are more accurate than the coarse solution in

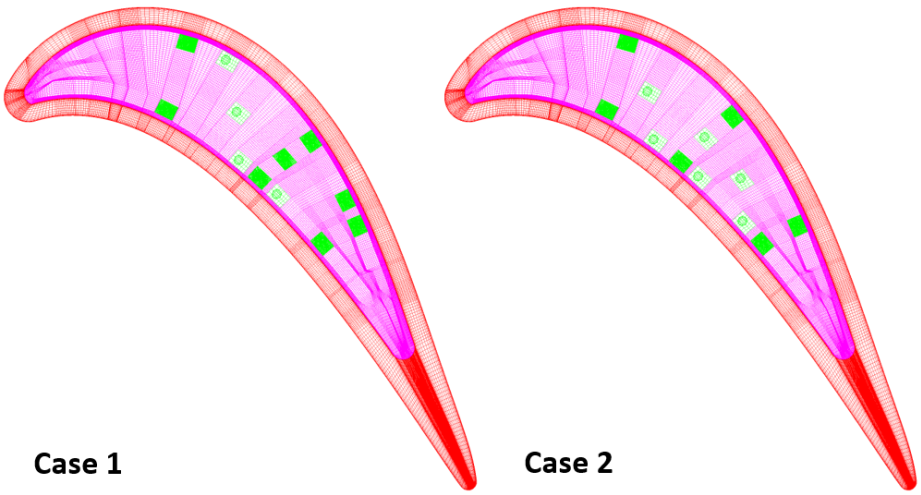


Figure 4.13: Cooling configurations of 12 cooling holes for Case 1 and Case 2.

blue. In this case the multi-scale method can save 0.4 million of mesh nodes. Because the computational time saved by reducing the number of mesh nodes is not sufficient to compensate the time spent on the source terms collection, the computational time of the multi-scale method in Case 1 is comparable to the fine mesh simulation.

The other interesting observation is that the source terms can not only present the influence of the mesh resolution but also the flow injection. It is because the source terms are generated by the difference between the numerical set-up of the current case and the initial conditions. When the governing equation is discretised on the coarse mesh without injection while the initial condition is the fine mesh results with injection, the source terms obtained will have two effects: refining the coarse block and adding injection. Therefore by adding the source terms on the coarse mesh without injection holes, the solution can be similar to the fine mesh results with injection holes. The results are shown in plot d) of Figure 4.14. In this implementation, the coarse blocks in Case 1 do not have real flow injection. The injection effect is purely produced by the propagated source terms. The solution using the converged source terms are shown to be similar to the fine mesh solution and the multi-scale solution with flow injection.

In Case 2, the multi-scale method is implemented more ambitiously. Only six fine blocks are used to collect the source terms. The other six blocks are all coarse blocks. In Figure 4.16, the multi-scale results are shown to have good agreement with the fine results while the coarse results show discrepancies.

The quantitative study of Case 2 is shown in Figure 4.17 where the multi-scale method

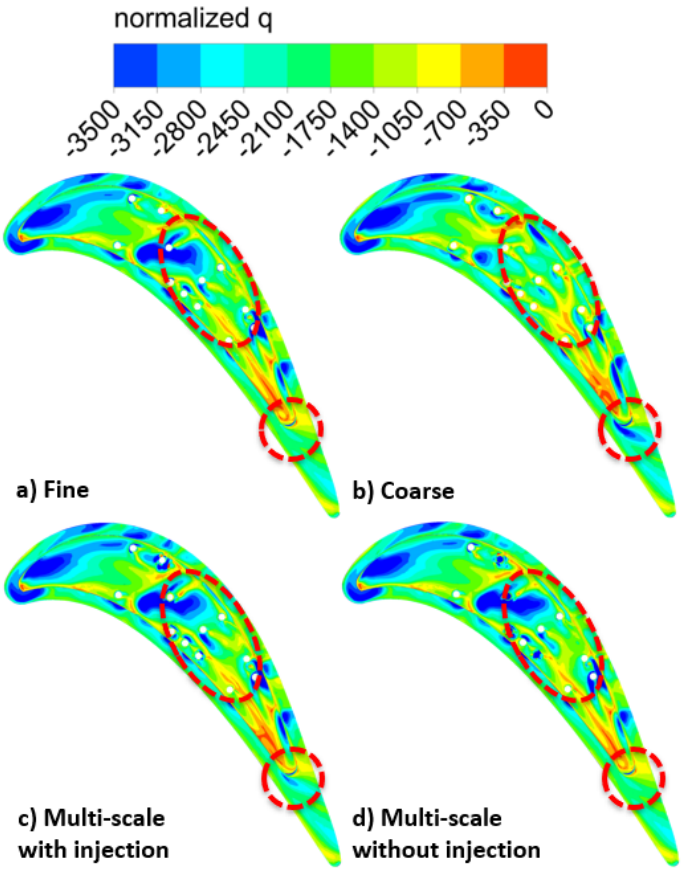


Figure 4.14: Normalized heat flux contours on the tip for Case 1. Multi-scale method with and without injection both can reproduce the fine mesh solution.

is found to improve the prediction. Because in Case 2, six coarse blocks are used rather than four coarse blocks in Case 1, more (0.7 million) number of nodes are saved. The gain on the computational time is also increased.

Because in Case 1 and Case 2 different amounts of holes are resolved, the influence of the number of the resolved holes can be investigated. Here Case 1 has eight resolved blocks, and Case 2 has six. Comparing to the fine mesh solutions, the two cases using multi-scale method have different RMSE of the circumferential averaged HTC values on the tip surface. In Case 1, the relative RMSE improved by multi-scale method comparing to the coarse mesh solution is 7% while in Case 2 the improvement is 3%. On the other hand, the computational cost in Case 1 is longer than the fine mesh simulation while in Case 2 it is shorter. Therefore as the number of resolved holes decreases, the gain obtained in the RMSE will decrease, but the improvement in the computational time will increase.

Moreover, the interaction between the cooling flow and the base flow can be observed

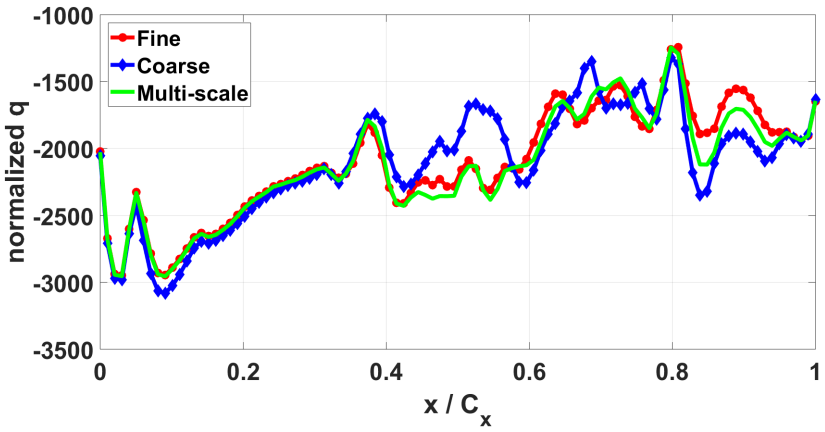


Figure 4.15: Circumferential averaged normalized heat flux at tip in Case 1.

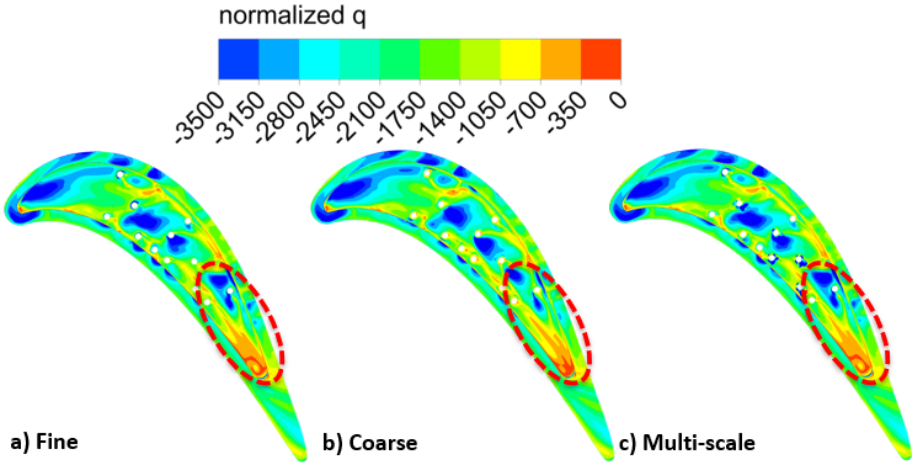


Figure 4.16: Normalized heat flux contours on the tip for Case 2.

by comparing the heat flux contours of the fine mesh solution in Figure 4.14 and Figure 4.16. It is noted that from Case 1 to Case 2 by varying the cooling configurations, the heat transfer contours have substantial changes. The large high heat transfer region (blue) at the half chord in Case 1 is split into three smaller high heat transfer regions in Case 2.

4.4 Applicability of Multi-scale Method in Commercial Solver

The implementation of the commercial solver enables other researchers to employ the multi-scale method in the similar manner as shown in this study. However, the major limitation of the multi-scale method in a commercial solver is the iterations needed

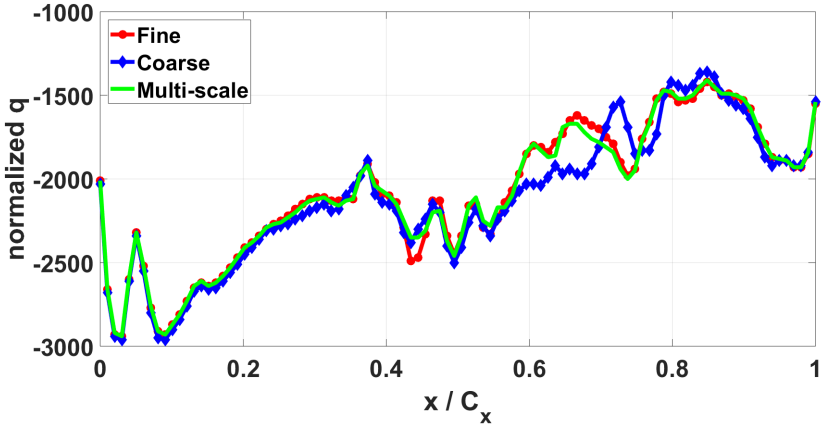


Figure 4.17: The circumferential averaged normalized heat flux at the tip in Case 2.

in the inner loop as stated in Section 3.3.1. In the commercial solver, such as CFX or Fluent, the visit of the right hand side value is prohibited. The right hand side value has to be collected from the residual with several iterations which increases the computational time. The iterations in the inner loop can be avoided in the open sourced code. The collection of the source terms can be obtained by reading the right hand side value of the discretized differential equations (as shown in Equation 3.11). Due to the time limitations of this project, the open sourced code is not used in this thesis.

In the outer loop, the iterations are implemented to propagate the source terms and to update the flow field. The number of the iterations in the outer loop is related to the flow field. If the repetitive blocks contained in the flow domain has similar flow structures, the number of iterations in the outer loop will reduce. Moreover, as the number of the repetitive blocks increases, more blocks can be resolved by the propagated source terms using multi-scale method. Thus, the number of the mesh nodes to resolve these repetitive blocks reduces.

4.5 Summary

In this chapter, the multi-scale method elaborated in Chapter 3 is validated against the experimental data as well as the fine mesh solution. The multi-scale method can reduce the number of mesh nodes while maintain the accuracy of the simulation in the case with large length scale disparities. In the tip cooling cases, 8% reduction of mesh nodes is obtained with 4 out of 12 holes modeled using coarse meshes and source terms; 13% reduction of mesh nodes is obtained with 6 out of 12 holes modeled

using coarse meshes and source terms. Due to the iterations needed to collect source terms, the computational time is not reduced by the multi-scale method. The multi-scale method might give further speed ups as the number of modelled cooling holes increases.

Chapter 5

Turbine Stage Design

Several unique flow features have been found in the transonic turbine as stated in Chapter 2. In this chapter, two turbine stages (one subsonic, one transonic) are designed using a parameterization system. The blade profile data at the midspan are attached in Appendix 1. In addition to those already stated in Chapter 3, more details of the parameterization system are introduced. First, the rotor and the stator 2D profiles at various radial sections are produced by the system using 11 blade design parameters. Then by using radial equilibrium, the 2D blade profiles are transferred into 3D and stacked along the stacking lines to form the 3D blade surface. Finally, blocks are automatically generated to accommodate the mesh for the blade profiles.

After the meshes of a subsonic stage and a transonic stage are generated by the parameterization system, they are simulated at realistic engine working conditions using the CFX CFD solver. From the CFD results, the aerodynamic efficiencies are found to be consistent with the performances exhibited in the Smith Chart. The agreement validates the designs of the stages and builds the foundation for an optimization case study using shaping and flow control.

5.1 Blade Parameterization System

5.1.1 2D Blade Profile Parameterization

In this study, the turbine blade surface is constructed by a 3D stacking line guiding several radial sections of 2D blade profiles at the stagnation point of the leading edge. The 2D blade profiles are determined using 11-parameters based on Pritchard's work [58]. The 11 parameters implemented in this method all have physical meanings so

that the designers can conveniently recognize the design features and integrate the previous blade designs into the parameterization system.

The 11 parameters listed in Table 5.1 are the blade leading edge radius r_{LE}, the trailing edge radius r_{TE}, the leading edge wedge angle $\epsilon_{wedge,LE}$, the trailing edge wedge angle $\epsilon_{wedge,TE}$, the leading edge metal angle β_{LE}, the trailing edge metal angle β_{TE}, the chord length C, the stagger angle $\alpha_{stagger}$, the throat width t, the unguided turning $\delta_{unguided}$ and the pitch p as shown in Figure 5.1.

Table 5.1: 11 parameters to generate blade profile.

name	parameter
leading edge radius	r_{LE}
trailing edge radius	r_{TE}
leading edge wedge angle	$\epsilon_{wedge,LE}$
trailing edge wedge angle	$\epsilon_{wedge,TE}$
leading edge metal angle	β_{LE}
trailing edge metal angle	β_{TE}
chord length	C
stagger angle	$\alpha_{stagger}$
throat width	t
unguided turning	$\delta_{unguided}$
pitch	p

By assigning the value of the 11 parameters, five points, $pt1$, $pt2$, $pt3$, $pt4$ and $pt5$, on the blade curve can be fixed. In Figure 5.1 the single blade geometry is shown in plot a) at the top. The geometric relationship between two adjacent blades is shown in plot b) at the bottom. These five points divide the blade profile into five portions: $curv1$, $curv2$, $curv3$, $curv4$ and $curv5$.

Among these curves, $curv5$ and $curv3$ are the leading edge and the trailing edge curve where circular curves are used. $curv1$, $curv2$ and $curv4$ are ninth order Bezier curves which are formed by 10 control points as illustrated in Figure 5.2.

Among the ten control points in the ninth order Bezier curve, only two of them need to be assigned. Comparing to the previous applications in blade design, the ninth order Bezier curve implemented here has a rather high order. This is to ensure third-order continuity. However, not all of the control points need to be assigned by the designer. Taking $curv1$ as an example, $cpt1$, $cpt2$, $cpt3$ and $cpt4$ are the control points used to provide the zeroth, first, second and third-order continuity with the circular curve $curv5$. Similarly, $cpt10$, $cpt9$, $cpt8$ and $cpt7$ are implemented to ensure the zeroth, first, second and third-order continuity with $curv2$. In the system, the

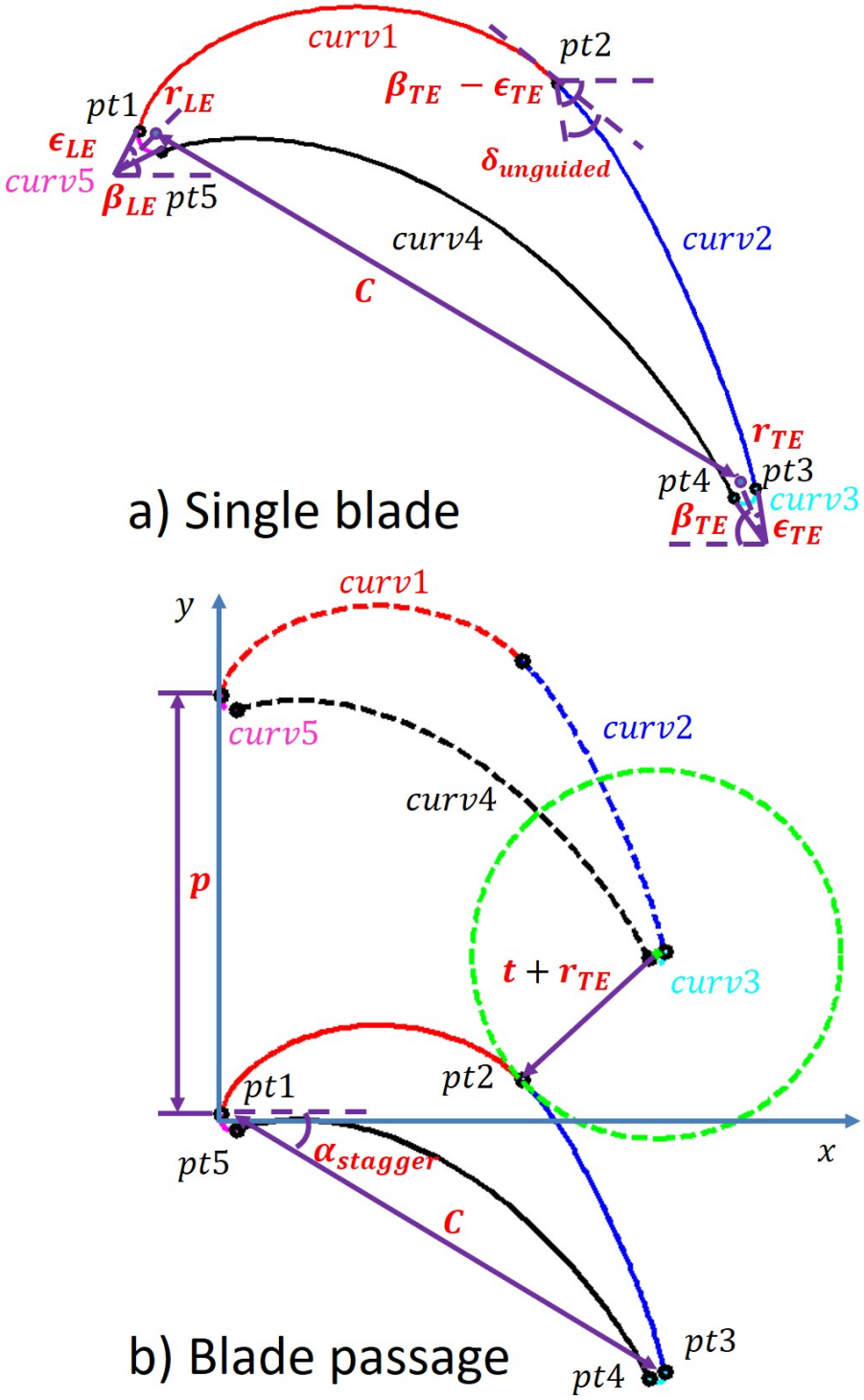


Figure 5.1: 11 parameters to parameterize airfoil.

axial coordinates (x) of these eight control points are fixed, and their circumferential coordinates (y) are computed to keep the zeroth, first, second and third deviation of the Bezier curve in line with the adjacent curves. Therefore all these eight control points are automatically decided by the system. The axial coordinates of $cpt5$ and $cpt6$ are set to equally separate the axial distance between $cpt4$ and $cpt7$. Only the circumferential coordinates of the control points $cpt5$ and $cpt6$ require assignment. Thus only two design variables are needed to fix the ninth order Bezier curve.

Hence for the blade passage, in addition to the 11 parameters used to fix the five points on the blade curve, another 6 design variables, $y_{5,curv1}$, $y_{6,curv1}$, $y_{5,curv2}$, $y_{6,curv2}$, $y_{5,curv4}$ and $y_{6,curv4}$, are needed to assign the circumferential coordinates of the control points so that the shape of $curv1$, $curv2$ and $curv4$ can be controlled .

In addition to the one introduced here, there are also other ways to parameterize blade surface such as using the Bezier-patches representation method by Casey [66], a superposition of baseline design and perturbation function, e.g. by Zhang and He [62], a combination of camber line and thickness distribution function, e.g. Arnone et al.'s work [1]. The main drawback of these methods is the lack of physical meanings for design variables. A universal parametric airfoil function proposed by Kulfan [12] also has physical meanings for some of the parameters. In this method, Bernstein polynomials instead of Bezier curves are used to keep continuity of curvature by definition. Due to the time limitations of this project, this method is not used in this thesis. The main difference between the Pritchard's 11-parameter method [58] and the one used in this study is that in Pritchard's work, $curv2$, the suction side curve downstream of throat, is a circular curve which implies the value of the trailing edge wedge angle, $\epsilon_{wedge,TE}$ depends on the other design variables, while in this research $curv2$ is the ninth order Bezier curve and $\epsilon_{wedge,TE}$ is an independent design variable.

5.1.2 Explanation on Keeping Third-order Continuity

The reason to keep the profile third-order continuous (C^3) throughout the blade is to improve the blade performance. Korakianitis [98] shows that when the blades have different distributions of curvature on the suction side, although the differences in blade profile caused by the curvature differences can be rather small, their boundary layer thickness and surface Mach number distribution can have distinct differences. This is shown in Figure 5.3 and Figure 5.4. Therefore to eliminate the loss caused by the discontinuity in curvature distribution, the blade profile is kept third-order continuity everywhere.

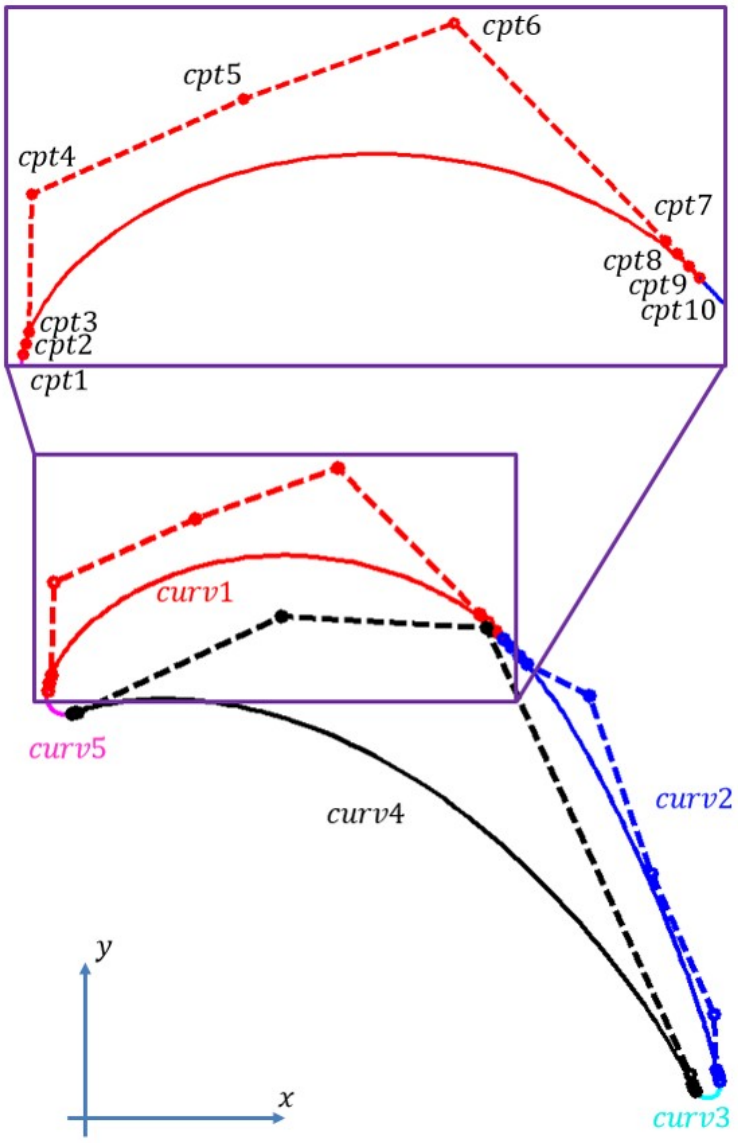


Figure 5.2: $Curv1$, $curv2$ and $curv4$ are generated by ninth order Bezier curves which are formed by 10 control points.

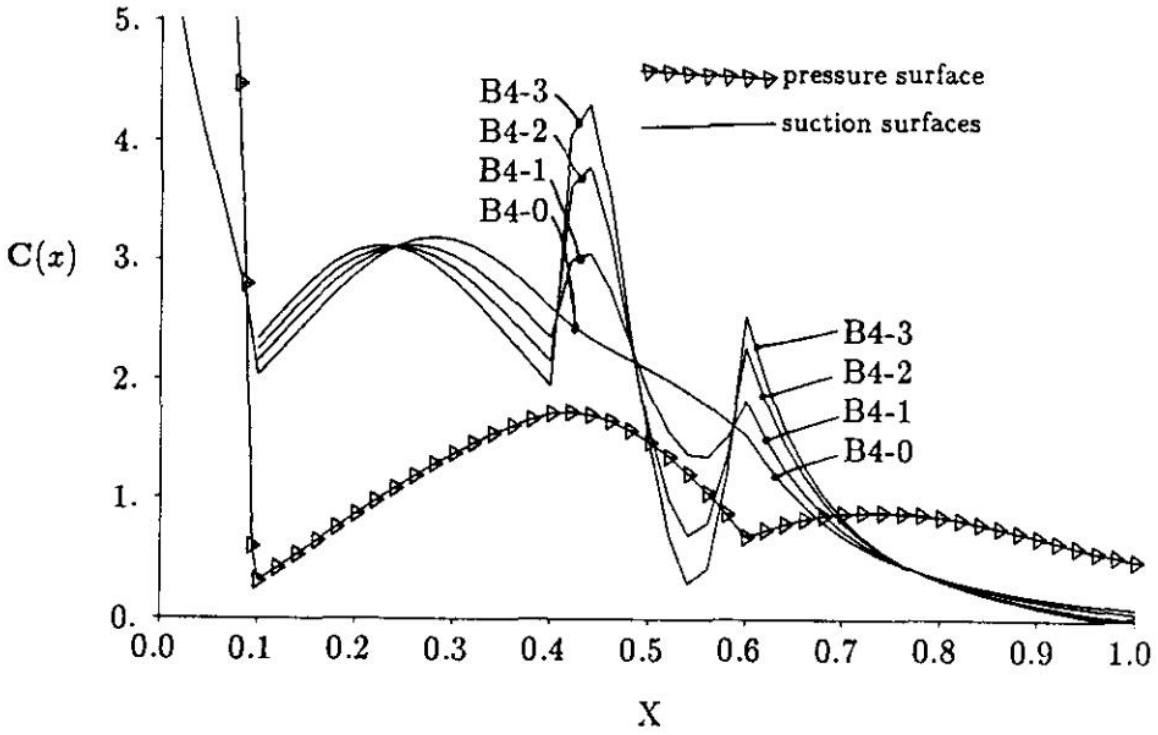


Figure 5.3: Figure from Korakianitis [98]. Surface-curvature Distribution - Four blades have the same pressure side curve but different curvature distribution in suction side curve.

Another way to understand this is to link the order of the Bezier curve with the blade curvature. Supposing a Bezier curve has the coordinates of (x, y), the curvature of the curve is computed in Equation 5.1

$$\kappa = \frac{\ddot{y}}{(1 + \dot{y}^2)^{\frac{2}{3}}} \tag{5.1}$$

where κ is the curvature; $\dot{y}$ and $\ddot{y}$ are the first order and second order derivative of Bezier curve.

Since there is a second derivative term in Equation 5.1, in order to keep the curvature of the blade to be C1 continuous, the Bezier curve implements one higher-order comparing to the second derivative. Thus it has to be third order continuous (C^3).

The reason to keep the curvature continuous can be explained by the relationship between the blade curvature and the force exerted from the blade. When flow passes through the blade, the curved blade profile will exert the centrifugal force on the flow as computed in Equation 5.2, where ρ and u are flow density and velocity, r is the blade curve radius. As shown in Equation 5.3, r is the reciprocal of blade curvature,

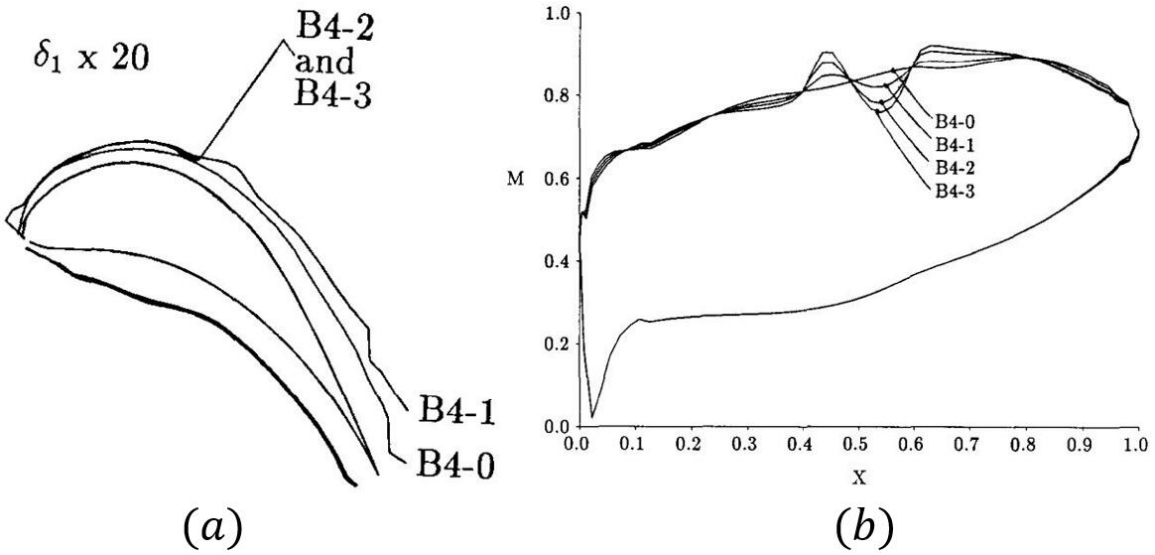


Figure 5.4: Figure from Korakianitis [98]. Different Performance of Four Blades with Different Curvature Distribution - Althoug the profiles of the four blades looks similar in (a), their displacement boundary layer thickness distribution as shown in (a) and the suface Mach number distributions in (b) are quite different.

κ. Thus the different distribution of blade curvature will induce different r and thus the different centrifugal force exerted on the flow.

$$f_{centrifugal} = \frac{\rho u^2}{r} \tag{5.2}$$

$$\kappa = \frac{1}{r} \tag{5.3}$$

5.1.3 3D Blade Parameterization

Stacking the 2D blade profiles to form a 3D blade surface involves two steps: firstly the radial equilibrium condition is used to determine the blade metal angle for the inlet and outlet of the blades at different radial sections ranging from hub to tip. In this step, the blade profiles can be tapered and twisted and then transferred from 2D into 3D. In the second step, a 3D Bezier curve is applied as the stacking line of the blade profiles to generate the possible lean and sweep.

5.1.3.1 Radial Equilibrium Condition

The radial equilibrium condition specifies the radial pressure gradient that is necessary to provide the centripetal force to maintain a circumferential movement. By assuming

the flow is steady, inviscid, adiabatic and axisymmetric, and there are no radial shifts of the meridional streamline, the Simple Radial Equilibrium (SRE) equation specifically for a free vortex design can be obtained:

$$\frac{1}{r^2}\frac{d}{dr}(r^2 u_\theta^2) + \frac{d}{dr}u_{ax}^2 = 0 \tag{5.4}$$

where r is radius coordinate; u_{ax} and u_θ are the flow axial and the tangential velocity.

This equation is derived from the combination of the first law of thermodynamics, Equation 5.5, the Gibbs' Equation, Equation 5.6, and the centrifugal force balance equation, Equation 5.7, where h is the flow enthalpy; e is the flow internal energy; P is the pressure; v is specific volume and s is entropy.

$$dh = de + Pdv + vdP \tag{5.5}$$

$$Tds = de + Pdv \tag{5.6}$$

$$\frac{dP}{dr} = \frac{\rho u_\theta^2}{r} \tag{5.7}$$

The Simple Radial Equilibrium (SRE) equation exhibits that at the same axial location once the radial variation of axial velocity u_{ax} are assigned, the radial variation of the circumferential velocity u_θ can be computed correspondingly. In this research the free vortex design assumption is implemented where the axial velocity u_{ax} is set as constant along radial direction. Therefore since du_{ax}/dr is equal to 0, by applying SRE equation, $d(ru_\theta)/dr = 0$ can be obtained which indicates that ru_θ has the constant value along the radial direction. Thus the radial variation of axial and circumferential velocity, $u_{ax}(r)$ and $u_\theta(r)$ can be computed from the axial and circumferential velocity at midspan, $u_{ax,m}$ and $u_{\theta,m}$ by Equation 5.8 and Equation 5.9 where r_m is the midspan radius.

$$u_{ax}(r) = u_{ax,m} \tag{5.8}$$

$$u_\theta(r) = \frac{u_{\theta,m} r_m}{r} \tag{5.9}$$

With the radial variation of the axial velocity, $u_{ax}(r)$, circumferential velocity, $u_\theta(r)$, and the blade rotational velocity, $U(r)$, at hand, one can derive the absolute flow angle distribution $\alpha(r)$ in the stator and the relative flow angle distribution $\beta(r)$ in the rotor which are also the blade metal angle in stator and rotor respectively. Ideally, such radial variation of blade metal angle should be applied to all the points along with the blade profile. Here the radial distribution of the blade metal angle is adopted only at the leading edge and the trailing edge where the metal angles β_{LE} and β_{TE} are already design variables of the blade profile as stated above. Therefore the radial equilibrium condition can be applied to derive the radial distribution of $\beta_{LE}(r)$ and $\beta_{TE}(r)$ along the span.

5.1.3.2 3D Stacking Line

The stacking line used in this study is generated by a 3D NURBS (Non-uniform rational basis spline) with four control points, A,B,C and D, as shown in Figure 5.5. In the figure x, θ and r represent the axial direction, the tangential direction and radial direction respectively. The 3D stacking is shown in light blue, and the control points are shown in purple. The first control point, A, which is the stagnation point of blade profile at the hub, is fixed in the coordinate system. The origin of the coordinate system is at the half span of the radial extension of point A. Here h represents span. r_B,r_C and r_D are the computed values to ensure B, C and D are located at the 0.2, 0.8 and 1 span of the blade.

The first control point, A, is fixed in the coordinate system. Due to the difference between the local coordinate system and the blade global coordinate system, the radial coordinates of the other three control points, B, C and D, are computed to ensure these three points are at 0.2, 0.8 and 1 span of the blade. In the local coordinate system, the tangential coordinates, θ, represents the lean angle of the blade. The sweep angle, α_x, is computed by the Equation 5.10. Thus the parameterization system for blade shape is capable of generating blades with designated design features, such as lean and sweep.

$$\alpha_x = \arctan \frac{r}{x} \tag{5.10}$$

As shown in Figure 5.6, the twist of the blade can be obtained by rotating the 2D blade profile around the defined rotating center for an assigned angle. The taper is conducted by shrinking/enlarging the blade profile to a certain taper length, δ_{taper}.

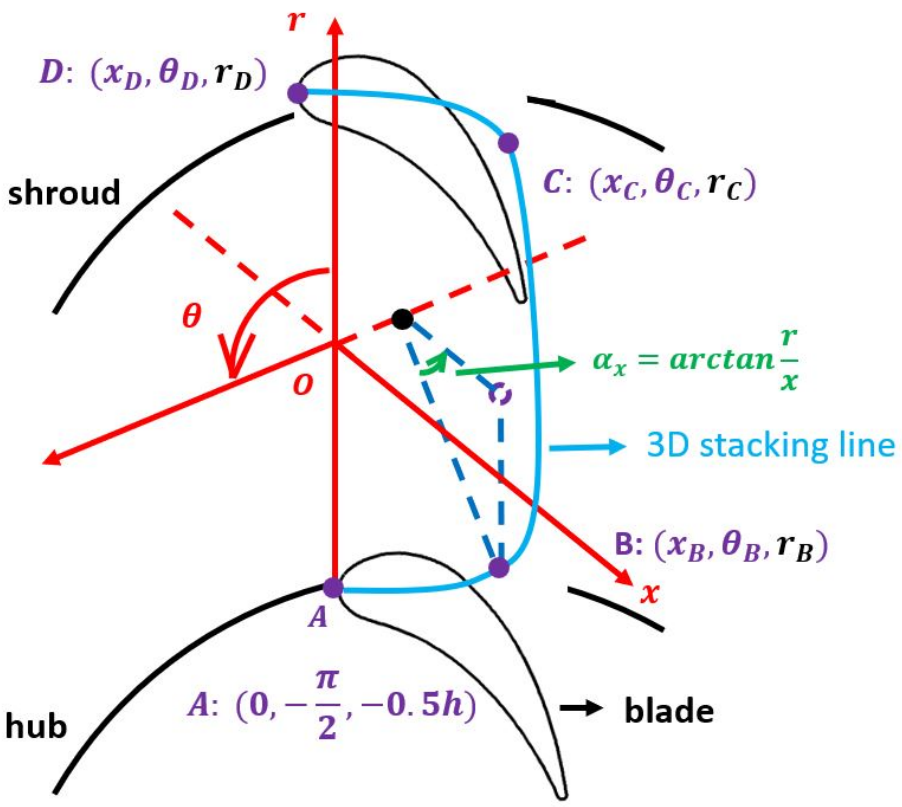


Figure 5.5: Local cylindrical coordinate system for 3D stacking NURBS.

δ_{taper} is computed by the taper angle, α_{taper} and radius difference between the tapered section and the midspan in Equation 8.

$$\delta_{taper} = \Delta r \tan(\alpha_{taper}) \tag{5.11}$$

5.2 Domain Blocking System

Once the turbine stage geometry is obtained, it is imported into the blocking system to form the block needed for meshing. Since in this research ICEM CFD is implemented as the meshing tool, a block domain corresponding to the blade geometry is required. Due to the large number of simulations involved in the optimization system, the working load of meshing is rather high. Thus to reduce the labour spent on meshing, a blocking system is developed to generate the block domain automatically.

Similar to the blade geometry generation system, the blocking system is also built in a 2D-3D manner. First, according to the 2D blade profile at each radial section, an op-

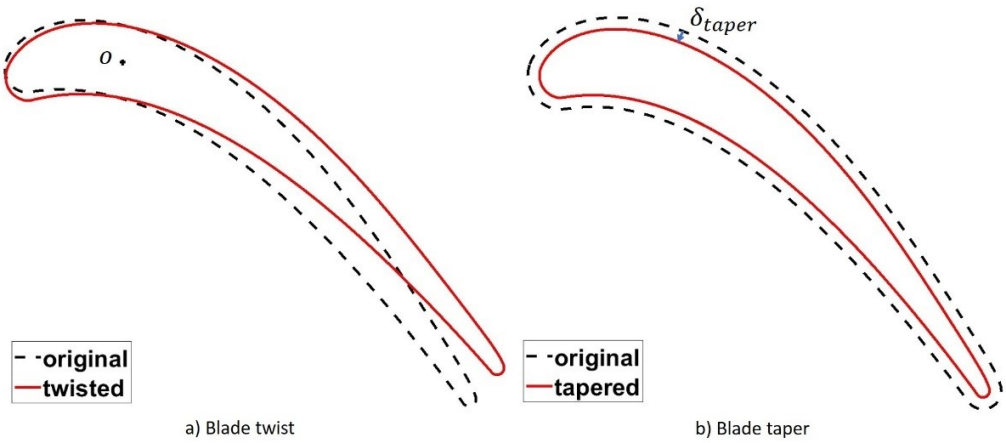


Figure 5.6: Twist and tapper of the blade in the parameterization system.

timized 2D block is formed. Then the 2D blocks are stacked along the radial direction using the same stacking line that has been implemented for the blade stacking.

Based on the geometric information from the 2D blade profile, an o-block is built using the shifted periodic topology by Li [29] as shown in Figure 5.7. For a high turning blade, in order to meet the periodic condition, the normal o-block will inevitably bring high skewness. This can be reduced by the shifted periodic topology because it applies periodicities on pairs of vertices with different indexes. In the blade passage, the blocking domain is bounded by the mid passage curves which are formed by the midpoints of two adjacent blade profiles shown as the curve $v1 - v2$ and the curve $v3 - v4$ in Figure 5.7. Moreover, to generate the tip clearance mesh, an additional inner o-block is formed inside the blade profile for the radial sections at the tip.

While generating the block, several vertices are designed to be able to move in order to search for the optimized block. In Figure 5.7 taking the vertices at the suction side of the trailing edge as an example, while the vertex $v5$ is moving on the o-block curve and the vertex $v6$ is moving along the tangential line of the mid passage curve $v1 - v2$, the block skewness is optimized by searching for the best combination of $v5$ and $v6$ with the maximum value of the smallest angle among $\angle 1$, $\angle 2$ and $\angle 3$, i.e. $max[(min(\angle 1, \angle 2, \angle 3))]$. By applying similar methods to the other moving vertices, the optimized 2D block is obtained. It will not only improve the mesh quality and hence the computational accuracy but also reduce the manual efforts involved in the blocking process. In the diagram, the blade used for blocking is in red solid line while two adjacent blades are in red dash line. The o-block curve is in black, and the

other blocking lines are in blue. The fixed vertices are in light blue while the moving vertices used for block optimization are in pink. The double-headed dash arrows in orange indicate how the periodicities are applied on pairs of vertices with different indexes.

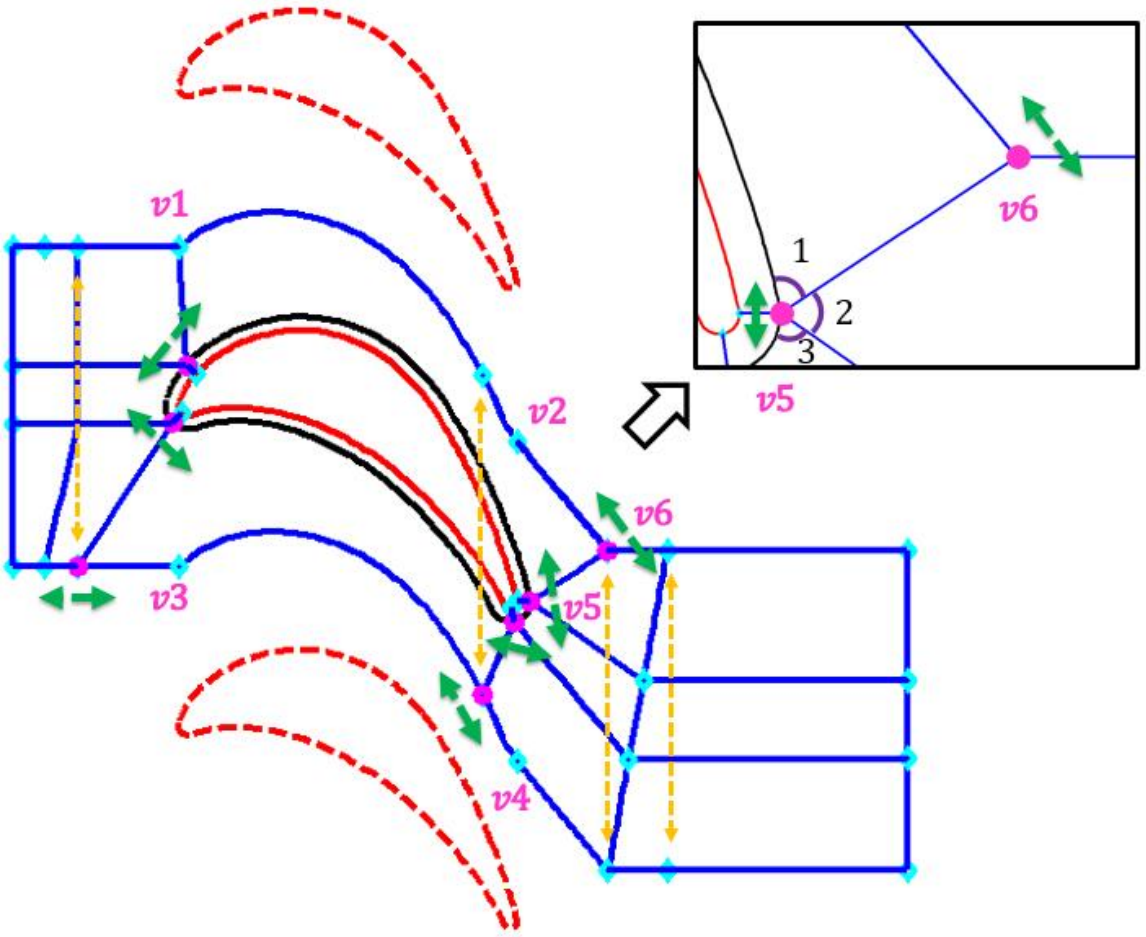


Figure 5.7: Optimized 2D block using shifted periodic topology.

By stacking the optimized 2D blocks along the 3D blade stacking line, the 3D block is formed as shown in Figure 5.8 for the stator and rotor. The 3D block then is imported into ICEM CFD where scripts are implemented to generate the mesh automatically.

5.3 Parameterization of Other Design Features

In order to accommodate the design features employed in the turbine stage, several add-on parts are integrated into the parameterization system. These parts are optional up to the designer's choice.

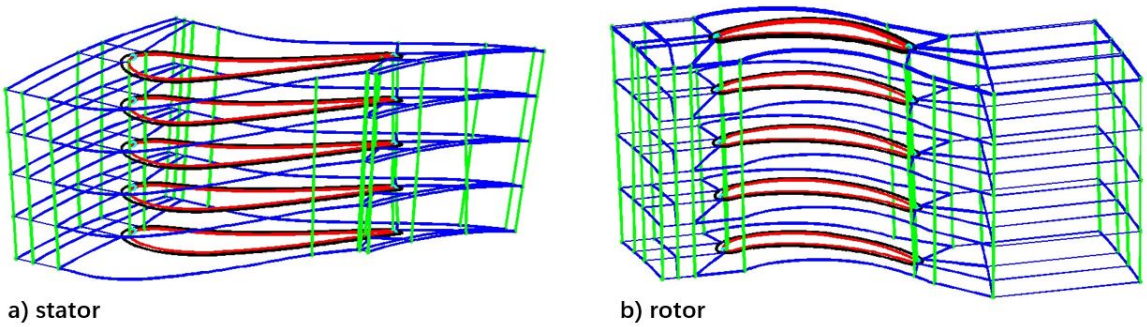


Figure 5.8: 3D stator and rotor blocks. Using the same color convention implemented in 2D block, the blade profiles are in red; the o-blocks are in black; the other 2D block lines are in blue. The stacking lines are in green.

5.3.1 Squealer Parameterization

In order to improve the turbine tip performance, a squealer can be added at the tip to block the tip leakage flow and to improve the cooling performance. This design feature has been widely used in the real engines such as CFM 56 and F100. The squealer is formed by a cavity at the tip, as shown in Figure 5.9. Three parameters are used to control the squealer geometry for a given tip clearance gap: the squealer width, w_{sq}, the axial cut-off percentage, x_{sq}, and the squealer height, h_{sq}.

The squealer curve is generated by drawing the normal lines perpendicular to the blade profiles with the assigned length of w_{sq}. This curve is cut off along the axial direction of the blade at the percentage of x_{sq}. The 'trailing edge' of the squealer at x_{sq} is re-drawn using a circular curve. The squealer cavity depth is controlled by the squealer height, h_{sq}. In order to accommodate future design investigations, both the squealer width and the squealer height can have varying values along the squealer curve.

Since an additional o-block is needed to generate the mesh at the squealer cavity, the blocking system is modified to integrate the new design feature, as shown in Figure 5.10. The blade profiles are in red. The o-blocks are in black. The other 2D block lines are in blue. The o-block for squealer is in pink.

5.3.2 Tip Cooling Parameterization

In order to add the cooling holes at the tip, the tip block is split to accommodate the cooling slots as shown in Figure 5.11. $m \times n$ cooling slots are generated at the tip where m is the number of rows of the cooling slots, and n is the number of column of

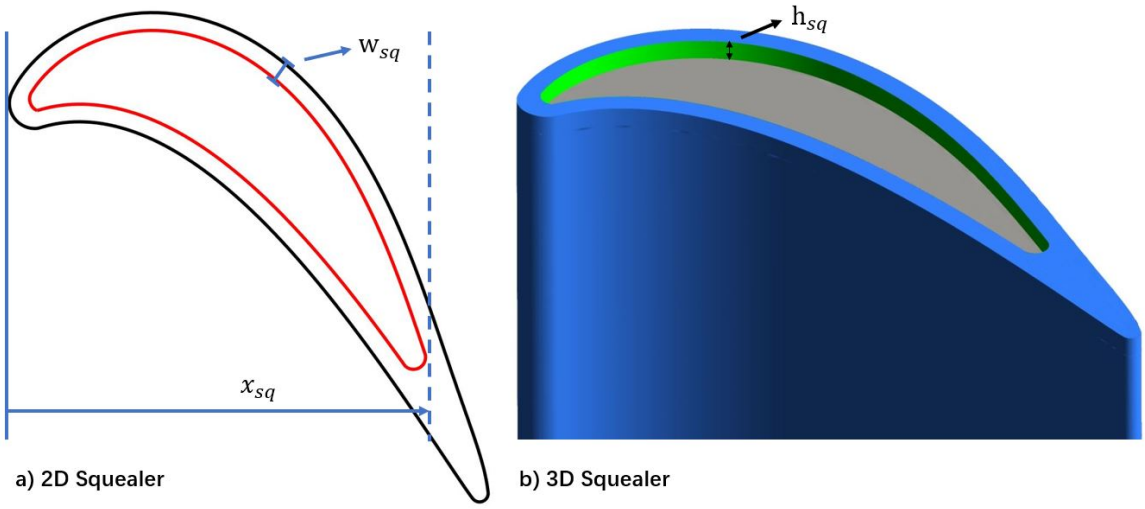


Figure 5.9: The parameterization of squealer. Three parameters are squealer width, w_{sq}, axial cut-off percentage, x_{sq}, and squealer height, h_{sq}

the cooling slots. Each cooling slot can be chosen to insert the block with or without an injection hole depending on whether there is cooling or not. In such way, the tip cooling configuration can be parameterized by a binary string where 0 and 1 represent if there is a cooling hole. Since some of the cooling slots are too small or too skewed, not all of the $m \times n$ cooling slots are suitable to insert cooling holes. Thus the length of the binary string could be smaller than $m \times n$.

5.4 Other Blade Parameterization Systems

In addition to the parameterization systems introduced above, the author also develop the parameterization of the blade film cooling system and the purge flow system. Although the implementations of these two systems will be not discussed in this thesis, they exhibit the versatility of the turbine stage parameterization system.

5.4.1 Blade Cooling Parameterization

The simulation of the turbine blade with cooling holes on the blade surface is challenging due to the large length scale difference between the cooling holes and the main passage. To reduce the computational difficulties, the blade cooling system is simplified: the internal cooling channel is not included, and the film cooling channels are modelled by cylindrical tubes ejecting coolant on the blade surface. The cylindrical cooling holes are designated by the location, the hole area a, the compound angle

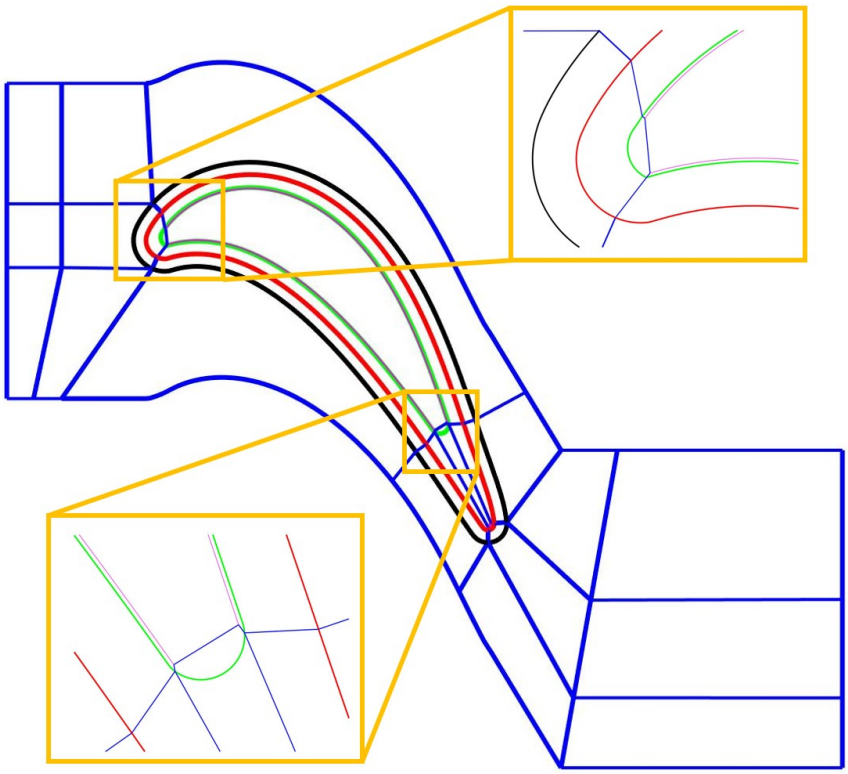


Figure 5.10: 2D block when the squealer is added at the blade.

γ_c, the ejection angle γ_e and the mass flow rate $\dot{m}_c$. In the future work, source terms may be added in the RANS solver to replace the real film cooling flow.

In order to deal with the large number of the cooling holes, a $m \times n$ matrix is designed to represent the blade cooling system, as shown in Figure 5.13. Starting from mid-chord of blade suction side at the tip, along with the blade profile the curve is equally divided into n sections; along with the radial direction, the span is equally divided into m sections. In such way, the blade surface is divided into $m \times n$ pieces. Each piece corresponds to an element in the matrix X. For example the ith section along blade profile and jth section along span will form the piece represented by element $x_{i,j}$ in matrix X. With this method, the blade surface is divided into $m \times n$ pieces and represented by a $m \times n$ matrix. Therefore by assuming the cooling holes is at the centre of each piece, a boolean matrix Θ uses 0 or 1 value to represent whether the cooling hole exists in each piece. It is defined to determine the distribution of cooling holes on the blade surface. The definition of matrix Θ brings an easier way to define the location of the cooling holes. Similarly the area a, compound angle γ_c,

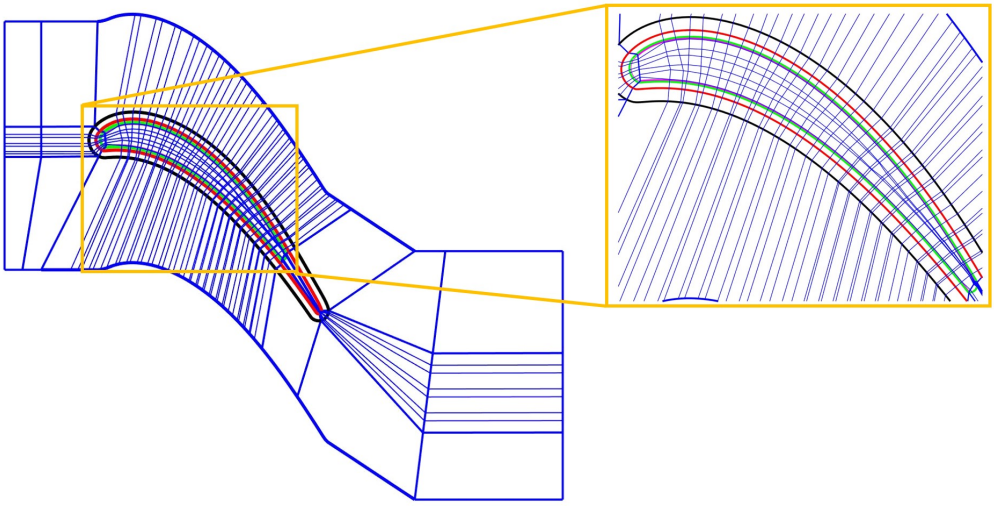


Figure 5.11: The block at the tip is split to accommodate the cooling slot.

the ejection angle γ_e and the mass flow rate $\dot{m}_c$ of the cooling holes can be specified using corresponding matrix A, Γ_c, Γ_e and $\dot{M}_c$. Therefore the blade cooling system can be parameterized by five $m \times n$ matrices. The number of design variables is five times of the number of cooling holes on the blade surface, i.e. the number of non-zero elements in the matrix Θ.

5.4.2 Purge Flow Parameterization

The purge flow parameterisation adopts solely two design variables thanks to the conclusion made by Zlatinov [63]. The research indicates that in the steady simulation with the mixing plane between stator and rotor, the majority of the purge loss is generated by the circumferential velocity mismatch between purge and mainstream flows. Therefore only two design variables, the purge flow mass fraction, f_m, and the swirl fraction of the rim speed, f_u are effective. These two design variables are defined by Equation 5.12 and Equation 5.13 respectively, where $\dot{m}_p$ and $\dot{m}_{main}$ are the mass flow rate of the purge flow and the main flow; $u_{\theta,p}$ and $u_{\theta,hub}$ are the circumferential velocity of the purge flow at purge slot exit and the hub. Since in CFD simulation, both of these two variables can by defined by the boundary conditions at the purge slot, there is no need to change the purge slot geometry. Thus the purge slot geometry is fixed in the model.

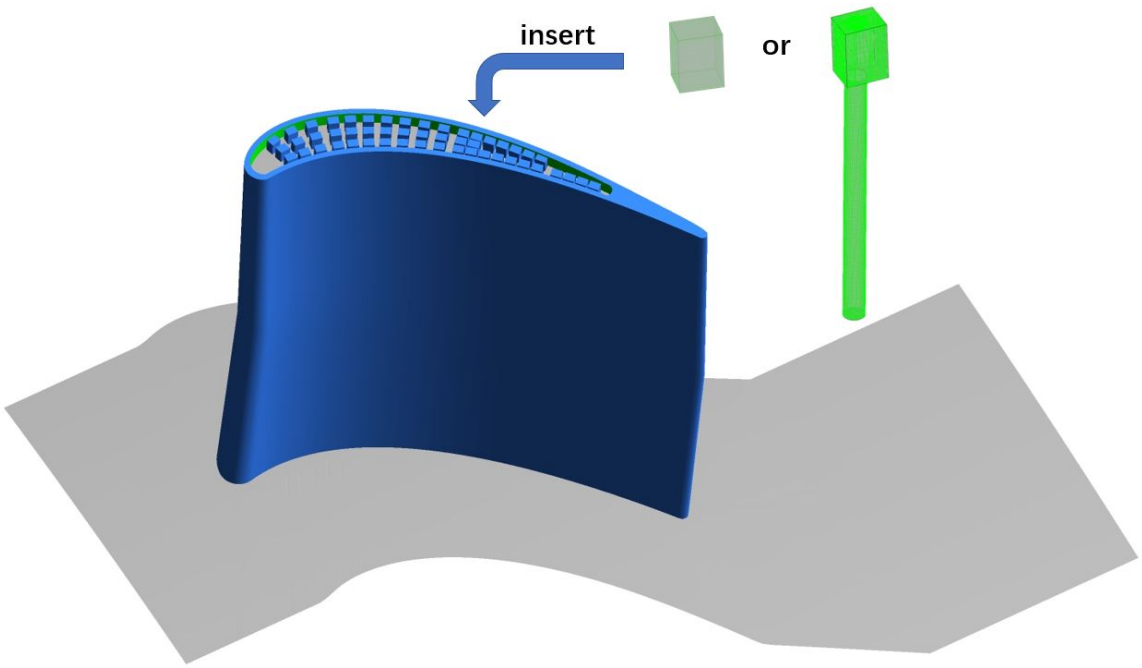


Figure 5.12: The blocks with or without injection holes are inserted into the cooling slots.

$$f_m = \frac{\dot{m}_p}{\dot{m}_{main}} \tag{5.12}$$

$$f_u = \frac{u_{\theta,p}}{u_{\theta,hub}} \tag{5.13}$$

5.5 Stage Design

With the parameterization system introduce above we can design the subsonic and the transonic turbine stage. The general procedure of the stage design is shown in Figure 5.14. In order to start from a reasonable design of turbine, the values of the design variables used in the parameterization system are computed by the correlated equations. Iterations are needed to modify the design variables so that the baseline stages have reasonable aerodynamic performance. Then the geometry and the blocks of the stator and rotor are generated by the parameterization system. By using the geometries and the blocks, the meshes are automatically formed by the ICEM CFD script. After that, the CFD solver employs the meshes to evaluate the performance of the stages. The computed results are investigated and delineated to imply the direction of future improvement. Several rounds of trial and error iterations are

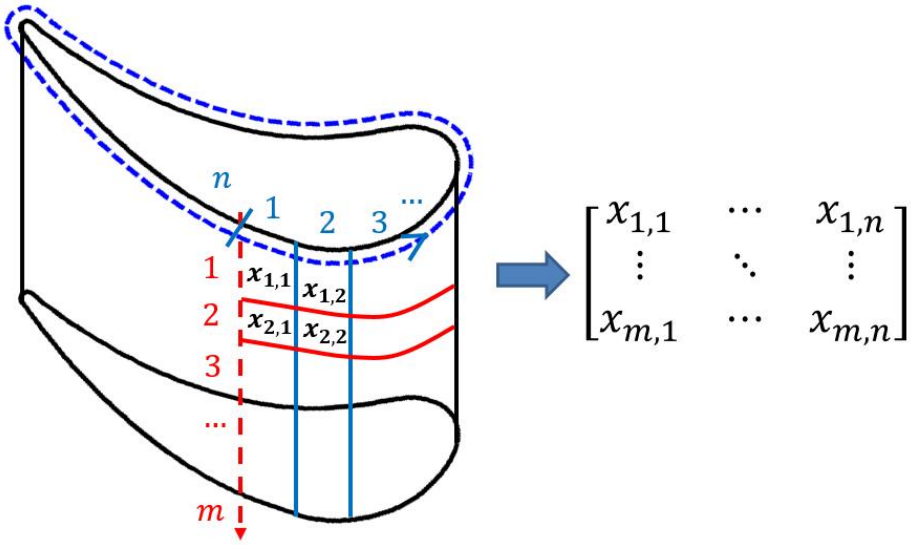


Figure 5.13: $m \times n$ matrix used to represent blade cooling system.

involved in obtaining the final blade design. At last, the subsonic and transonic turbine stages with high efficiency are generated. Since the procedure is similar for both the sub-sonic stage and transonic stage, only the design practice of the subsonic stage is exhibited here.

5.5.1 Midspan Blade Profile Design

Among the eleven parameters at midspan blade profile, the blade chord length C, the leading edge wedge angle $\epsilon_{wedge,in}$, trailing edge wedge angle $\epsilon_{wedge,in}$, and the velocity triangle are obtained from a priori experience. Then the leading edge metal angle β_{LE} and the trailing edge metal angle β_{TE} for both rotor and stator are derived from the velocity triangles. At last the stagger angle $\alpha_{stagger}$, the pitch p, the throat width t, the leading edge radius r_{LE}, the trailing edge radius r_{TE} and the unguided turning $\delta_{unguided}$ are computed from the correlated equations introduced in Wilson and Korakianitis's book [20]. The tip gap, in this case, is a constant equal to 0.8% of the span.

In the subsonic rotor, the flow coefficient,ϕ, the loading coefficient, ψ, and the reaction, R_η, are 0.70, 2.33 and 0.44 respectively which lead to the velocity triangle shown in Figure 5.15. In the diagram the station 1, 2 and 3 indicate the stator inlet, the stator outlet(or the rotor inlet) and the rotor outlet. The rotational speed U is in black, the absolute velocity u is in red, and the relative velocity w is in blue. The stator metal angles are the angles of the absolute velocity while the rotor metal

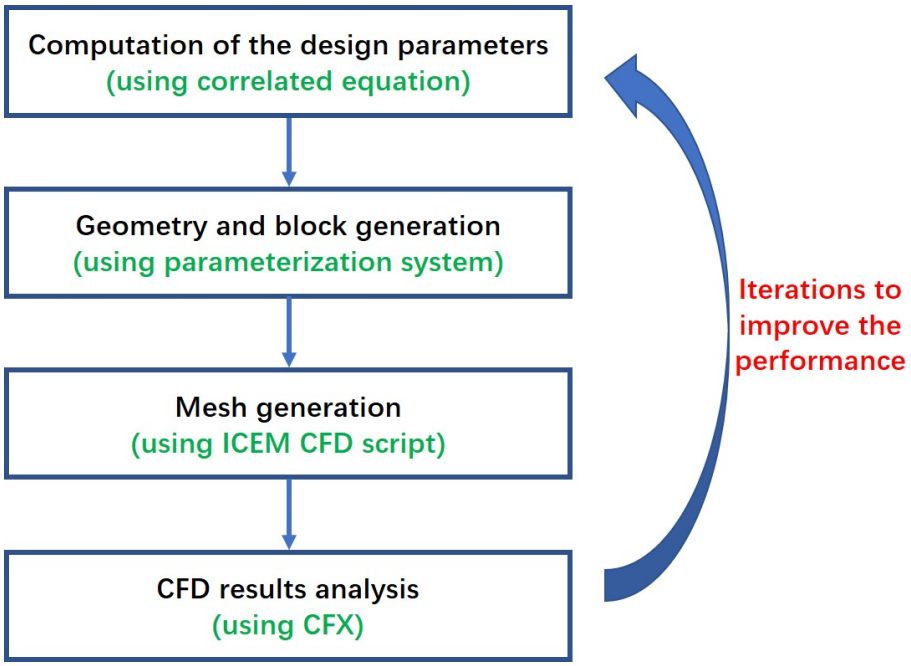


Figure 5.14: Turbine stage design procedure.

angles are the angles of the relative velocity. The midspan blade profiles of the stator and the rotor are shown on the left. From the velocity triangle, the metal angles, $\beta_{TE,stator}$, $\beta_{LE,rotor}$ and $\beta_{TE,rotor}$, can be computed as 68°, 46° and −67°. The stator inlet metal angel, $\beta_{LE,stator}$, is 0° by assuming the inlet flow is in the axial direction. The chord length C, the leading edge wedge angle $\epsilon_{wedge,LE}$, trailing edge wedge angle $\epsilon_{wedge,TE}$ for rotor are assigned as 26 mm, 30° and 5° correspondingly. For the stator, the chord length is 1.4 times of the rotor chord; the leading edge wedge angle $\epsilon_{wedge,in}$ and trailing edge wedge angle $\epsilon_{wedge,in}$ are 40° and 5°.

From the assigned value of the leading edge metal angle β_{LE} and the trailing edge metal angle β_{TE}, the stagger angle, $\alpha_{stagger}$, can be derived from the correlation diagram shown in Figure 5.16. From the figure, the stagger angle $\alpha_{stagger}$ for stator and rotor are 51° and 30° respectively. The value obtained in Figure 5.16 is the initial guess for the blade profile. Further iterations are needed to change these parameters and to improve the efficiency. Therefore, the stagger angle used in the stator is different from the value indicated in Figure 5.16.

Then the rotor pitch, p_{rotor}, can be computed by the tangential lift coefficient C_L which is defined as the normalized tangential loading acting on the blade surface as shown in Equation 5.14 where the F_{tan} is the tangential loafing, A_{tan} is the tangential blade area and $\frac{1}{2}\rho_{TE}w_{TE}^2$ is the incompressible dynamic head at trailing edge.

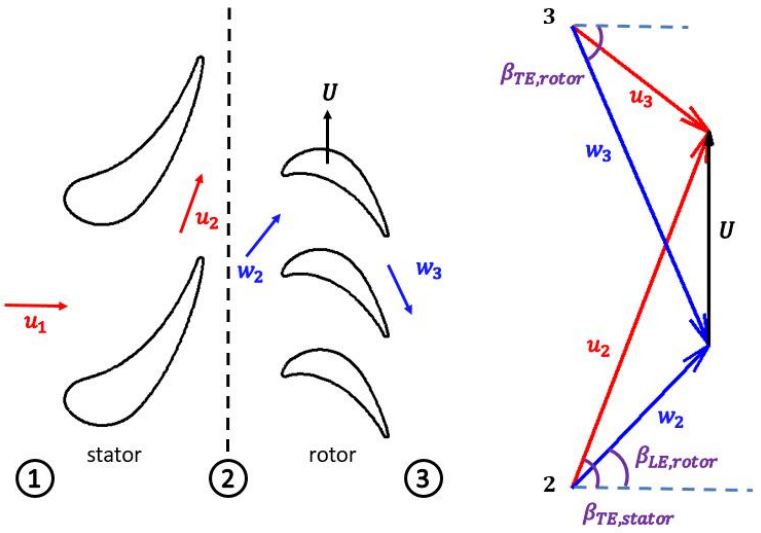


Figure 5.15: The velocity triangle of the baseline model.

$$C_L = \frac{F_{tan}}{A_{tan}\frac{1}{2}\rho_{TE}w_{TE}^2} \tag{5.14}$$

The tangential loading F_{tan} is computed by applying Newton's law to the fluid deflection through the blade as exhibited in Equation 5.15 where $\dot{m}$ is the mass flow rate in rotor passage;w_{LE} and w_{LE} are the relative flow velocities, β_{LE} and β_{TE} are the blade metal angle.

$$F_{tan} = \dot{m}(w_{LE}\sin\beta_{LE} - w_{TE}\sin\beta_{TE}) \tag{5.15}$$

By combining Equation 5.14 and Equation 5.15, Equation 5.16 is derived to calculate the pitch p with the tangential lift coefficient C_L, the chord length C, the leading edge metal angle β_{LE} and the trailing edge metal angle β_{TE} and the stagger angle $\alpha_{stagger}$. In the current design practice [20] the variation range of C_L is $0.9 \sim 1.2$ and the value of 0.9 is implemented in this research. Therefore the obtained rotor pitch p_{rotor} is 22 mm. Here the ratio of the blade count between stator and rotor is taken to be $1:2$. The stator pitch, p_{stator}, will be twice large of p_{rotor}, i.e. 44 mm.

$$C_L = 2(\frac{p}{C})\frac{\cos^2\beta_{TE}}{\cos\beta_{stagger}}(\tan\beta_{LE} - \tan\beta_{TE}) \tag{5.16}$$

The throat width, t, can be computed by the correlations among the trailing edge flow angle, α_{TE}, the pitch, p, the Mach number at throat, M_t, and the equivalent

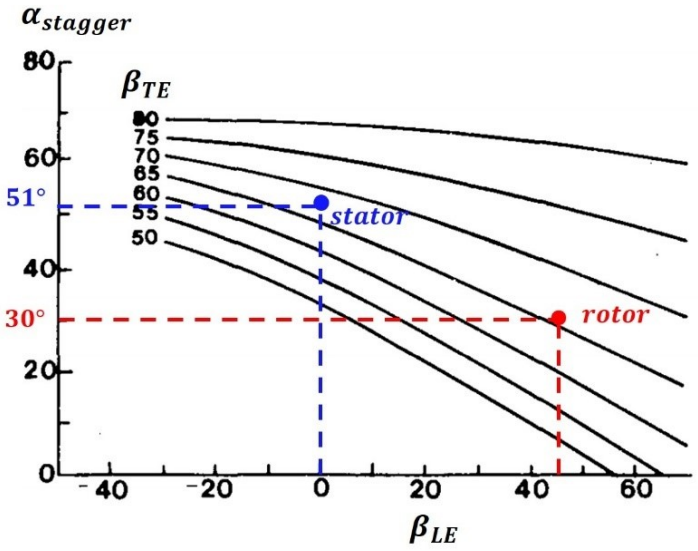


Figure 5.16: Correlation of stagger angle for typical turbine blade sections. From Kacker and Okapuu [93].

radius of curvature of *curve*2 (the blade suction side downstream of throat), r_{ss}, as exhibited in Equation set 5.17 taken from Wilson [20].

$$\alpha_{TE} = \begin{cases} \frac{7}{6}(|\cos^{-1}\frac{t}{p}| - 10°) + 4°(\frac{p}{r_{ss}}) & (0 \leq M_t \leq 0.5) \\ |\cos^{-1}\frac{t}{p}| - \sin^{-1}(\frac{t}{p})|(\frac{p}{r_{ss}})^{1.786+4.128(p/r_{ss})}| & (M_t = 1) \\ |\alpha_{TE}|_{0\leq M_t \leq 0.5} - (2M_t - 1)(|\alpha_{TE}|_{0\leq M_t \leq 0.5} - |\alpha_{TE}|_{M_t=1}) & (0.5 \leq M_t \leq 1) \end{cases} \tag{5.17}$$

Although in this study the curve at suction side downstream of throat, *curve*2, is a ninth order Bezier curve, an equivalent radius of this curve is used to represent the turning of the blade as illustrated in Figure 5.17 where two normals perpendicular to the tangential lines of *curv*2 at points *pt*2 and *pt*3 intersect at point O_r. The length between O_r and *pt*2 and the length between O_r and *pt*3 are $r_{ss,1}$ and $r_{ss,2}$ respectively. The equivalent radius of curvature, r_{ss}, is assumed to be the mean value of $r_{ss,1}$ and $r_{ss,2}$ as shown in Equation 5.18. In the current design practice [20] the ratio of pitch p to r_{ss} is between 0.25 and 0.625. In a high subsonic turbine, the throat Mach number is between 0.5 and 1. Therefore the third equation in Equation set 5.17 is implemented to obtain the throat width value. In the first iteration of the design process, the throat Mach number of 0.8 is taken which leads the throat width to pitch ratio to equal to 0.7. This value is the initial guess for the throat width to pitch

ratio. The throat width to pitch ratio is corrected to 0.5 by the CFD simulations in the following iterations to improve the aerodynamic performance of the subsonic blade.

$$r_{ss} = \frac{1}{2}(r_{ss,1} + r_{ss,2}) \tag{5.18}$$

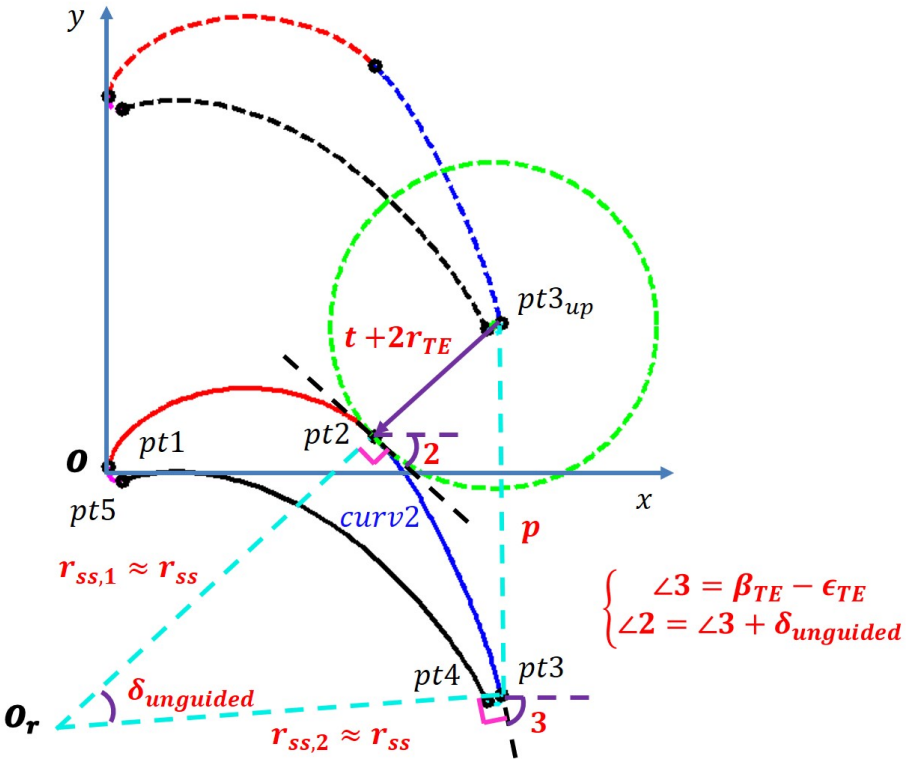


Figure 5.17: Equivalent radius of curvature r_{ss} and triangle $\triangle O_r - pt4_{up} - pt3$ used to compute the throat width, t, and the unguided turning, $\delta_{unguided}$. $O_r - pt2$ and $O_r - pt3$, whose length are approaximated by their mean value, r_{ss}, are the normals of $curv2$ at $pt2$ and $pt3$.

In Figure 5.17 since $O_r - pt2$ and $O_r - pt3$ are normal to $curv2$ at $pt2$ and $pt3$, their intersection angle is equal to the unguided turning, $\delta_{unguided}$. Therefore using r_{ss} to approximate the length $r_{ss,1}$ and $r_{ss,2}$, the unguided turning $\delta_{unguided}$ can be computed by solving the triangle $\triangle O_r - pt4_{up} - pt3$ via law of cosines as shown in Equation 5.19.

$$\cos \delta_{unguided} = \frac{(t + 2r_{TE} + r_{ss})^2 + r_{ss}^2 - p^2}{2r_{ss}(t + 2r_{TE} + r_{ss})} \tag{5.19}$$

From the design guideline, the ratio of the leading edge radius r_{LE} to the pitch p is between 0.05 to 0.10 where in this study 0.08 is used for stator and 0.03 is implemented for the rotor. The ratio of the trailing edge radius r_{TE} to the chord C is between 0.015 to 0.050 where 0.015 is applied for stator and 0.017 is adopted for the rotor. Thus the value of r_{LE} and r_{TE} for stator and rotor can be computed. The 11 parameters and the flow angles at the midspan of the stator and the rotor in the subsonic and the transonic stages are summarized in Table 5.2. It is noted that although the trailing edge radius is computed by the chord length, in Table 5.2 the trailing edge radius is shown by the ratio to the axial chord. The transonic rotor has lower trailing edge radius.

Table 5.2: 11 parameters and flow angles at the midspan of the stator and the rotor in the subsonic and the transonic stages.

Name	Parameter	Subsonic rotor	Transonic rotor	Subsonic stator	Transonic stator
Axial chord length	C_{ax}	26.0 mm	27.1 mm	$1.4C_{ax,r}$	$1.4C_{ax,r}$
Pitch	p	$0.84C_{ax,r}$	$1.00C_{ax,r}$	$1.20C_{ax,r}$	$1.40C_{ax,r}$
Stagger angle	$\alpha_{stagger}$	$-30°$	$-35°$	$-47°$	$-50°$
Throat width	t	$0.44C_{ax,r}$	$0.56C_{ax,r}$	$0.46C_{ax,r}$	$0.60C_{ax,r}$
Unguided turning	$\delta_{unguided}$	5°	30°	15°	28°
LE radius	r_{LE}	$0.03C_{ax,r}$	$0.05C_{ax,r}$	$0.10C_{ax,r}$	$0.05C_{ax,r}$
TE radius	r_{TE}	$0.02C_{ax,r}$	$0.015C_{ax,r}$	$0.02C_{ax,r}$	$0.015C_{ax,r}$
LE wedge angle	$\epsilon_{wedge,LE}$	30°	40°	40°	40°
TE wedge angle	$\epsilon_{wedge,TE}$	5°	10°	5°	5°
LE metal angle	β_{LE}	46°	31.6°	0°	0°
TE metal angle	β_{TE}	$-66.5°$	$-65.1°$	68°	64°

Some other important parameters to generate the stages are listed in Table 5.3. The ratio of the blade counts in the stator and the rotor is 1:2 in both the subsonic and the transonic stages. The inner radius and the outer radius in the two stages are constant through the passage thus the span, i.e., the duct height, is also constant.

Table 5.3: Additional key parameters in the stages.

Name	Parameter	Subsonic stage	Transonic stage
Stator blade count	N_{stator}	32	32
Rotor blade count	N_{rotor}	64	64
Inner radius	r_{inner}	207 mm	258 mm
Outer radius	r_{outer}	241 mm	294 mm
Tip clearance	h_{tip}	0.8%	0.8%
Stacking method	n_{stack}	Free vortex	Free vortex

5.5.2 Baseline Blade Stacking

To keep the radial equilibrium of the 3D blades, a free vortex design, as stated in Section 5.1.3, is used to generate five sections (including midspan) of blade profiles ranging from hub to tip. Starting from the midspan velocity triangles, by implementing Equation 5.8 and Equation 5.9, the axial velocity, $u_{ax,i}$, and the circumferential velocity, $u_{\theta,i}$ at the ith section can be computed. Then from the velocity triangle at each section, the blade leading edge and the trailing edge metal angles, $\beta_{LE,i}$ and $\beta_{TE,i}$ at the ith section can also be calculated. By assuming the stagger angle, $\alpha_{stagger,i}$, and the ratio of pitch p to r_{ss} are constant, Equation 5.16 and Equation 5.17 are implemented to evaluate the pith, p_i and the throat width, t_i, sequentially. The unguided turning, $\delta_{unguided,i}$, can be estimated by Equation 5.19. At last on the assumption that the chord length C_i, the leading edge wedge angle $\epsilon_{wedge,LE,i}$, trailing edge wedge angle $\epsilon_{wedge,TE,i}$, the leading edge radius $r_{LE,i}$ and the trailing edge radius $r_{TE,i}$ are all constant, the 11 parameters at each radial section can be obtained.

In the stator, 3 radial sections, hub, midspan and casing, are used to generate the 3D blade. In the rotor, 5 sections including hub, midspan, squealer floor section, tip and casing, are employed. The profiles at these sections are shown in Figure 5.18. It is noted that as the radius of the section increases, due to the increasing rotational speed, in rotor the absolute value of the blade metal angles decreases at the leading edge and in-creases at the trailing edge to comply the free vortex design.

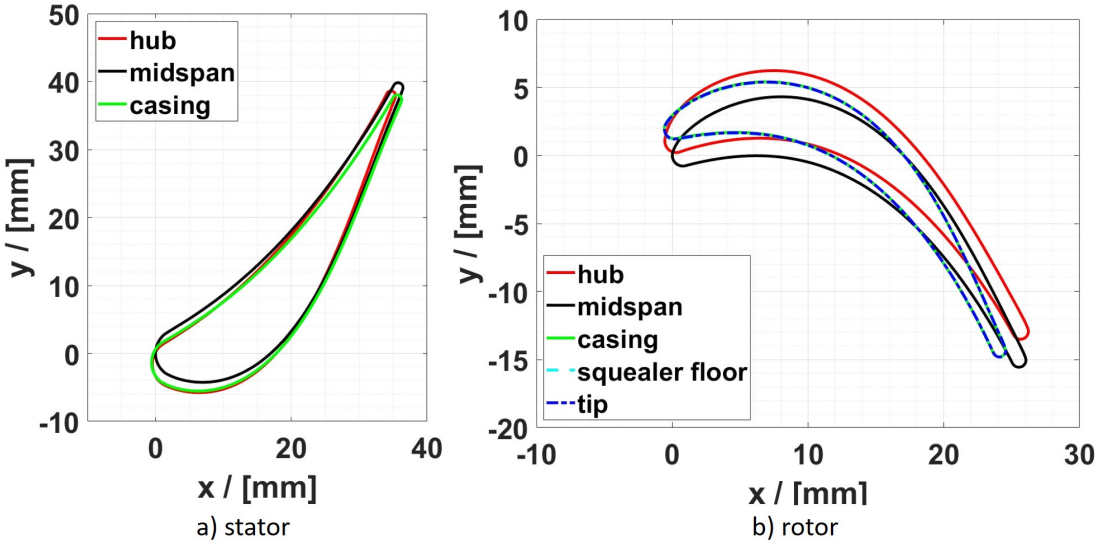


Figure 5.18: Blade 2D profiles at different radial sections in the stator and the rotor of the subsonic stage.

The similar design techniques are implemented in the blade design of the transonic stage. The profiles at different radial sections in the transonic stages are shown in Figure 5.19.

The comparison of the blade midspan profiles in the subsonic and transonic turbine stage is shown in Figure 5.20. The blade profiles are normalized by the stator chord length in axial direction x and by stator pitch in circumferential direction y. It is noted that compared to the subsonic stage, the transonic blades, both stator and rotor, are thinner and the transonic rotor has a blunter leading edge and less turning.

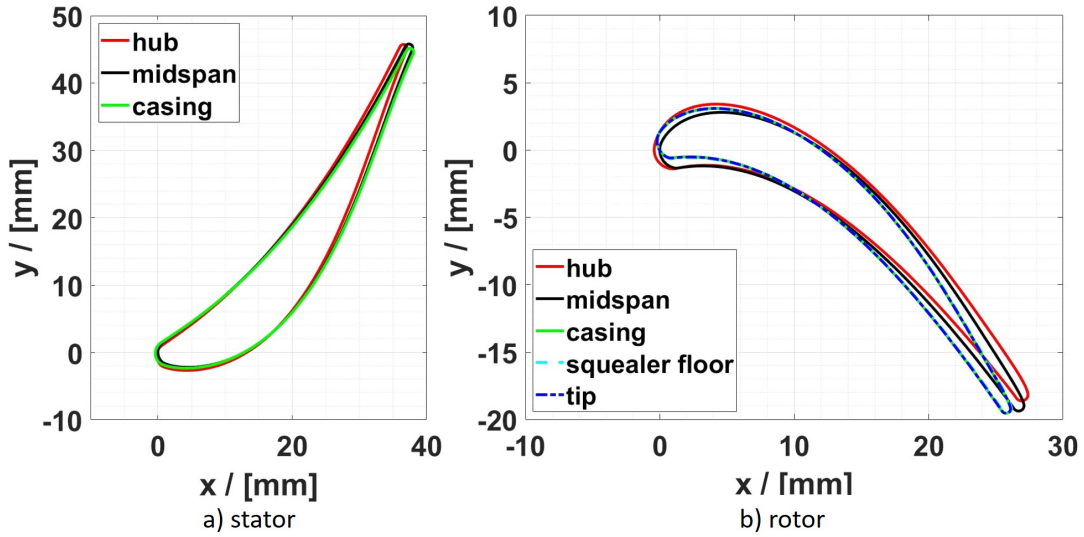


Figure 5.19: Blade 2D profiles at different radial sections in the stator and the rotor of the transonic stage.

The radial variation of the flow coefficient, the loading coefficient and the reaction for the rotor are illustrated in Figure 5.21. As the radius increases, the reaction rises. However as stated in Wilson's book [20], the extreme reaction may lead to high relative Mach number and the distortion of the velocity diagram, the reaction should be greater than 0.3 at the hub and smaller than 1.0 at the shroud.

5.6 CFD Simulation of Subsonic Turbine Stage

5.6.1 Numerical Attributes for Flow Solver

In this study, ICEM CFD is implemented to automatically generate the structured mesh. Then the flow solver, ANSYS CFX RANS solver, will take the mesh to run the CFD simulations. The turbulence model used in the solver is $k-\omega$ SST with low

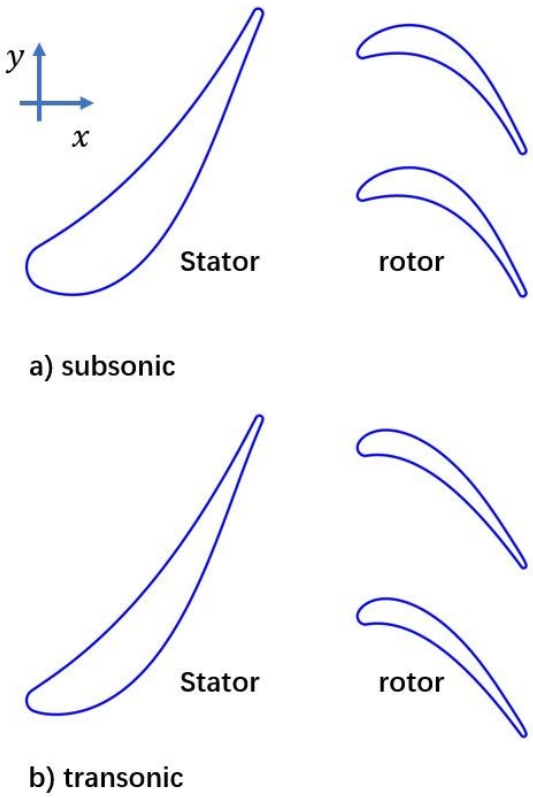


Figure 5.20: Comparison of the blade midspan profiles in the subsonic and transonic turbine stage.

Reynolds number model used at the wall ($y^+ \approx 1$). The advection scheme is second order, and the turbulence numerics are set to high resolution (maintains second order as much as possible) to balance the numerical accuracy and stability.

The computational domain of the subsonic stage and the transonic stage are shown in Figure 5.22 and Figure 5.23 respectively. They indicate 1/32 of a hypothetical turbine stage with 32 stators and 64 rotors. In the diagram $C_{ax,stator}$, and $C_{ax,rotor}$ are the axial chord length of stator and rotor. l_{span} is the rotor span. The stage inlet, the mixing plane interface and the outlet is marked as station 1, 2 and 3. The rotors in both stages are rotating at 9500 rpm. The tip clearance between shroud and tip is 0.8% of the span. For the baseline cases, the flat tip is used. The interface between stator and rotor uses the mixing plane approximation. Periodic boundary conditions are employed for the blade passage boundary. The wall in the CFD model implements the adiabatic wall boundary conditions. The boundary conditions are listed in Table 5.4. In the table, the inlet boundary condition, the rotating speed of the two stages are the same. The turbulence intensity of 10% at the NGV inlet is a typical value

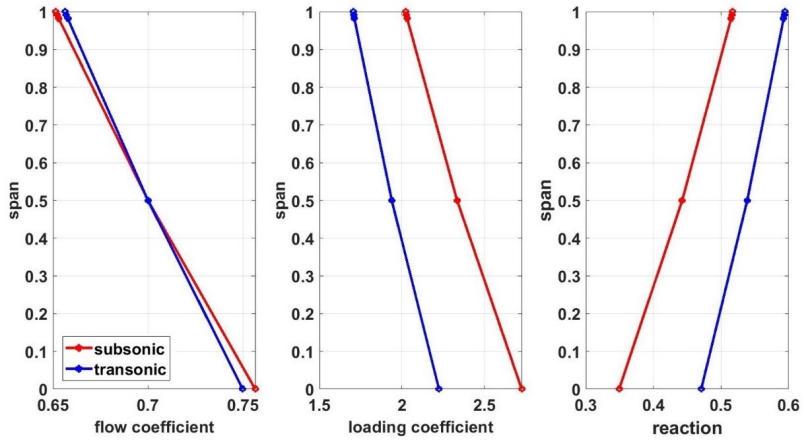


Figure 5.21: Radial variation of the flow coefficient, the loading coefficient and the reaction for rotor. The span is computed by $(r - r_{hub})/l_{span}$ where r_{hub} is the hub radius, l_{span} is the blade span.

which has been measured or used in the previous studies [26] [11] [100] [27].

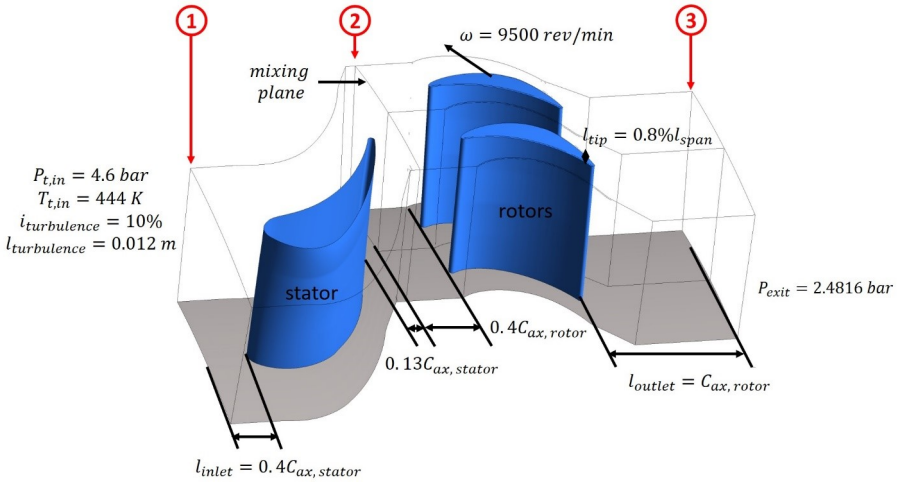


Figure 5.22: Computational domain of the subsonic turbine.

From the CFD simulation, the exit Mach number in the subsonic stage and the transonic stage are 0.7 and 1.1 respectively. The Reynolds number in both the subsonic and the transonic turbine stage are matched. The Reynolds number can be computed by

$$Re = \frac{\rho_{exit} u_{exit} C_{ax}}{\mu} \tag{5.20}$$

where ρ_{exit} and u_{exit} is the density and the velocity at the rotor exit plane; C_{ax} is the chord length; μ is the dynamic viscosity. The Reynolds number in the subsonic stage

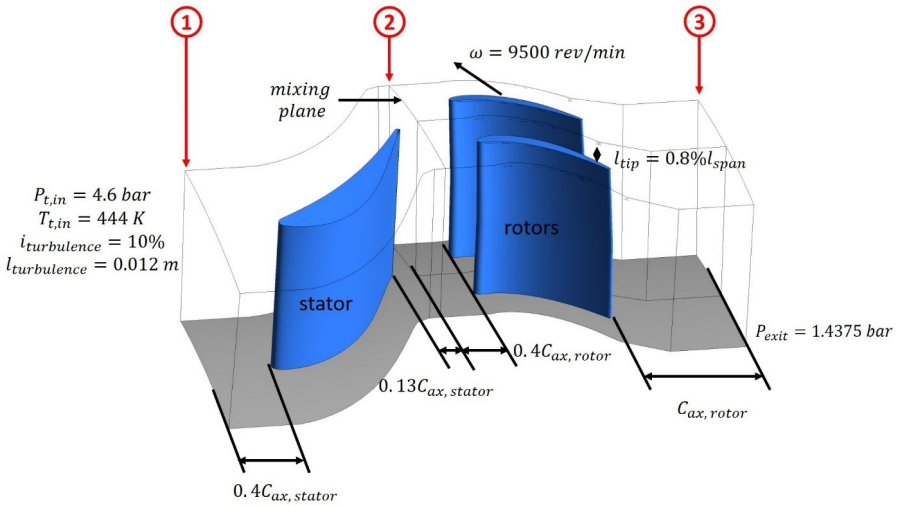


Figure 5.23: Computational domain of the transonic turbine.

Table 5.4: Boundary conditions of the subsonic and the transonic turbine stages.

Name	Parameter	Subsonic stage	Transonic stage
Inlet stagnation pressure	$P_{t,in}$	4.6 bar	4.6 bar
Inlet stagnation temperature	$T_{t,in}$	444 K	444 K
Turbulence intensity	k	10%	10%
Turbulence length scale	$l_{turbulence}$	0.012 m	0.012 m
Rotating speed	Ω	9500 rpm	9500 rpm
Exit pressure	P_{exit}	2.4816 bar	1.4375 bar
Pressure ratio	$P_{exit}/P_{t,in}$	0.54	0.31
Exit Mach number	M_{exit}	0.7	1.1
Reynolds number	Re	8.9×10^5	8.8×10^5

and the transonic stage are 8.9×10^5 and 8.8×10^5 respectively.

From this definition, the aerodynamic efficiency of the subsonic and the transonic stages can be computed and compared with the conventional wisdom such as Smith's chart. The Turbine Smith's Chart is the contour plots of stage efficiency versus flow coefficient and stage loading coefficient [16]. The data point on the chart are obtained from 70 Rolls-Royce test rigs prior to 1965. It represents the specific machine's best efficiency over a range of pressure ratios. Due to the restriction of the experimental instruments, the tests are based on the following assumptions:
1) turbine inlet temperature is only 100 to 200°C other than the real inlet temperature of the order of 1000°C;
2) There is no subsidiary airflow;
3) The efficiencies are corrected to represent the zero tip leakage turbine.

The comparisons between the CFD results and the Smith's Chart predicted efficiency are shown in Figure 5.24. In the Figure, the x and y axis represent the flow coefficient and the loading coefficient, respectively. The circled number indicates the efficiency of the performance contour. The baseline model point is shown as the red point. In the subsonic stage midspan, the flow coefficient and the loading coefficient are 0.7, 2.33 respectively; the computed efficiency is 91.80% for the blade with 0.8% of tip clearance. In the transonic stage midspan, the flow coefficient and the loading coefficient are 0.7, 1.94 respectively. The computed efficiency is 91.63% for the blade with 0.8% of tip clearance. On Smith's Chart, the predicted efficiency in the subsonic and the transonic stages is 89.5% and 91.7% respectively. It is noted that the efficiencies on Smith's chart are obtained from the cases with zero tip clearance. They are different from the CFD computed cases where the tip clearance is 0.8%. Smith's chart also does not include the effect of Mach number, reaction, lift coefficient, design style, aspect ratio, 3D design, etc. Thus, the efficiencies predicted by Smith's Chart are not expected to be exactly the same as the ones computed in the CFD simulations.

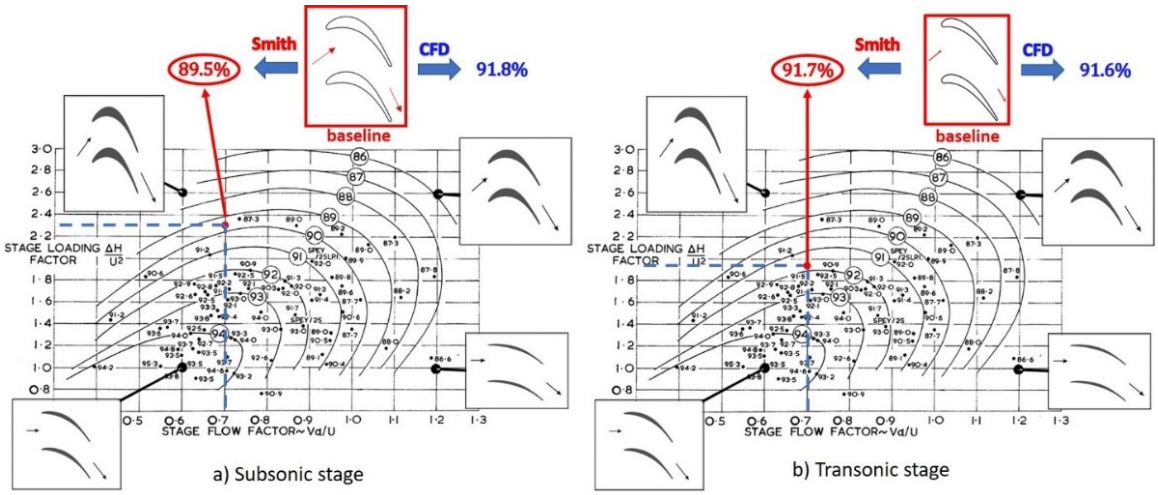


Figure 5.24: Baseline model efficiency in the subsonic and the transonic stages shown in Turbine Smith's Chart.

The loading plots at the midspan and the 95% span are shown in Figure 5.25. The loading is evaluated by the isentropic Mach number, M_{isen}, which is computed in Equation 5.21

$$M_{isen} = \sqrt{\frac{2}{\gamma - 1}[(\frac{P_{t,rel}}{P})^{\frac{\gamma+1}{\gamma}} - 1]} \tag{5.21}$$

where P is the pressure at the blade surface; γ is the ratio of specific heat; $P_{t,rel}$ is the relative stagnation pressure at the rotor inlet.

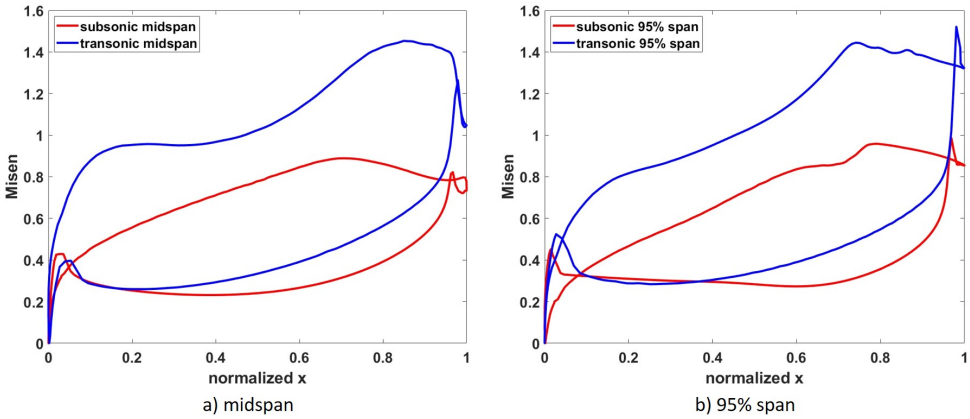


Figure 5.25: Loading plots of the rotor blade at the midspan and the 95% span in the subsonic and transonic stages. The blades have flat tips with tip clearance of 0.8% of span.

From the figure, at midspan, the subsonic rotor has a smooth acceleration on the suction side up to the peak Mach number and a smooth deceleration to the trailing edge. In contrast, the transonic stage has a less smooth acceleration up to the peak, which is further back on the surface. The deceleration in the transonic stage starts at 85% axial chord. There is a sudden (shock-induced) deceleration close to the trailing edge. At the 95% span, the front portions of the suction side look more similar for both the subsonic and the transonic stages, with relatively smooth acceleration up to the peak. At the tip, the leakage flow crosses the tip and rolls up to form the tip leakage vortex. Relative to the case at the midspan, the tip leakage vortex in the transonic stage changes the shock pattern and leads to an earlier and weaker shock at the 95% span. Thus, the flow has an earlier deceleration at 72% axial chord. There is no sudden deceleration at the trailing edge.

In the subsonic stage, the isentropic Mach number is lower than one throughout the blade. On the suction side of the transonic stage, downstream of the 50% axial chord, the isentropic Mach number becomes greater than one at both the midspan and the 95% span. The different loadings of the two stage are not only influenced by the Mach number but also by the blade designs and the pitches. When the flow is not choked, the loading affects the direction and pressure drop seen by the tip flow. When the flow is choked, the leakage flow is determined by the upstream capacity.

5.7 Summary

In this chapter, a subsonic stage and a transonic turbine stage are designed using the parameterization system. The parameterization system is conducted in a 2D-3D manner. First, the 2D blade profile is designed using 11 parameters. Then a free vortex design is employed to set the angles of the blade profiles at different sections along the radial direction. At last, a 3D stacking line is implemented to guide these profiles so that the sweep, lean, taper and twist of the 3D blade can be obtained. In order to have reasonably good initial guess for the stages parameters, correlations are taken to compute the design parameters needed in the parameterization system. The CFD results indicate that the efficiencies of both the subsonic stage and the transonic stage are comparable to those predicted on Smith Chart. The consistency shows that the blade is well designed and can be used for further optimization.

Chapter 6

Uncooled Turbine Blade Analysis

Once the subsonic and the transonic turbine stages are designed, we can implement them in the turbine flow investigation. In the conventional turbine design procedure, the blade is designed sequentially: first, the uncooled blade shape is optimized, then the cooling holes are added to the optimized uncooled blade. The efficiency of the uncooled blades decides what shape of the blade is used for the cooling hole design. Thus in this chapter, we will first follow the conventional way of the turbine design to study the uncooled blade performance by varying the squealer height. It also provides a better perspective to understand the fluid dynamics of the turbine tip leakage flow because comparing to the cooled blade, the flow field in the tip region is simpler and the over tip leakage (OTL) flow is easier to be trace.

6.1 Cascade with Varying Squealer Height

In this section, the performance of the uncooled turbine cascade with varying squealer height is examined. The cascade has been widely used to investigate the turbine performance, both experimentally and numerically. It reveals the turbine's main flow features without blade rotation. Using the cascade gives us the first insight on how the blade efficiency changes with the squealer height.

In order to keep a consistent calculation, the cascade geometry implemented in this study was derived from Ma's paper [31]. The CFD set-up has been introduced in section 3.2 and validated in Chapter 4. The squealer height, normalized by the span, h_{sq}, varies from 0.5% to 2%. Two tip clearances, 0.5% and 1% of the span, are used.

The aerodynamic efficiency of the cascade is calculated by Equation 3.13. The efficiency variation with the squealer height is illustrated in Figure 6.1 a). As the tip

clearance increases, the efficiency reduces. At a tip clearance of 0.5%, the highest efficiency is at the squealer height of 1% while at a tip clearance of 1%, the highest efficiency of the cases tested is at the squealer height of 2%.

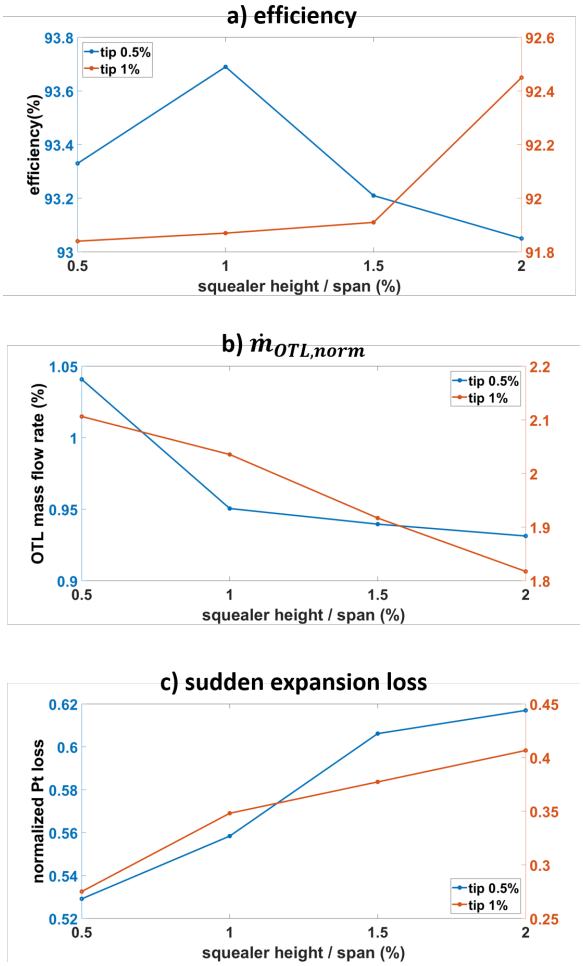


Figure 6.1: Variation of the aerodynamic efficiency, the OTL mass flow rate and sudden expansion loss with increasing squealer height at two different tip clearances.

The variation of the efficiency with the squealer height is attributed to two competing factors: the blockage effect that reduces the OTL mass flow rate and the sudden flow expansion that rises the loss generation caused by the sudden area change when the OTL flow passing through the squealer cavity. As the squealer height increases the OTL mass flow rate decreases, but the sudden expansion loss increases as shown in Figure 6.1 b) and c). The OTL mass flow rate is obtained by Equation 6.1

$$\dot{m}_{OTL,norm} = \frac{\dot{m}_{OTL}}{\dot{m}_{main}} \tag{6.1}$$

where $\dot{m}_{OTL}$ is the mass flow rate cross the tip clearance at the suction side; $\dot{m}_{main}$ is the main blade passage mass flow rate.

The sudden expansion loss, which represents the total pressure loss over the squealer normalized by the dynamic head, is computed by Equation 7.1

$$Y_{expansion} = \frac{Pt_{sqPS} - Pt_{sqSS}}{Pt_{sqSS} - P_{sqSS}} \tag{6.2}$$

where Pt_{sqPS} and Pt_{sqSS} represent the mass flow averaged total pressure at the squealer pressure side and at the squealer suction side respectively; P_{sqSS} is the mass flow averaged static pressure at the squealer suction side.

The increasing sudden expansion loss with the increasing squealer height can be explained by basic fluid dynamics: the sudden expansion loss increases with the flow area ratio between the exit and the inlet of the bulk cavity region. In this case, the flow area ratio is proportional to the squealer height. At the tip region, the sudden expansion loss has multiple influences. First, it is a source of tip leakage loss. Second, it reduces the total pressure of the OTL flow which also reduces the leakage mass flow rate, and thus loss.

These two competing effects, the raising sudden expansion loss effect and the reduced leakage mass flow rate, make the efficiency variation in tip clearance of 0.5% non-monotonic. As the tip clearance rises to 1%, the mass flow rate of the OTL flow increases so that the blockage effect plays a more critical role than the sudden expansion loss effect. Therefore, at the tip clearance of 1% the efficiency increases with the squealer height.

6.2 Turbine Stage with Varying Squealer Height

From the simulation of the transonic cascade, we find that the aerodynamic performance of the squealer is determined by the competing effects between the blockage of the OTL flow and the expansion loss. The next question is if the phenomenon stays the same in the turbine stage where the casing wall is counter-rotating against the rotor blade? It is a more engine representative working condition. Moreover, since the transonic blade has shown several unique flow features relative to the subsonic one, the subsonic and the transonic turbine stages designed in Chapter 5 are used to investigate the influence brought by the counter-rotating casing.

6.2.1 Optimization of Turbine Squealer Height

Since the subsonic and the transonic stages working in the same Reynolds number are designed and validated in Chapter 5, we can use them to optimize the squealer height

to investigate their influence towards the aerothermal performance of the stages. A Kriging surrogated model is used to interpolate between the discrete data points to estimate the optimal design. The design variable is the squealer height ranging from 0% to 3%. The design objectives are the total-total efficiency and the normalized heat load. For each design, two simulations, one with the adiabatic wall boundary condition and one with the constant wall temperature boundary condition, are run to calculate the total-total efficiency and the normalized heat load respectively.

The total-total efficiency of the uncooled stage is defined by the ratio between the actual work and the ideal work:

$$\eta = \frac{h_{t,1} - h_{t,3}}{h_{t,1} - h_{t,3,is}} \tag{6.3}$$

where 1 and 3 represent the stator inlet and the rotor outlet; h_t is the stagnation enthalpy; $h_{t,is}$ is the ideal stagnation enthalpy assuming the process from station 1 to station 3 is isentropic.

If the specific heat at constant pressure, C_p, is constant through the passage, Equation 6.4 can be further written as

$$\eta = \frac{1 - \frac{T_{t,3}}{T_{t,1}}}{1 - (\frac{P_{t,3}}{P_{t,1,is}})^{\frac{\gamma-1}{\gamma}}} \tag{6.4}$$

where T_t and P_t are total temperature and total pressure.

In the cases used to compute the tip heat flux, the wall temperature of the rotor blade, T_w, is set to constant. The ratio between the inlet total temperature and the wall temperature, $T_{t,1}/T_w$, is 1.25. The normalized heat load is computed by Equation 6.5:

$$HL_{normalized} = \frac{\int_{tip} qdA - \int_{flattip} qdA}{\int_{flattip} qdA} \tag{6.5}$$

where the integral of the heat flux, q, over the tip surface are normalized by the integral of the heat flux on the flat tip. In the squealer tip, the tip surface includes the squealer floor, the squealer wall and the squealer rim.

The work flow to optimize the squealer height is shown in Figure 6.2. Firstly, the parameterization system is used to generate the blade geometry and the mesh blocks. Then ICEM CFD script is implemented to automatically generate the structured

mesh. The sampling generates a series of representing geometries of the squealer height by alternating the design variables in the parameterization system. Then these representing geometries are imported into the flow solver to evaluate the aerodynamic efficiency and normalized heat load. Two metamodels using the Kriging method are implemented to build the relationship between the squealer height and the two design objectives respectively. Then the metamodels are employed to predict the optimal design with either highest aerodynamic efficiency or the lowest normalized heat load.

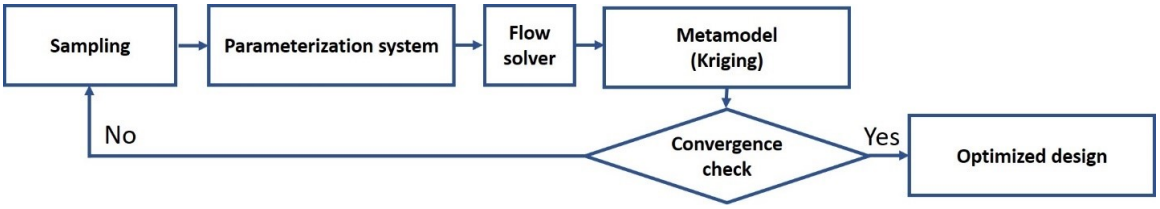


Figure 6.2: Flow chart of optimization system.

The predicted optimal design will be validated in the flow solver in the next iteration to check if the optimization is converged. Two conditions need to be fulfilled in order to pass the convergence check:1) the difference between the predicted performance and the CFD computed performance is smaller than 0.1%; 2) in two consecutive iterations, the variation of the optimal design objectives is smaller than 0.1%. Once the convergence check is passed, the relationship built by a metamodel is deemed to be valid. Otherwise, when the criteria of the convergence check fail, new samples in the next iteration are generated for the further refinement of the metamodel. Both the global and the local optimal designs in the metamodel prediction are included in the new samples to improve the metamodel and to prevent the system becoming trapped in the local optimization.

ANSYS CFX RANS solver is used as the flow solver. The same solver setup as in Section 5.6.1 was used for this study. The sampling and iterations of the optimization are shown in Figure 6.3, firstly, the initial sampling is conducted by evenly distributing the squealer height between 0% to 3% with the distance of 0.5%. The Kriging method is employed in two metamodels to interpolate the efficiency and the normalized heat load of these test samples. The optimal designs with the highest efficiency or the lowest normalized heat load are predicted by the two metamodels respectively. If the predicted results do not pass the convergence check, the predicted optimal designs are evaluated in the next iteration to improve the metamodel with more test data. Both the global and the local optimal designs are computed in order to prevent the solver from trapping in the local optimization. If the criteria for the optimization

convergence check is passed, the optimal design indicated by the Pareto front can be obtained.

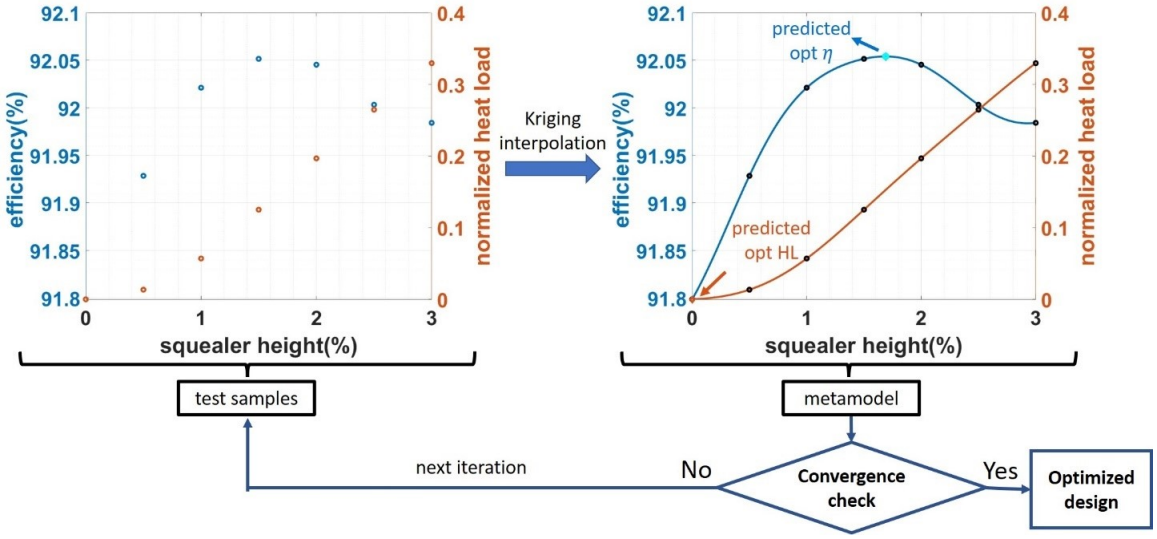


Figure 6.3: Sampling and iterations of optimization.

Eight iterations and nine iterations are need respectively for the subsonic stage and the transonic stage to converge in the optimizer. The results of the optimization are shown in Figure 6.4 where the x axis shows the normalized heat load; y axis shows the aerodynamic efficiency; the colored contour shows the squealer height. Each black circle on the plots represents one simulation with designated squealer height. As the optimization converges, the Pareto fronts for the two stages are indicated by the dash lines.

The comparisons of the efficiency and the normalized heat load in the two stages are illustrated in plot a) and plot b) of Figure 6.5. In plot a), as the squealer height increases from 0% (flat tip) to 1.5%, the efficiencies in the subsonic stage and the transonic stage both rise. Comparing to the transonic stage, the subsonic stage has higher slope of increment of efficiency and the peak value with higher squealer height. As the squealer height becomes greater than 1.5%, the efficiencies in the two stages both reduce. The transonic one has higher slop of reduction. At the squealer height of 3%, the subsonic stage has 0.18% higher efficiency comparing to the flat tip; while the efficiency in the transonic stage drops to the level comparable to the efficiency of the flat tip. It implies that the squealer in the transonic tip cannot bring efficiency gain as much as the squealer in the subsonic stage. In plot b), as the squealer height increases, the heat load in both the subsonic and the transonic stages rises almost

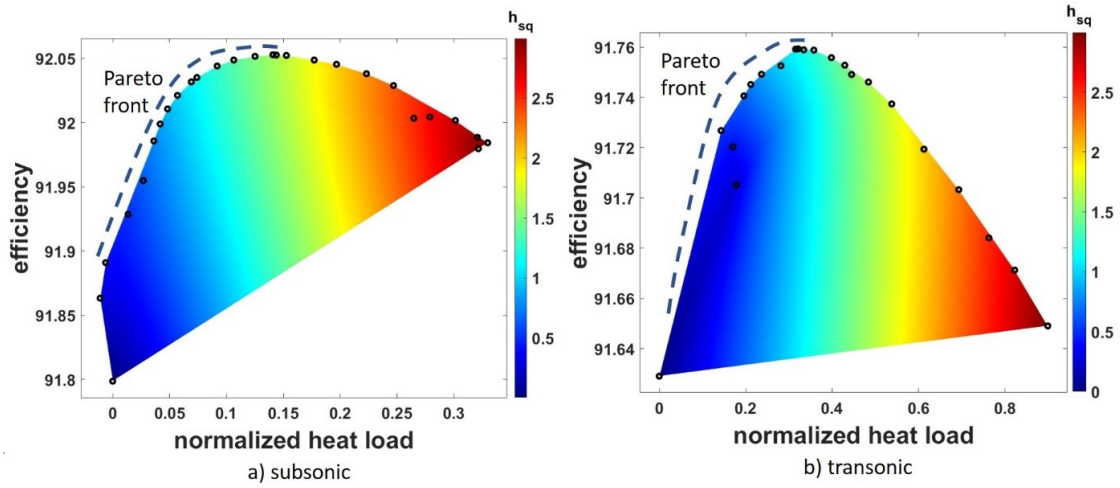


Figure 6.4: Optimization of the squealer height in the subsonic and the transonic stage. The tip clearance is 0.8% of span. Note that the different vertical and horizontal axis ranges on the two plots.

linearly. The slope of the increment of the heat load in the transonic stage is greater than the one in the subsonic stage. For both the efficiency and the heat load, both tips with squealer height over 1.5% of span have shown detrimental effect on the aerothermal performance of the blade.

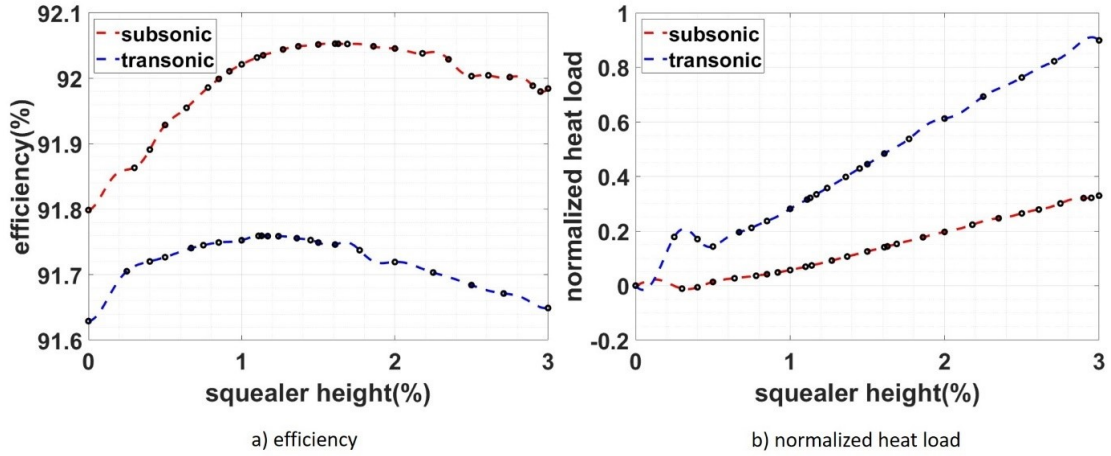


Figure 6.5: Comparison of the efficiency and normalized heat load in the subsonic and the transonic stage.

It is noted that the Mach number is not the only difference between the two stages. The subsonic and the transonic stage are working in different design points and several parameters such as the velocity triangles, the turning, the loading and the reaction are not the same. The aim of this study is to let the two stages work in their operating

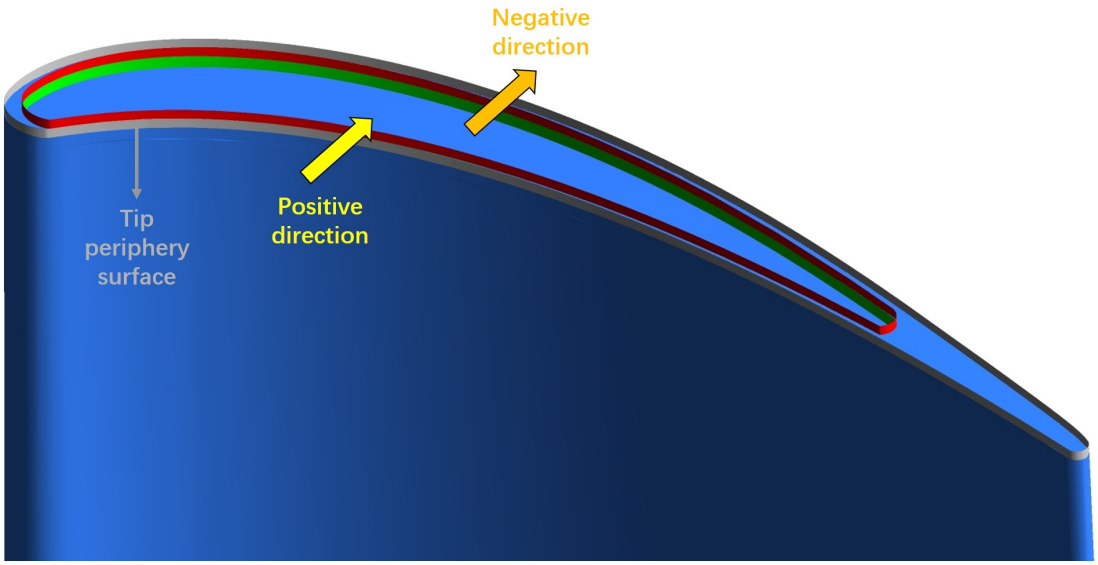


Figure 6.6: The tip periphery surface used to investigate the OTL flow. When the fluid flows into the tip, it is in the positive direction. When the fluid leaves the tip, it is in the negative direction.

points respectively with the same Reynolds number. The effect of other parameters need to be investigated in the future research.

In order to reduce the difficulty to analyze the results, in the following sections, only the cases with the squealer height ranging from 0% to 3% with the interval of 0.5% will be discussed in detail for both the uncooled and the cooled blades.

6.2.2 Over Tip Leakage Mass Flow Rate Variation

In order to explore the reason for the variation of the efficiency with the squealer height, the flow field in the tip region is investigated in detail. As illustrated in Figure 6.6, the tip periphery surface is imported into the computational domain. The surface is uniformly split into 200 pieces along the blade profile. The local averaged flow variables, such as velocity, density, mass flow rate, entropy, etc., are evaluated piece by piece to obtain a whole picture of the flow passing the tip region.

From the results obtained at the tip periphery surface, the mass flow rate at each piece of the tip periphery surface is evaluated. As shown in Figure 6.6, whether the flow velocity vector points inside or outside of the tip gap, the flow direction is deemed positive or negative. The sum of the positive tip leakage mass flow rate is found to

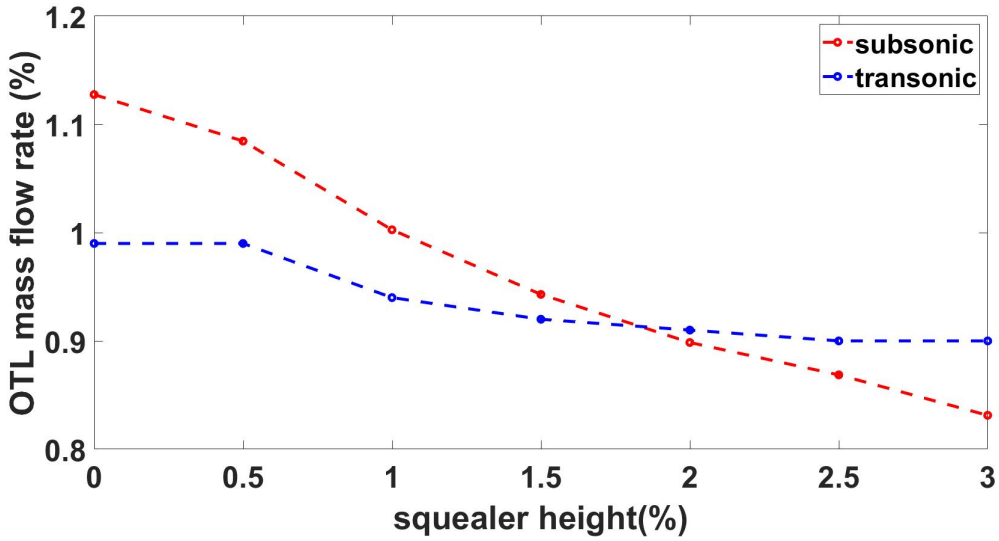


Figure 6.7: The OTL mass flow rates at various squealer height for the subsonic and the transonic turbine stages. The tip gap in the two stages are both 0.8% of the span. The rim thickness in the two stages are the equal to their trailing edge thickness.

be equal to the sum of the negative tip leakage mass flow rate. It indicates the mass conservation across the tip gap. Thus either the positive or the negative local mass flow rate can be summed up to calculate the tip leakage mass flow rate.

The variation of the tip leakage mass flow rate with the squealer height is shown in Figure 6.7. The normalized OTL mass flow rate is computed in Equation 6.1. From the figure, as the squealer height increases, the OTL mass flow rate in both the subsonic and the transonic stages decreases. This is in line with the previous studies in the turbine cascade where the leakage mass flow rate reduces with the increasing squealer height.

The blockage effect can be illustrated in Figure 6.8 where the mass flux vectors of the OTL flow along the tip periphery surface are plotted for the squealer height of 0%, 0.5% and 3%. The mass flux vector at the ith piece in the tip periphery surface is computed by

$$\vec{F_i} = (\frac{1}{A_i}\int_{A_i} \rho u_{rel} dA, \frac{1}{A_i}\int_{A_i} \rho v_{rel} dA) \tag{6.6}$$

where A_i is the area of the ith piece in the tip periphery surface, ρ, u_{rel} and v_{rel} are the mass flow averaged density, relative axial velocity and relative circumferential velocity at the ith piece in the tip periphery surface.

As defined previously, the mass flow rate vector in the positive direction (entering the tip gap) is in red, and the negative direction (leaving the tip gap) is in blue. For the subsonic rotor, the OTL flow enters the tip gap through the pressure side and the leading edge of the tip periphery surface. As the squealer height increases, the mass flow rate from the pressure side of the tip reduces. More OTL flow enters the tip gap through the leading edge of the gap. Compared to the flat tip ($h_{sq} = 0$), the tips with squealers exhibit two regions of velocity deficit on the suction side of the blade indicated by 'location 1' and 'location 2' with the dashed arrows as shown in Figure 6.8. As the squealer height increases from 0.5% to 3%, location 1 moves upstream and the velocity deficit at location 2 becomes more significant as shown in Figure 6.8.

For the transonic stages, the OTL flow also enters the tip gap through the PS and the leading edge of the tip periphery surface. However, the squealer is less effective to change the OTL flow distribution. The large velocity deficit region noted as location 1 and location 2 can still be found, but with a smaller velocity deficit.

6.2.3 Vorical Structure in Turbine Stage

6.2.3.1 Vortex Identification and Quantification Method

The vortices generated by the OTL flow are found to have influence on the aerothermal performance of the rotor. In this study, the vortical structure in the tip region is studied and modeled by the vortex identification techniques. The difficulty of identifying the vortex core is to distinguish the 'swirling' (rigid-body rotation) from the shearing motion. Here, the location of the vortex core is identified by the isosurface bounded by Lambda 2 criterion proposed by Jeong and Hussain [36]. The basic idea of the Lambda 2 criterion is that in the swirling motion, where the centrifugal force is balanced by the pressure force, there exist a local minimum pressure on the axis of the vortex. Thus by taking the symmetric part of the gradient of the Navier-Stokes equations, we have:

$$\frac{DS_{ij}}{Dt} - \upsilon S_{ij,kk} + \Omega_{ik}\Omega_{ki} + S_{ik}S_{ki} = -\frac{1}{\rho}P_{.ij} \tag{6.7}$$

where t is the time; υ is the kinematic viscosity; ρ is the density; P is the pressure; i, j, k are used for the Einstein notation; S and Ω are the symmetric and asymmetric part of the velocity gradient tensor, J:

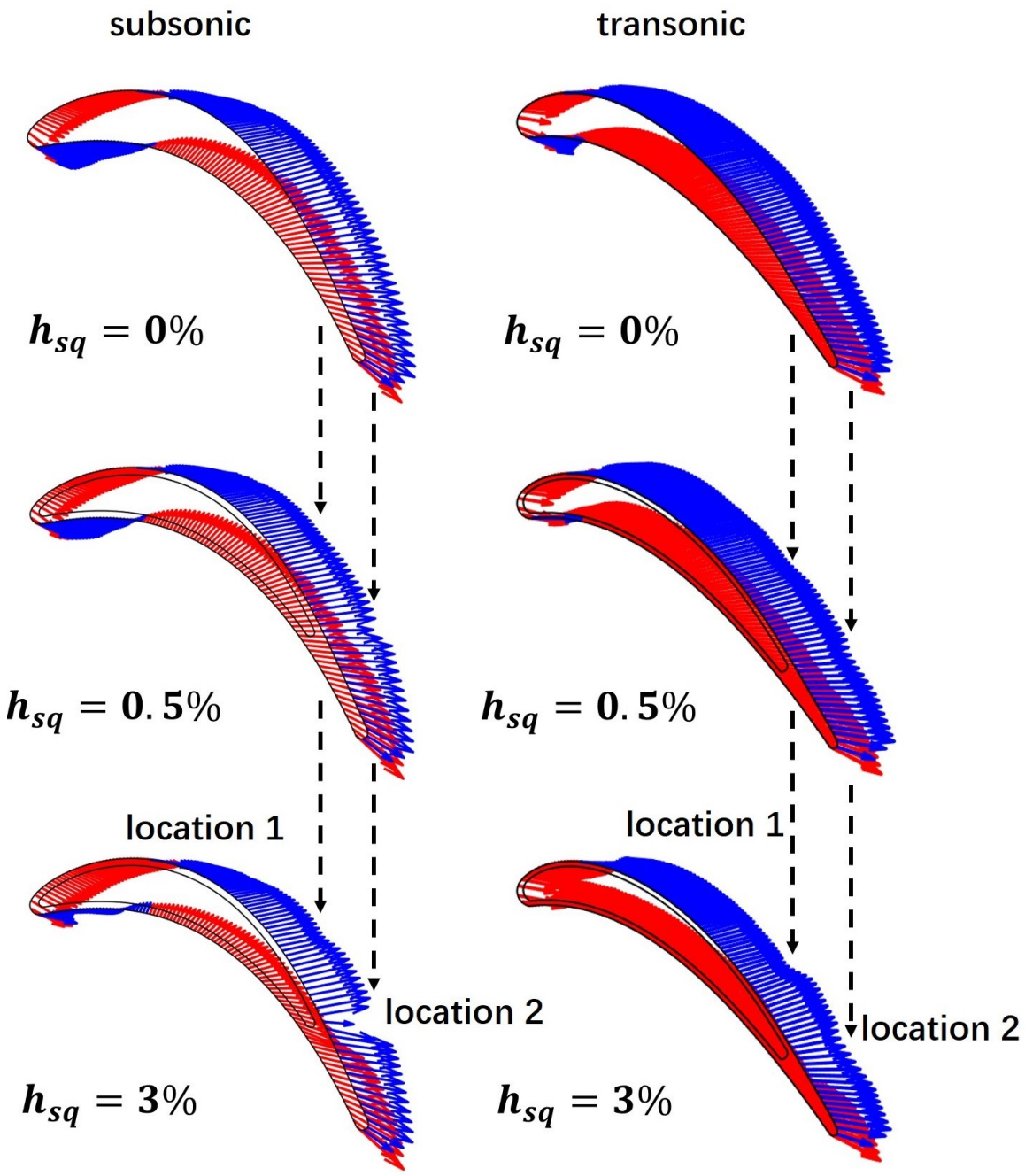


Figure 6.8: The mass flux vectors along the tip periphery surface are plotted for the squealer height of 0%, 0.5% and 3%. h_{sq} is the squealer height. Location 1 and location 2 indicate the places with large velocity deficit.

$$J = \nabla \vec{u} = \begin{bmatrix} \partial_x u_x & \partial_y u_x & \partial_z u_x \\ \partial_x u_y & \partial_y u_y & \partial_z u_y \\ \partial_x u_z & \partial_y u_z & \partial_z u_z \end{bmatrix} \tag{6.8}$$

$$S = \frac{J + J^T}{2} \tag{6.9}$$

$$\Omega = \frac{J - J^T}{2} \tag{6.10}$$

In Equation 6.7, a local pressure minimum requires two eigenvalues of the tensor, $P_{.ij}$, to be positive. Because the first two terms on the left hand side of the Equation 6.7 represent unsteady irrotational straining and viscous effects, respectively, only $\Omega_{ik}\Omega_{ki}+S_{ik}S_{ki}$ is attributed to the rigid body rotation. Thus, two negative eigenvalues of $\Omega_{ik}\Omega_{ki} + S_{ik}S_{ki}$ are required to have the local pressure minimum caused by the swirling. Since $\Omega_{ik}\Omega_{ki} + S_{ik}S_{ki}$ is symmetric, their three eigenvalues are λ_1, λ_2 and λ_3 are all real numbers. Assuming $\lambda_1 \leqslant \lambda_2 \leqslant \lambda_3$, then the requirements of the local minimum pressure caused by the swirling is equivalent that λ_2 is negative. Therefore, by assigning a specific negative value of λ_2 as the threshold, the vortex core can be identified.

The Lambda 2 criterion is built in CFX CFD-Post. Taking the value of $-1.1\times10^{10}s^{-2}$ (in CFX it is normalized as level 0.0064) as the threshold for λ_2, the vortex core in the case of transonic turbine rotor is illustrated in Figure 6.9 where the color of the isosurface is determined by the sign of the axial vorticity, ω_x: when the axial vorticity, ω_x, is positive, the vortices rotate counterclockwise (viewing opposite to the axial direction), the isosurface is in red; when the axial vorticity, ω_x, is negative, the vortices rotate clockwise, the isosurface is in blue.

Once the vortex is identified by the Lambda 2 criterion, the vorticity is used to quantitatively evaluate the strength of the vortex. The strength of the vortex is computed by integrating the vorticity over the intersection area between the axial cut plane and the vortex tube surrounded by the Lambda 2 isosurface as shown in Figure 6.9. The vorticity is used to quantify the vortex strength because 1) the regions with the strongest swirling have already been incorporated in the Lambda 2 isosurface; 2) the generation of the vorticity can be understood by Equation 6.11:

$$\frac{D\vec{\omega}}{Dt} = (\vec{\omega}\cdot\nabla)\vec{u} - \vec{\omega}(\nabla\cdot\vec{u}) - \nabla\times(\frac{1}{\rho}\nabla P) + \nabla\times\vec{f}_{visc} + \nabla\times\vec{f}_{body} \tag{6.11}$$

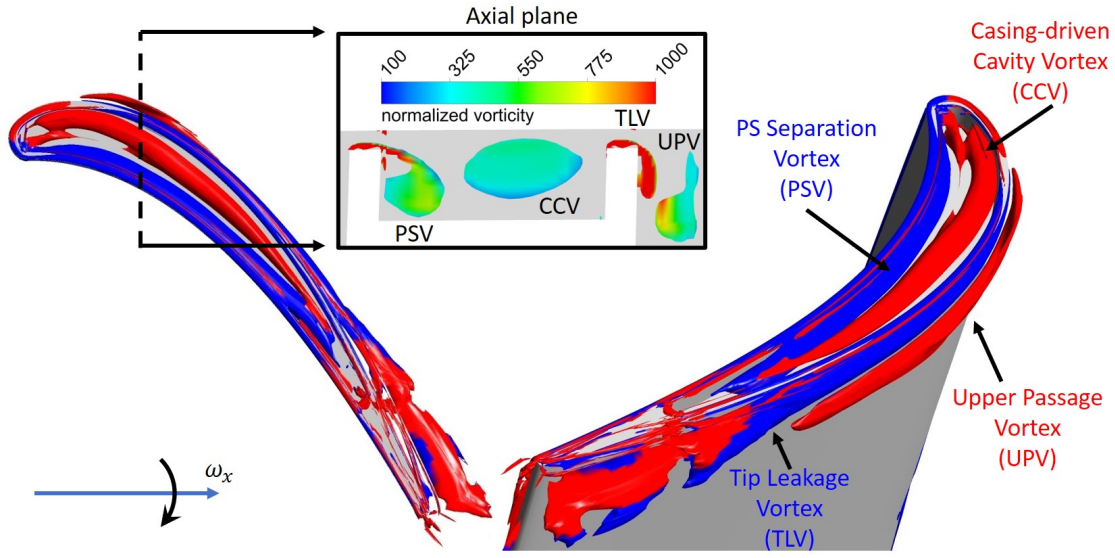


Figure 6.9: Identification and quantification of the vortex in the tip region. The transonic blade with squealer height of 3% is used as an example.

where the first two terms on the right hand side of the Equation 6.11 represent the transportation of the vorticity, $\vec{\omega}$. The third term represents the vorticity generated by the density and pressure gradient. The last two terms show the vorticity production by the viscous force or other body force. The other metrics to evaluate the vorticity, such as velocity swirling strength in CFX, although exclude the shearing from the vorticity, has no clear link to the source of vorticity generation. Moreover, by comparing the vorticity strength with the velocity swirling strength, the same trend of variation is observed. Therefore, the vorticity is implemented in this study to quantify the strength of the vortex.

6.2.3.2 Vortical structure

From Figure 6.9, four groups of vortices are found to form the vortical structure in the squealer tip region. They are the Casing-Driven Cavity Vortices (CCV), the Pressure-Side Separation Vortices (PSV), the Tip Leakage Vortices (TLV) and the Upper Passage Vortices (UPV) as shown in Figure 6.10. In order to understand the formation of the vortices two special test cases are compared with the baseline case. In the baseline case, the squealer height is 3% and the casing has the no-slip and counter-rotating wall boundary conditions. The special testes cases are 1) the case with the squealer height of 3% and the casing has no relative movement to the rotor (equivalent cascade case); 2) the case with the flat tip and the same casing boundary

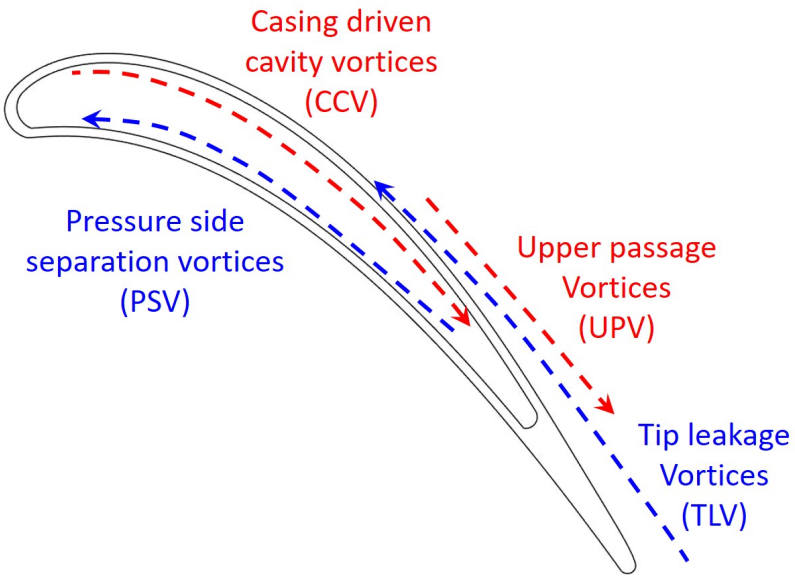


Figure 6.10: Vortical structures in the squealer tip region.

conditions with the baseline case. The boundary conditions of the four cases are summarized in Table 6.1.

Table 6.1: Boundary conditions for the test cases.

Cases	Squealer height	Casing relative motion
Test case 1	3%	Counter-rotating
Test case 2	3%	Rotating with rotor (Equivalent cascade case)
Test case 3	0%	Counter-rotating

The vortical structures in these cases are shown in Figure 6.11 where the same Lambda 2 criterion used in Figure 6.9 are implemented to show the isosurface of the vortex cores. In order to quantitatively study the strength of the vortices, the vorticity on the $A - A$ cutting plane is also shown in Figure 6.11.

The difference between plot a) and plot b) indicates that the relative movement of the casing plays the key role to the generation of the CCV and the PSV because when the casing has no relative movement (cascade equivalent case) as shown in plot b), only a small portion of the PSV is formed along the pressure side edge and no clear CCV is observed. In the baseline case as shown in plot a), the casing relative movement forms the CCV inside the squealer cavity in the way similar to the well-studied 'lid driven cavity flow'. The formation of CCV and PSV will be discussed in the next sections. The small fragment of vortices at the frontal portion of the blade in plot b1) is attributed to the main flow entering from the suction side of the tip.

Outside of the tip, the relative casing movement scrapes the casing boundary layer. The scraping results in two differences between plot a) and plot b):

1) it changes the trajectory of the TLV tube. In plot a) the TLV is attached to the suction side profile of the tip. In plot b), without the casing relative movement, the TLV leaves the suction side profile at point B with a different angle.

2) it intensifies the UPV. The intensified UPV forms a counter-rotating vortex pair with the TLV. From the vortex dynamics, the counter-rotating vortex pair of the TLV and the UPV generates a velocity field that pushes each other to the suction side of the tip as shown in plot a2).

These two effects results in the TLV close to the tip suction side. From vortex dynamics, the vortex tube moves with the flow material line and the bending of the vortex tube will increase the vorticity. Thus, because of the bending effect caused by the casing movement and the UPV, the vorticity of the TLV in plot a) is greater than the one in plot b).

By comparing plot a) with plot c), the squealer cavity is found to be essential to the generation of the CCV because in the flat tip, no equivalent vortex could be identified. Without the cavity, the OTL flow can directly cross the tip. While in the presence of the squealer cavity, the flow path is changed by the PSV and the CCV.

6.2.3.3 Explanation of Casing-Driven Cavity Vortices (CCV)

From the previous discussion, the casing relative movement and the squealer cavity are found to be essential to the generation of the CCV. Combing these factors, we are reminded about the 'lid driven cavity flow' which has been a widely studied benchmark problem [85] [48] [69] [59]. Therefore, the CCV in the tip is modelled similarly as shown in Figure 6.12. From the previous work on the 'lid driven cavity flow', the vortical structure and the vorticity is influenced by the driven Reynolds number and the aspect ratio which are computed by

$$Re_{driven} = \frac{\rho_{SS} U L}{\mu} \tag{6.12}$$

$$AR = \frac{h_{sq}}{L} \tag{6.13}$$

where ρ_{SS} is the mass averaged density along the tip suction side; U is the velocity of the casing; L is the width of the cavity; μ is the dynamic viscosity; h_{tip} and h_{sq} are the tip gap and the squealer height.

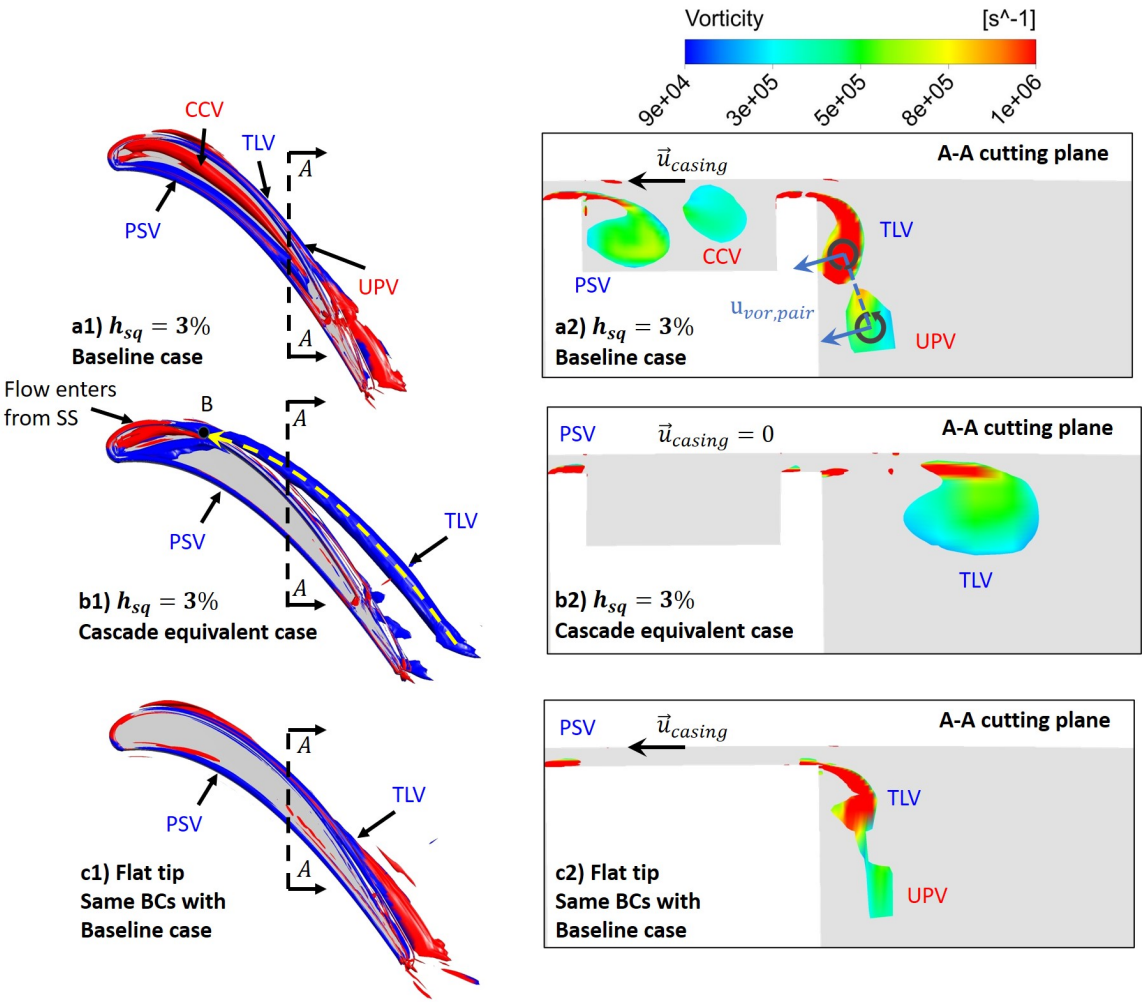


Figure 6.11: The vortical structures in the baseline case and two test cases.

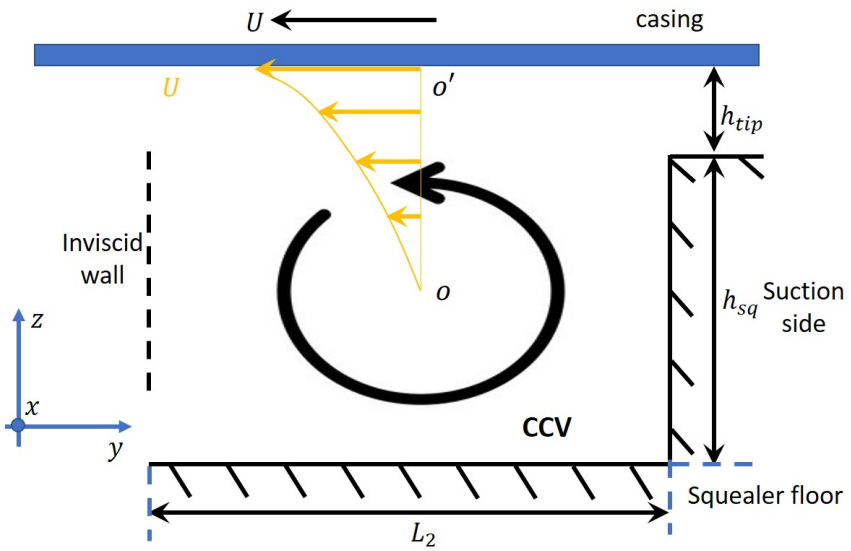


Figure 6.12: Schematic for the generation of the CCV.

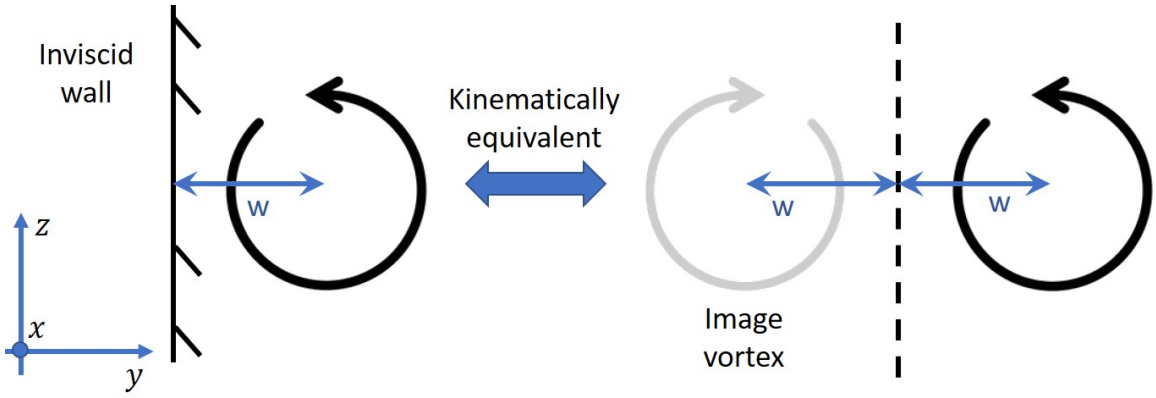


Figure 6.13: The velocity field generated by an inviscid wall is kinematically equivalent to an image vortex.

$$Re_{driven} = \frac{\rho_{SS} U L}{\mu} \tag{6.14}$$

Because in the squealer cavity, there are two counter-rotating vortices as shown in plot a) of Figure 6.11. The left hand side boundary of the CCV in Figure 6.12 is deemed to be an inviscid wall. This can be explained by Figure 6.13. Supposing a vortex has a distance of w from an inviscid wall, the velocity on the wall in the y direction is 0, i.e., no penetration. From vortex dynamics, the flow field generated by the vortex and the inviscid wall is kinematically equivalent to the one generated by the vortex and its counter-rotating image vortex. In this case, although the strength of the CCV and PSV is not necessarily the same, the velocities in the y direction generated by the two vortices are more or less cancelled by each other. Therefore, the penetration of flow between the two vortices is reduced. Thus, an inviscid wall can be implemented to segregate the two vortices and to simplify the model.

6.2.3.4 Explanation of Pressure-Side Separation Vortices (PSV)

The PSV is generated by the separation of the OTL flow from the pressure side of the tip as shown in Figure 6.14. The CFD evidence of the flow pattern is shown in Figure 6.15 where the 2D streamlines combined with the velocity vectors at axial cut plane with 15% of the axial chord is illustrated. As the OTL flow enters from the pressure side, a separation bubble is formed along the pressure side edge. Depending on the size of the separation bubble and the thickness of the squealer rim, the OTL flow may or may not have reattachment on the squealer rim. Downstream of the separation bubble, the flow will separate again due to the squealer cavity. The separations

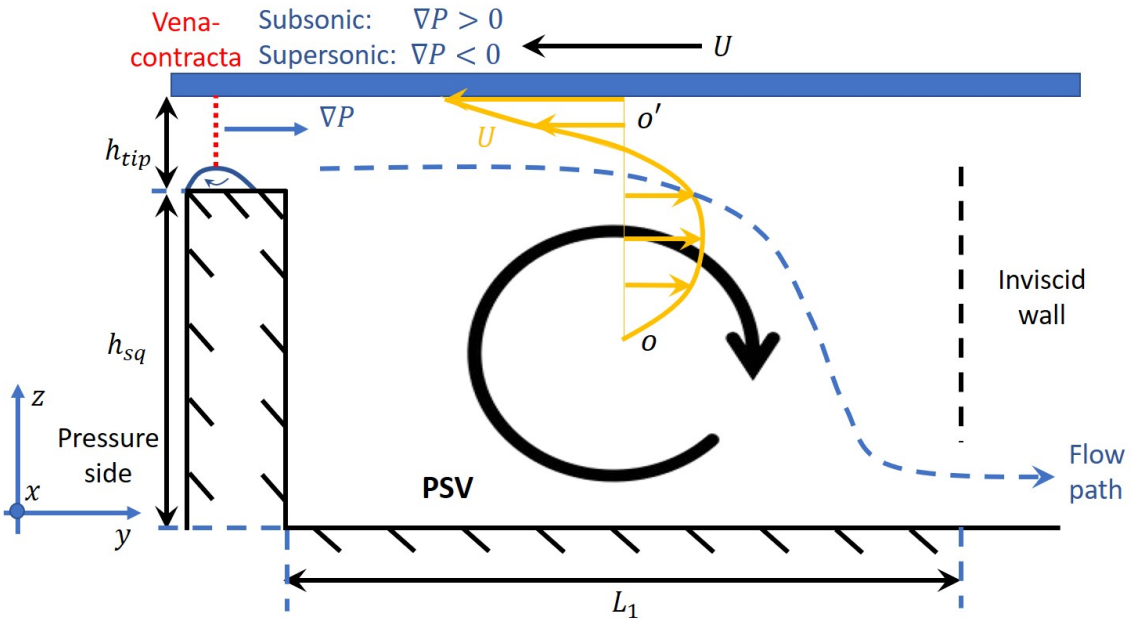


Figure 6.14: Schematic for the generation of the PSV.

along the pressure side edge and inside of the squealer cavity form the Pressure-side Separation Vortex (PSV). Because in the flat tip there is no cavity, the size of the PSV is much smaller than the one in the squealer tip as shown in plot a) and plot c) of Figure 6.11. The separation inside of the squealer cavity can be modelled by the well-studied case of the 'open-cavity flow' except for the moving casing. From the 'open-cavity flow' model, the flow structure is influenced by the aspect ratio, AR computed by Equation 6.13, the Reynolds number and the Mach number of the free stream flow. Similar to the model of the CCV, the right hand side boundary of the model of the PSV is an inviscid wall. The inviscid wall influences the PSV in two-fold: 1) it blocks the OTL and generates an adverse pressure gradient; 2) it changes the aspect ratio of the cavity for the PSV.

6.2.3.5 Impact of Vorical Flow Structure

The velocity deficit shown in Figure 6.8 is attributed to the vortical structures caused by the squealer, as illustrated in Figure 6.16 where the Casing-driven Cavity Vortex (CCV), the Pressure-side Separation Vortex (PSV) and Tip Leakage Vortex (TLV) are indicated by the streamlines of the OTL flow in two colors based on the sign of ω_x, the vorticity in axial direction. In Figure 6.16, if ω_x is positive, the streamlines in red indicate the flow rotates counter-clockwise; if ω_x is negative, the streamlines in blue indicate the flow rotates clockwise.

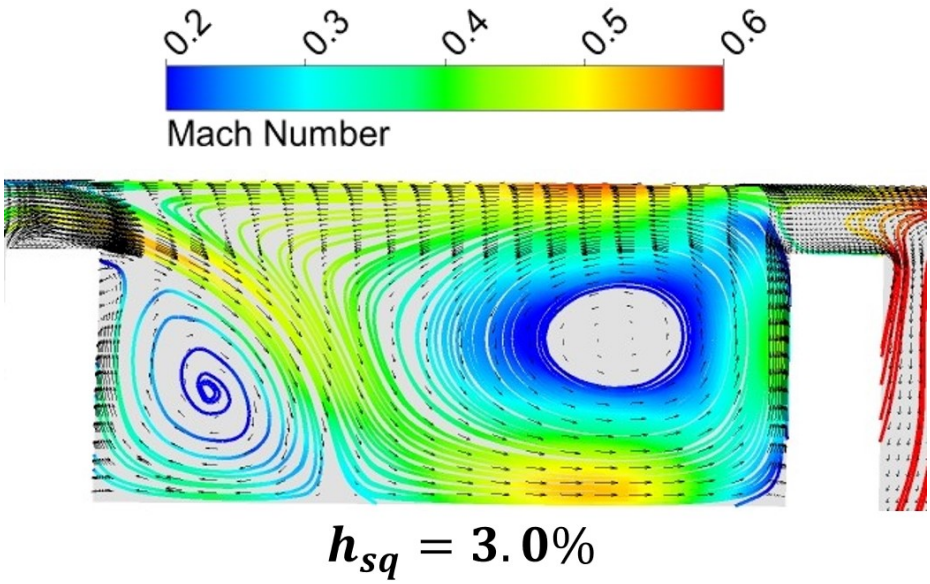


Figure 6.15: The 2D streamlines combined with the velocity vectors at axial cut plane with 15% of the axial chord. The case in the transonic stage with the squealer height of 3% is taken as an example.

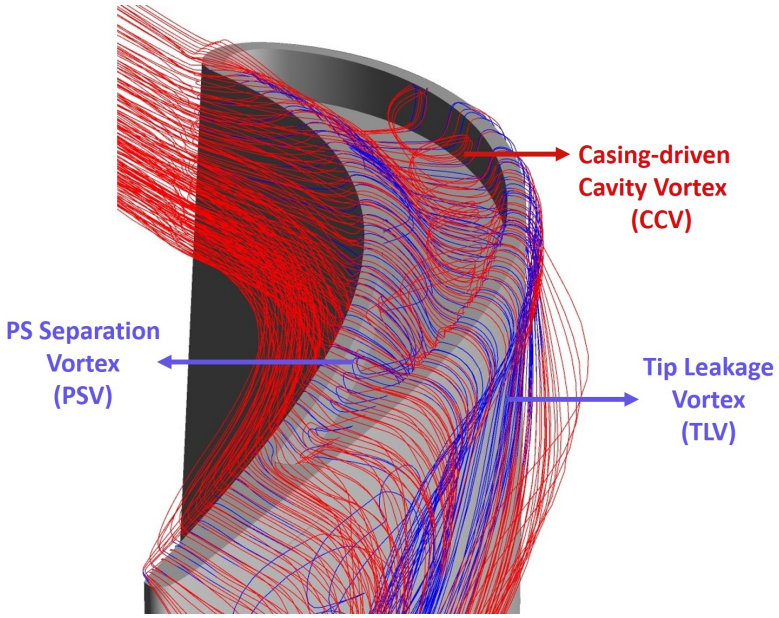


Figure 6.16: The vortex structure at the tip. This example is taken at the squealer height of 3% in the transonic stage.

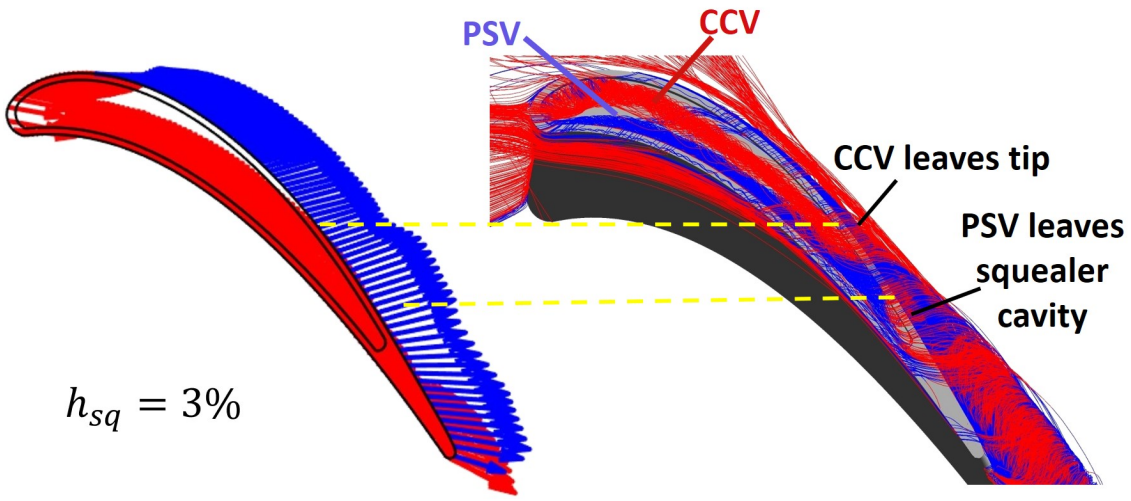


Figure 6.17: The mass flow rate deficit can be explained by the vortex structure at the tip. This example is taken at the squealer height of 3% in the transonic stage.

Taking the transonic case with squealer height of 3% as an example as shown in Figure 6.17, the velocity deficit locations are in line with the locations where the CCV and the PSV leave the tip gap. The velocity deficit at location 1 and location 2 are at about 60% and 80% of the blade axial chord along the axial direction. They are consistent with the locations where the CCV leaves the tip gap and the PSV leaves the squealer cavity. It is the same case for both the subsonic and transonic rotors with various squealer height. Thus, the velocity deficit region can be attributed to the vortices formed by the squealer cavity.

The comparison of the vortical structures on the flat tip and the squealer tip in the subsonic and transonic stages are shown by the vortex cores in Figure 6.18. The isosurface is bounded by the Lambda 2 criterion which implements the negative values of the second eigenvalue of the symmetry square of velocity gradient tensor. In the figure, when the axial vorticity, ω_x, is positive, the vortices rotate counterclockwise, the isosurface is in red; when the axial vorticity, ω_x, is negative, the vortices rotate clockwise, the isosurface is in blue. In the cases with the flat tip, the OTL flow separates at the pressure side edge. No major vortical structures are found on the suction side of the tip except for the tip leakage vortices. In the cases with the squealer tip, two counter-rotating vortices, the PSV and the CCV, are generated by the cavity for both the subsonic and the transonic stages. Following the streamlines in green, the PSV is formed by the OTL flow coming from the pressure side of the tip. Following the streamlines in red, the CCV is formed by the flow from the suction

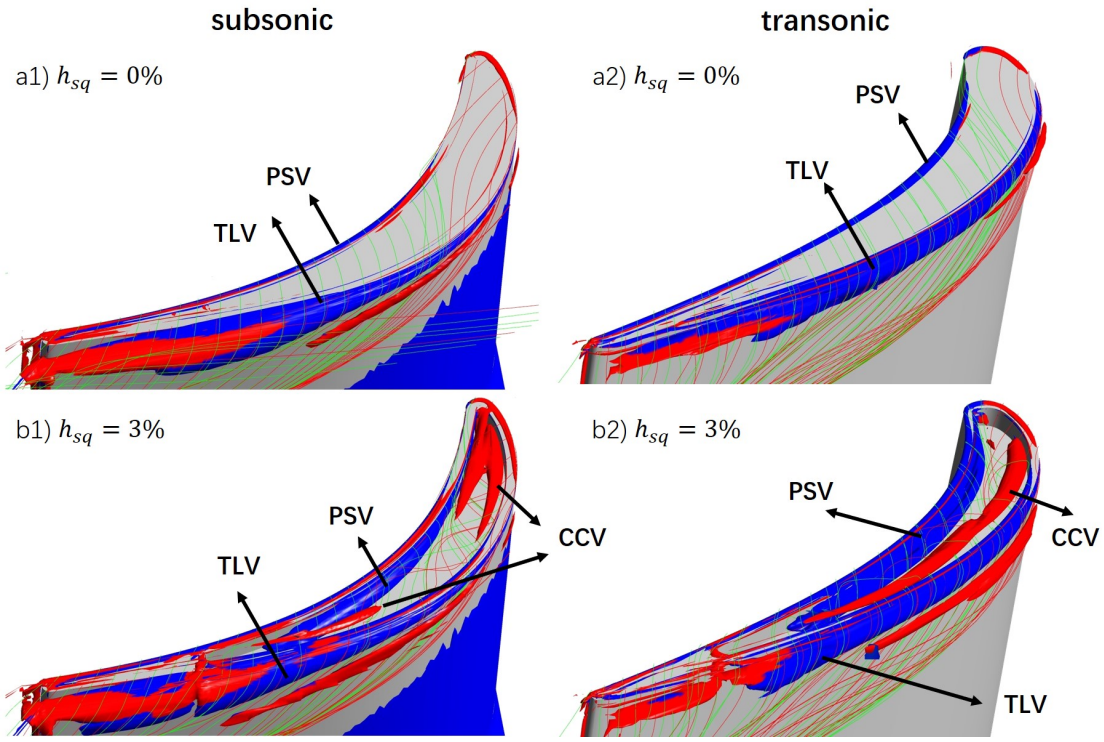


Figure 6.18: The vortical structures of the OTL flow at the tip region for the subsonic and the transonic rotors with and without squealer tip. The vortices are illustrated by the vortex core region. The streamlines coming from the pressure side and the leading edge of the tip are shown in green and red, respectively. The blade surface is in grey.

side due to the casing relative movement.

The effect of the squealer cavity is demonstrated by the velocity vector plot at the axial cut plane of 40% squealer axial chord in Figure 6.19. In the cases with the flat tip as shown in plot a1) and plot a2), the boundary layer of the casing is mainly attached to the wall and the OTL flow has a straight route passing from the pressure side to suction side as indicated by the blue dashed arrows. However, in the cases with the squealer cavity as shown in plot b1) and plot b2), the casing wall boundary layer detaches and rolls up to form vortices rotating in the counter-clockwise direction noted by CCV. Because of the presence of the two counter-rotating vortices, the OTL flow in the squealer tip cannot directly cross the tip as in the flat tip. Instead, the OTL flow first dives into the cavity following the streamline of PSV and then flows through the bottom of the cavity and impinges on the suction side of the cavity wall following the streamline of CCV. Finally, the OTL leaves the cavity along the suction side of the cavity wall. The path of the OTL flow in the squealer tip is also indicated

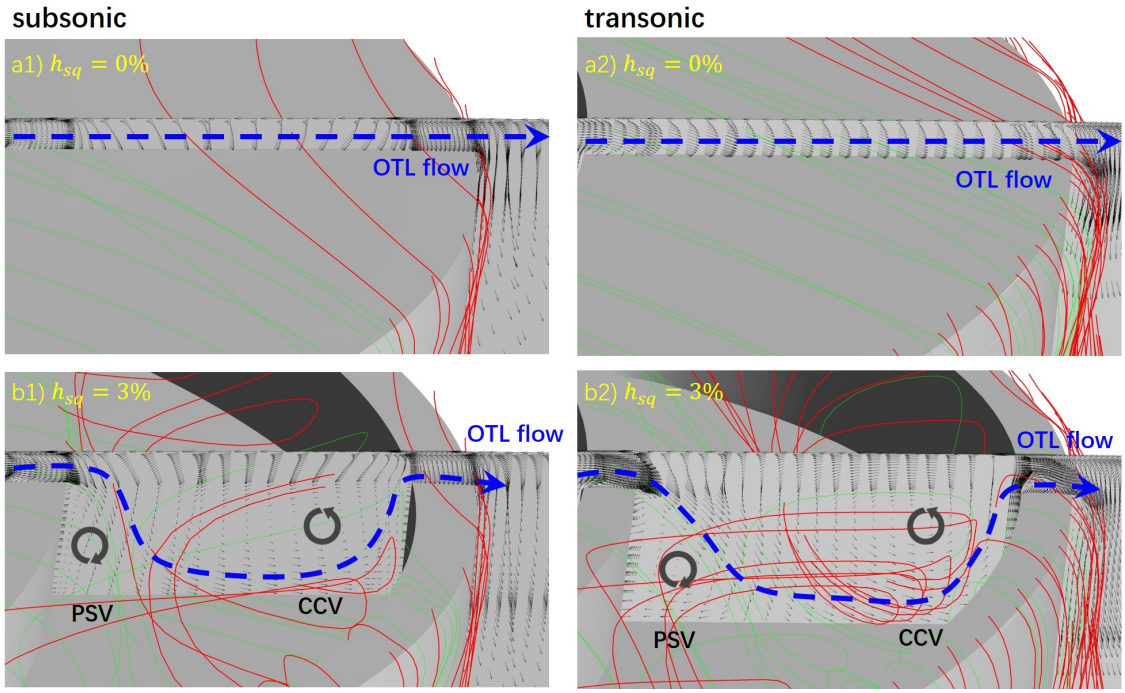


Figure 6.19: The velocity vector plot at the axial cut plane for the subsonic and the transonic rotors with and without squealer tip. From the direction of the velocity vectors, the rotating direction of the vortices are marked by black arrows.

by the blue dashed arrows. The 'detour' caused by the counter-rotating vortex pair explains the sealing effect of the squealer cavity so that the mass flow rate of the OTL flow on the squealer tip is lower than the one on the flat tip.

6.2.4 Tip Loss Generation Analysis

6.2.4.1 Total Loss in the Turbine Stage

From the previous section, the increase in the squealer height has shown to reduce the OTL mass flow rate. However, as shown in Figure 6.5, the variation of the efficiency with increasing squealer height for both the subsonic and the transonic turbine stages is not monotonic. This reminds us of the findings in the transonic cascade, where the aerodynamic performance of the rotor is influenced by two competing effects, the blockage of the OTL flow and the expansion loss. Therefore, this section investigates the variation of the loss generation with the increasing squealer height in the turbine stages.

Because in the turbine stage, the rotating blade will do work to the passage flow, the total temperature is not constant through the rotor domain. Therefore the total

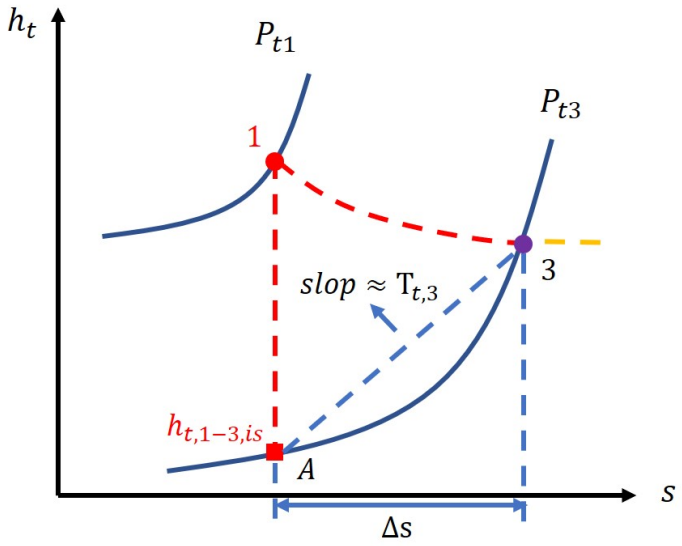


Figure 6.20: Computation of the equivalent efficiency.

pressure can not be used to compute the loss generation as indicated in Equation 3.4. Thus, unlike the case in a turbine cascade, the loss generation in the turbine stage is evaluated by the entropy generation, Δs, as shown in Equation 3.2. In the equation, the difference of the entropy flux between the rotor exit plane and the stator inlet plane is divided by the mass flow rate of the passage. The loss generation, Δs, is normalized by

$$\Delta s_{norm} = \frac{\Delta s T_{exit}}{\frac{1}{2} u_{exit}^2} \tag{6.15}$$

where T_{exit} and u_{exit} are the mass flow averaged temperature and absolute velocity at the rotor exit plane.

In order to directly compare the loss generation with the aerodynamic efficiency, the equivalent efficiency proposed by Denton [43], η_{lost}, is employed. As shown in Figure 6.20, in the turbine stage the aerodynamic efficiency is computed by the Equation 6.16

$$\eta = \frac{h_{t,1} - h_{t,3}}{h_{t,1} - h_{t,1-3,is}} \tag{6.16}$$

where h_t is the stagnation enthalpy; station 1 and station 3 represent the stator inlet and the rotor outlet; station A refers to the station assuming the process from station 1 to station 3 is isentropic.

By combining the first law of thermodynamics, Equation 5.5 and the Gibbs' Equation, Equation 5.6 and neglecting the difference between static and stagnation conditions, we have:

$$T_t ds = dh_t - v dP_t \tag{6.17}$$

Thus, along the constant total pressure curve from station A to station 3, by integral Equation 6.17, the total enthalpy $h_{t,3}$ can be calculated by

$$h_{t,3} = h_{t,1-3,is} + \int T_t ds \tag{6.18}$$

The computation of the equivalent efficiency is to assume from station A to station 3 the temperature is constant and the value is equal to the exit stagnation temperature, $T_{t,3}$. Therefore, the total enthalpy $h_{t,3}$ can be computed by:

$$h_{t,3} = h_{t,1-3,is} + T_{t,3}\Delta s \tag{6.19}$$

where Δs is the entropy generation between the station 1 and the station 3, i.e. between the stator inlet and the rotor exit.

By combining Equation 6.16 and Equation 6.19, the equivalent efficiency, $\eta_{equivalent}$ can be computed by:

$$\eta_{equivalent} = 1 - \frac{T_{t,3}\Delta s}{h_{t,1} - h_{t,1-3,is}} \tag{6.20}$$

Therefore, the comparison between the efficiency and the equivalent efficiency with varying squealer height are illustrated in Figure 6.21. For both the subsonic and the transonic stages, the variations of the efficiency are in line with the variations of the equivalent efficiency. The discrepancy between the efficiency and the equivalent efficiency is about 0.1% in the subsonic stage and 0.2% in the transonic stage. The relative lower value of the equivalent efficiency comparing to the efficiency is attributed to the assumption we take in the derivation of the equivalent efficiency: 1) the difference between static and stagnation are neglected; 2) in Equation 6.18 the exit total temperature $T_{t,3}$, which is higher than the total temperature at station A, is adopted through the process from station A to station 3, thus the total temperature is overestimated.

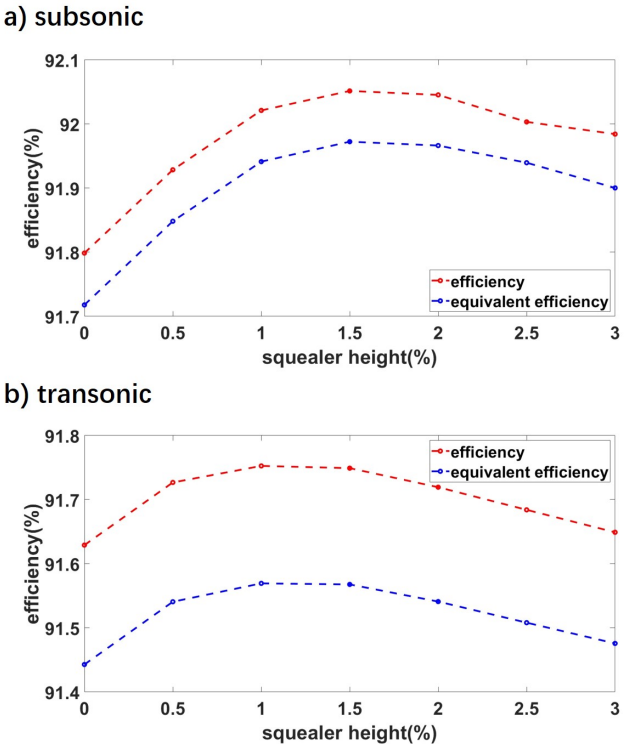


Figure 6.21: The variations of the efficiency and the equivalent efficiency with increasing squealer height for both the subsonic and the transonic stages.

6.2.4.2 Loss Sources in the Turbine Stage

In order to quantitatively study the loss generation in the turbine stage, the total entropy generation is attributed into three sources: the loss generated without the OTL flow, the loss caused by the OTL flow inside of the tip gap region and the loss induced by the OTL flow outside of the tip gap. The loss generated without the OTL flow, $\Delta\dot{S}_{baseline}$, is the baseline loss assuming the rotors have no tip clearance. It includes the majority of the losses in the turbine stage except for those caused by the OTL flow. To calculate the baseline loss, the entropy generation in a turbine stage with zero tip clearance is computed. Since the same stage is used for various squealer height, the baseline loss is assumed to stay the same while the squealer height increases.

The loss generated by the OTL flow inside of the tip gap region, $\Delta\dot{S}_{in-tip}$, is calculated by the entropy flux difference through the tip periphery surface:

$$\Delta\dot{S} = \int_{A_{exit}} s\rho\vec{u}\cdot d\vec{A} - \int_{A_{inlet}} s\rho\vec{u}\cdot d\vec{A} \tag{6.21}$$

where the inlet flow corresponds to those elements on the tip periphery surface with a positive (inward pointing) direction; the exit flow corresponds to those pieces on the tip periphery surface with a negative (outward pointing) direction as illustrated in Figure 6.6.

The loss generated by the OTL flow outside of the tip gap, $\Delta\dot{S}_{out-tip}$, is attributed to the mixing of the OTL flow with the main flow. When the OTL flow leaves the tip gap, the tip leakage vortices are generated and the velocity difference is found between the OTL flow and the passage flow. The mixing of the two streams of the flow induces additional entropy generation. It is computed by subtracting the baseline loss and the in-tip loss from the total loss.

Correspondingly, the total loss generated in the turbine stage consists of three sources, the baseline loss, the in-tip loss and the out-tip loss as shown in Equation 6.22:

$$\Delta\dot{S}_{total} = \Delta\dot{S}_{baseline} + \Delta\dot{S}_{in-tip} + \Delta\dot{S}_{out-tip} \tag{6.22}$$

In Equation 6.22, the entropy flux difference, $\Delta\dot{S}$, instead of the entropy flux rate, Δs, is employed. This is because the entropy generated by the in-tip loss only contributes to part of the main flow, i.e. the OTL flow. Thus the influence of the in-tip loss needs to be weighted by the OTL mass flow rate. The entropy flux difference computed in Equation 6.22 is normalized by

$$\Delta s_{norm} = \frac{\Delta\dot{S}T_{exit}}{\frac{1}{2}u_{exit}^2\dot{m}_{main}} \tag{6.23}$$

where $\dot{m}_{main}$ is the main stream mass flow rate; T_{exit} and u_{exit} are the mass flow averaged temperature and absolute velocity at the rotor exit plane.

The three sources of the loss for the subsonic and the transonic stages are shown in Figure 6.22 where the baseline loss is in blue, the in-tip loss is in red, and the out-tip loss is in yellow. In both the subsonic and the transonic stages, the baseline loss is the major source of loss. In the subsonic stages, the baseline loss takes about 80% of the total loss which means the loss generated by the tip accounts for 20% of the total loss. In the transonic stages, the percentage of the tip induced loss in the total loss is about 15%, which is smaller than the one in the subsonic stage. From the figure, it is noted that majority of the tip induced loss is generated by the out-tip loss.

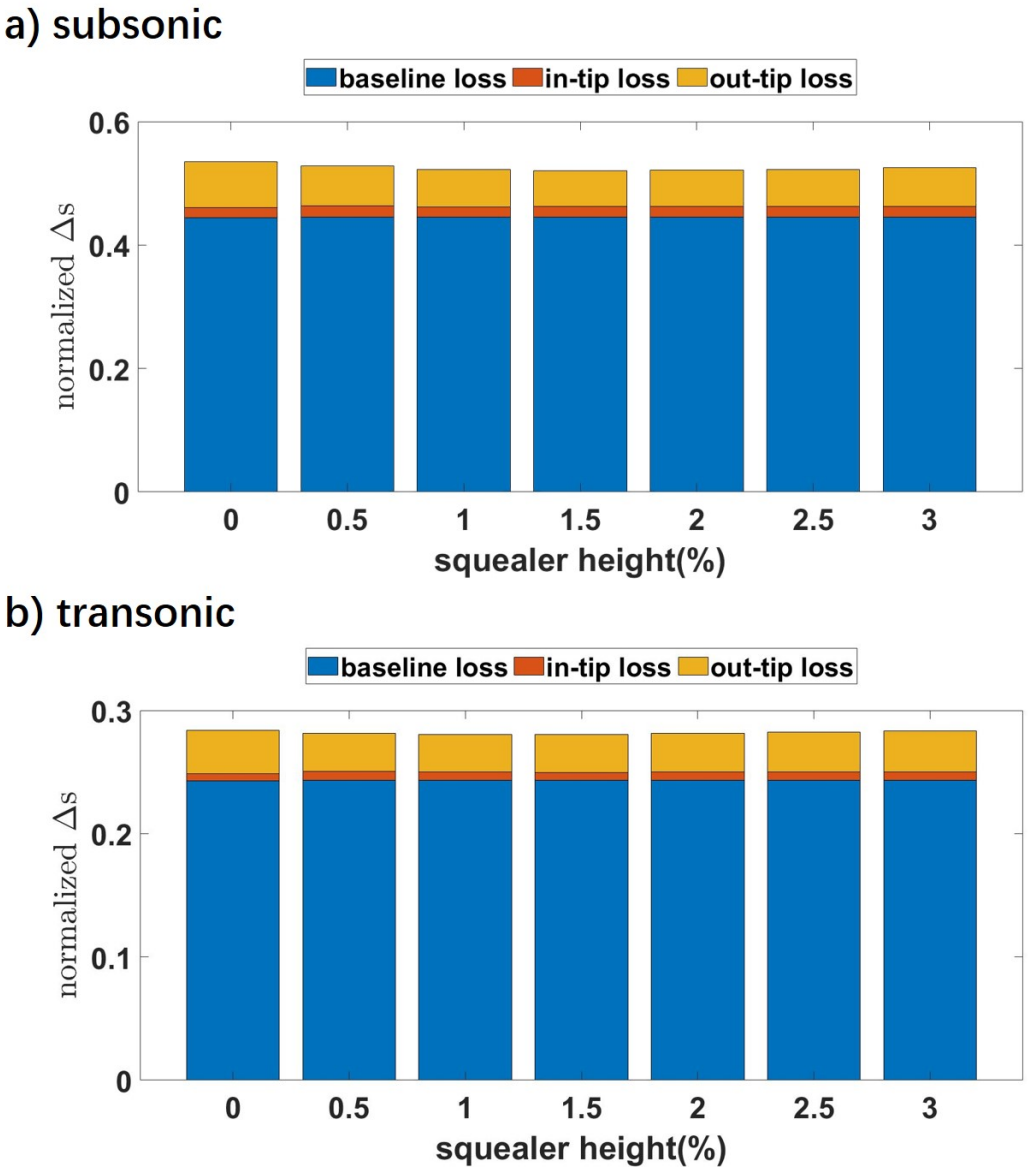


Figure 6.22: Three sources of total loss generated in the turbine stage: the baseline loss, the in-tip loss and the out-tip loss.

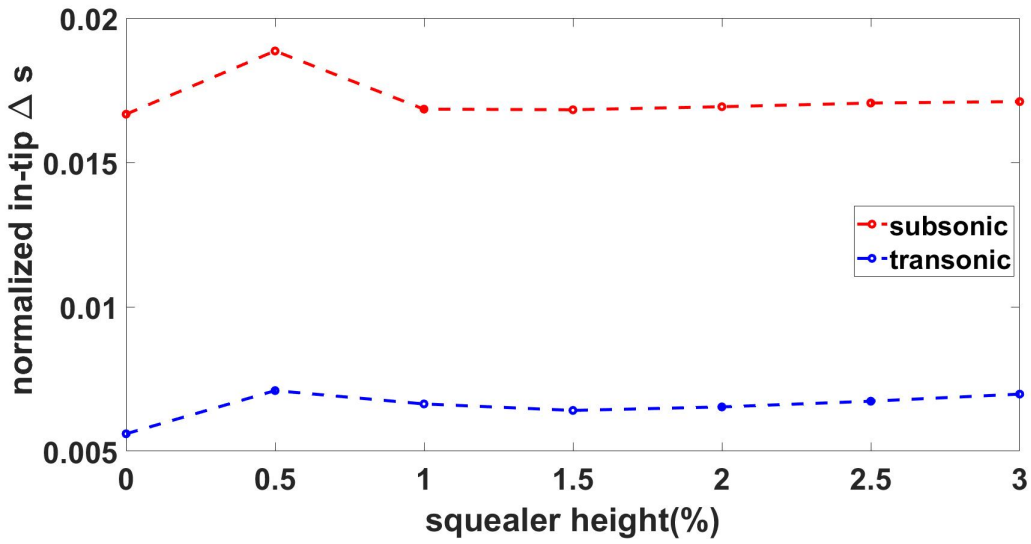


Figure 6.23: Variation of the in-tip loss with increasing squealer height in the subsonic and transonic stage.

The variation of the in-tip loss with the squealer height is exhibited in Figure 6.23. As the squealer height increases from 0% to 1%, the in-tip loss in both the subsonic and the transonic stage first increases and then decreases. As the squealer height further rises to 3%, the in-tip-loss in the subsonic and the transonic stages remains in a relatively constant value. The non-monotonic variation of the in-tip loss is partially attributed to the competing effect between the blockage of the OTL flow and the sudden expansion loss. On the one hand, as the squealer height increases, the blockage caused by the squealer cavity is enhanced. Thus, the OTL mass flow rate is reduced as shown in Figure 6.7. On the other hand, the sudden expansion loss, which is related to the ratio between the tip gap and the squealer height, is increased. These two competing effects work together resulting to the variation of the in-tip-loss as illustrated in Figure 6.23.

6.2.4.3 Out-tip Mixing Loss Model

In Figure 6.22 the out-tip loss is computed by subtracting the baseline loss and the in-tip loss from the total loss. In order to instigate the reason for the variation of the out-tip loss, the tip leakage loss model from Denton [43] is adopted. The loss model is illustrated in Figure 6.24. When the OTL flow, $\vec{u}_{OTL}$, leaves the tip, it mixes with the main flow, $\vec{u}_{main}$, with an injection angle of α as exhibited in plot a). The entropy generated in this process can be calculated by the simplified mixing loss model shown in plot b) where two streams of flow mix into the uniform flow, $\vec{u}_e$. Assuming the mass

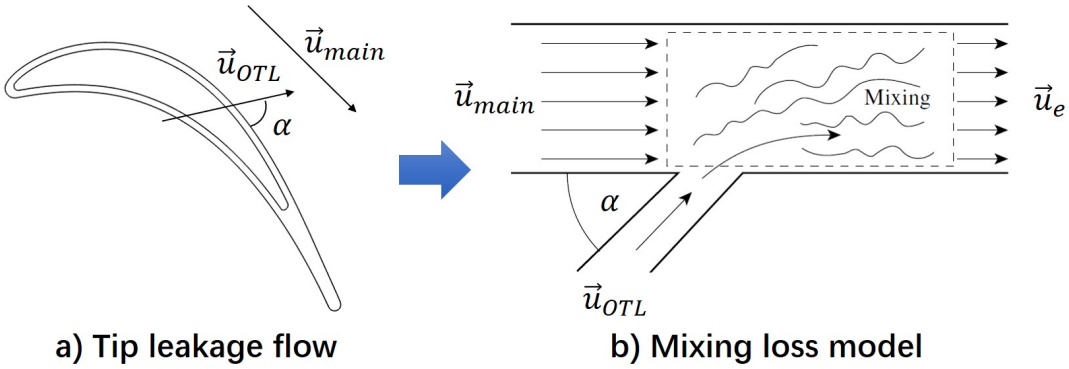


Figure 6.24: Mixing loss model used to compute the out-tip loss. Plot a) is the case in the tip leakage flow. Plot b) is simplified loss model from Greitzer et al.[25].

flow rate of the OTL flow is small compared to the mainstream flow, by combining the mass, momentum, and energy conservation equations with the Gibbs equation across the control volume, the entropy generation at each piece of the tip periphery surface can be computed by

$$\Delta s = C_p \frac{\dot{m}_{OTL}}{\dot{m}_{main}} \left[(1+\frac{\gamma-1}{2} M^2_{main})(\frac{T_{t,OTL}}{T_{t,main}} - 1) + (\gamma-1) M^2_{main} (1 - \frac{u_{OTL}}{u_{main}} \cos\alpha) \right] \quad (6.24)$$

where C_p is the specific heat at constant pressure; γ is the ratio of specific heats; $\dot{m}$ is the mass flow rate; M is the Mach number; T_t is the stagnation temperature; u is the velocity in relative frame of reference; α is the angle between the two streams; $main$ denotes the main flow; OTL denotes the OTL flow that leaves the tip to mix with the main flow.

If we neglect the work done by the relative moving casing, the stagnation temperature of the OTL flow is equal to the stagnation temperature of the main flow. The first term Equation 6.24 becomes zero. Equation 6.24 is simplified to

$$\Delta s = C_p (\gamma - 1) M^2_{main} \frac{\dot{m}_{OTL}}{\dot{m}_{main}} (1 - \frac{u_{OTL}}{u_{main}} \cos\alpha) \quad (6.25)$$

From Equation 6.25, three terms determine the loss: the mainstream Mach number in a relative frame of reference, M_{main}, the ratio of the mass flow rate between the OTL flow and the main flow, $\frac{\dot{m}_{OTL}}{\dot{m}_{main}}$, the normalized velocity difference between the OTL flow and the main flow along the main flow direction, $1 - \frac{u_{OTL}}{u_{main}} \cos\alpha$. Here, the main flow near the tip region is assumed to have the direction tangential to the blade profile. Thus the angle between the two streams, α, is obtained by calculating the angle difference between the OTL flow and the tangential angle of the blade profiles.

The main flow Mach number, M_{main}, and the main flow velocity, u_{main}, is obtained in the baseline case which has no tip clearance. The baseline case represents the flow without the disturbance of the OTL flow.

At each piece of the tip periphery surface, these three terms are computed. Then the loss is calculated by Equation 6.25. To better visualize the variation of these terms along the blade, they are exhibited by the normals perpendicular to the blade profile. Their amplitudes are illustrated by the length of the normals. Since out-tip loss is generated only at the location where the OTL flow leaves the tip, only the pieces with the negative flow direction are used to evaluate the out-tip loss as shown in Figure 6.25. In plot b1), b2), d1) and d2), the mass flow rate and the loss is divided by the ratio between the local area of the tip periphery surface piece, A_i, and the total area of the tip periphery surface, A_{total}, to keep their magnitudes independent on the size of the surface discretization.

In the figure, plot a1) and plot a2) show the main flow Mach number at the tip. Mach number 1 is indicated by the dashed line. In plot a1), the main flow Mach number of the subsonic stage is smaller than one throughout the tip region. In plot a2), the main flow of the transonic stage becomes supersonic at the rear portion of the suction side. The higher main flow Mach number induces more out-tip loss. It also indicates the chance for the flow to be choked.

In plot b1) and plot b2), the normalized OTL mass flow rate per unit area is illustrated. The mass flow rate for the squealer height of 0%, 0.5% and 3% are in black, red and blue, respectively. Comparing to the mass flow rate profiles in the flat tip, the mass flow rate deficits in the case with the squealer height of 0.5% and 3% are attributed to the velocity deficit regions in the location 1 and location 2 shown Figure 6.8 where the two vortices, the CCV and the PSV, leave the squealer cavity.

In plot c1) and c2), the normalized velocity difference between the OTL flow and main flow in the main flow direction is illustrated. It is the last term of Equation 6.25:

$$u_{diff} = 1 - \frac{u_{OTL}}{u_{main}} \cos\alpha \tag{6.26}$$

The normalized velocity difference of value one is shown in the dashed line as a reference. From the mid portion to the rear portion of the blade, the velocity difference first increases then decreases in both the subsonic and the transonic stages except for part of the frontal portion in the transonic stage. At the mid portion, the squealer induces a higher velocity difference. At the rear portion, velocity difference in the

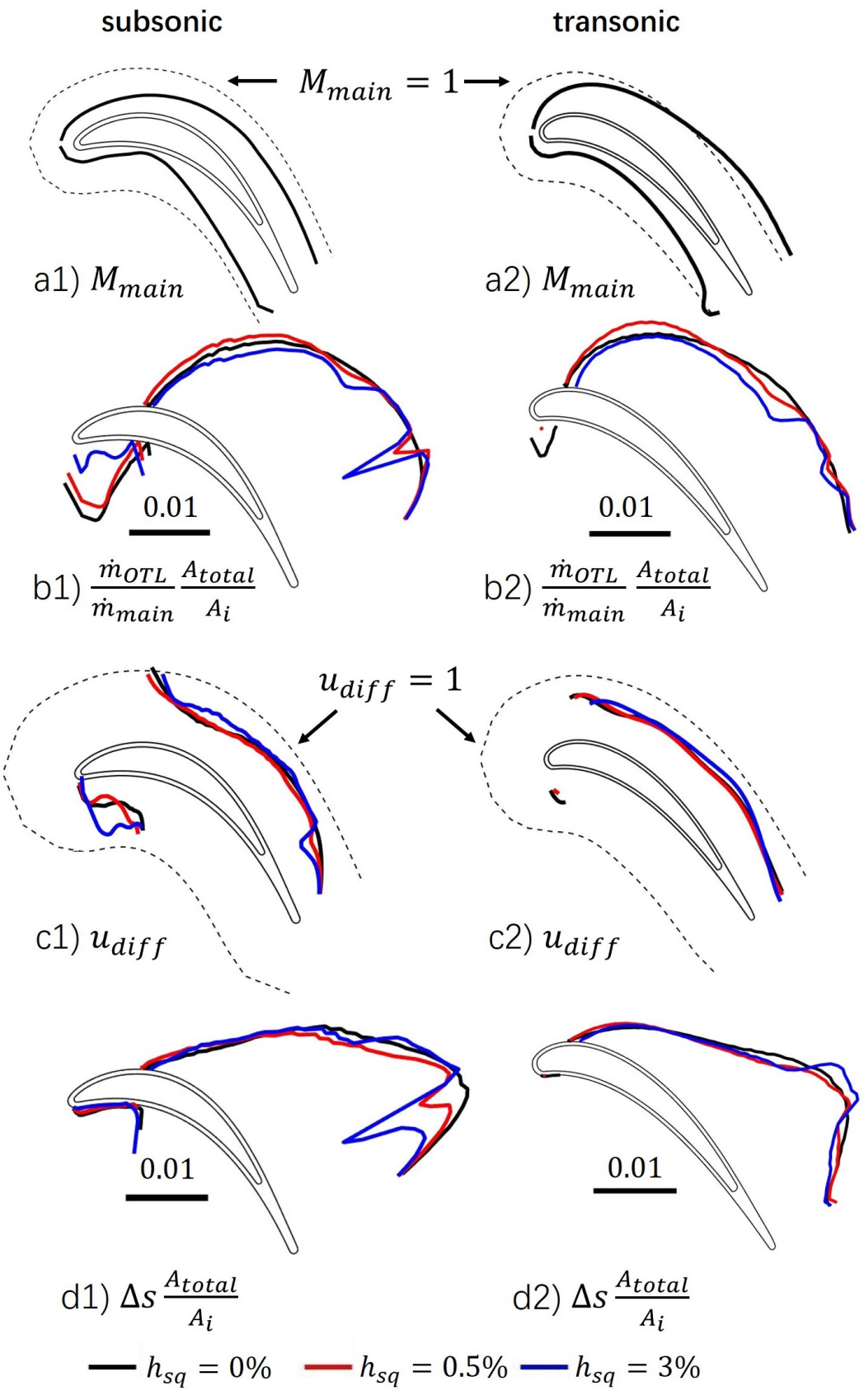


Figure 6.25: Three terms in Equation 6.25 used to compute the out-tip loss.

subsonic stage is reduced by the squealer while no significant variation is induced in the transonic stage.

In Figure 6.26, the two terms used to compute the velocity difference, the velocity ratio, $\frac{u_{OTL}}{u_{main}}$ and the cosine of the flow angle difference, $\cos\alpha$, are exhibited along the blade profile. The value of one is represented by the dashed line as a reference. From the mid to the rear portion of the suction side, the velocity ratio in the subsonic stage is relatively constant except for the rear region while in the transonic stage it slightly increases then deceases. At the mid portion, the cosine of the flow angle difference starts with low value which indicates that the OTL flow crosses the tip almost perpendicular to the blade profile. Downstream of that to the rear portion, the cosine value first decreases and then increases which represents the OTL flow first tends to be vertical to the tip profile and then tends to flow along with the main flow direction.

At the mid portion, the presence of squealer cavity slightly reduces the velocity ratio and the cosine value of the flow angle difference which results from the vortical structures that block the OTL flow and change the OTL flow direction more perpendicular to the direction of the vortex tubes. At the rear portion, because the PSV leaves the squealer cavity, the relative movement of the casing scraps the PSV to be along the tip profile. Therefore, the OTL flow direction is more in line with the tip profile and the cosine value of the flow angle difference increases. These observation are consistent with the mass flux plot shown in Figure 6.8. Comparing to the subsonic stage, the leaving of the PSV induces less change in the velocity ratio and the cosine value of the flow angle difference in the transonic stage.

In plot d1) and plot d2) of Figure 6.25, the normalized out-tip losses per unit area are illustrated. The mixing loss is computed locally by Equation 6.25 and then normalized by Equation 6.15. The loss is divided by the ratio between the local area of the tip periphery surface piece, A_i, and the total area of the tip periphery surface, A_{total}. It is noted that due to the high main flow Mach number and large OTL mass flow rate, the majority of the out-tip loss is generated at the rear portion of the blade.

The total out-tip loss is computed by the sum of the out-tip loss on each tip periphery surface piece. The loss calculated by the loss model can be compared with the one in section 6.2.4.2 where the out-tip loss is calculated by subtracting the baseline loss and the in-tip loss from the total loss. The comparison of the losses in both the subsonic and the transonic stages are shown in Figure 6.27. The losses evaluated in Section

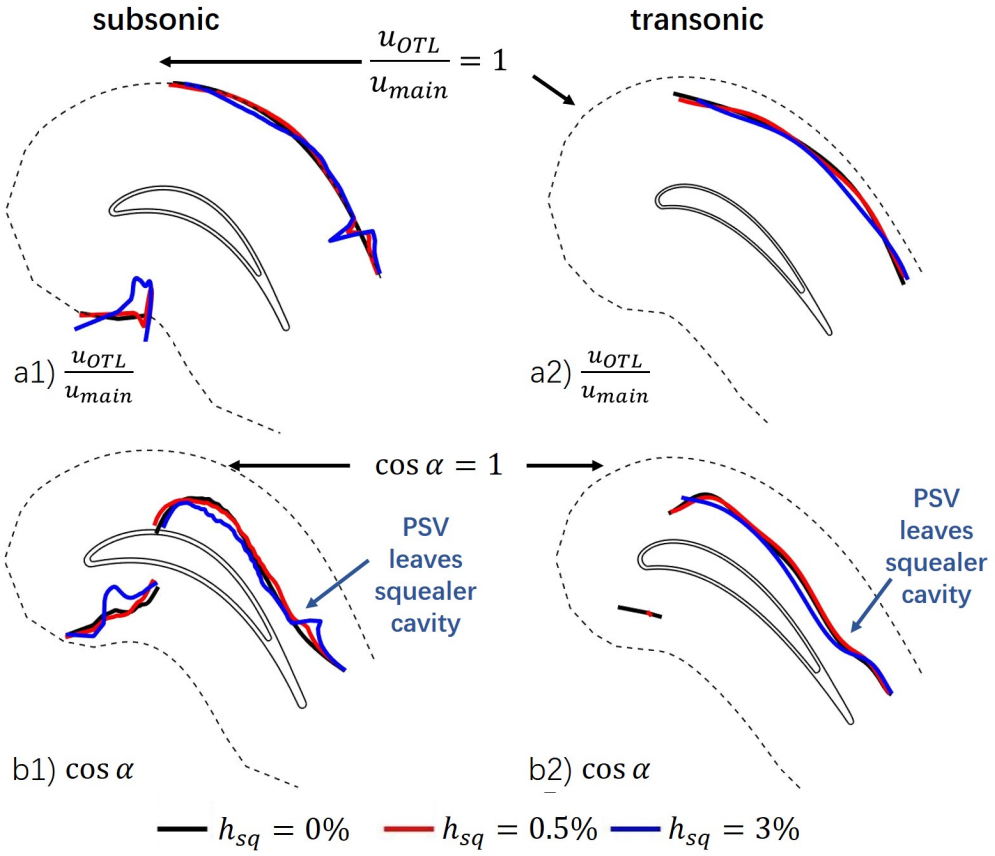


Figure 6.26: Two terms in Equation 6.26 are used to compute the velocity difference between the main flow and the OTL flow in the main flow direction.

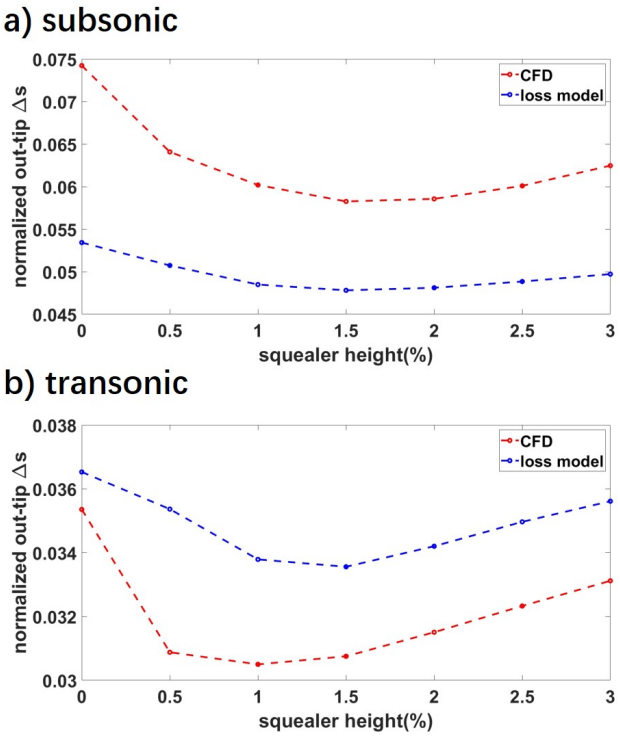


Figure 6.27: Comparison of the out-tip loss computed by the CFD results shown in section 6.2.4.2 and by the loss model.

6.2.4.2 are in blue and the losses computed by the loss model are in red. In both the subsonic and transonic stages, the loss model is able to catch the general trend of the loss. The comparison between the CFD results and the loss model validates Denton's tip leakage loss model and explains the specific variation of the loss.

6.2.4.4 Choking in the Transonic Stage

In Figure 6.7 as the squealer height increases, the OTL mass flow rate in the transonic turbine has a lower variation comparing to the one in the subsonic stage. It can be partially attributed the choking of the OTL flow at the rear portion of the blade. The relative influence of the choking comparing to other factors is not covered in this study. In the transonic stage, close to the rear portion of suction side, the flow becomes supersonic, while in the subsonic stage the flow remains subsonic except for a small portion of the rear region as shown in Figure 6.28. The supersonic flow leads to the choking of the OTL flow so that the choking mass flow rate is solely determined by the upstream flow capacity as shown in Equation 6.27.

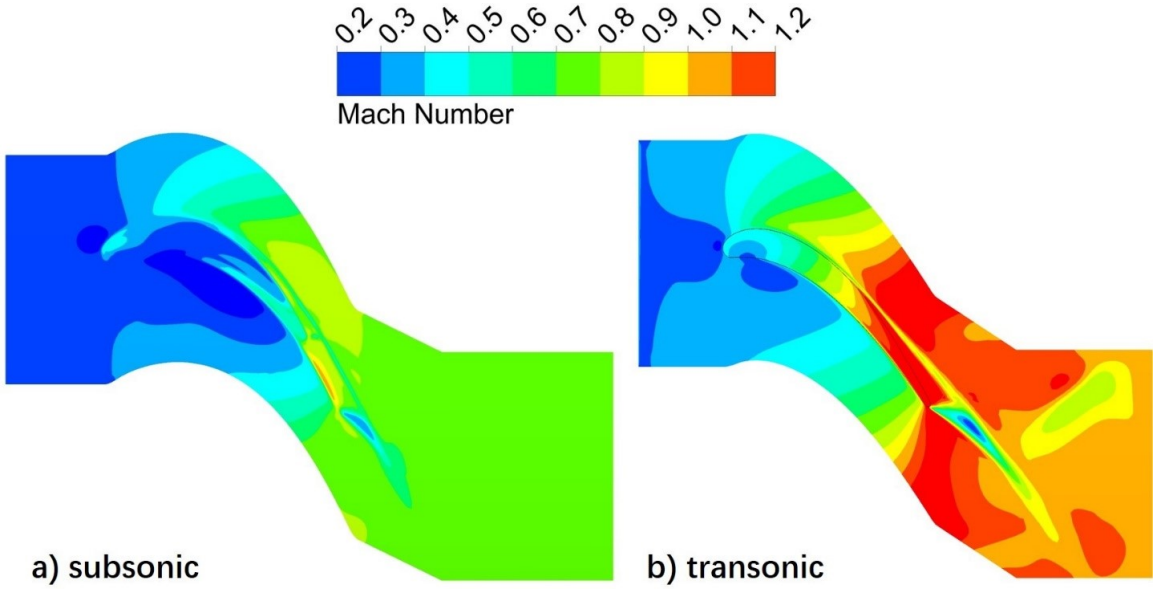


Figure 6.28: Mach number contour at the tip region in the subsonic and the transonic stages with flat tip. The contour located in the middle of the casing and the tip.

$$\dot{m} = C_d A \frac{P_t}{T_t} \sqrt{\frac{\gamma}{R}} \left(\frac{\gamma+1}{2}\right)^{\frac{\gamma+1}{2(\gamma-1)}} \tag{6.27}$$

where C_d is the discharge coefficient; P_t and T_t are the stagnation pressure and stagnation temperature on the pressure side of the tip; A is the flow area.

6.2.4.5 Influence of Squealer Height on Heat Transfer Performance

The heat transfer performance in this study is evaluated by the normalized heat load computed in Equation 6.5 computed in the case with the isothermal wall boundary condition. As the squealer height increases from 0% to 3%, the normalized heat load in the subsonic and the transonic stages rises nearly linearly as shown in Figure 6.29 where the black dots represent the heat load computed in the CFD simulation; the dash lines indicate the results predicted by the metamodel. The slope of increment in the transonic stage is higher than the one in the subsonic stage. The total heat load on the tip is the sum of the heat load on three surfaces: the squealer rim, the cavity floor and the cavity wall. The break-down of the total heat load is shown in Figure 6.30 where the x axis is the squealer height and the y axis is the ratio between the heat load on the specified surfaces and the heat load on the flat tip as computed in Equation 6.28. It is noted that the total heat load is mainly driven by the surface area increment of the tip rim.

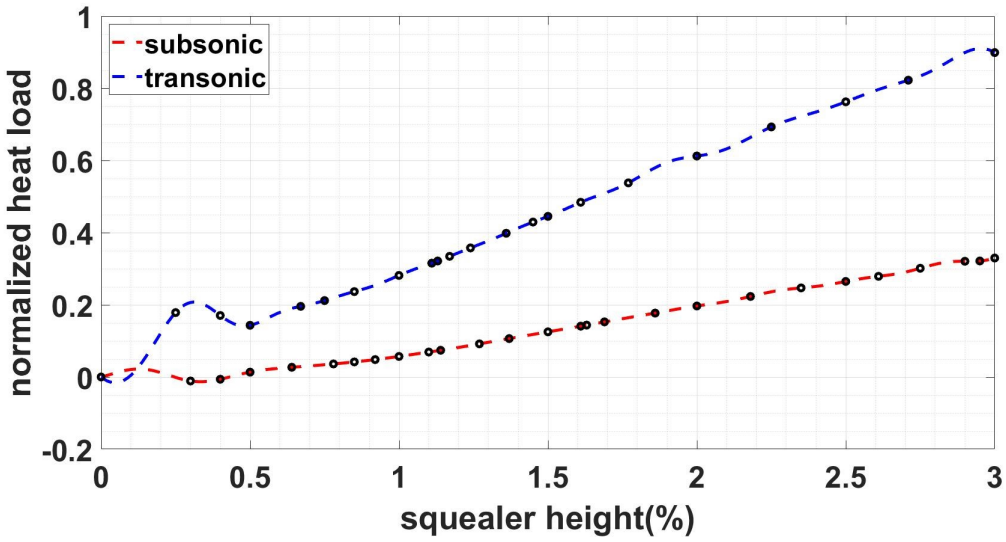


Figure 6.29: Variation of the normalized heat load with squealer height in the subsonic and transonic stages.

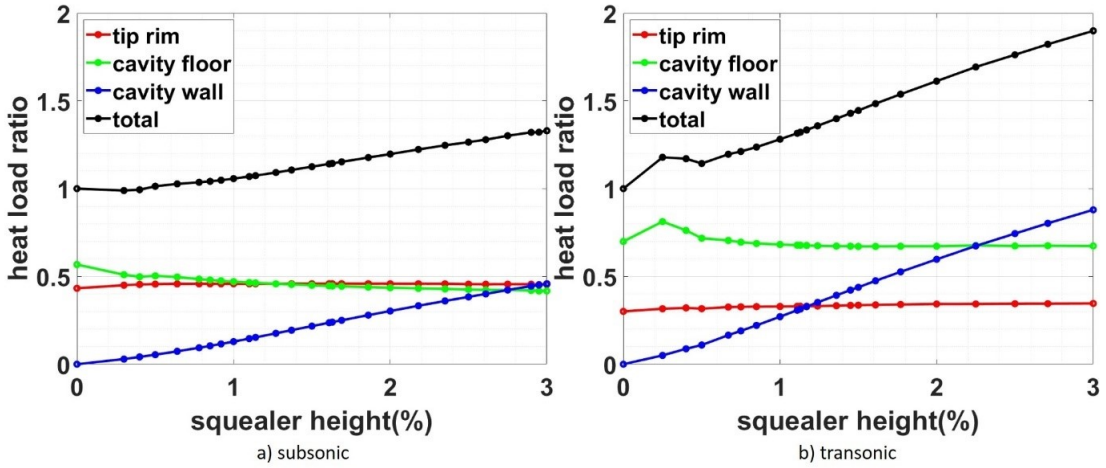


Figure 6.30: Variation of the heat load ratio on the tip rim, cavity floor and cavity wall with squealer height in the subsonic and transonic stages.

$$HLR = \frac{\int_{tip} qdA}{\int_{flattip} qdA} = \frac{\int_{squealerrim} qdA}{\int_{flattip} qdA} + \frac{\int_{cavityfloor} qdA}{\int_{flattip} qdA} + \frac{\int_{cavitywall} qdA}{\int_{flattip} qdA} \quad (6.28)$$

From Equation 6.5 and Equation 6.28, the difference between $HL_{normalized}$ and HLR is 1. The reason to use HLR instead of $HL_{normalized}$ in Figure 6.30 is to prevent the value of the heat load to be negative. From the figure, the variations of the heat load on the tip rim and the cavity floor are marginal comparing with the variation of the heat load on the cavity wall. Thus, in both the subsonic and the transonic stages, the linear variation of the total heat load is mainly due to the heat load on the cavity wall. The heat load ratio on the cavity wall is computed by equation 6.29:

$$HLR_{cavitywall} = \frac{\int_{cavitywall} qdA}{\int_{flattip} qdA} = \frac{h_{sq}}{h_{span}} \frac{h_{span} \int_{cavitywall} qdL}{\int_{flattip} qdA} \quad (6.29)$$

where q is the heat flux; A is the area of the specified surface; L is the periphery length of the squealer cavity and h_{sq} is the squealer height. From Equation 6.29, the linear variation of the heat load ratio on the cavity wall with the squealer height is mainly due to the linear term of h_{sq}/h_{span}. Thus, on the cavity wall the area instead of the heat flux distribution is the major cause to the variation of the heat load. The slopes of the curves in Figure 6.30 are determined by the term of $h_{span} \int_{cavitywall} qdL / \int_{flattip} qdA$. The heat flux contours on the cavity wall with various squealer height in the subsonic and the transonic stages are illustrated in Figure 6.31. It is noted that the heat flux increment with the squealer height in the transonic stage is higher than the one in the subsonic stage. This is attributed to the higher Mach number of the OTL flow in the transonic stage which induces stronger impingement on suction side of the cavity wall.

Because the areas of the tip rim and the cavity floor remain constant as the squealer height increases, the variations of the heat load on these two surfaces are due to the change of the heat flux distribution. The heat flux contours on these two surfaces with various squealer height in the subsonic and the transonic stages are shown in Figure 6.32. From the figure, the subsonic stage has much higher heat flux compare to the one in the transonic stage.

On the tip, a distinctive high heat flux strip at the rear portion of the subsonic blade is observed while in the transonic blade the high heat flux strip is at the mid-chord and the heat flux magnitude is lower. The high heat flux strip is caused by the flow

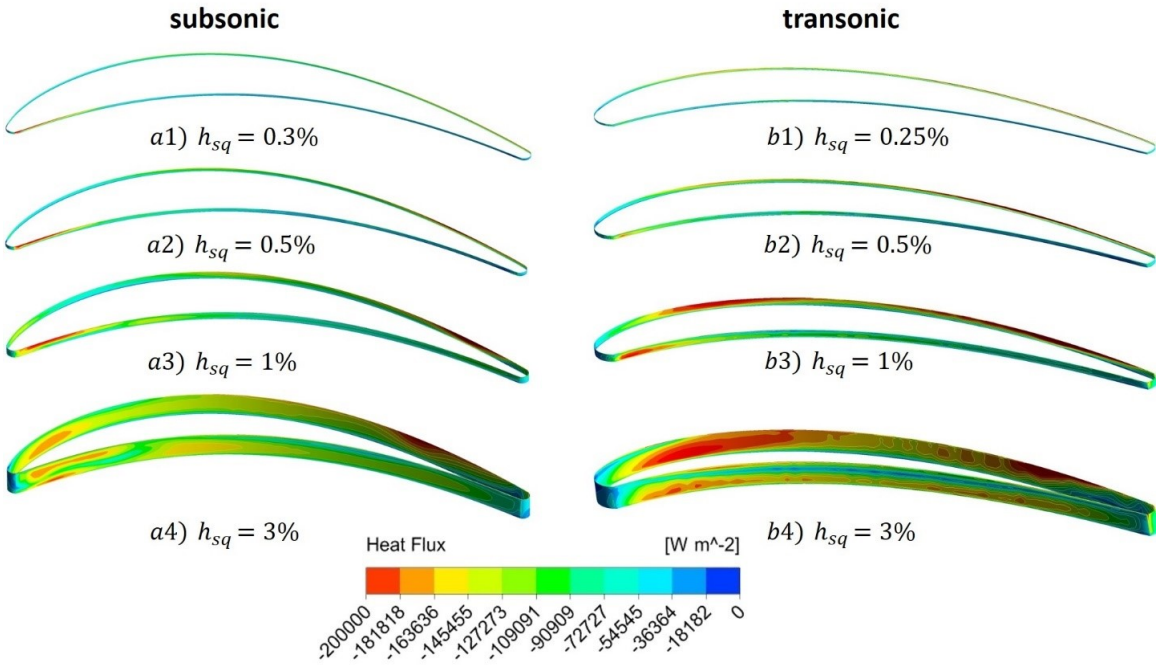


Figure 6.31: Heat flux contours on the cavity wall with various squealer height in the subsonic and the transonic stages.

separation and reattachment induced by the vortical structure discussed previously. In the midfield between the CCV and the PSV, the OTL is entrained by the two counter-rotating vortices.

The different magnitude of the heat flux in the subsonic and the transonic stage is explained in Section 2.2.2. It is due to the convergent-divergent nozzle generated by the separation bubble on the pressure side edge. In the subsonic stage, the OTL flow is mainly subsonic. Therefore, downstream of the vena-contracta of the convergent-divergent nozzle, the flow is decelerated which induces an adverse pressure gradient and increases the turbulent mixing. In the transonic stage, because of the supersonic nature of the flow, the OTL through the vena-contracta of the convergent-divergent nozzle is accelerated. Thus an accelerating pressure gradient is formed so that the separation bubble is shorten.

Figure 6.33 shows the turbulent viscosity ratio contour on the $A - A$ cutting planes. The turbulent viscosity ratio is computed by the ratio between the turbulent viscosity and the laminar viscosity. It is noted that the turbulent viscosity ratio in the transonic stage is lower than the one in the subsonic stage. The turbulence is damped by the flow acceleration (as opposed to the deceleration in the subsonic case). The decrease of the turbulent dissipation also reduces the heat transfer flux in the transonic tip.

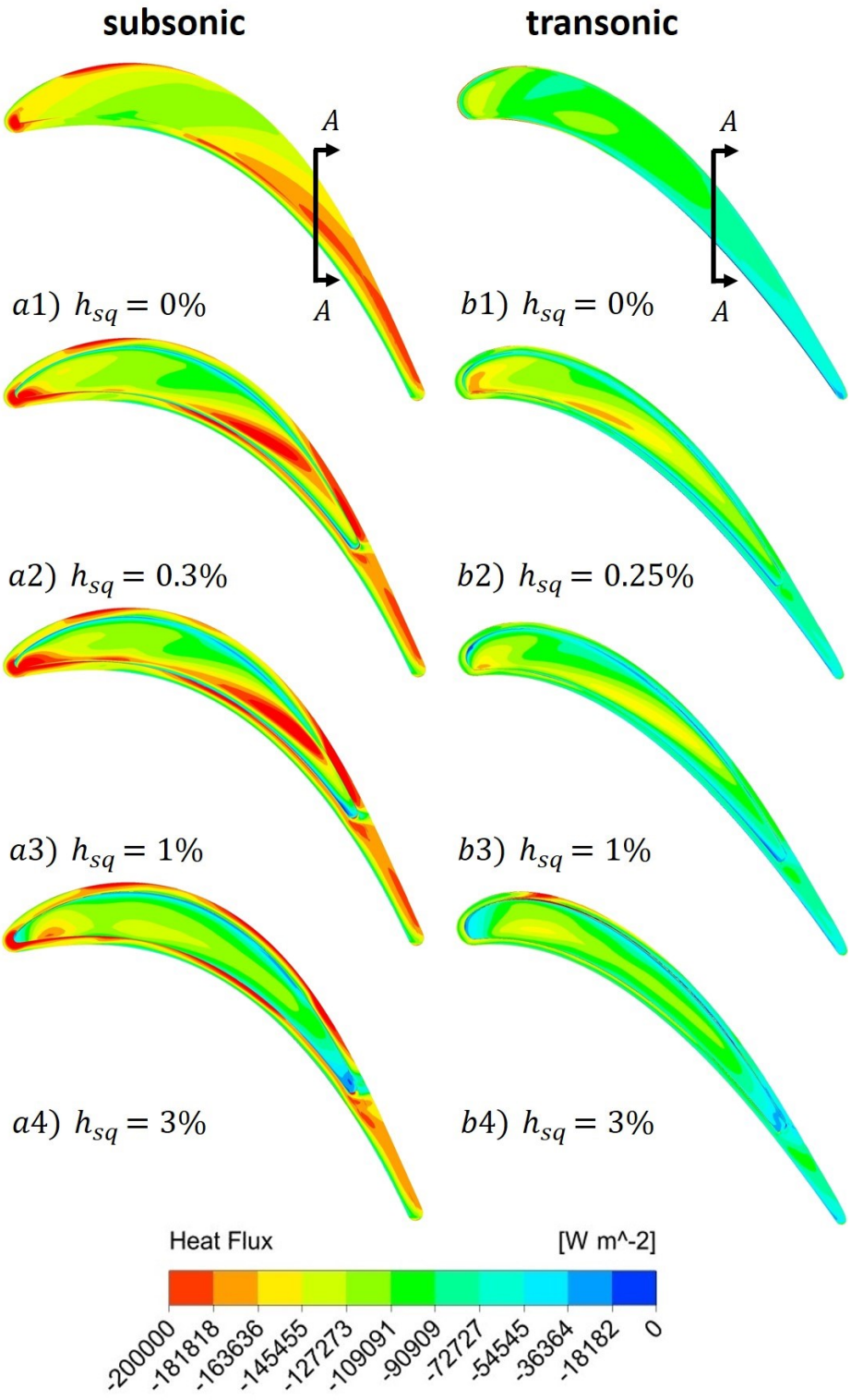


Figure 6.32: Heat flux contours on the tip with various squealer height in the subsonic and the transonic stages.

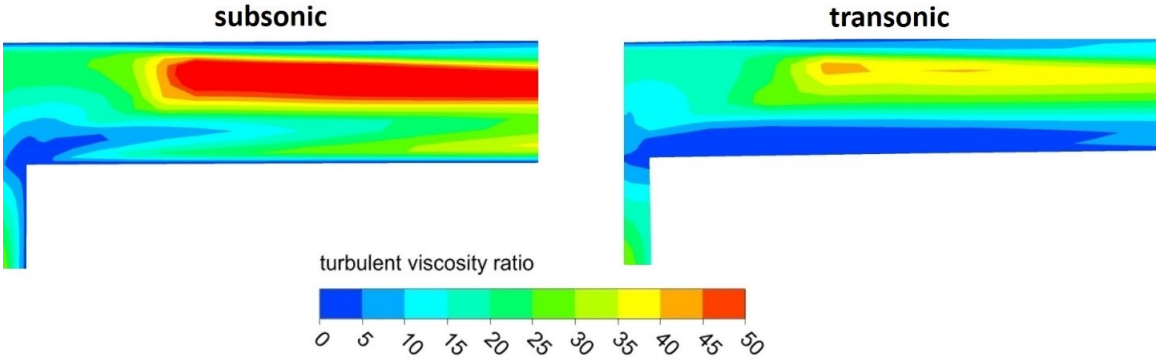


Figure 6.33: Turbulent viscosity ratio plot on the pressure side edge of the flat tip in the subsonic and transonic stages.

6.3 Summary

In this chapter, the aerodynamic performance of the uncooled turbine blades in investigated in details. First, the variation of the efficiency with the squealer height in the transonic cascade is evaluated. The non-monotonic variation of the efficiency is due to two competing effects: the blockage of the OTL flow and the sudden expansion loss caused by the squealer. Then the turbine stages working in the subsonic and the transonic region are analyzed. In the tip gap, by adding squealer, two counter-rotating vortices are generated. They bring blockage of the OTL flow and induce a velocity deficit when leaving the tip. In order to quantitatively assess the aerodynamic performance of the stage, the entropy generation is used to calculate the loss. The loss in the turbine stage is attributed into three sources: the baseline loss, the in-tip loss and the out-tip loss. Denton's tip leakage loss model is implemented to evaluate the out-tip loss. The model is shown to well predict the general trend of the loss. In the subsonic turbine stage, the squealer is found to increase the efficiency up to 0.25%. In contrast, the transonic stage shows only around half the efficiency improvement (up to 0.12%) at the optimal squealer height. Finally, the flow analysis on the heat transfer performance of the tip is discussed to explain the variation of the heat flux with the squealer height. Due to different loading, reaction and velocity triangles of the two stages, different performances cannot be completely attributed to the Mach number.

Chapter 7

Cooled Turbine Blade Analysis

Following the flow analysis of the uncooled blade in Chapter 6, the cooling holes are added on the turbine blade tip in this chapter. We will focus on the sequence of optimization in the turbine design. In the previous design in the open literature, the turbine blade is typically designed sequentially: first, the uncooled blade is optimized by blade shaping, then the cooling holes are added on the optimized blade to search for the optimal cooling configuration. The sequential optimization works well when the cooling flow is additive to the uncooled base flow. However, the coolant is found to have interactions with the base flow in the transonic turbine blade. The design objective that the coolant passively forms a thin, cool, insulating blanket along the external surface of the blade is no longer valid. Thus in this chapter, we will investigate the influence of the non-linearity nature of the transonic turbine flow towards the blade optimization sequence. To investigate the performance improvement that the concurrent optimization may bring, we will first follow the general method used in the open literature to optimize the tip sequentially. Then we will compare it with the design obtained by combining the shaping and the flow injection.

In order to reduce the difficulties in the optimization, simplified shaping and flow control are used: in terms of the shaping only the squealer height is optimized; in terms of the flow control the sole variable is the distribution of the cooling holes. The geometry (area and angles) and the number of the cooling holes are the same during the optimization so that the variation of the overall mass flow rate is relatively small ($<0.02\%$ of the main flow). Two levels of turbine models working in the transonic region are employed to run the optimization: the turbine cascade and the turbine stage. The blade geometry, the boundary condition and the numerical set-ups are all kept the same as those in Chapter 6. The blade mesh is adapted in order to

accommodate the cooling holes. The details of the adaption are elaborated in Section 5.3.2. The tip region is split into small blocks so that $m \times n$ cooling slots are generated at the tip where m is the number of rows of the cooling slots, and n is the number of column of the cooling slots. In the optimizer using genetic algorithm, the cooling configurations are coded by a binary string which uses '1' or '0' to represent whether or not the cooling holes are inserted into the cooling slots. Similar to the blade wall boundary condition, the wall of the cooling holes are adiabatic.

7.1 Aerothermal Optimization (cascade)

In this section, the squealer height and tip cooling hole position of the turbine cascade is optimized. The aerothermal performance of the cascade obtained by the sequential optimization and by the concurrent optimization is compared. The design variables of the optimization in the turbine cascade are the aerodynamic efficiency, η, computed by Equation 3.13, the cooling effectiveness, eff, calculated in Equation 3.20 and the wall temperature variance, T_{var}, evaluated in Equation 3.25.

7.1.1 Cascade Optimization Conducted Sequentially

Following the sequential optimization procedure, firstly, the shape of the cascade needs to be optimized. Because the only design variable in the shaping is the squealer height and the design space of the squealer height from 0% to 2% is already gone through, the optimized shape of the cascade can be obtained directly from the results in section 6.1. For the tip clearance of 0.5% of the span, the optimal squealer height is 1%. For the tip clearance of 1% of the span, the squealer height of 2% has the best aerodynamic performance. In this section, only the cascade with tip clearance of 0.5% is implemented in further optimization. Therefore, of these designs, the optimal design is the case with squealer height of 1%.

Then the cooling holes are added on the optimized uncooled cascade. During the optimization, the coolant mass flow rate is controlled by fixing the number of cooling holes to 10. Therefore the coolant mass flow rate is between 0.45% and 0.53% of the mainstream mass flow rate. The variation (18%) of the coolant mass flow rate might have an effect on the results which is beyond the scope of this research.

As an initial Design of Experiments (DOE), 30 cases with different cooling configurations are created. Subsequently, three iterations were run to explore the potential performance gain. In each iteration, ten new cooling configurations are generated.

The optimization is stopped when the last two iterations do not bring additional performance improvement.

The results of the sequentially optimization are shown in Figure 7.1 where the three objectives, the efficiency, the cooling effectiveness and the temperature variance are shown in x axis, y axis and the colour contour respectively. Each dot in the figure represents one simulation. The uncooled cases are also marked at the bottom of the figure because the cooling effectiveness is 0 in these cases. As a reference point, the case with squealer height (2% span) and cooling configuration similar to the one used in Ma's [31] work is also simulated to illustrate the relative performance gain of the optimization. Relative to the reference case, the optimized efficiency can be increased by 0.7%.

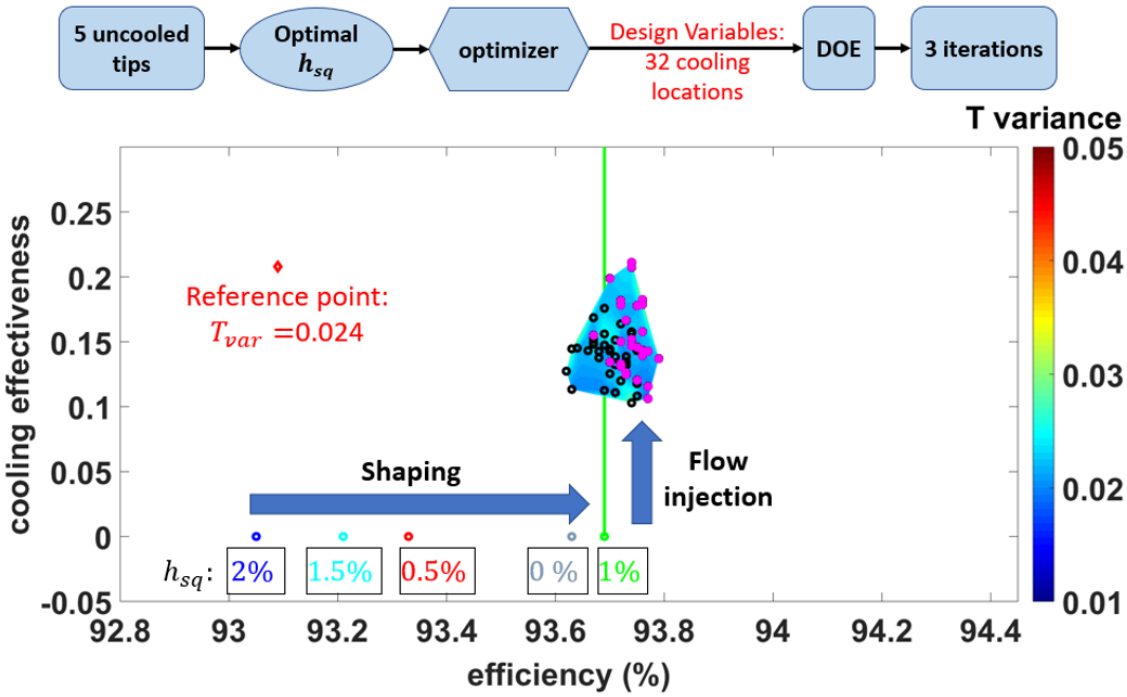


Figure 7.1: Tip optimization (cascade) conducted in a sequential manner. h_{sq} is the squealer height.

From the figure, the efficiency may increase or decrease by adding the cooling. The properly arranged cooling holes can improve the flow structure so that the efficiency of the cooled case can be increased by up to 0.1%. Since there are three objectives in this optimization, the Pareto front is a 3D surface. This 3D surface is projected into the 2D plot to indicated the Pareto front by the pink dots.

7.1.2 Cascade Optimization Conducted Concurrently

In the previous section, the tip is optimized sequentially. The idea of this optimization is to assume that the cooling flow is additive to the mainstream. By adding the cooling, the best performed uncooled blade can become the best performance cooled blade. However, in the turbine tip the interactions between the coolant and the OTL flow bring a high non-linearity to the system. These interaction effects are hard to account for in sequential design (without lots of iterations as shown in Figure 1.3). Therefore in this study, we will explore what may be missed by the sequential optimization.

Within the optimizer, the combination of squealer height and flow injection is obtained by adding two more bits to the chromosome representing the cooling configurations. Gray coding is implemented to ensure two successive values differ in only one bit. As an initial Design of Experiments (DOE), 30 cases with different squealer heights and cooling configurations are created. Then 12 iterations were run before the optimizer gets converged. In each iteration, ten new cooling configurations are generated.

The results are shown in Figure 7.2. The performance contour obtained from the optimization is split into four segments based on the squealer height. In the figure, each segment forms an isolated contour island indicating the performance range that each blade can reach. Comparing Figure 7.2 with Figure 7.1, more design space is explored so that the optimizer can evaluate some design features unachievable by the sequential optimization. The most prominent gain is the efficiency obtained from the flat tip where 0.8% efficiency improvement is brought by the concurrent optimization. The heat transfer performance is also improved. In the sequential optimization, the optimizer is trapped in the design with a relatively low cooling effectiveness and a high-temperature variance. It can be improved by adding cooling on the tip with a different squealer height. Compared to the case with the highest cooling effectiveness obtained by the sequential optimization, the combined optimization can improve the cooling effectiveness by up to 19% and the temperature variance by up to 30%.

In Figure 7.2, the performances of the uncooled blades with a squealer height of 0%, 0.5%, 1%, 1.5% and 2% are marked by the dots in grey, red, green, cyan and blue respectively. The cooling effectiveness in these cases is zero. The coloured arrows link the uncooled blade to the cooled one with the same squealer height. It is noted that for the blades with the squealer height of 0.5% and 1.5%, the efficiency decreases by adding the cooling holes. For the blade with squealer height of 1%, some of the

cooled blades have higher efficiency while the other blades have lower efficiency. The interesting results come from the blade with a squealer height of 0% and 2%: the efficiencies of all the cases are increased by adding the cooling holes. It contradicts the expectation that the cooling holes always bring additional loss.

Moreover, by adding the cooling holes the rank (based on efficiency) of the cooled blade has changed. The flat tip has the second efficiency among the uncooled blades. However, among the cooled blades has the highest rank in efficiency. The blade with the squealer height of 2% has the lowest efficiency among the uncooled blades; by adding the cooling holes its efficiency is not the last any more. It indicates the cooling holes are not additive to the uncooled geometry at the tip region. An 'optimized' uncooled squealer height may not provide a most suitable base configuration for cooling design and optimization.

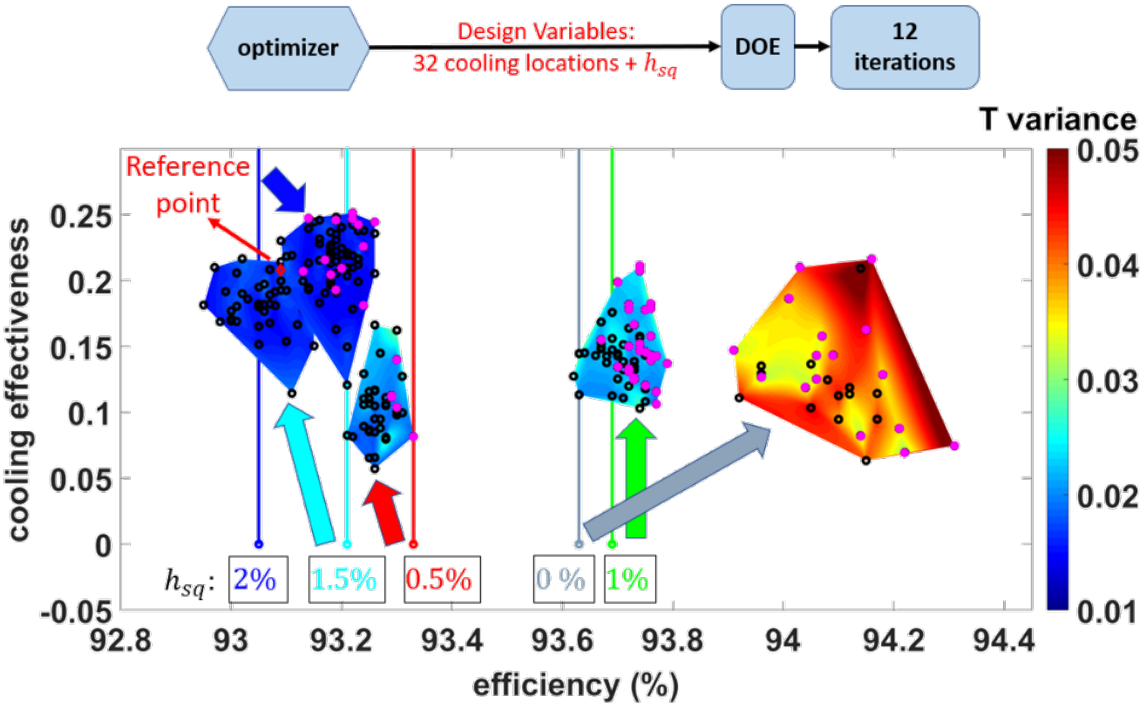


Figure 7.2: Tip optimization (cascade) combining squealer height and flow injection. h_{sq} is the squealer height.

7.1.3 Impact of Flow Injection on Efficiency

The change in the efficiency caused by the cooling configurations can be explained by the dual function of the cooling flow. On the one hand, the injection at the tip brings a blockage to the OTL flow. On the other hand, the mixing of the coolant with the

main flow generates an additional loss. The well-designed cooling configuration can keep the blockage effect while mitigating the mixing loss.

From figure 7.2, the cooling injection in the flat tip is found to increase the efficiency of the turbine cascade. The influence of the injection is illustrated in Figure 7.3, where the local mass flux vectors of the OTL flow along the tip periphery surface are plotted for the squealer height of 0% and 1% without and with cooling. The tip periphery surface is a surface that crosses the tip clearance along the tip rim. The mass flux vector at ith piece in the tip periphery surface is computed by

$$\vec{F_i} = (\frac{1}{A_i}\int_{A_i} \rho u dA, \frac{1}{A_i}\int_{A_i} \rho v dA) \tag{7.1}$$

where A_i is the area of the ith piece in the tip periphery surface, ρ, u_{rel} and v_{rel} are the mass flow averaged density, relative axial velocity and relative circumferential velocity at the ith piece in the tip periphery surface.

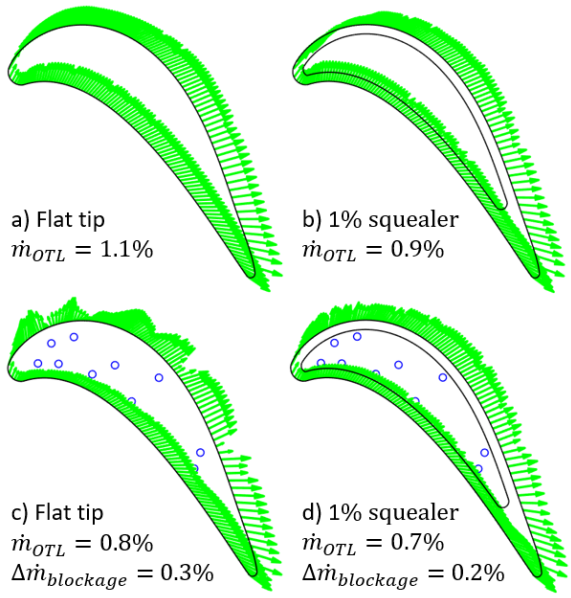


Figure 7.3: The local mass flux vectors along the tip rim for the flat tip and the squealer tip without and with cooling injection.

For the uncooled blades, by comparing plot a) with plot b) in Figure 7.3, the tip with the squealer height of 1% is shown to have a lower OTL mass flow rate due to the blockage effect brought by the squealer cavity. This is the main reason for the higher aerodynamic efficiency in the uncooled squealer tip relative to the flat tip. However, by adding cooling holes on the flat tip, several locations with significant velocity deficit

are observed in plot c). These locations indicate the blockage induced by the injection of the cooling flow. A similar blockage effect still exists on the cooled squealer tip in plot d) but with relatively minor intensity. The injected coolant through the squealer cavity has lost part of its momentum so that the blockage effect towards the OTL flow is mitigated.

From the quantitative analysis, the OTL mass flow rate on the flat tip is reduced by 0.3% due to the coolant injection. The same blockage effect in the tip with the squealer height of 1% can only lead to the reduction of the OTL mass flow rate of 0.2%. Here the OTL mass flow rate is calculated from the tip periphery surface on the pressure side so that the cooling mass flow rate is not included. By including the mass flow rate of the coolant, the total mass flow rate at the suction side in the cooled case will be larger than the one in the uncooled case. The lower loss in the cooled case may be attributed to the redistribution of the OTL mass flow rate to the main flow which will be investigated in the future research.

The impact of the cooling configuration on the efficiency can be illustrated by comparing the case with the highest efficiency and the case with the lowest efficiency when the squealer height is 1% of the span. This is shown in Figure 7.4. In the case with the highest efficiency, the cooling holes are at the frontal portion of the squealer. While in the lowest-efficiency designs, the majority of the cooling holes locates at the rear portion of the squealer. It can be attributed to the location of the mixing because at the frontal portion of the blade, the mainstream Mach number is relatively low. From Denton's model, the mixing loss is proportional to the square of the mainstream Mach number as shown in Equation 6.25. Thus, the low Mach number at the frontal portion of the blade induces the lower loss.

7.1.4 Impact of Squealer Height on Heat Transfer

Figure 7.2 shows that both the cooling effectiveness and the temperature variance are improved as the tip squealer height increases. This is in line with the previous finding by Mhetras [90]. The reason can be illustrated in plot a), plot b), plot c) and plot d) of Figure 7.5 where four blades with different squealer heights have the same cooling configuration. As the squealer height is low ($h_{sq} = 0.5\%$), the coolant has interactions with the OTL flow. As indicated in the previous research [31] [75], the counter-rotating vortex pairs are formed downstream of the cooling holes. One leg of the counter-rotating vortex pair entrains the hot OTL flow to the cavity floor, and the other leg elevates the coolant off the floor. These vortex pairs generate a series

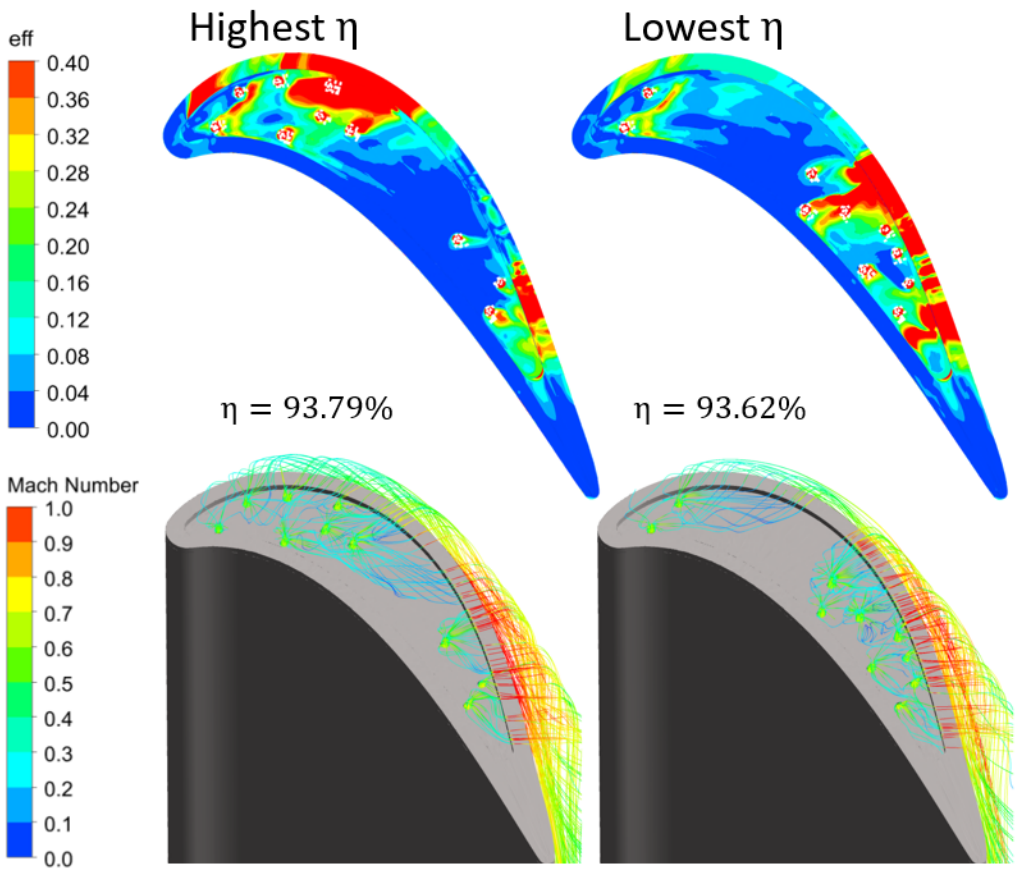


Figure 7.4: Comparison of cases with the highest and lowest efficiency when the squealer height is 1% of the span.

of high cooling effectiveness strips (red) downstream of the cooling holes, as shown in Figure 7.5 a). The counter-rotating vortex pairs energize the coolant and direct it straight to leave the cavity. Therefore, the locations uncovered by the route of the counter-rotating vortex pairs remain uncooled. As the squealer height increases, the coolant is trapped in the cavity as shown by the streamline plots. The cooling flow covers a larger area and has longer residence time in the cavity to cool the tip. Thus both cooling effectiveness and the temperature variance can be improved.

7.2 Aerothermal Optimization (Turbine Stage)

From the previous section, the concurrent optimization is found to bring better aerothermal performance in the transonic turbine cascade comparing to the sequential optimization. The question now is if it is the same case in the turbine stage. To answer this question, the transonic turbine stage design obtained by the sequential

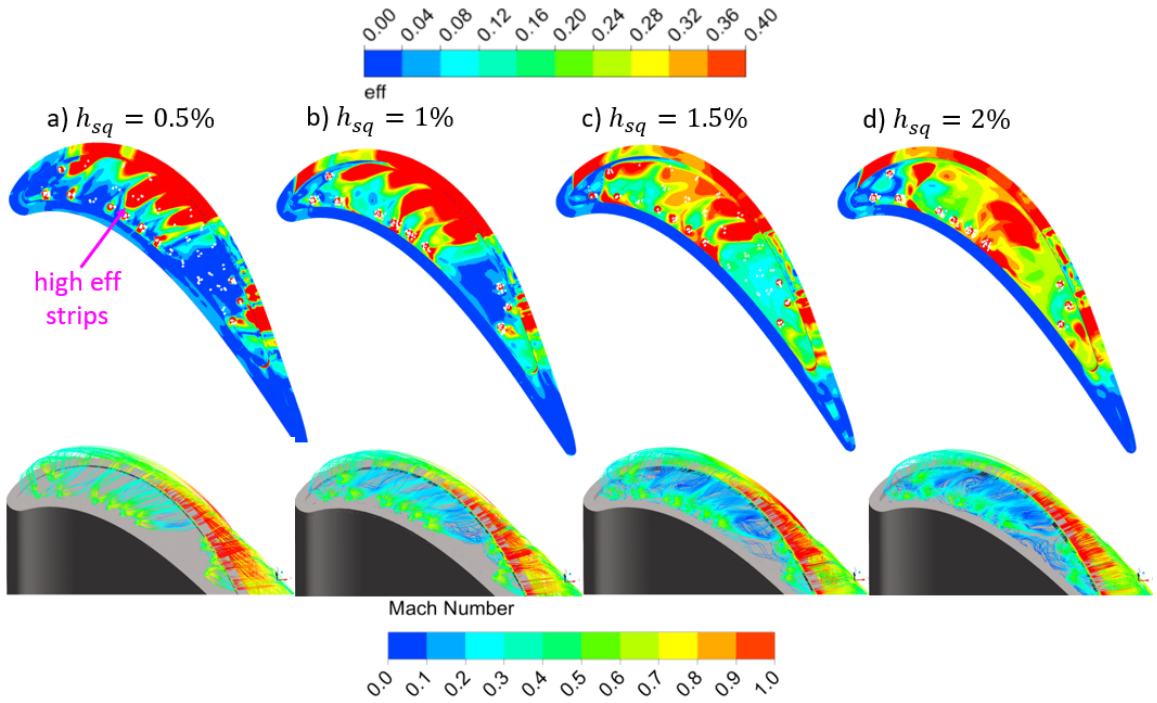


Figure 7.5: Example to illustrate the heat transfer performance varying with the squealer height. h_{sq} is the squealer height.

optimization is compared with the one computed by the concurrent optimization.

In addition to the boundary conditions of the transonic turbine stage stated in Table 5.4, the boundary condition of the cooling flow is listed in Table 7.1. The mass flows rate of the cooling flow is 0.2% of the main flow. In order to keep the coolant mass flow rate varying marginally with different cooling configurations (<0.04% of the mass flow rate of the main flow), the number of the cooling holes is fixed to twenty. The diameter (1% of the axial chord) and the angle (90°) of these twenty cooling holes are the same throughout the optimization. The blowing ratio of the cooling flow is generally smaller than 1 ($0.5 \sim 0.7$).

In the shaping of the transonic turbine stage, the only design variable is the squealer height. The rotor tip block is split into 3×21 pieces to conduct the cooling configuration optimization. Among them, 50 blocks are suitable to accommodate the cooling slots. The twenty cooling holes are distributed among the 50 possible cooling slots. The cooling configuration is coded by a 50-bit binary string that uses '0' and '1' to represent the presence of the cooling holes. When the squealer height and the flow injection is optimized concurrently, the binary string is extended to include the squealer height variation. The design objectives of the optimization in the turbine

cascade are the aerodynamic efficiency η evaluated by Equation 3.19 and the cooling effectiveness, eff calculated by Equation 3.20. In the cooled stage simulation, the computational cost is higher than the one in the cascade. In order to reduce the number of iterations to get the Pareto front, the temperature variance, which is used as the design objective in the cascade optimization, is not employed. Thus, only the cooling effectiveness is implemented to represent the heat transfer performance.

Table 7.1: Boundary conditions of the cooling flow in the transonic turbine stages.

Name	Parameter	Value
Cooling flow inlet stagnation pressure in stationary frame of reference	$P_{t,c}$	4.6 bar
Cooling flow inlet stagnation temperature in stationary frame of reference	$T_{t,c}$	400 K

7.2.1 Stage Optimization Conducted Sequentially

Similar to the optimization in the turbine cascade, the shaping in the sequential optimization has been completed in Section 6.2. For the transonic stage, the squealer height of 1% has the highest aerodynamic efficiency. Thus it is used as the optimized squealer height for the further cooling design.

As an initial Design of Experiments (DOE), 30 cases with different cooling configurations are created. In order to enlarge the search domain and accelerate the convergence of the optimization, the 30 cases are manually selected so that several representative cooling configurations are not missed in the initial design. The examples of the representative cooling configurations include: all cooling holes along the pressure side, along the suction side, along the camber line of the tip; all the cooling holes at the leading edge, at the trailing edge and at the centre of the tip, and several cases having zigzag cooling holes along the blade. Once the simulation of the initial designs is completed, the optimizer using a genetic algorithm will make ranking for these designs based on the performance of the design objectives. Only the cases with high ranking can be selected as the parents for the next generation of design. The binary strings (chromosome) of the parent cases are crossovered and mutated to reproduce the design in the next iteration. In this optimization, ten new designs are generated at each iteration. Three more iterations are run to explore the potential performance gain. The optimization is stopped when the last two iterations do not bring additional performance improvement.

The results of sequentially optimization are shown in plot a) of Figure 7.6 where the two objectives, the efficiency and the cooling effectiveness are shown in x axis and

y axis respectively. Each dot in the figure represents one simulation. The uncooled cases are also marked at the bottom of the figure because the cooling effectiveness is zero in these cases. From the figure, by adding the cooling, the efficiency decreases about 0.1∼0.2%. The Pareto front is noted by the grey curve.

7.2.2 Stage Optimization Conducted Concurrently

Once the sequential optimization is completed, we can conduct it concurrently. In the concurrent optimization, both the squealer height and the cooling configuration are optimized. In addition to the binary string representing the cooling configurations, three additional bits are added into the chromosome to include the variation of the squealer height. In the initial Design of Experiments (DOE), 30 cases with different squealer heights and cooling configurations are created. The parents of the next generation are selected by the optimizer using the Non-dominated Sorting Genetic Algorithm (NSGA-II). Both the aerodynamic efficiency and the cooling effectiveness are taken into account when the ranking is sorted by the optimizer. The selected parents are used to reproduce the new generation of designs. In each iteration, ten new designs are generated. Fifteen iterations were run before the Pareto front is obtained.

The concurrent optimization results are shown in plot b) of Figure 7.6 where the black dots represent the data obtained from the optimization. The uncooled results are also shown at the bottom of the plot, where the cooling effectiveness is zero. Compared to the sequential optimization results, the optimal design in the concurrent optimization has 0.06% increase in the efficiency and 0.04 improvement in the cooling effectiveness. The additional gain brought by the concurrent optimization implies the potential performance improvement missed by the sequential optimization. Similar to the case in the transonic cascade, the transonic stage shows that the cooling flow is not additive. The presence of the coolant changes the flow structure of the main flow so that the optimized uncooled blade does not have the optimal performance in the cooled blade. It contradicts with the general pre-conception that the coolant is passively transported in the main flow.

In plot b) of Figure 7.6, the results are generated by stages with various squealer heights. The influence of squealer height and flow injection is mixed together. In order to investigate the influence of the cooling flow injection, the uncooled and the cooled stage using the same squealer need to be compared. Therefore, the results in plot b) of Figure 7.6 are sorted by squealer height using different colours, as shown in

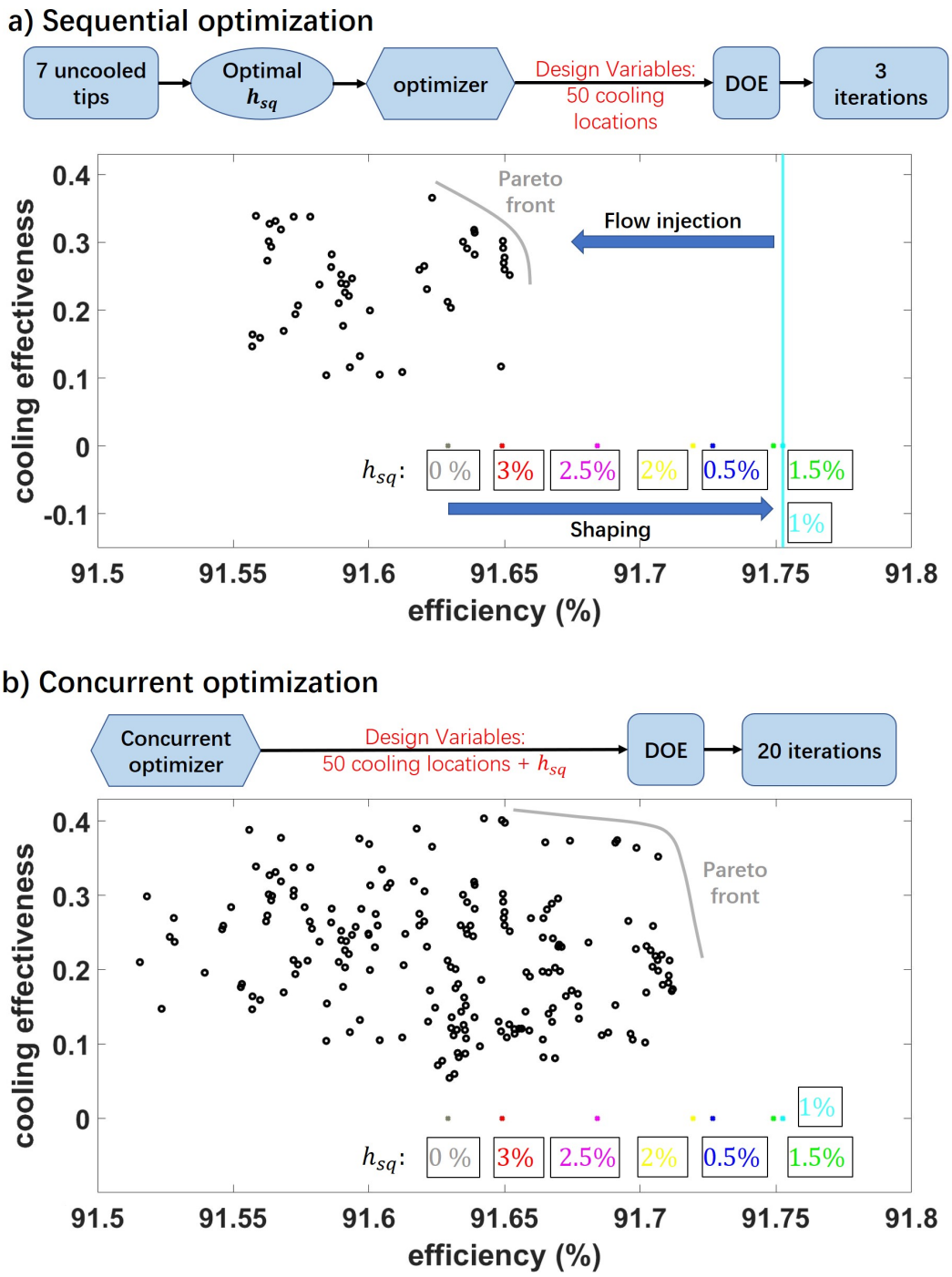


Figure 7.6: Aerothermal optimization (turbine stage) obtained by the sequential optimization and the concurrent optimization.

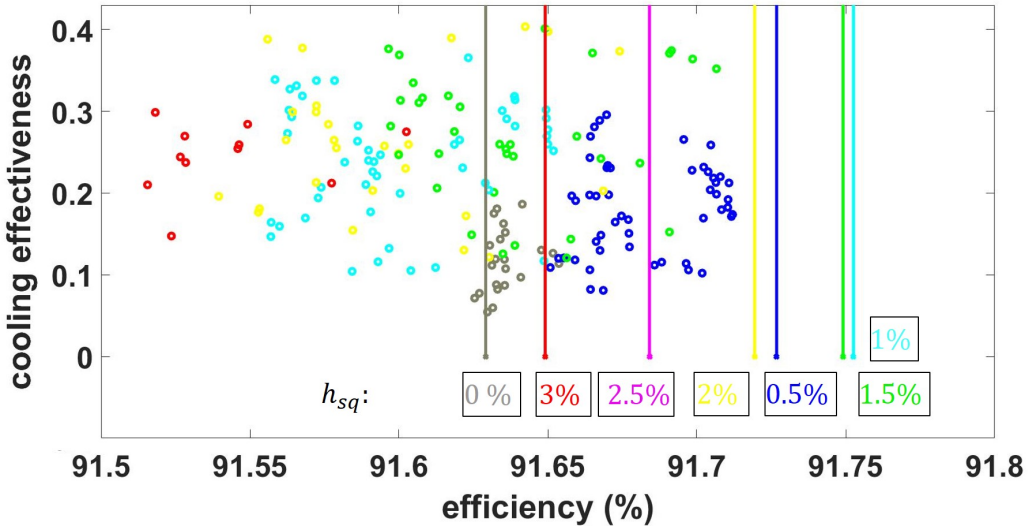


Figure 7.7: Concurrent aerothermal optimization (turbine stage). The results are sorted by the squealer height using different colors.

Figure 7.7. The results obtained from the squealer height of 0%, 0.5%, 1%, 1.5%, 2%, 2.5% and 3% are in grey, blue, cyan, green, yellow, magenta and red respectively. The uncooled efficiency is marked by the vertical line to indicate the efficiency difference between the uncooled stages and the cooled one. From the relative position between the vertical line and the data points in the same colour, it is noted that by adding the cooling holes, the efficiencies in most of the stages reduce except for the cases with the flat tip shown in grey. The cooling flow in the cases with recessed cavity all brought additional loss. It is different from the observations in section 7.1.2 where the coolant in the cases with squealer height of 0%, 1% and 2% may improve the aerodynamic performance of the cascade.

7.2.3 Impact of the Cooling Configuration

The flat tip is the only case that can improve the aerodynamic efficiency by adding cooling injection. It is because the coolant at the flat tip has the direct interaction with the OTL flow. The injections form the air curtains that prevent the OTL flow from crossing the tip. However, comparing to the flat tip of the turbine cascade shown in Figure 7.2, the gain obtained from the coolant is relatively small.

Taking a closer examination of the flat tip, the results are shown in Figure 7.8. Three groups of data are selected to represent the influence of the cooling configuration: group 1 has the three cases with the highest cooling effectiveness; group 2 has the

three cases with the best aerodynamic efficiency, and group 3 is taken from the cases with the lowest efficiency and cooling effectiveness. Within the same group, the blades are ordered by the efficiency: from the left to the right the efficiency increases. The wall temperature shown in Figure 7.8 is normalized by the stator inlet stagnation temperature in the stationary frame of the reference:

$$T_{norm} = \frac{T}{T_{t,inlet,stator}} \tag{7.2}$$

From group 1, it is noted that the cooling configuration can be improved by arranging the cooling holes along the pressure side. It is a relatively straightforward conclusion because the cooling flow along the pressure side has the longest path to travel on the tip. The area passed by the coolant is well protected.

From group 2, the best aerodynamic efficiency is obtained by the cooling holes concentrated at the leading edge of the blade. Two reasons are attributed to this. First, as shown in plot a2) and plot b2) of Figure 6.25, the Mach number is relatively low near the leading edge. Since the mixing loss between the coolant and the main flow can be computed by Equation 6.25, the mixing loss is a quadratic function of main flow Mach number. Thus the smaller main flow Mach number can substantially reduce the loss. It is also observed in the turbine cascade of section 7.1.3. Second, as shown in Figure 6.8, part of the OTL enters the tip from the suction side of the leading edge. Thus the cooling injection near the leading edge can block the OTL flow from both the suction side and the pressure side of the tip while in rest places the coolant can only block the flow from the pressure side.

From group 3, the cooling configurations show the opposite features of group 1 and group 2. The cooling holes are either concentrated at the trailing edge or along the suction side. The cooling holes near the trailing edge generate additional loss because it mixes with the main flow in high Mach number. Also because at the trailing edge the flow is already choked, the cooling injection can hardly bring any blockage effect to the OTL flow. The cooling holes along the suction side of the blade have the shortest path on the tip. The coolant only has a limited cooling area along the suction side. Thus the cooling effectiveness is relatively low. The cooling holes along the suction side also have low aerodynamic efficiency because they are far away from the place where the OTL enters the tip; thus, little blockage effect can be brought by the coolant.

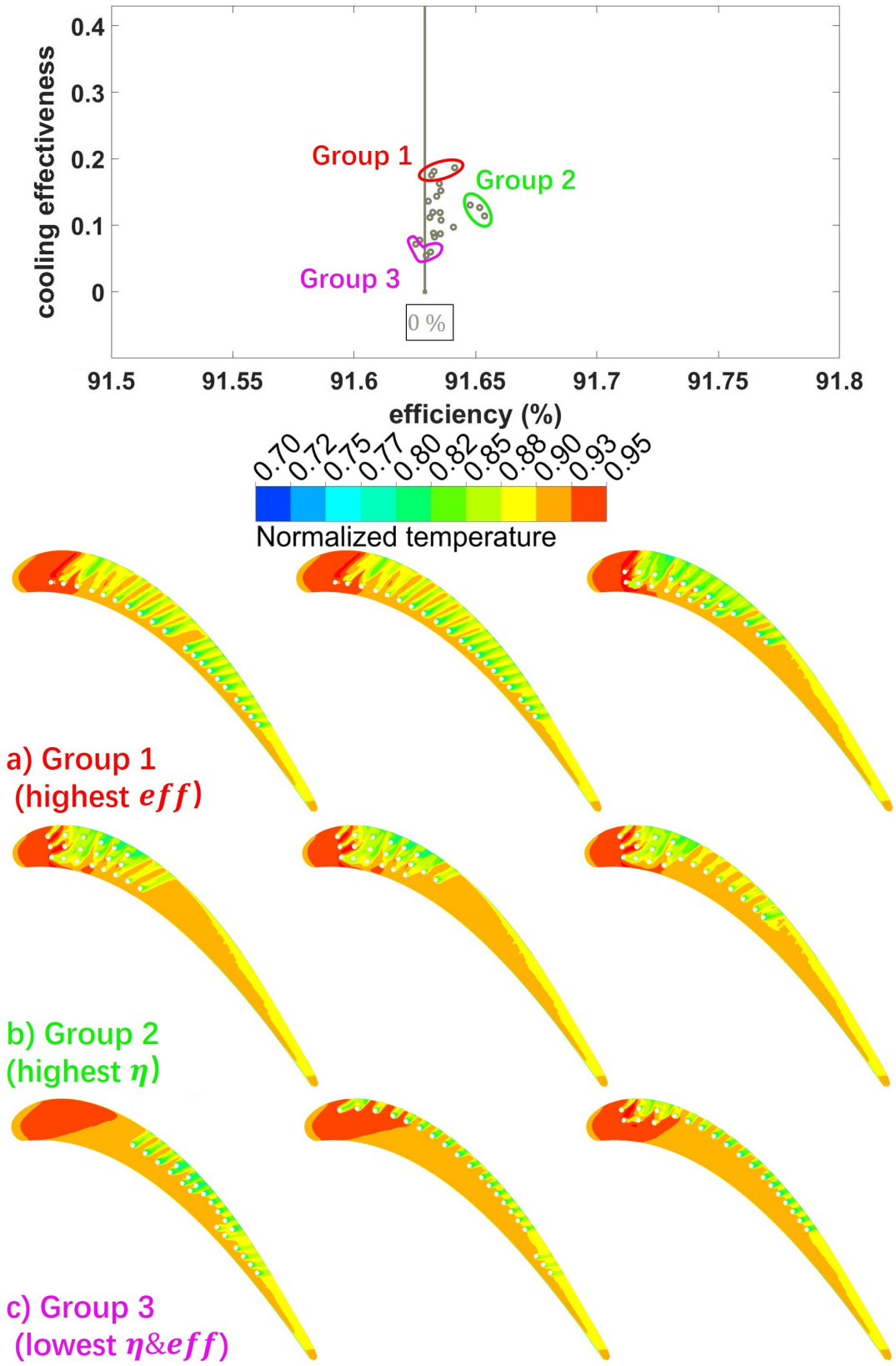


Figure 7.8: The performance of the cooled turbine stage with flat tip.

The similar observation is also made in the cases with squealers. As an example, the performance of the cooled turbine stages with squealer height of 0.5% is shown in Figure 7.9. In the figure, group 1 and group 2 are taken from the results in the Pareto front with the highest effectiveness and the highest efficiency, respectively. Group 3 has the lowest efficiency and worst cooling effectiveness. The normalized temperature contours for the three groups are shown. Within the group, the three cases are sorted by the efficiency: from the left to the right, the efficiency increases.

From group 1, best cooling effectiveness is from the case with the cooling holes distributed along the pressure side of the blade. However, the efficiency, in this case, is relatively low. An improvement is brought by putting one-third of the cooling holes along the pressure side and the rest of the cooling holes along the camber line. It is a trade-off configuration between the case with cooling holes along the pressure side and the case with cooling holes concentrated at the leading edge. In this way, a favourable balance between the cooling area and the blockage of the OTL flow can be maintained. Also, as shown in group 2, the best efficiency is obtained by this design feature. Group 3 in both the flat tip and the tip with squealer has the same design feature. The cooling holes either distribute along the suction side or concentrate at the trailing edge.

7.2.4 Impact of the Squealer Height

By comparing the three groups in Figure 7.8 and those in Figure 7.9, it is noted that the squealer height of 0.5% substantially improves the cooling effectiveness. It is in line with the observation of the turbine cascade in Section 7.1.4. The squealer can trap the coolant in the cavity, so that the cooling flow covers a larger area and has longer residence time in the cavity to cool the tip.

However, in the turbine stage with the rotating casing, as the squealer height further increases, the cooling effectiveness is reduced. From Figure 7.10, when the squealer height increases from 0.5% to 3%, the cooling flow can hardly cool the tip at the frontal portion of the cavity. This unique feature in the turbine stage is attributed to the vortex generated by the casing movement. As illustrated in Figure 6.18, the counter-rotating vortex pair, the PSV and the CCV, is generated at the frontal portion of the cavity by the casing relative movement. As the squealer height increases, the size of the vortices core gets larger. The vortex interacts with coolant and the OTL flow. It entrains the hot OTL flow to enter the cavity and diverts the direction of

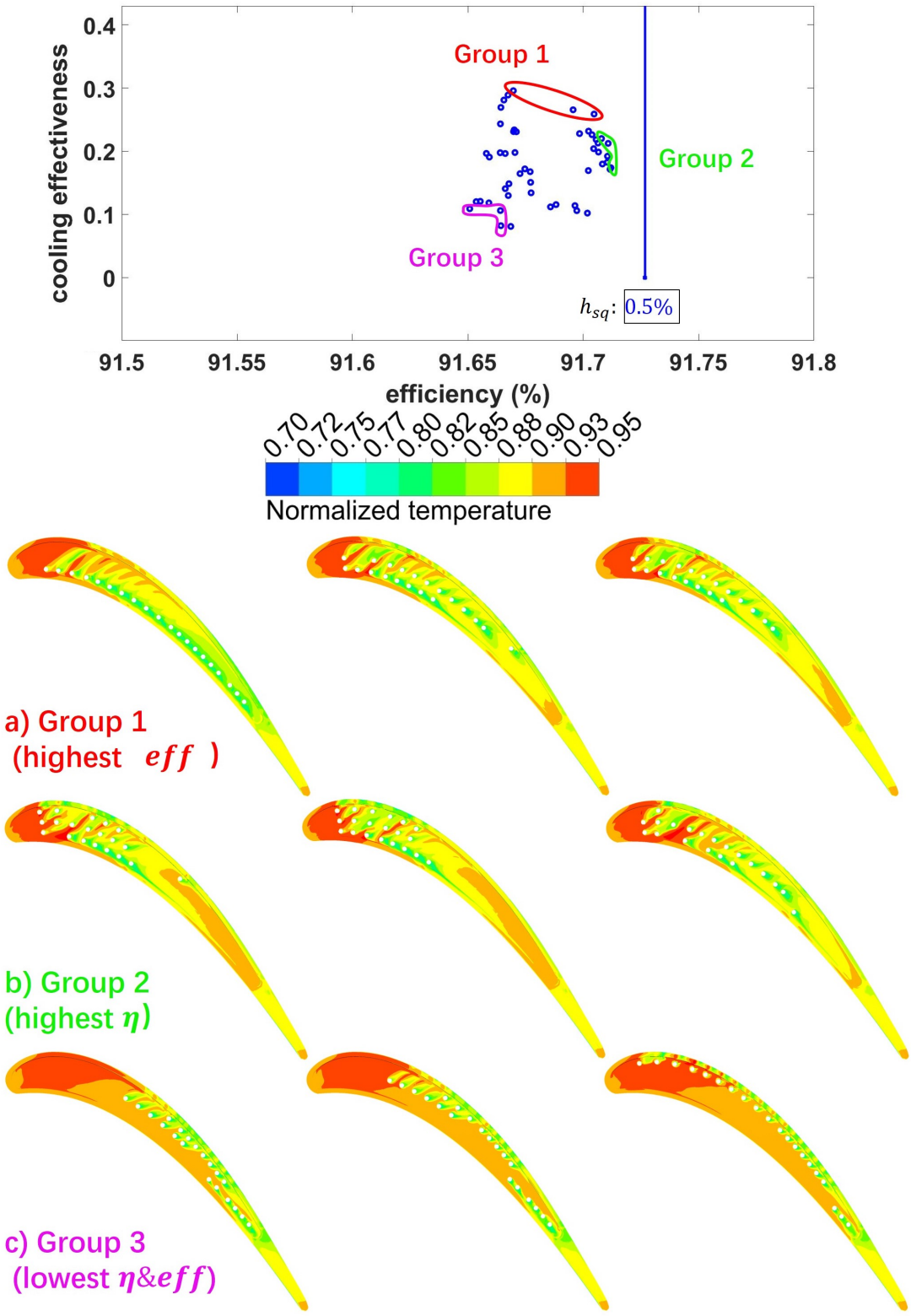


Figure 7.9: The performance of the cooled turbine stage with squealer height of 0.5%.

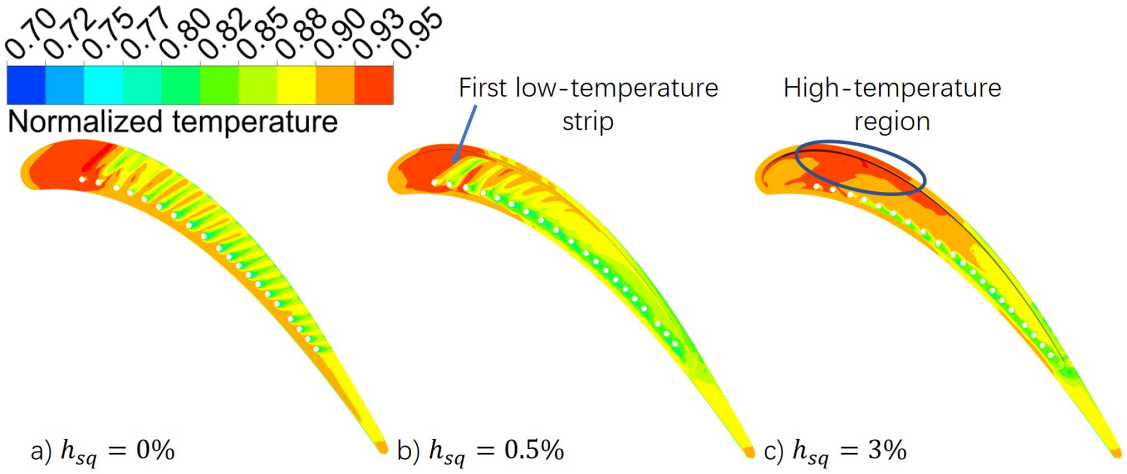


Figure 7.10: The cooling effectiveness at various squealer height but the same cooling configuration.

the cooling flow. Thus the cooling effectiveness at the frontal portion of the blade is reduced.

The interactions of the vortex with the cooling flow are shown in Figure 7.11 where the streamlines coming from the suction side of the blade are in red; the streamlines of the coolant from first cooling hole are in blue. The coolant from the rest of the cooling holes is not illustrated in the figure to make the flow pattern easier to be recognized. From plot a) of Figure 7.11, the coolant from the first cooling hole moves straight from the pressure side to the suction side. It forms the first low-temperature strip in plot b) of Figure 7.10. The situation is changed when the squealer height increases to 3%, as shown in plot b) of Figure 7.11. The vortex interacts severely with the cooling flow and diverts the direction of the coolant. It leads to the high-temperature region at the frontal portion of the tip as exhibited in plot c) of Figure 7.10. Therefore, although the increasing squealer height can trap the coolant in the cavity, because of the additional vortical structure generated by the casing relative movement, the hot OTL flow may be entrained to the tip surface. The competing effect between the trapping of the coolant and the entrainment of the OTL flow leads to the non-monotonic variation of the cooling effectiveness with the squealer height.

7.3 Summary

In this chapter, the cooling holes are added in the tip of the transonic turbine cascades and the transonic turbine stages. The cooled blades are optimized by both

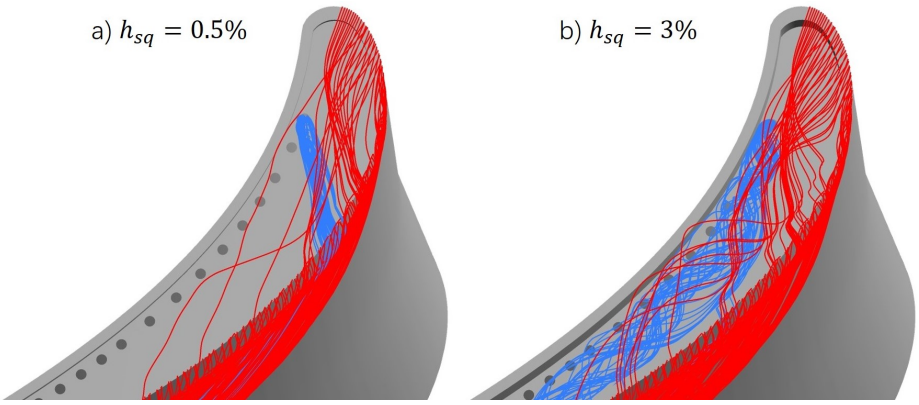


Figure 7.11: The interaction between the vortex and the cooling flow.

the sequential method and the concurrent method. In the sequential optimization, the squealer height optimization and the cooling design are conducted in a sequence: first, the turbine squealer height is optimized based on their efficiency, then the cooling holes are added to the uncooled blade with the highest efficiency to generate the Pareto front that balances the aerodynamic and the heat transfer performance of the turbine. In the concurrent optimization, the squealer height and the flow control of the cooling configuration are conducted simultaneously. The optimization of the turbine cascade and the turbine stage both indicate that the concurrent optimization brings a better aerothermal performance compared to the sequential one. Because of the interaction between the coolant and the OTL flow, the cooling flow is no longer additive to the OTL flow. It contradicts with the design objective that the coolant passively transport with the main flow.

Then the influence of the cooling injection is investigated in the turbine cascades and turbine stages working in the transonic condition. The cooling flow is found to improve the aerodynamic efficiency in some cases for both the turbine cascades and the turbine stages. The reason is attributed to the blockage effect brought by the injection of the cooling flow. This air curtain effect has been found in the previous research [24]. It contradicts the general pre-conception that the cooling flow always generates additional loss. Comparing to the turbine cascade, the turbine stage tends to have less cases with improved efficiency. It is because the relative movement of the rotating casing already generates the blockage of the OTL flow in the turbine stage. Therefore the gain brought by the coolant is relatively low comparing the cases in the turbine cascade.

Finally, the influence of the squealer height towards the heat transfer performance

is studied for both the transonic turbine cascades and the transonic turbine stages. In the transonic turbine cascade, the cooling effectiveness is found to raise with the squealer height. It is because the increasing depth of the squealer cavity tends to trap the coolant from leaving the tip region. Thus the cooling flow has a longer path to cool the tip. However, in the turbine stages, the variation of the cooling effectiveness to the squealer depth is no longer monotonic. As the squealer height increases, the rotating casing generates a vortex that entrains the OTL flow to the tip surface. The competing effect between the trapping of the cooling flow and the entrainment of the OTL flow induces the non-monotonic variation of the cooling effectiveness with the squealer height.

Chapter 8

Conclusions and Suggested Future Work

In this thesis, the tips of the turbine cascades and the turbine stages are optimized using sequential and concurrent methods. The turbine stage working in the subsonic and the transonic region are generated by a parameterization system. In order to obtain a fast and accurate simulation of the turbine blade with cooling holes, the multi-scale method is implemented. It is the first-of-its-kind work to implement the multi-scale methodology in a commercial solver. The multi-scale method is validated against the experimental data and fine mesh results. It indicates a potential to provide faster and accurate predictions for practical cases with large number of cooling holes. Moreover, Denton's tip leakage model is employed in the turbine stage to evaluate the mixing loss between the leakage flow and the main flow. The model is shown to well predict the general trend of the loss in both the subsonic and the transonic stages. Depending on the different levels of models taken into account, the conclusion can be drawn on the following aspects.

8.1 Sequential and Concurrent Optimizations

In this research, the transonic turbine cascades and the transonic stages are optimized both sequentially and concurrently. The optimizer uses Non-dominated Sorting Genetic Algorithm (NAGA-II) to search the design space so that the three objectives, the aerodynamic efficiency, the cooling effectiveness and the temperature variance, are optimized by the variation of the squealer heights and the cooling configurations. As the optimization converges, a Pareto front is formed that combines the three objectives. The multi-scale method is implemented to save the computation time and

the meshing time for the cooling holes. The key findings for both the turbine cascade and the turbine stages on the design implication are the following:

1) By comparing the results from the sequential optimization with those from the optimization combining shaping and flow injection concurrently, it is found that the concurrent optimization can obtain better aerothermal performances. The sequential optimization can not achieve these performances. It indicates that the shaping-cooling sequential optimization method may miss the potential to improve the performance of the blade further.

2) The aerodynamic efficiency ranking obtained from the uncooled blade tip shapes is changed after adding the cooling. It is due to the interactions between the coolant and the OTL flow. Therefore at the tip, the coolant film is not passive and additive. It also challenges the shaping-cooling sequential optimization because an 'optimised' uncooled blade tip shape may not provide the most suitable base configuration for cooling design and optimization.

3) In some cases, by adding the cooling holes, the aerodynamic efficiency is increased. It is because the coolant can block the OTL flow and reduce the tip leakage loss. Therefore by adequately designing the cooling scheme, the coolant can improve the aerodynamic efficiency.

8.2 Transonic and Subsonic Stages

In this thesis, the turbine stages working at the subsonic and the transonic conditions are designed respectively by the parameterization system. The simulations of the two stages are conducted with various squealer height. The squealer height is found to have two major opposing effects on the aerodynamic efficiency: the blockage effect to reduce the tip leakage mass flow rate and the sudden expansion loss effect to generate additional losses. The squealer increases both of these two effects. The two competing effects decide the variation of the efficiency with the squealer height.

In both the subsonic and the transonic stages, the Reynolds number is kept the same. However different performance at the tip region has been found. For squealer height varying from 0% (flat tip) to 3%, the squealer in the subsonic turbine stage can increase efficiency up to 0.2% and reduce the OTL mass flow rate up to 0.3%. The squealer in the transonic stage, on the other hand, has a less improvement: the maximum efficiency gain is 0.1% and the maximum reduction of OTL mass flow rate is 0.1%.

8.3 Turbine Cascades and Turbine Stages

In this work, both the turbine cascades and the turbine stages are simulated. Due to the relative movement of the turbine casing, the turbine stages have shown several unique features compared to the turbine cascade. For the turbine stage with squealer, the relative rotation of the casing wall against the turbine tip generates a vortex pair in the squealer cavity. It causes the velocity deficit of the over tip leakage flow on the suction side which contributes the most to the blockage effect of the squealer cavity.

The turbine stage also shows different heat transfer performance as the squealer height increases compared to the turbine cascade. In the turbine cascade, as the squealer height increases the heat transfer performances, both the cooling effectiveness and the temperature variance are improved. It is because the increased squealer height traps the coolant and mitigates from its original path. It also entrains the over tip leakage flow to the tip surface. Thus as the squealer height raises, the cooling effectiveness in the turbine stage may reduce. the interaction between the coolant and the OTL flow. However, in the turbine stage, the increasing squealer height induces a counter-rotating cavity vortex that can divert the cooling flow

8.4 Suggested Future Work

The following two works are suggested for the future study:

1) In this thesis, the multi-scale method has shown a potential to reduce the computational cost in the presence of the large length scale disparity. Thus in the turbine film cooling design where hundreds of cooling holes are computed, the gain from the multi-scale method could be high. The application of the multi-scale method in the film cooling design is suggested.

2) In this work, the sequential and the concurrent optimization are conducted at the turbine tip region. The concurrent optimization is found to bring better aerothermal performance than the sequential one. It will be interesting to see if it is the same case in the turbine blade design where the blade geometry and the film cooling configuration is optimized.

Bibliography

[1] Arnone A, Bonaiuti D, Focacci A, Pacciani R, Greco ASD, and Spano E. Parametric optimization of a high-lift turbine vane. *ASME. Turbo Expo: Power for Land, Sea, and Air*, GT2004-54308, 2004.

[2] Hehn A, Mosdzien M, Grates D, and Jeschke P. Aerodynamic optimization of a transonic centrifugal compressor by using arbitrary blade surfaces. *ASME. Turbo Expo: Power for Land, Sea, and Air*, GT2017-63470, 2017.

[3] Hergt A, Meyer R, Muller MW, and Engel K. Loss reduction in compressor cascades by means of passive flow control. *ASME. Turbo Expo: Power for Land, Sea, and Air*, 6:269–280, 2008.

[4] Oyama A, Liou MS, and Obayashi S. Transonic axial-flow blade optimization: Evolutionary algorithms/three-dimensional navier-stokes solver. *Journal of Propulsion and Power*, 20(4):612–619, 2004.

[5] Rahim A, Khanal B, He L, and Romero E. Effect of nozzle guide vane lean under influence of inlet temperature traverse. *ASME. J. Turbomach.*, 136(7):071002, 2013.

[6] Rahim A and He L. Rotor blade heat transfer of high pressure turbine stage under inlet hot-streak and swirl. *ASME. J. Eng. Gas Turbines Power*, 137(6):062601, 2015.

[7] Wheeler APS, Atkins NR, and He L. Turbine blade tip heat transfer in low speed and high speed flows. *ASME J. Turbomach.*, 133(4):041025–041025–9, 2011.

[8] Virdi AS, Zhang Q, He L, Li HD, and Hunsley R. Aerothermal performance of shroudless turbine blade tips with relative casing movement effects. *Journal of Propulsion and Power*, 31(2):527–536, 2015.

[9] Wheeler AS, Korakianitis T, and Banneheke S. Tip-leakage losses in subsonic and transonic blade rows. *ASME J. Turbomach.*, 135(1):011029–011029–7, 2012.

[10] Mischo B, Behr T, and Abhari RS. Flow physics and profiling of recessed blade tips: impact on performance and heat load. *ASME J. Turbomach.*, 130(2):021008, 2008.

[11] Zlatinov M. B., Tan C.S., Montgomery M., Islam T., and Harris M. Turbine hub and shroud sealing flow loss mechanisms. *ASME J. Turbomach.*, 134(6):061027, 2012.

[12] Kulfan BM. A universal parametric geometry representation method – "cst". *45th AIAA Aerospace Sciences Meeting and Exhibit*, 2007-0062, 2007.

[13] De Maesschalck C, Andreoli V, Paniagua G, Gillen T, and Barker B. Aerothermal optimization of turbine squealer tip geometries with arbitrary cooling injection. *ASME paper GT2019-91208*, 2019.

[14] Wu CH. A general theory of three-dimensional flow in subsonic and supersonic turbomachines of axial, radial, and mixed-flow types. *NACA technical Note*, 2604:Washington D.C., 1952.

[15] Li CX, Guo ZD, Song LM, Li J, and Feng ZP. Design optimization of a 3d parameterized vane cascade with non-axisymmetric endwall based on a modified ego algorithm and data mining techniques. *ASME. Turbo Expo: Power for Land, Sea, and Air*, GT2017-63738, 2017.

[16] Coull J D and Hodson H P. Blade loading and its application in the mean-line design of low pressure turbines. *ASME. J. Turbomach.*, 135(2):021032, 2012.

[17] Yang D, Yu X, and Feng Z. Investigation of leakage flow and heat transfer in a gas turbine blade tip with emphasis on the effect of rotation. *ASME. J. Turbomach.*, 132(4):041010, 2010.

[18] Culley DE, Braunscheidel EP, and Bright MM. Impulsive injection for compressor stator separation control. *AIAA*, 3633, 2005.

[19] Van den Braembussche RA, Islek AA, and Alsalihi Z. Aerothermal optimization of micro-gasturbine compressors including heat transfer. *International Gas Turbine Conference*, pages 2–7, 2003.

[20] Wilson DG and Korakianitis T. *The design of high-efficiency turbomachinery and gas turbines*. MIT press, 2014.

[21] O'Dowd DO. Aero-thermal performance of transonic high-pressure turbine blade tips. *DPhil dissertation, Oxford University*, 2010.

[22] O'Dowd DO, Zhang Q, He L, Cheong BY, and Tibbott II. Aerothermal performance of a cooled winglet at engine representative mach and reynolds numbers. *ASME J. Turbomach.*, 135(1):011041–011041–10, 2012.

[23] Zitzler E, Deb K, and Thiele L. Comparison of multiobjective evolutionary algorithms: Empirical results. evolutionary computation. *Evolutionary computation*, 8(2):173–195, 2000.

[24] Curtis E.M., Denton J.D., Longley J.P., and Rosic B. Controlling tip leakage flow over a shrouded turbine rotor using an air-curtain. *ASME Turbo. Expo.*, 48883:885–894, 2009.

[25] Greitzer EM, Tan CS, and Graf MB. *Internal Flow: Concepts and Applications*. New York: Cambridge University Press, 2004.

[26] Beard P. F. *On Transient Turbine Efficiency Measurements With Engine Representative Inlet Flows.* PhD thesis, University of Oxford, Department of Engineering Science, 2010.

[27] Zhong F. and Zhou C. Tip gap size effects on thermal performance of cavity-winglet tips in transonic turbine cascade with endwall motion. *J. Glob. Power Propuls. Soc.*, 1:41–54, 2017.

[28] Papadakis G and Bergeles G. A local grid refinement method for three-dimensional turbulent recirculating flows. *International journal for numerical methods in fluids.*, 31(7):pp.1157–1172, 1999.

[29] Li H. Shifted periodic grids for two- and three-dimensional cascade flows. *AIAA paper*, pages 94–0754, 1994.

[30] Liu H, Shen X, Zhu XC, Du ZH, Yang H, and Yang R. The aerodynamic optimization design of turbine cascade with non-axisymmetric endwall and experimental validations. *ASME. Turbo Expo: Power for Land, Sea, and Air*, GT2017-63898, 2017.

[31] Ma H, Zhang Q, He L, Wang Z, and Wang L. Cooling injection effect on a transonic squealer tip - part I: experimental heat transfer results and CFD validation. *J. Eng. Gas Turbines Power*, 139(5):052506–052506–9, 2017.

[32] Ma H, Zhang Q, He L, Wang Z, and Wang L. Cooling injection effect on a transonic squealer tip - part II: analysis of aerothermal interaction physics. *J. Eng. Gas Turbines Power*, 139(5):052507–052507–9, 2017.

[33] Ma H, Zeng W, Jiang H, and Hong J. Impact of cooling injection on shock wave over a flat tip in high pressure turbine. *ASME. J. Turbomach.*, 144(1):011012, 2021.

[34] Tang H, Liu S, and Luo H. Design optimization of profiled endwall with consideration of cooling and rim seal flow effects. *ASME. Turbo Expo: Power for Land, Sea, and Air*, GT2016-57219, 2016.

[35] Hartsel J. Prediction of effects of mass-transfer cooling on the blade-row efficiency of turbine airfoils. *10th Aerospace Sciences Meeting*, page 11, 1972.

[36] Jeong J and Hussain F. On the identification of a vortex. *J. of Fluid Mechanics*, 285:69–94, 1995.

[37] Kwak J and Han JC. Heat transfer coefficient and film-cooling effectiveness on a gas turbine blade tip. *ASME J. Heat Transfer.*, 125(3):494–502, 2003.

[38] Kwak J and Han JC. Heat transfer coefficients and film cooling effectiveness on the squealer tip of a Gas turbine blade. *ASME J. Turbomach.*, 125(4):648–657, 2003.

[39] Moore J and Elward KM. Shock formation in overexpanded tip leakage flow. *ASME J. Turbomach.*, 115(3):392–399, 1993.

[40] Han JC. Recent studies in turbine blade cooling. *International Journal of Rotating Machinery*, 10(6):443–457, 2004.

[41] Coull JD, Atkins NR, and Hodson HP. Winglets for improved aerothermal performance of high pressure turbines. *ASME J. Turbomach.*, 136(9):091007, 2014.

[42] Denton JD. Throughflow calculations for axial flow turbines. *Trans. ASME, Journal of Engineering for Power*, 100, 1978.

[43] Denton JD. Loss mechanisms in turbomachines. *ASME J. Turbomach.*, 115(4):621–656, 1993.

[44] Denton JD. Multall: An open source, cfd based, turbomachinery design system. *ASME. Turbo Expo: Power for Land, Sea, and Air*, pages V02BT41A027–V02BT41A027, 2017.

[45] Alonso JJ, LeGresley PA, Legresley PA, and Alonso J. Airfoil design optimization using reduced order models based on proper orthogonal decomposition. *AIAA Fluids, 2000 Conference and Exhibit*, page 2000–2545, 2000.

[46] Johnson JJ, King PI, Clark JP, and Ooten MK. Genetic algorithm optimization of an hpt vane pressure side film cooling array. *ASME. Turbo Expo: Power for Land, Sea, and Air*, GT2012-68049, 2012.

[47] Park JS, Lee DH, Rhee DH, Kang SH, and Cho HH. Heat transfer and film cooling effectiveness on the squealer tip of a turbine blade. *Energy*, 72:331–343, 2014.

[48] Batchelor G K. On steady laminar flow with closed streamlines at large reynolds number. *J. of Fluid Mechanics*, 1(2):177–190, 1956.

[49] Deb K, Pratap A, Agarwal S, and Meyarivan TAMT. A fast and elitist multiobjective genetic algorithm: Nsga-ii. ieee transactions on evolutionary computation. *Evolutionary computation*, 6(2):182–197, 2002.

[50] Krishnababu S K, Newton P J, Dawes W N, Lock G D, Hodson H P, Hannis J, and Whitney C. Aerothermal investigations of tip leakage flow in axial flow turbines—part i: Effect of tip geome-try and tip clearance gap. *ASME. J. Turbomach.*, 131(1):011006, 2008.

[51] He L. Block-spectral approach to film-cooling modeling. *ASME J. Turbomach.*, 134(2):021018, 2012.

[52] He L. Block-spectral mapping for multi-scale solution. *Journal of Computational Physics*, 250:13–26, 2013.

[53] He L. Fourier spectral modelling for multi-scale aero-thermal analysis. *International Journal of computational fluid dynamics*, 27(2):118–129, 2013.

[54] He L. Multiscale block spectral solution for unsteady flows. *International Journal for Numerical Methods in Fluids*, 86(10):655–678, 2018.

[55] Prandtl L. Uber flussigkeitsbewegung bei sehr kleiner reibung. *Proc. Third Int. Math. Congr.*, pages 484–491, 1904.

[56] Yang L, Min Z, Parbat SN, and Chyu M. Optimization of hybrid-linked jet impingement cooling channels based on response surface methodology and genetic algorithm. *ASME. Turbo Expo: Power for Land, Sea, and Air*, GT2017-63278, 2017.

[57] Smith LH. The radial equilibrium equation of turbomachinery. *Trans. ASME Journal of Engineering for Power*, 88:1–12, 1966.

[58] Pritchard LJ. An eleven parameter axial turbine airfoil geometry model. *ASME paper 85-GT-219*, 1985.

[59] Cheng M and Hung KC. Vortex structure of steady flow in a rectangular cavity. *Computers and fluids*, 35(10):1046–1062, 2006.

[60] Paty M, Cernat B C, De Maesschalck C, and Lavagnoli S. Experimental and numerical investigation of optimized blade tip shapes—part ii: Tip flow analysis and loss mechanisms. *ASME. J. Turbomach.*, 141(1):011007, 2019.

[61] Staats M and Nitsche W. Experimental investigations on the efficiency of active flow control in a compressor cascade with periodic non-steady outflow conditions. *ASME. Turbo Expo: Power for Land, Sea, and Air*, pages V02AT39A006–V02AT39A006, 2017.

[62] Zhang M and He L. Combining shaping and flow control for aerodynamic optimization. *AIAA Journal*, 53(4):888–901, 2015.

[63] Zlatinov MB. Secondary air interaction with main flow in axial turbines. Master's thesis, Massachusetts Institute of Technology, Department of Aeronautics and Astronautics, 2011.

[64] Dunn MG and Haldeman CW. Time-averaged Heat flux for a recessed tip, lip, and platform of a transonic turbine blade. *ASME J. Turbomach.*, 122(4):692–698, 2000.

[65] Oldfield MLG. Impulse response processing of transient heat transfer gauge signals. *ASME J. Turbomach.*, 130(2), 2008.

[66] Casey MV. A computational geometry for the blades and internal flow channels of centrifugal compressors. *J. Eng. Power*, 105(2):288–295, 1983.

[67] Casey MV, Gersbach F, and Robinson C. An optimization technique for radial compressor impellers. *ASME. Turbo Expo: Power for Land, Sea, and Air*, Parts A, B, and C:2401–2411, 2008.

[68] Yin MY, Li J, Song LM, Li B, Zhong GY, Fan XP, Sun Q, and Feng ZP. Aerodynamic optimization design of last stage long blade for steam turbine using self-adaptive differential evolutionary algorithms and rans solutions. *ASME. Turbo Expo: Power for Land, Sea, and Air*, GT2017-63502, 2017.

[69] Shankar P N and Deshpande M D. Fluid mechanics in the driven cavity. *Annual review of fluid mechanics*, 32(1):93–136, 2000.

[70] Cumpsty NA and Horlock JH. Averaging nonuniform flow for a purpose. *ASME J. Turbomach.*, 128:120–129, 2006.

[71] Key NL and Arts T. Comparison of turbine tip leakage flow for flat tip and squealer tip geometries at high-speed conditions. *ASME J. Turbomach.*, 128(2):213–220, 2006.

[72] Bindon J P and Morphis G. The development of axial turbine leakage loss for two profiled tip geometries using linear cascade data. *ASME. J. Turbomach.*, 114(1):198–203, 1992.

[73] Ireland P and Dailey G. Aerothermal performance of internal cooling systems in turbomachines. *In Internal Cooling In Turbomachinery (von Karman Institute, Belgium, May)*, 2010-05:8–12, 2010.

[74] Palafox P, Oldfield M L G, LaGraff J E, and Jones T V. Piv maps of tip leakage and sec-ondary flow fields on a low-speed turbine blade cascade with moving end wall. *ASME. J. Turbomach.*, 130(1):011001, 2007.

[75] Duan PH, Tan CS, Scribner A, and Malandra A. Loss generation in transonic turbine blading. *ASME J. Turbomach.*, 140(4):041006–041006–12, 2018.

[76] Duan PH and He L. Application of multiscale methodology for transonic turbine blade tip cooling design. *ASME. J. Turbomach.*, 142(8):081011, 2020.

[77] Duan PH and He L. Optimization of turbine cascade squealer tip cooling design by combin-ing shaping and flow injection. *ASME. J. Turbomach.*, 143(11):111007, 2021.

[78] Zhang Q, O'Dowd DO, He L, Oldfield MLG, and Ligrani PM. Transonic turbine blade tip aerothermal performance with different tip gaps part I: Tip heat transfer. *ASME J. Turbomach.*, 133(4):041027–041027–9, 2011.

[79] Zhang Q and He L. Overtip choking and its implications on turbine blade-tip aerodynamic performance. *J. of Propulsion and Power*, 27(5):1008–1014, 2011.

[80] Zhang Q and He L. Tip-shaping for hp turbine blade aerothermal performance management. *ASME J. Turbomach.*, 135(5):051025–051025–7, 2013.

[81] Zhang Q and He L. Turbine blade tip aero-thermal management: some recent advances and research outlook. *J. Glob. Power Propuls. Soc.*, 1:271 – 287, 2017.

[82] Zhang Q, He L, Wheeler APS., Ligrani PM, and Cheong BCY. Overtip shock wave structure and its impact on turbine blade tip heat transfer. *ASME J. Turbomach.*, 133(4):041001–041001–8, 2011.

[83] Zhang Q, O'Dowd D O, He L, Wheeler A P S, Ligrani P M, and Cheong B C Y. Overtip shock wave structure and its impact on turbine blade tip heat transfer. *ASME. J. Turbomach.*, 133(4):041001, 2011.

[84] Atkins N R, Thorpe S J, and Ainsworth R W. Unsteady effects on transonic turbine blade-tip heat transfer. *ASME. J. Turbomach.*, 134(6):061002, 2012.

[85] Burggraf O R. Analytical and numerical studies of the structure of steady separated flows. *J. of Fluid Mechanics*, 24(1):113–151, 1966.

[86] Novak RA. Streamline curvature computing procedures for fluid flow problems. *Trans. of ASME, Journal of Engineering for Power*, 89:478–490, 1967.

[87] Lotz RD. Aerodynamic optimization process for turbocharger compressor impeller. *ASME. Turbo Expo: Power for Land, Sea, and Air*, GT2017-64365, 2017.

[88] Bunker RS. A review of turbine blade tip heat transfer. *Annals of the New York Academy of sciences*, 934(1):pp.64–79, 2001.

[89] Jiang S, Li Z, Li J, and Song L. Effects of the novel rib layouts on the tip leakage flow pat-tern and heat transfer performance of turbine blade. *J. Aerospace Engineering.*, 234(8):1446–1459, 2020.

[90] Mhetras S, Narzary D, Gao Z, and Han JC. Effect of a cutback squealer and cavity depth on film-cooling effectiveness on a gas turbine blade tip. *ASME J. Turbomach.*, 130(2):021002, 2008.

[91] Teng S, Han JC, and Azad GMS. Detailed heat transfer coefficient distributions on a large-scale gas turbine blade tip. *Journal of Heat Transfer*, 123(4):803–809, 2001.

[92] Xue S and Ng WF. Turbine blade tip external cooling technologies. *Aerospace*, 5(3):90, 2018.

[93] Kacker SC and Okapuu U. A mean line prediction method for axial flow turbine efficiency. *ASME. J. Eng. Power*, 104(1):111–119, 1982.

[94] Thorpe SJ, Yoshino S, Thomas GA, Ainsworth RW, and Harvey NW. Blade-tip heat transfer in a transonic turbine. *Journal of Power and Energy*, 219(6):421–430, 2005.

[95] Lu SP, Chi ZR, Wang ST, Wen FB, and Feng GT. Full three-dimensional optimization platform of turbine blades considering the film cooling. *ASME. Turbo Expo: Power for Land, Sea, and Air*, pages V06BT43A002–V06BT43A002, 2013.

[96] Buyukli T, Salnikov A, and Fedorchenko Y. High-load compressor blisk-type impeller multidisciplinary optimization. *ASME. Turbo Expo: Power for Land, Sea, and Air*, GT2017-64116, 2017.

[97] Hofer T and Arts T. Aerodynamic investigation of the tip leakage flow for blades with different tip squealer geometries at transonic conditions. *ASME Paper GT2009-59909*, 2009.

[98] Korakianitis T. Prescribed-curvature distribution airfoils for the preliminary geometric design of axial turbomachinery cascades. *ASME J. Turbomach.*, 115(2):325–333, 1993.

[99] Verstraete T, Amaral S, and Van den Braembussche RA. Design and optimization of the internal cooling channels of a high pressure turbine blade—part ii: Optimization. *ASME. Turbo Expo: Power for Land, Sea, and Air*, GT2008-51080, 2008.

[100] Palmer T.R., Tan C.S., Zuniga H., Little D., Montgomery M., and Malandra A. Quantifying loss mechanisms in turbine tip shroud cavity flows. *ASME J. Turbomach.*, 138(9):091006, 2016.

[101] Andreoli V, Braun J, Paniagua G, De Maesschalck C, Bloxham M, Cummings W, and Langford L. Aerothermal optimization of fully cooled turbine blade tips. *ASME J. Turbomach.*, 141(6):061007–061007–10, 2019.

[102] Zander V and Nitsche W. Control of secondary flow structures on a highly loaded compressor cascade. *Proceedings of the Institution of Mechanical Engineers, Part A: Journal of Power and Energy*, 227:674–682, 2013.

[103] Ning W and He L. Some modeling issues on trailing-edge vortex shedding. *AIAA Journal*, 39(5):787–793, 2001.

[104] Song YJ, Guo ZD, Song LM, Li J, and Feng ZP. Knowledge-based aero-thermal multi-disciplinary design optimization of a high temperature blade. *ASME. Turbo Expo: Power for Land, Sea, and Air*, GT2017-63880, 2017.

[105] Zhong YJ and Li SY. A 3d shape design and optimization method for natural laminar flow nacelle. *ASME. Turbo Expo: Power for Land, Sea, and Air*, GT2017-64379, 2017.

[106] Liu Z, Liu Z, and Feng Z. Unsteady analysis on the effects of tip clearance height on hot streak migration across rotor blade tip clearance. *ASME. J. Eng. Gas Turbines Power.*, 136(6):082605, 2014.

[107] Schabowski Z and Hodson H. The reduction of over tip leakage loss in unshrouded axial turbines using winglets and squealers. *ASME J. Turbomach.*, 136(4):041001, 2014.

[108] Schabowski Z, Hodson H, Giacche D, Power B, and Stokes MR. Aeromechanical optimization of a winglet-squealer tip for an axial turbine. *ASME J. Turbomach.*, 136(7):071004, 2014.

[109] Wang Z, Zhang Q, Liu Y, and He L. Impact of cooling injection on the transonic over-tip leakage flow and squealer aerothermal design optimization. *J. Eng. Gas Turbines Power*, 137(6):GTP–14, 2015.

Appendix 1

The blade geometries of the subsonic and the transonic turbine stages are uploaded in the following link:

https://drive.google.com/drive/folders/1ZLLDtXquG1Mb5i8zc7RQd0isKhzTN6hC?usp=sharing

Or

https://pan.baidu.com/s/1hiaEw5sJ8a9uOLW7CGogbg

pin：turb

The midspan rotor blade profiles for both the subsonic and the transonic stages are shown here as examples:

1, Subsonic rotor profile at the midspan (unit: [mm])

240.4906620215	133.9654555069	1031.4365063982
240.6961942750	134.6511200384	1031.3472188707
240.9742498756	135.3594092906	1031.2544983255
241.3248853208	136.0879325018	1031.1586127398
241.7479027916	136.8341622669	1031.0598537605
242.2428653004	137.5954488535	1030.9585357592
242.8091114954	138.3690341777	1030.8549948372
243.4457701188	139.1520654365	1030.7495877684
244.1517741210	139.9416083966	1030.6426908679
244.9258744299	140.7346603365	1030.5346987753
245.7666533751	141.5281626404	1030.4260231475
246.6725377679	142.3190130438	1030.3170912521

247.6418116354	143.1040775270	1030.2083444601
248.6726286110	143.8802018590	1030.1002366338
249.7630239793	144.6442227882	1029.9932324117
250.9109263764	145.3929788808	1029.8878053906
252.1141691455	146.1233210069	1029.7844362088
253.3705013476	146.8321224740	1029.6836105376
254.6775984270	147.5162888086	1029.5858169847
256.0330725331	148.1727671864	1029.4915449212
257.4344824959	148.7985555130	1029.4012822399
258.8793434580	149.3907111555	1029.3155130573
260.3651361606	149.9463593268	1029.2347153709
261.8893158859	150.4627011253	1029.1593586856
263.4493210539	150.9370212312	1029.0899016227
265.0425814743	151.3666952627	1029.0267895275
266.6665262542	151.7491967936	1028.9704520891
268.3185913606	152.0821040363	1028.9213009905
269.9962268379	152.3631061917	1028.8797276026
271.6969036809	152.5900094706	1028.8461007409
273.4181203631	152.7607427882	1028.8207644983
275.1574090198	152.8733631353	1028.8040361720
276.9123412867	152.9260606297	1028.7962042991
278.6805337932	152.9171632499	1028.7975268164
280.4596533118	152.8451412546	1028.8082293581
282.2474215616	152.7086112903	1028.8285037059
284.0416196680	152.5063401899	1028.8585064050
285.8400922765	152.2372484641	1028.8983575553
287.6407513230	151.9004134881	1028.9481397924
289.4415794580	151.4950723847	1029.0078974639
291.2406331268	151.0206246060	1029.0776360137
293.0360453045	150.4766342136	1029.1573215771
294.8260278865	149.8628318594	1029.2468807954
296.6088737340	149.1791164658	1029.3462008530
298.3829583745	148.4255566057	1029.4551297392
300.1467413579	147.6023915826	1029.5734767364
301.8987672674	146.7100322081	1029.7010131342
303.6376663859	145.7490612771	1029.8374731660
305.3621550173	144.7202337380	1029.9825551663
307.0710354634	143.6244765556	1030.1359229413
308.7631956551	142.4628882656	1030.2972073470
310.4376084402	141.2367382162	1030.4660080653
312.0933305251	139.9474654946	1030.6418955688
313.7295010720	138.5966775354	1030.8244132616
315.3453399519	137.1861484069	1031.0130797838
316.9401456523	135.7178167715	1031.2073914644

318.5132928396	134.1937835167	1031.4068249074
320.0642295778	132.6163090532	1031.6108396935
321.5924742015	130.9878102757	1031.8188811798
323.0976118446	129.3108571827	1032.0303833777
324.5792906235	127.5881691521	1032.2447718891
326.0372174765	125.8226108682	1032.4614668811
327.4711536576	124.0171878980	1032.6798860760
328.8809098855	122.1750419117	1032.8994477363
330.2663411486	120.2994455477	1033.1195736220
331.6273411639	118.3937969159	1033.3396918980
332.9638364923	116.4616137399	1033.5592399689
334.2757803081	114.5065271360	1033.7776672202
335.5631458248	112.5322750258	1033.9944376434
336.8259193748	110.5426951842	1034.2090323244
338.0640931451	108.5417179198	1034.4209517750
339.2776575683	106.5333583901	1034.6297180877
340.4665933682	104.5217085492	1034.8348768968
341.6308632608	102.5109287317	1035.0359991278
342.7704033110	100.5052388713	1035.2326825209
343.8851139434	98.5089093577	1035.4245529140
344.9748506097	96.5262515329	1035.6112652752
346.0394141097	94.5616078292	1035.7925044741
347.0785405691	92.6193415512	1035.9679857846
348.0918910710	90.7038263049	1036.1374551157
349.0790409438	88.8194350771	1036.3006889666
350.0394687034	86.9705289668	1036.4574941073
350.9725446512	85.1614455733	1036.6077069885
351.8775191270	83.3964870424	1036.7511928852
352.7535104167	81.6799077754	1036.8878447864
353.5994923165	80.0159018021	1037.0175820394
354.4142813503	78.4085898219	1037.1403487678
355.1965236442	76.8620059150	1037.2561120797
355.9446814551	75.3800839254	1037.3648600890
356.6570193546	73.9666435190	1037.4665997740
357.3315900685	72.6253759174	1037.5613547029
357.9662199710	71.3598293100	1037.6491626561
358.5584942342	70.1733939440	1037.7300731801
359.1057416333	69.0692868949	1037.8041451102
359.6050190064	68.0505365167	1037.8714441008
360.0530953693	67.1199665737	1037.9320402065
360.4464356864	66.2801800514	1037.9860055571
360.7811842958	65.5335426502	1038.0334121731
361.0531479904	64.8821659584	1038.0743299690
361.2577787534	64.3278903064	1038.1088249932

361.2687684853	64.2933990891	1038.1109617154
361.2797582172	64.2589078008	1038.1130972915
361.2996567329	64.1892986131	1038.1174037379
361.3174564287	64.1191252556	1038.1217403448
361.3331413179	64.0484507484	1038.1261031092
361.3466973129	63.9773385624	1038.1304880170
361.3581122385	63.9058525621	1038.1348910466
361.3673758423	63.8340569489	1038.1393081728
361.3744798041	63.7620162030	1038.1437353708
361.3794177436	63.6897950255	1038.1481686203
361.3821852258	63.6174582805	1038.1526039085
361.3827797649	63.5450709365	1038.1570372346
361.3812008271	63.4726980085	1038.1614646131
361.3774498305	63.4004044994	1038.1658820773
361.3715301439	63.3282553414	1038.1702856831
361.3634470843	63.2563153381	1038.1746715124
361.3532079114	63.1846491059	1038.1790356761
361.3408218215	63.1133210161	1038.1833743180
361.3262999392	63.0423951372	1038.1876836176
361.3096553074	62.9719351771	1038.1919597936
361.2909028755	62.9020044260	1038.1961991065
361.2700594860	62.8326656995	1038.2003978621
361.2471438594	62.7639812821	1038.2045524142
361.2221765775	62.6960128715	1038.2086591673
361.1951800647	62.6288215227	1038.2127145796
361.1661785678	62.5624675935	1038.2167151653
361.1351981347	62.4970106901	1038.2206574976
361.1022665905	62.4325096134	1038.2245382110
361.0674135126	62.3690223066	1038.2283540034
361.0306702046	62.3066058027	1038.2321016388
360.9920696673	62.2453161731	1038.2357779496
360.9516465701	62.1852084778	1038.2393798381
360.9094372188	62.1263367154	1038.2429042793
360.8654795239	62.0687537747	1038.2463483224
360.8198129662	62.0125113872	1038.2497090929
360.7724785611	61.9576600804	1038.2529837941
360.7235188220	61.9042491328	1038.2561697092
360.6729777223	61.8523265291	1038.2592642028
360.6209006555	61.8019389173	1038.2622647222
360.5673343947	61.7531315667	1038.2651687992
360.5123270506	61.7059483273	1038.2679740515
360.4559280280	61.6604315902	1038.2706781837
360.3981879819	61.6166222496	1038.2732789890
360.3391587716	61.5745596661	1038.2757743499

360.2788934143	61.5342816310	1038.2781622399
360.2174460374	61.4958243325	1038.2804407238
360.1548718299	61.4592223233	1038.2826079596
360.0912269930	61.4245084893	1038.2846621986
360.0265686894	61.3917140202	1038.2866017866
359.9609549921	61.3608683812	1038.2884251649
359.8944448321	61.3319992868	1038.2901308707
359.8270979456	61.3051326755	1038.2917175378
359.7589748204	61.2802926870	1038.2931838976
359.6901366413	61.2575016400	1038.2945287792
359.6206452355	61.2367800122	1038.2957511103
359.5505630168	61.2181464223	1038.2968499175
359.4799529297	61.2016176126	1038.2978243267
359.4088783926	61.1872084345	1038.2986735636
359.3374032415	61.1749318348	1038.2993969540
359.2655916716	61.1647988443	1038.2999939239
359.1935081809	61.1568185675	1038.3004640000
359.1212175111	61.1509981751	1038.3008068100
359.0487845902	61.1473428966	1038.3010220821
358.9762744740	61.1458560164	1038.3011096460
358.9037522876	61.1465388705	1038.3010694323
358.8312831669	61.1493908454	1038.3009014728
358.7589322001	61.1544093784	1038.3006059006
358.6867643694	61.1615899604	1038.3001829498
358.6148444925	61.1709261395	1038.2996329554
358.5432371643	61.1824095269	1038.2989563534
358.4720066990	61.1960298046	1038.2981536804
358.4012170725	61.2117747346	1038.2972255736
358.3309318645	61.2296301699	1038.2961727702
358.2612142018	61.2495800672	1038.2949961074
358.1921267014	61.2716065014	1038.2936965217
358.1237314145	61.2956896816	1038.2922750490
358.0560897703	61.3218079690	1038.2907328236
357.9892625213	61.3499378965	1038.2890710780
357.9233096884	61.3800541895	1038.2872911423
357.8582905075	61.4121297888	1038.2853944436
357.7942633755	61.4461358750	1038.2833825050
357.7312857984	61.4820418942	1038.2812569456
357.6694143398	61.5198155859	1038.2790194790
357.6087045696	61.5594230115	1038.2766719129
357.5492110144	61.6008285852	1038.2742161479
357.4909871083	61.6439951058	1038.2716541770
357.4340851454	61.6888837902	1038.2689880839
357.3785562321	61.7354543084	1038.2662200425

357.3244502419	61.7836648197	1038.2633523155
357.2718157702	61.8334720101	1038.2603872532
357.2207000906	61.8848311317	1038.2573272921
357.1711491129	61.9376960426	1038.2541749538
357.1232073413	61.9920192484	1038.2509328431
357.0769178349	62.0477519450	1038.2476036469
357.0323221685	62.1048440626	1038.2441901325
356.9894603959	62.1632443104	1038.2406951458
356.9483710135	62.2229002231	1038.2371216094
356.9090909257	62.2837582076	1038.2334725213
356.8716554120	62.3457635918	1038.2297509521
356.8360980952	62.4088606731	1038.2259600441
356.7481482403	62.5741675580	1038.2160100646
356.6601983854	62.7394728566	1038.2060337648
356.4163794852	63.2062731094	1038.1777193909
356.1070246910	63.8002968274	1038.1413834949
355.7344558683	64.5128530974	1038.0973469696
355.3009347445	65.3355215583	1038.0458947574
354.8086642019	66.2601492027	1037.9872844248
354.2597895719	67.2788471299	1037.9217536640
353.6563999274	68.3839872581	1037.8495268037
353.0005293766	69.5681990026	1037.7708204067
352.2941583560	70.8243659244	1037.6858480250
351.5392149240	72.1456223532	1037.5948241849
350.7375760538	73.5253499862	1037.4979676652
349.8910689272	74.9571744658	1037.3955041334
349.0014722272	76.4349619352	1037.2876681972
348.0705174321	77.9528155749	1037.1747049287
347.0998901080	79.5050721181	1037.0568709128
346.0912312029	81.0862983463	1036.9344348706
345.0461383392	82.6912875651	1036.8076779041
343.9661671074	84.3150560597	1036.6768934059
342.8528323595	85.9528395301	1036.5423866764
341.7076095020	87.6000895071	1036.4044742852
340.5319357893	89.2524697477	1036.2634832145
339.3272116173	90.9058526121	1036.1197498170
338.0948018160	92.5563154211	1035.9736186195
336.8360369435	94.2001367960	1035.8254410023
335.5522145787	95.8337929815	1035.6755737792
334.2446006152	97.4539541517	1035.5243777044
332.9144305540	99.0574807023	1035.3722159286
331.5629107973	100.6414195274	1035.2194524233
330.1912199413	102.2030002861	1035.0664503946
328.8005100699	103.7396316562	1034.9135707023

327.3919080477	105.2488975804	1034.7611702988
325.9665168137	106.7285535035	1034.6096007031
324.5254166740	108.1765226043	1034.4592065216
323.0696665956	109.5908920229	1034.3103240254
321.6003054993	110.9699090849	1034.1632797956
320.1183535533	112.3119775247	1034.0183894421
318.6248134665	113.6156537090	1033.8759564050
317.1206717815	114.8796428617	1033.7362708428
315.6069001681	116.1027952926	1033.5996086131
314.0844567165	117.2841026300	1033.4662303483
312.5542872307	118.4226940590	1033.3363806292
311.0173265217	119.5178325665	1033.2102872594
309.4744997009	120.5689111943	1033.0881606395
307.9267234732	121.5754492998	1032.9701932425
306.3749074305	122.5370888270	1032.8565591900
304.8199553447	123.4535905862	1032.7474139263
303.2627664615	124.3248305452	1032.6428939909
301.7042367930	125.1507961299	1032.5431168857
300.1452604117	125.9315825368	1032.4481810337
298.5867307432	126.6673890557	1032.3581658271
297.0295418599	127.3585154037	1032.2731317603
295.4745897741	128.0053580700	1032.1931206443
293.9227737314	128.6084066710	1032.1181558976
292.3749975037	129.1682403160	1032.0482429100
290.8321706829	129.6855239831	1031.9833694732
289.2952099739	130.1610049033	1031.9235062748
287.7650404882	130.5955089550	1031.8686074500
286.2425970366	130.9899370655	1031.8186111849
284.7288254231	131.3452616211	1031.7734403684
283.2246837381	131.6625228835	1031.7330032852
281.7311436513	131.9428254130	1031.6971943463
280.2491917054	132.1873344963	1031.6658948510
278.7798306091	132.3972725802	1031.6389737759
277.3240805306	132.5739157086	1031.6162885849
275.8829803909	132.7185899626	1031.5976860571
274.4575891569	132.8326679040	1031.5830031255
273.0489871348	132.9175650196	1031.5720677244
271.6582772634	132.9747361674	1031.5646996390
270.2865864074	133.0056720228	1031.5607113543
268.9350666506	133.0118955245	1031.5599088996
267.6048965895	132.9949583205	1031.5620926834
266.2972826260	132.9564372118	1031.5670583166
265.0134602612	132.8979305948	1031.5745974207
263.7546953886	132.8210549012	1031.5844984173

262.5222855873	132.7274410358	1031.5965472975
261.3175614153	132.6187308106	1031.6105283673
260.1418877027	132.4965733761	1031.6262249689
258.9966648452	132.3626216487	1031.6434201750
257.8833300973	132.2185287346	1031.6618974544
256.8033588655	132.0659443502	1031.6814413097
255.7582660017	131.9065112376	1031.7018378839
254.7496070966	131.7418615772	1031.7228755379
253.7789797726	131.5736133956	1031.7443453967
252.8480249774	131.4033669697	1031.7660418666
251.9584282775	131.2327012274	1031.7877631221
251.1119211508	131.0631701441	1031.8093115648
250.3102822806	130.8962991363	1031.8304942540
249.5553388486	130.7335814511	1031.8511233124
248.8489678280	130.5764745534	1031.8710163064
248.1930972772	130.4263965099	1031.8899966050
247.5897076327	130.2847223713	1031.9078937176
247.0408330027	130.1527805511	1031.9245436149
246.5485624602	130.0318492037	1031.9397890345
246.1150413363	129.9231526009	1031.9534797743
245.7424725136	129.8278575070	1031.9654729763
245.4331177195	129.7470695532	1031.9756334053
245.1892988192	129.6818296121	1031.9838337244
245.0133991095	129.6331101719	1031.9899547705
244.9763801154	129.6229971234	1031.9912250677
244.9393611213	129.6128840625	1031.9924952658
244.8649084771	129.5942164190	1031.9948396532
244.7900744972	129.5771156064	1031.9969869680
244.7148926728	129.5615892878	1031.9989363276
244.6393966505	129.5476444209	1032.0006869305
244.5636202179	129.5352872544	1032.0022380576
244.4875972878	129.5245233260	1032.0035890718
244.4113618833	129.5153574592	1032.0047394185
244.3349481229	129.5077937613	1032.0056886254
244.2583902046	129.5018356219	1032.0064363029
244.1817223911	129.4974857109	1032.0069821443
244.1049789942	129.4947459777	1032.0073259256
244.0281943594	129.4936176500	1032.0074675059
243.9514028510	129.4941012335	1032.0074068270
243.8746388361	129.4961965114	1032.0071439138
243.7979366695	129.4999025448	1032.0066788742
243.7213306785	129.5052176729	1032.0060118989
243.6448551472	129.5121395138	1032.0051432617
243.5685443014	129.5206649658	1032.0040733189

243.4924322931	129.5307902084	1032.0028025098
243.4165531854	129.5425107042	1032.0013313560
243.3409409372	129.5558212010	1031.9996604616
243.2656293878	129.5707157342	1031.9977905132
243.1906522421	129.5871876293	1031.9957222791
243.1160430552	129.6052295051	1031.9934566096
243.0418352178	129.6248332767	1031.9909944365
242.9680619406	129.6459901596	1031.9883367730
242.8947562400	129.6686906732	1031.9854847134
242.8219509232	129.6929246455	1031.9824394324
242.7496785734	129.7186812173	1031.9792021854
242.6779715353	129.7459488471	1031.9757743076
242.6068619006	129.7747153168	1031.9721572138
242.5363814935	129.8049677364	1031.9683523980
242.4665618568	129.8366925504	1031.9643614329
242.3974342374	129.8698755438	1031.9601859695
242.3290295727	129.9045018481	1031.9558277366
242.2613784764	129.9405559487	1031.9512885402
242.1945112250	129.9780216910	1031.9465702629
242.1284577442	130.0168822884	1031.9416748635
242.0632475954	130.0571203296	1031.9366043762
241.9989099627	130.0987177861	1031.9313609104
241.9354736398	130.1416560209	1031.9259466493
241.8729670168	130.1859157964	1031.9203638500
241.8114180678	130.2314772834	1031.9146148420
241.7508543385	130.2783200694	1031.9087020274
241.6913029333	130.3264231688	1031.9026278792
241.6327905040	130.3757650313	1031.8963949411
241.5753432370	130.4263235521	1031.8900058265
241.5189868422	130.4780760819	1031.8834632176
241.4637465413	130.5309994367	1031.8767698645
241.4096470566	130.5850699086	1031.8699285845
241.3567125995	130.6402632762	1031.8629422608
241.3049668603	130.6965548157	1031.8558138419
241.2544329973	130.7539193118	1031.8485463403
241.2051336262	130.8123310689	1031.8411428317
241.1570908106	130.8717639232	1031.8336064539
241.1103260513	130.9321912539	1031.8259404054
241.0648602775	130.9935859952	1031.8181479447
241.0207138368	131.0559206489	1031.8102323891
240.9779064865	131.1191672963	1031.8021971132
240.9364573845	131.1832976107	1031.7940455478
240.8963850809	131.2482828705	1031.7857811792
240.8577075097	131.3140939719	1031.7774075470

240.8204419805	131.3807014418	1031.7689282435
240.7846051710	131.4480754511	1031.7603469121
240.7502131198	131.5161858285	1031.7516672461
240.7172812184	131.5850020733	1031.7428929871
240.6858242053	131.6544933697	1031.7340279237
240.6558561587	131.7246286003	1031.7250758899
240.6273904904	131.7953763602	1031.7160407642
240.6004399399	131.8667049709	1031.7069264671
240.5750165686	131.9385824950	1031.6977369604
240.5511317545	132.0109767496	1031.6884762454
240.5287961870	132.0838553219	1031.6791483612
240.5080198620	132.1571855827	1031.6697573831
240.4888120779	132.2309347016	1031.6603074210
240.4711814308	132.3050696616	1031.6508026177
240.4551358111	132.3795572738	1031.6412471475
240.4406823998	132.4543641924	1031.6316452137
240.4278276655	132.5294569295	1031.6220010478
240.4165773611	132.6048018703	1031.6123189071
240.4069365216	132.6803652879	1031.6026030730
240.3989094615	132.7561133586	1031.5928578494
240.3924997734	132.8320121772	1031.5830875606
240.3877103259	132.9080277715	1031.5732965494
240.3845432622	132.9841261186	1031.5634891758
240.3830000000	133.0602731591	1031.5536698140
240.3830812298	133.1364348129	1031.5438428517
240.3847869152	133.2125769944	1031.5340126872
240.3881162930	133.2886656275	1031.5241837278
240.3930678731	133.3646666614	1031.5143603878
240.3996394394	133.4405460850	1031.5045470867
240.4078280510	133.5162699430	1031.4947482467
240.4176300431	133.5918043505	1031.4849682910
240.4290410289	133.6671155084	1031.4752116419
240.4420559016	133.7421697183	1031.4654827182
240.4566688366	133.8169333980	1031.4557859336
240.4728732939	133.8913730960	1031.4461256946
240.4906620215	133.9654555069	1031.4365063982

2, Transonic rotor profile at the midspan (unit: [mm])

53.9092631799	33.6690728731	273.9789684116
53.9574759770	33.7945936340	273.9635140691
54.0220652128	33.9301935979	273.9467531518
54.1031977208	34.0734807068	273.9289680054
54.2009623983	34.2222074452	273.9104271794

54.3153747369	34.3742664305	273.8913861504
54.4463812500	34.5276860418	273.8720878377
54.5938637991	34.6806260901	273.8527629475
54.7576438188	34.8313735341	273.8336301803
54.9374864390	34.9783382449	273.8148963326
55.1331045066	35.1200488225	273.7967563188
55.3441625048	35.2551484666	273.7793931372
55.5702803707	35.3823909049	273.7629777999
55.8110372117	35.5006363805	273.7476692441
56.0659749194	35.6088477002	273.7336142410
56.3346016825	35.7060863461	273.7209473129
56.6163953980	35.7915086518	273.7097906697
56.9108069796	35.8643620442	273.7002541745
57.2172635662	35.9239813519	273.6924353427
57.5351716270	35.9697851826	273.6864193816
57.8639199658	36.0012723675	273.6822792727
58.2028826238	36.0180184762	273.6800759008
58.5514216796	36.0196724003	273.6798582289
58.9088899488	36.0059530068	273.6816635218
59.2746335809	35.9766458616	273.6855176157
59.6479945550	35.9316000225	273.6914352329
60.0283130738	35.8707249012	273.6994203411
60.4149298556	35.7939871953	273.7094665529
60.8071883248	35.7014078885	273.7215575631
61.2044367008	35.5930593188	273.7356676218
61.6060299847	35.4690623155	273.7517620372
62.0113318451	35.3295834017	273.7697977072
62.4197164015	35.1748320646	273.7897236735
62.8305699061	35.0050580906	273.8114816951
63.2432923243	34.8205489659	273.8350068375
63.6572988130	34.6216273413	273.8602280731
64.0720210977	34.4086485604	273.8870688883
64.4869087474	34.1819982512	273.9154478951
64.9014303478	33.9420899792	273.9452794407
65.3150745735	33.6893629633	273.9764742147
65.7273511577	33.4242798512	274.0089398476
66.1377917604	33.1473245572	274.0425814991
66.5459507353	32.8590001583	274.0773024324
66.9514057942	32.5598268511	274.1130045719
67.3537585708	32.2503399671	274.1495890422
67.7526350815	31.9310880478	274.1869566848
68.1476860858	31.6026309774	274.2250085519
68.5385873438	31.2655381752	274.2636463745
68.9250397729	30.9203868447	274.3027730034

69.3067695023	30.5677602824	274.3422928229
69.6835278260	30.2082462440	274.3821121335
70.0550910540	29.8424353689	274.4221395064
70.4212602618	29.4709196627	274.4622861055
70.7818609382	29.0942910383	274.5024659798
71.1367425317	28.7131399156	274.5425963238
71.4857778944	28.3280538791	274.5825977068
71.8288626251	27.9396163951	274.6223942720
72.1659143103	27.5484055875	274.6619139043
72.4968716632	27.1549930726	274.7010883692
72.8216935614	26.7599428540	274.7398534222
73.1403579832	26.3638102770	274.7781488905
73.4528608409	25.9671410428	274.8159187275
73.7592147143	25.5704702835	274.8531110420
74.0594474806	25.1743216972	274.8896781021
74.3536008440	24.7792067445	274.9255763168
74.6417287627	24.3856239055	274.9607661954
74.9238957749	23.9940579990	274.9952122869
75.2001752223	23.6049795626	275.0288831011
75.4706473730	23.2188442952	275.0617510117
75.7353974411	22.8360925612	275.0937921447
75.9945135065	22.4571489575	275.1249862530
76.2480843313	22.0824219426	275.1553165780
76.4961970755	21.7123035286	275.1847697012
76.7389349108	21.3471690355	275.2133353858
76.9763745324	20.9873769097	275.2410064116
77.2085835694	20.6332686039	275.2677784026
77.4356178934	20.2851685217	275.2936496508
77.6575188253	19.9433840244	275.3186209352
77.8743102405	19.6082055015	275.3426953398
78.0859955726	19.2799065047	275.3658780698
78.2925547147	18.9587439452	275.3881762676
78.4939408201	18.6449583540	275.4095988305
78.6900769999	18.3387742065	275.4301562295
78.8808529204	18.0404003095	275.4498603316
79.0661212974	17.7500302524	275.4687242248
79.2456942899	17.4678429212	275.4867620480
79.4193397915	17.1940030764	275.5039888245
79.5867776201	16.9286619935	275.5204203015
79.7476756061	16.6719581676	275.5360727942
79.9016455789	16.4240180801	275.5509630361
80.0482392515	16.1849570298	275.5651080343
80.1869440036	15.9548800262	275.5785249314
80.3171785629	15.7338827459	275.5912308724

80.4382885844	15.5220525525	275.6032428774
80.5495421289	15.3194695787	275.6145777201
80.6501250385	15.1262078718	275.6252518102
80.7391362115	14.9423366018	275.6352810815
80.8155827751	14.7679213320	275.6446808838
80.8783751565	14.6030253523	275.6534658780
80.9263220520	14.4477110758	275.6616499346
80.9277179009	14.4421582675	275.6619409069
80.9291137499	14.4366054533	275.6622317674
80.9315906892	14.4254255969	275.6628170362
80.9337508992	14.4141804008	275.6634052670
80.9355926612	14.4028788113	275.6639959841
80.9371145100	14.3915298197	275.6645887114
80.9383152347	14.3801424551	275.6651829720
80.9391938800	14.3687257770	275.6657782888
80.9397497468	14.3572888684	275.6663741851
80.9399823931	14.3458408285	275.6669701849
80.9398916335	14.3343907653	275.6675658132
80.9394775404	14.3229477885	275.6681605965
80.9387404432	14.3115210022	275.6687540629
80.9376809284	14.3001194979	275.6693457430
80.9362998388	14.2887523467	275.6699351695
80.9345982733	14.2774285926	275.6705218785
80.9325775857	14.2661572452	275.6711054091
80.9302393836	14.2549472724	275.6716853038
80.9275855273	14.2438075932	275.6722611095
80.9246181282	14.2327470709	275.6728323771
80.9213395471	14.2217745057	275.6733986621
80.9177523926	14.2108986281	275.6739595250
80.9138595185	14.2001280916	275.6745145315
80.9096640221	14.1894714658	275.6750632530
80.9051692412	14.1789372299	275.6756052665
80.9003787520	14.1685337658	275.6761401553
80.8952963657	14.1582693513	275.6766675092
80.8899261259	14.1481521535	275.6771869246
80.8842723052	14.1381902226	275.6776980048
80.8783394018	14.1283914853	275.6782003606
80.8721321358	14.1187637383	275.6786936100
80.8656554459	14.1093146424	275.6791773789
80.8589144848	14.1000517163	275.6796513013
80.8519146157	14.0909823306	275.6801150191
80.8446614076	14.0821137020	275.6805681830
80.8371606313	14.0734528873	275.6810104520
80.8294182544	14.0650067780	275.6814414942

80.8214404367	14.0567820951	275.6818609868
80.8132335254	14.0487853831	275.6822686160
80.8048040499	14.0410230051	275.6826640777
80.7961587167	14.0335011381	275.6830470773
80.7873044041	14.0262257674	275.6834173300
80.7782481565	14.0192026823	275.6837745609
80.7689971791	14.0124374714	275.6841185054
80.7595588321	14.0059355181	275.6844489090
80.7499406245	13.9997019963	275.6847655276
80.7401502086	13.9937418664	275.6850681277
80.7301953738	13.9880598711	275.6853564864
80.7200840400	13.9826605319	275.6856303917
80.7098242519	13.9775481455	275.6858896423
80.6994241721	13.9727267799	275.6861340480
80.6888920751	13.9682002720	275.6863634298
80.6782363401	13.9639722237	275.6865776198
80.6674654448	13.9600459996	275.6867764614
80.6565879586	13.9564247241	275.6869598093
80.6456125357	13.9531112788	275.6871275298
80.6345479081	13.9501083005	275.6872795005
80.6234028788	13.9474181789	275.6874156108
80.6121863148	13.9450430547	275.6875357614
80.6009071401	13.9429848180	275.6876398651
80.5895743283	13.9412451067	275.6877278460
80.5781968959	13.9398253052	275.6877996402
80.5667838948	13.9387265433	275.6878551956
80.5553444052	13.9379496955	275.6878944718
80.5438875283	13.9374953799	275.6879174402
80.5324223792	13.9373639580	275.6879240843
80.5209580797	13.9375555345	275.6879143991
80.5095037508	13.9380699568	275.6878883917
80.4980685055	13.9389068157	275.6878460810
80.4866614417	13.9400654451	275.6877874977
80.4752916349	13.9415449231	275.6877126844
80.4639681309	13.9433440723	275.6876216954
80.4526999388	13.9454614610	275.6875145969
80.4414960235	13.9478954042	275.6873914668
80.4303652989	13.9506439650	275.6872523947
80.4193166206	13.9537049563	275.6870974819
80.4083587789	13.9570759422	275.6869268412
80.3975004919	13.9607542401	275.6867405971
80.3867503985	13.9647369229	275.6865388855
80.3761170515	13.9690208214	275.6863218538
80.3656089107	13.9736025266	275.6860896607

80.3552343365	13.9784783925	275.6858424762
80.3450015829	13.9836445391	275.6855804815
80.3349187911	13.9890968553	275.6853038687
80.3249939829	13.9948310025	275.6850128411
80.3152350546	14.0008424177	275.6847076129
80.3056497703	14.0071263172	275.6843884088
80.2962457562	14.0136777007	275.6840554644
80.2870304941	14.0204913548	275.6837090257
80.2780113156	14.0275618576	275.6833493491
80.2691953965	14.0348835830	275.6829767012
80.2605897506	14.0424507045	275.6825913586
80.2522012247	14.0502572009	275.6821936081
80.2440364926	14.0582968603	275.6817837460
80.2361020503	14.0665632851	275.6813620783
80.2284042104	14.0750498977	275.6809289203
80.2209490974	14.0837499451	275.6804845967
80.2137426424	14.0926565043	275.6800294411
80.2067905790	14.1017624885	275.6795637959
80.2000984382	14.1110606518	275.6790880123
80.1794880049	14.1401595495	275.6775970004
80.1588775716	14.1692582896	275.6761029170
80.1024156567	14.2476324146	275.6720634569
80.0312515265	14.3453786729	275.6669942353
79.9459099777	14.4616990157	275.6609164564
79.8469020661	14.5958019433	275.6538484506
79.7347254017	14.7469027461	275.6458061705
79.6098644446	14.9142237461	275.6368036566
79.4727908003	15.0969945363	275.6268534740
79.3239635153	15.2944522192	275.6159671197
79.1638293727	15.5058416449	275.6041554021
78.9928231876	15.7304156489	275.5914287918
78.8113681022	15.9674352888	275.5777977456
78.6198758823	16.2161700811	275.5632730026
78.4187472118	16.4758982377	275.5478658550
78.2083719888	16.7459069019	275.5315883924
77.9891296208	17.0254923841	275.5144537208
77.7613893205	17.3139603973	275.4964761578
77.5255104009	17.6106262928	275.4776714029
77.2818425713	17.9148152942	275.4580566855
77.0307262323	18.2258627328	275.4376508897
76.7724927719	18.5431142808	275.4164746575
76.5074648602	18.8659261852	275.3945504711
76.2359567458	19.1936655006	275.3719027146
75.9582745507	19.5257103215	275.3485577163

75.6747165659	19.8614500133	275.3245437722
75.3855735471	20.2002854438	275.2998911514
75.0911290100	20.5416292123	275.2746320846
74.7916595261	20.8849058785	275.2488007357
74.4874350178	21.2295521906	275.2224331587
74.1787190541	21.5750173121	275.1955672390
73.8657691463	21.9207630470	275.1682426216
73.5488370433	22.2662640645	275.1405006258
73.2281690269	22.6110081222	275.1123841482
72.9040062078	22.9544962885	275.0839375539
72.5765848208	23.2962431625	275.0552065577
72.2461365201	23.6357770944	275.0262380958
71.9128886755	23.9726404031	274.9970801883
71.5770646671	24.3063895938	274.9677817944
71.2388841813	24.6365955730	274.9383926602
70.8985635062	24.9628438636	274.9089631610
70.5563158270	25.2847348182	274.8795441374
70.2123515217	25.6018838312	274.8501867278
69.8668784564	25.9139215498	274.8209421967
69.5201022809	26.2204940850	274.7918617607
69.1722267244	26.5212632198	274.7629964119
68.8234538906	26.8159066185	274.7343967403
68.4739845535	27.1041180337	274.7061127562
68.1240184527	27.3856075138	274.6781937124
67.7737545893	27.6601016091	274.6506879274
67.4233915209	27.9273435779	274.6236426105
67.0731276575	28.1870935922	274.5971036898
66.7231615567	28.4391289426	274.5711156422
66.3736922196	28.6832442440	274.5457213282
66.0249193858	28.9192516405	274.5209618309
65.6770438293	29.1469810109	274.4968762991
65.3302676538	29.3662801738	274.4735017971
64.9847945885	29.5770150935	274.4508731598
64.6408302832	29.7790700864	274.4290228543
64.2985826040	29.9723480272	274.4079808492
63.9582619289	30.1567705567	274.3877744900
63.6200814431	30.3322782895	274.3684283837
63.2842574347	30.4988310228	274.3499642906
62.9510095901	30.6564079459	274.3324010245
62.6205612894	30.8050078514	274.3157543622
62.2931399024	30.9446493460	274.3000369611
61.9689770833	31.0753710639	274.2852582864
61.6483090669	31.1972318800	274.2714245470
61.3313769639	31.3103111252	274.2585386405

61.0184270561	31.4147088026	274.2466001081
60.7097110924	31.5105458041	274.2356050974
60.4054865841	31.5979641297	274.2255463352
60.1060171002	31.6771271069	274.2164131088
59.8115725631	31.7482196111	274.2081912553
59.5224295443	31.8114482881	274.2008631602
59.2388715595	31.8670417768	274.1944077628
58.9611893644	31.9152509333	274.1888005697
58.6896812500	31.9563490563	274.1840136751
58.4246533383	31.9906321123	274.1800157872
58.1664198779	32.0184189628	274.1767722604
57.9153035389	32.0400515918	274.1742451325
57.6716357093	32.0558953332	274.1723931660
57.4357567897	32.0663390999	274.1711718922
57.2080164894	32.0717956122	274.1705336578
56.9887741214	32.0727016266	274.1704276730
56.7783988984	32.0695181651	274.1708000584
56.5772702279	32.0627307441	274.1715938919
56.3857780080	32.0528496024	274.1727492519
56.2043229226	32.0404099299	274.1742032568
56.0333167375	32.0259720946	274.1758900987
55.8731825949	32.0101218691	274.1777410694
55.7243553099	31.9934706564	274.1796845781
55.5872816656	31.9766557134	274.1816461570
55.4624207085	31.9603403740	274.1835484546
55.3502440441	31.9452142700	274.1853112135
55.2512361325	31.9319935494	274.1868512310
55.1658945837	31.9214210932	274.1880823001
55.0947304535	31.9142667298	274.1889151281
55.0382685386	31.9113274451	274.1892572306
54.9970476720	31.9134275913	274.1890127984
54.9852477495	31.9152640771	274.1887990398
54.9734478271	31.9171005615	274.1885852689
54.9499168362	31.9211861981	274.1881096468
54.9264620128	31.9256832292	274.1875860617
54.9030906463	31.9305902549	274.1870146560
54.8798100006	31.9359057474	274.1863955854
54.8566273112	31.9416280521	274.1857290185
54.8335497829	31.9477553874	274.1850151371
54.8105845883	31.9542858459	274.1842541359
54.7877388648	31.9612173946	274.1834462229
54.7650197127	31.9685478757	274.1825916187
54.7424341930	31.9762750071	274.1816905570
54.7199893251	31.9843963834	274.1807432844

54.6976920848	31.9929094765	274.1797500605
54.6755494019	32.0018116363	274.1787111575
54.6535681583	32.0111000916	274.1776268606
54.6317551855	32.0207719511	274.1764974677
54.6101172630	32.0308242040	274.1753232893
54.5886611157	32.0412537214	274.1741046488
54.5673934121	32.0520572566	274.1728418819
54.5463207619	32.0632314470	274.1715353372
54.5254497146	32.0747728143	274.1701853756
54.5047867566	32.0866777662	274.1687923706
54.4843383099	32.0989425970	274.1673567078
54.4641107299	32.1115634893	274.1658787856
54.4441103030	32.1245365149	274.1643590143
54.4243432453	32.1378576359	274.1627978165
54.4048157003	32.1515227064	274.1611956271
54.3855337371	32.1655274731	274.1595528928
54.3665033483	32.1798675775	274.1578700725
54.3477304486	32.1945385565	274.1561476370
54.3292208724	32.2095358442	274.1543860687
54.3109803724	32.2248547733	274.1525858620
54.2930146176	32.2404905764	274.1507475229
54.2753291917	32.2564383876	274.1488715690
54.2579295913	32.2726932440	274.1469585291
54.2408212240	32.2892500872	274.1450089438
54.2240094069	32.3061037651	274.1430233647
54.2074993652	32.3232490331	274.1410023545
54.1912962301	32.3406805561	274.1389464873
54.1754050374	32.3583929101	274.1368563478
54.1598307259	32.3763805837	274.1347325318
54.1445781361	32.3946379801	274.1325756457
54.1296520085	32.4131594185	274.1303863064
54.1150569819	32.4319391362	274.1281651415
54.1007975925	32.4509712904	274.1259127888
54.0868782719	32.4702499597	274.1236298964
54.0733033462	32.4897691462	274.1213171222
54.0600770344	32.5095227773	274.1189751345
54.0472034472	32.5295047078	274.1166046110
54.0346865856	32.5497087213	274.1142062392
54.0225303398	32.5701285328	274.1117807161
54.0107384879	32.5907577900	274.1093287480
53.9993146947	32.6115900759	274.1068510503
53.9882625107	32.6326189104	274.1043483476
53.9775853708	32.6538377524	274.1018213731
53.9672865934	32.6752400020	274.0992708688

53.9573693793	32.6968190022	274.0966975852
53.9478368108	32.7185680414	274.0941022812
53.9386918505	32.7404803553	274.0914857235
53.9299373405	32.7625491289	274.0888486870
53.9215760019	32.7847674988	274.0861919544
53.9136104331	32.8071285552	274.0835163157
53.9060431099	32.8296253443	274.0808225684
53.8988763842	32.8522508701	274.0781115171
53.8921124833	32.8749980968	274.0753839733
53.8857535094	32.8978599510	274.0726407554
53.8798014389	32.9208293240	274.0698826880
53.8742581215	32.9438990736	274.0671106022
53.8691252802	32.9670620268	274.0643253350
53.8644045102	32.9903109817	274.0615277293
53.8600972787	33.0136387101	274.0587186337
53.8562049244	33.0370379593	274.0558989018
53.8527286569	33.0605014547	274.0530693927
53.8496695567	33.0840219019	274.0502309702
53.8470285746	33.1075919891	274.0473845025
53.8448065312	33.1312043891	274.0445308626
53.8430041173	33.1548517620	274.0416709273
53.8416218930	33.1785267573	274.0388055773
53.8406602880	33.2022220157	274.0359356968
53.8401196009	33.2259301725	274.0330621735
53.8400000000	33.2496438585	274.0301858980
53.8403015223	33.2733557037	274.0273077637
53.8410240743	33.2970583384	274.0244286665
53.8421674312	33.3207443962	274.0215495046
53.8437312377	33.3444065161	274.0186711779
53.8457150079	33.3680373447	274.0157945881
53.8481181252	33.3916295386	274.0129206383
53.8509398426	33.4151757666	274.0100502326
53.8541792833	33.4386687122	274.0071842758
53.8578354405	33.4621010753	274.0043236732
53.8619071777	33.4854655752	274.0014693304
53.8663932296	33.5087549524	273.9986221526
53.8712922020	33.5319619709	273.9957830449
53.8766025721	33.5550794208	273.9929529113
53.8823226897	33.5781001198	273.9901326551
53.8884507768	33.6010169162	273.9873231779
53.8949849290	33.6238226908	273.9845253799
53.9019231155	33.6465103590	273.9817401592
53.9092631799	33.6690728731	273.9789684116